UNIVERSIDADE DE LISBOA
INSTITUTO SUPERIOR TÉCNICO

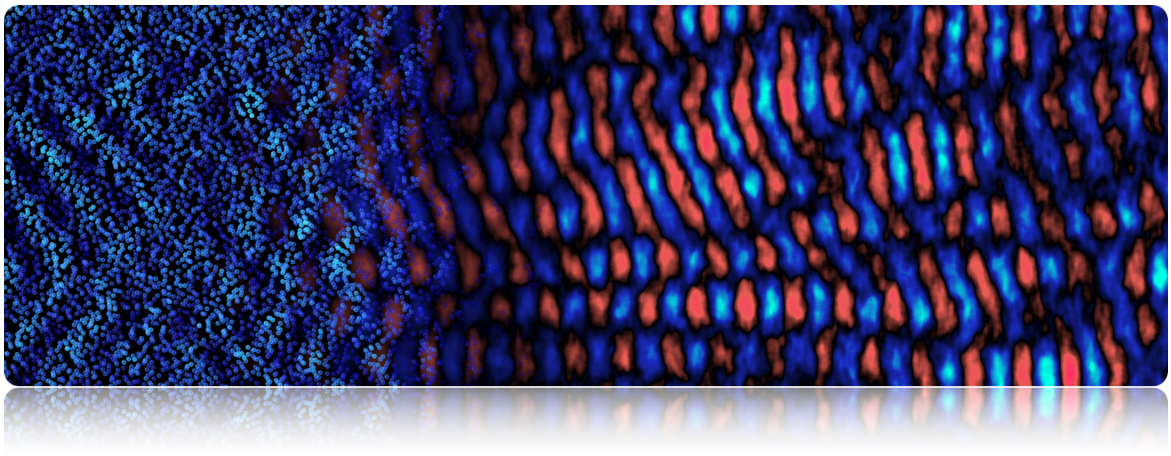

Kinetic Instabilities in Extreme Plasma Physics: Laboratory and Astrophysical Dynamics

Pablo Jaime Bilbao Santiago

Supervisor: Doctor Luís Miguel de Oliveira e Silva

Thesis approved in public session to obtain the PhD Degree in

Physics

Jury final classification: Pass with Distinction and Honour

2025

UNIVERSIDADE DE LISBOA
INSTITUTO SUPERIOR TÉCNICO

Kinetic Instabilities in Extreme Plasma Physics: Laboratory and Astrophysical Dynamics

Pablo Jaime Bilbao Santiago

Supervisor: Doctor Luís Miguel de Oliveira e Silva

Thesis approved in public session to obtain the PhD Degree in

Physics

Jury final classification: Pass with Distinction and Honour

Jury

Chairperson: Doctor Frederico Ricardo Pereira Fiúza, Instituto Superior Técnico, Universidade de Lisboa
Members of the committe:
Doctor Vladimir Tikhonchuk, Université de Bordeaux, França
Doctor Dmitri Uzdensky, Rudolf Peierls Centre for Theoretical Physics, University of Oxford, UK
Doctor Luís Miguel de Oliveira e Silva, Instituto Superior Técnico, Universidade de Lisboa
Doctor Jorge Miguel Ramos Domingues Ferreira Vieira, Instituto Superior Técnico, Universidade de Lisboa

Funding Institution: Fundação para a Ciência e a Tecnologia (FCT)

2025

Resumo:
A física de plasmas extremos explora regimes em que campos eletromagnéticos intensos, níveis de radiação elevada e efeitos de eletrodinâmica quântica (QED) alteram de forma fundamental o comportamento da matéria. Estas condições ocorrem em alguns dos ambientes astrofísicos mais extremos, como pulsares, buracos negros e choques relativistas, e estão cada vez mais acessíveis em experiências laboratoriais envolvendo lasers de alta intensidade e feixes de partículas. Esta Tese investiga como a reação à radiação, através do arrefecimento por emissão sincrotrão e betatrão, reestrutura o espaço de fases e desencadeia instabilidades cinéticas numa variedade de condições extremas de plasma. Em primeiro lugar, mostramos que o arrefecimento sincrotrão em plasmas fortemente magnetizados conduz genericamente à formação de distribuições de momento anisotrópicas em forma de anel, instáveis à instabilidade ciclotrónica electrónica (ECMI). A reação à radiação mantém a inversão populacional e permite a emissão coerente prolongada para além da saturação clássica. Em segundo lugar, demonstramos que a radiação betatrão em plasma wakefields induz efeitos semelhante em feixes de alta energia, formando feixes em formato de donut com anisotropias no ângulo de inclinação. Estas características são confirmadas por teoria analítica e simulações tridimensionais de larga escala. Por fim, simulações no contexto da experiência Fireball no CERN demonstram como feixes relativistas de eletrões e positrões desenvolvem instabilidades coletivas em condições laboratoriais realistas, fornecendo os primeiros análogos diretos da dinâmica de plasmas de pares em ambientes astrofísicos. Em conjunto, estes estudos representam dois fios condutores interligados da física de plasmas extremos, o arrefecimento radiativo e a cinética de pares, e estabelecem as bases para uma teoria cinética de plasmas estruturados radiactivamente, fundamentada em resultados teóricos, simulações e experiências, e abrindo novas vias para a exploração de processos astrofísicos de alta energia em laboratório.

Palavras-chave: Física de plasmas extremos; Arrefecimento síncrotron; Radiação betatron; Plasmas de pares; Instabilidades cinéticas

Abstract:
Extreme plasma physics explores regimes where strong electromagnetic fields, intense radiation, and quantum electrodynamics (QED) effects fundamentally alter the behavior of matter. These conditions are found in some of the most energetic astrophysical environments, such as pulsars, black holes, and relativistic shocks, and are increasingly accessible in laboratory experiments using high-intensity lasers and particle beams. This Thesis investigates how radiation reaction, through synchrotron and betatron cooling, reshapes phase space and triggers kinetic instabilities across a range of such extreme plasma conditions. First, we show that synchrotron cooling in strongly magnetized plasmas generically leads to anisotropic, ring-shaped momentum distributions that are unstable to the electron cyclotron maser instability (ECMI). Radiation reaction sustains population inversion and enables prolonged coherent emission beyond classical saturation. Second, we demonstrate that betatron radiation in plasma wakefields produces similar structuring in high-energy beams, forming spatially "donut beams" with momentum pitch-angle anisotropies. These features are confirmed through analytical theory and large-scale three-dimensional simulations. Finally, simulations in the context of the Fireball experiment at CERN demonstrate how relativistic electron-positron beams develop collective instabilities under realistic laboratory conditions, providing the first direct analogues of astrophysical pair-plasma dynamics. Together, these studies represent two interconnected threads of extreme plasma physics, radiative cooling and pair-plasma kinetics, and lay the groundwork for a kinetic theory of radiatively structured plasmas, bridging theory, simulation, and experiment, and opening new paths toward probing high-energy astrophysical processes in the laboratory.

Keywords: Extreme plasma physics; Synchrotron cooling; Betatron radiation; Pair plasmas; Kinetic instabilities

ACKNOWLEDGMENTS

> "Every new invention is a synthesis, the resultant of innumerable inventions which have preceded it ... Each discovery, each advance, each increase in the sum of human riches, owes its being to the physical and mental travail of the past and the present. By what right then can any one whatever appropriate the least morsel of this immense whole and say – This is mine, not yours?"
>
> — Peter Kropotkin - The conquest of bread 1892 [1]

The work presented in this thesis is not solely the result of my individual efforts, but is deeply shaped by the contributions of countless others. It reflects my interactions with mentors, colleagues, and the collective knowledge and discoveries of those who came before me. It also would not have been possible without the unwavering support of friends and loved ones, who encouraged me through challenging times, and the environments that gave me space to learn, grow, and work over the past years.

This work belongs as much to the community around me as it does to me.

Thank you to Luís O. Silva, from whom I have learned not only how to do physics, but how to be a scientist, and everything that comes with it. You may not have written this, but your fingerprints are all over it.

To everyone in GoLP: Thales Silva, Diogo Carvalho, Chiara Badiali, Fabio Cruz, Filipe Cruz, Francisco Assunção, Camilla Willim, Robert Babjak, Lucas Gamiz, Lucas Ansia, Pablo Claveria, Ankur Nath, Bernardo Barbosa, Bernardo Malaca, Bhushan Thakur, Rui Torres, Miguel Pardal, Bertrand Martinez, Cláudia Romao, Susana Muinos, Marija Vranic, Thomas Grismayer, Jorge Vieira, Frederico Fiuza, Ricardo Fonseca; thank you for the conversations, the collaborations, and the camaraderie.

Thanks to Gianluca Gregori for hosting me in Oxford, giving me a glimpse into the art of collaborating with experiments, and for the constant reminder to keep the writing of papers in mind. To everyone in the Simon Room in Oxford, thank you for welcoming me and for the long physics discussions, oftentimes over a couple of pints at the Lamb & Flag. Charlie Arrowsmith, Pontus Svensson, Alessandro Forte, Hannah Poole, Jack Halliday, Celia Stergiou: thank you. To everyone involved in the Fireball experiment: Bob Bingham, Nikolaos Charitonidis, and Eva Los, thank you for your insight and discussions.

Thank you to Robbie Ewart, Michael Nastac & Alexander Schekochihin for sending me on a small side quest into phase-space volumes and turbulence. These results didn't make it into the thesis, but they offered a fascinating new lens through which to think about simulations.

Thanks to the bouldering Lisbon "cult" for these years of friendship and strength, both mental and, surprisingly, dactyl. Sports were key to helping me get through these years.

To my dearest friends (some of you already mentioned, but no double-dipping!), who were there when things got tough, weird, or in-between: George, Skander, Jamie, Cláudia, Charlie, Oliveira, thank you.

A special thank you to Sara and Pipoca. A significant portion of this thesis was written in the early hours of the morning, when I could find the peace and time to work. Thank you for helping me find that space. I couldn't have finished this without your support.

And last but not least, my family. To my parents, Jaime and Tania, and my sisters, Carmen and Elena: thank you for always believing in me, even at times when I didn't. I could not have made it without you.

To everyone I've worked with, learned from, and shared this journey with, thank you. Your contributions, whether through guidance, encouragement, support, or collaboration, have left a lasting impact on me and on this work. I'm afraid it's impossible to name everyone, as many of you deserve thanks for shaping both this thesis and my growth as a researcher and person, but I hope I've managed to do some justice. To all of you: thank you.

This work was supported by the Fundação para a Ciência e a Tecnologia (FCT, Portugal) through Grant No. UI/BD/151559/2021 and the research project X-MASER (No. 2022.02230 PTDC). Additional support came from the European Research Council (ERC) under the Horizon 2020 programme (Grant No. 695088 – InPairs), and the European Union's Horizon 2020 research and innovation programme under Grant Agreement No. 653782.

Simulations were performed at LUMI (Finland), funded by the EuroHPC-JU project EHPC-REG-2021R0038, and at Deucalion (Portugal), funded by the FCT project Masers in Astrophysical Plasmas (MAPs), No. 2024.11062.CPCA.A3.

CONTENTS

LIST OF FIGURES

To Jaime and Tania

for their unrelentless support
and love.

CHAPTER 1

INTRODUCTION

> The problems are solved, not by giving new information, but by arranging what we have known since long.
>
> *Ludwig Wittgenstein – Philosophical Investigations 1953 [2]*

1.1 EXTREME PLASMA PHYSICS

Plasma physics is the study of the collective dynamics of charged particle systems and, for much of its history, has operated within the framework of classical electromagnetism and classical kinetic theory. Since its formal development in the 20th century [3–5], the field has made remarkable progress, predicting different many micro-instabilities [6, 7], developing theories of turbulence and transport [8], and reproducing stellar conditions in the laboratory [9–11]. These insights have been instrumental both in controlled fusion research, through devices such as tokamaks and stellarators, and in interpreting the behavior of space and astrophysical plasmas [12, 13].

Yet these achievements have largely been confined to regimes where classical physics suffices. A new frontier is now emerging: that of extreme plasma physics, where radiative processes, relativistic energies, strong-field effects, and quantum electrodynamical (QED) phenomena begin to couple to plasma dynamics. Thus, entering the regime of extreme plasma physics. The term extreme physics has its origins in the 2003 National Academy of Sciences report Frontiers in High Energy Density Physics: The X-Games of Contemporary Science [14].[1] This report defined a broad frontier for exploring matter under extreme conditions of temperature, density, and field strength, conditions that bridge astrophysics and high-energy-density laboratory physics. Extreme plasmas, in this sense, are those in which one or more fundamental physical scales (relativistic, radiative, or QED) begin to couple strongly to collective plasma behavior.

[1] See also the framing in Uzdensky et al. [15], which emphasizes the role of relativistic, radiative, and QED effects in defining "extreme" plasma regimes.

As we will see, extreme plasma conditions span a wide range of laboratory and astrophysical environments, each considered "extreme" with respect to different physical parameters. Thus, the regime of extreme plasma physics can be defined in multiple ways. For example, one may consider plasmas with thermal energies approaching the rest mass of the electron, $T_e \sim 0.51$ MeV (or $\sim 6 \times 10^9$ K) [14, 15]; or environments where the electromagnetic field strength approaches the QED critical (Schwinger) field, at which the electric field does work of $\sim m_e c^2$ across a Compton wavelength, $E_{\rm Sc} = m_e^2 c^3/e\hbar \approx 1.3 \times 10^{18}$ V/m, or equivalently $B_{\rm Sc} \approx 4.4 \times 10^9$ T [15]; under such strong fields QED enters into the non-linear regime; here effects such as Schwinger pair production, where the fields lead to the spontaneous creation of electron-positron pairs (this process also occurs at lower field intensities, the rate is exponentionally suppressed) become important [16]. In such regimes, QED effects can arise from interactions between high-energy photons and particles, leading to processes such as electron-positron pair production, as discussed in early studies of relativistic plasmas [17]. Or they can arise via interaction of photons comprising the electromagnetic fields, when moderate electromagnetic fields are Lorentz-boosted into the interacting particle's rest frame. This is captured by the dimensionless quantum parameter

$$\chi = \frac{\sqrt{-(F_{\mu\nu} p^\nu)^2}}{E_{\rm Sc} m_e c}, \tag{1.1}$$

where e is the electron charge, $F_{\mu\nu}$ the electromagnetic field tensor, p^ν the particle's four-momentum and the dependence on $\hbar$ is included in the Schwinger field strength $E_{\rm Sc}$ [18, 19]. When $\chi \gtrsim 0.1$, quantum corrections to radiation become significant; for $\chi \sim 1$, nonlinear QED processes such as stochastic photon emission and multiphoton pair production emerge [20]. This threshold can be reached by accelerating particles to ultrarelativistic energies even in fields well below the QED critical strength, making the χ parameter central to defining the onset of strong-field quantum effects.

Recent theoretical and computational work has begun to elucidate how extreme-field effects couple to collective plasma dynamics [21–25]. A key ingredient in these regimes is the emission of radiation by charged particles undergoing acceleration in strong electromagnetic fields. This process, commonly referred to as radiation reaction, can significantly alter particle trajectories and energy distributions. When the energy loss becomes comparable to or exceeds the kinetic energy of the particles, the system enters a regime of radiative cooling, in which large amounts of thermal energy are continuously emitted. More precisely, we will study scenarios where the energy radiated by a charged particle over the characteristic timescale, Γ^{-1} (with Γ being the instability growth rate or characteristic frequency of a given process), becomes comparable to the particle's kinetic energy E_0. For instance, in the case of synchrotron emission, the cooling time is $t_s = E_0/P_s$, where P_s is the synchrotron power (this applies to any other emission emchanism). As we will see, there are plasma processes with $\Gamma^{-1} \gtrsim t_s$, but more importantly, there are processes that are *triggered* or qualitatively transformed by radiative losses themselves. In this case, a unified treatment of radiation reaction and collective plasma physics is needed.

Moreover, the plasma composition itself may evolve in extreme plasmas [17], pair plasmas composed of electrons and positrons, or more exotic species such as muon-antimuon or pion

pairs, can emerge via high energy interactions or be generated by the fields themselves. These developments mark a shift in the field, as now plasma physics necessitates to be coupled to quantum, radiative, and compositionally exotic components. Extreme plasma physics is thus a broad and evolving research area, expanding the already rich landscape of plasma science. It concerns itself with the study of matter under the most extreme conditions accessible in nature or the laboratory. Among its central questions are [14, 15]: How does matter behave under extreme conditions of temperature, density, and field strength? Can collective plasma processes be understood in the presence of ultra-strong fields and relativistic motion? Can macroscopic relativistic, radiation-cooled, or quantum pair plasmas be created and studied in the laboratory? How do radiative losses and QED effects modify instabilities, shocks, and turbulence in such settings? And can laboratory experiments serve as analogues to astrophysical phenomena such as magnetar flares, gamma-ray bursts (GRBs), or relativistic jets?

These questions sit at the intersection of plasma physics, astrophysics, and high-field QED. This thesis addresses a subset of these challenges, focusing on how radiative effects reshape plasma dynamics at the kinetic level. Our approach combines analytical theory with large-scale, first-principles simulations capable of capturing the full nonlinear evolution of plasmas under radiative and quantum effects. We begin by examining astrophysical contexts where such conditions arise naturally.

1.1.1 Extreme Plasmas in Astrophysics

Compact objects such as black holes and neutron stars, are among the most extreme physical systems in the universe. Their intense gravitational and magnetic fields, coupled with rapid rotation, make them natural laboratories for studying extreme plasma physics. The surface magnetic fields of these objects can exceed 10^{14} G [26, 27], as shown in the P-$\dot{P}$ diagram in Fig. 1.1. While such extreme values are characteristic of magnetars, even ordinary radio pulsars exhibit magnetic fields in the range 10^{11}-10^{13} G, well above the threshold where relativistic, radiative, and strong-field plasma effects become significant [15]. These field strengths imply that the surrounding plasma environments are not only highly magnetized and relativistic, but also subject to strong radiative and, in some cases, QED effects.

Extreme astrophysical plasmas are dominated by QED and radiative effects; in fact, around compact objects, these plasmas are generated via efficient pair-creation, due to the sufficiently strong fields, approaching $E \lesssim E_{\rm Sc}$, that compact objects possess. This occurs either through one-photon processes in ultra-magnetized environments (e.g., magnetic pair production in magnetars [21, 22, 28, 29]).[2] These effects inject new particles and alter wave, particle interactions in fundamental ways [30, 31]. In the most extreme settings, general relativistic effects may also become important [32, 33], completing a picture in which radiation, relativity, and collective plasma dynamics are coupled.

Such extreme conditions give rise to a wide range of energetic and physically rich astrophysical phenomena. These include the dynamics of neutron star [30, 34, 35] and black-hole

[2] Or if an ultra-strong electric is present, via vacuum breakdown in the presence of ultra-intense electromagnetic fields [16]. This would be rare in astrophysical objects.

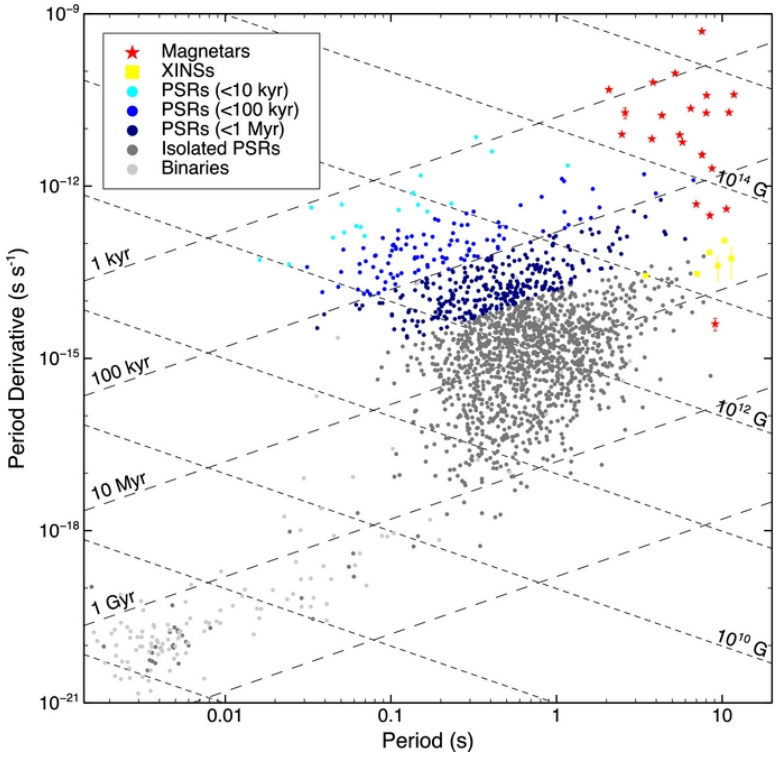

FIGURE 1.1: Spin period (P) vs. spin-down rate ($\dot{P}$) diagram showing both pulsars, including PSRs (radio pulsars) and XINSs (X-ray Isolated Neutron Stars), and magnetars, using data from the McGill Magnetar Catalog alongside known Galactic pulsars [46]. The surface magnetic field strength is estimated by equating the spin-down luminosity to the energy loss of a rotating magnetic dipole in vacuum, yielding $B_{\rm surf} \approx 3.2 \times 10^{19} \sqrt{P\dot{P}}\,\mathrm{G}$ [47].

[36] magnetospheres, GRBs [37], and relativistic jets from active galactic nuclei (AGN) [38]. More recently, fast radio bursts (FRBs) have emerged as one of the most compelling puzzles in high-energy astrophysics [39, 40]. FRBs are millisecond-duration radio transients with brightness temperatures exceeding 10^{35} K, implying an underlying emission mechanism that must be both coherent and extremely efficient [41, 42], and cannot originate from a large spatial region due to its coherence and frequency, which pinpoints compact objects as their likely origin [43]. While their extragalactic origin is now well established, the physical processes responsible for their generation remain actively debated. The short duration, high luminosity, and polarization properties of FRBs point toward compact object progenitors, with magnetars emerging as the leading candidates. The observed connection between FRBs and magnetars, most notably, the detection of bursts coinciding with magnetar glitches, has reinforced this link [34, 44, 45]. These observations support models in which FRBs originate from the dynamics of pair plasmas within low-twist magnetospheres, where extreme magnetic fields, relativistic particle populations, and radiative processes interact to produce coherent emission. Understanding these processes is critical to interpreting high-energy signatures across the electromagnetic spectrum.

Numerous theoretical frameworks have been proposed to explain coherent emission in pulsar and magnetar magnetospheres, including antenna mechanisms [43] , shock-driven synchrotron masers [42, 48], and Free-electron-laser [49]. Recent kinetic simulations have explored aspects of these mechanisms, typically relying on idealized or externally prescribed particle distributions. However, the self-consistent generation of maser-prone distributions via radiative processes has received comparatively little attention. This is one of the gaps that the present work seeks to address.

Beyond pulsars and magnetars, other astrophysical systems also operate in extreme plasma regimes shaped by strong radiation, relativistic dynamics, and collective effects. GRBs, for instance, involve ultra-relativistic outflows where kinetic energy is rapidly converted into high-energy radiation, probably through shocks and magnetic reconnection. Similarly, black hole coronae and AGNs, exhibit signatures of strong-field and radiative plasma physics on large scales.

Blazars, a subclass of AGN with jets pointing toward Earth, emit gamma rays with hard spectra extending into the TeV range [50]. As these high-energy photons propagate through the intergalactic medium, which acts as a tenuous, collisionless plasma, they are expected to interact with the extragalactic background light, producing electron-positron ($e^{\pm}$) pairs through photon-photon collisions [51].Thus, these systems provide a natural testbed for studying the propagation and cooling of ultra-relativistic leptonic beams in low-density, weakly magnetized environments, and illustrate how extreme plasma processes shape the high-energy universe on cosmological scales.

Turbulence is another ubiquitous plasma process that is fundamentally reshaped in extreme astrophysical environments. In standard magnetized plasmas, turbulent energy cascades from large to small scales following universal spectral laws, such as the Kolmogorov or Goldreich-Sridhar scalings [8]. However, in relativistic and strongly radiative regimes, such as the magnetized coronae of accreting black holes or the jets of blazars, radiative losses can dominate the energy budget, altering both the dynamics and the dissipation pathways [52–54]. Recent particle-in-cell simulations have shown that when the radiative cooling time becomes shorter than the turbulence turnover time, $t_{\rm IC}/t_0 \lesssim 1$, most of the turbulence power is directly transferred to photons via bulk Comptonization [55, 56]. In this fast-cooling regime, the cascade is effectively damped at large scales, steepening the turbulence spectrum and suppressing energy transfer to kinetic scales. This behavior emerges naturally for conditions expected in black-hole coronae, with magnetizations $\sigma_e \gtrsim 1$, Thomson optical depths $\tau_T \sim 1$, and large-amplitude Alfvénic fluctuations. Under these conditions, up to 80% of the injected turbulent power is radiated before reaching small scales, producing a non-universal, radiation-dominated cascade [56]. This interplay between turbulence, reconnection, and radiative losses leads to complex, spatially structured emission. In blazar jets, similar radiative turbulence has been proposed as a source of *in situ* electron-positron pair production, demonstrating that turbulence can drive not only particle energization but also changes in plasma composition [57]. These findings highlight that turbulence in extreme plasmas is governed not just by classical fluid parameters, but by a combination of magnetization, compactness, and radiative cooling, placing it in a distinct regime of kinetic extreme plasma dynamics.

Astrophysical systems such as magnetar magnetospheres, fast radio bursts, GRBs, blazar jets, and black-hole coronae exemplify the diversity of extreme plasma environments. In these settings, relativistic motion, strong fields, and radiative processes combine to produce plasma behavior that departs sharply from classical expectations, often involving turbulence, nonthermal acceleration, and coherent emission modified by radiative and quantum effects. Although such conditions are most naturally found around compact objects, recent advances in laboratory capabilities are beginning to make them accessible in controlled experiments, opening the door to studying extreme plasma physics in the lab and deepening the connection between astrophysical observations, simulations, and high-energy laboratory science.

1.1.2 Extreme Plasmas in the Laboratory

A wide range of high-energy plasma phenomena, once considered the exclusive domain of astrophysics, are now being investigated in the laboratory. Experimental platforms have made significant progress in studying radiation reaction, relativistic shocks, pair production, and magnetized plasma dynamics under extreme conditions. These advances are the result of rapid developments in high-power laser systems, accelerator technology, and precision diagnostics, which have dramatically expanded the reach of laboratory plasma physics.

This shift was already anticipated two decades ago in the National Academies report Frontiers in High Energy Density Physics [14], which outlined a vision for exploring matter under extreme conditions of temperature, density, and electromagnetic fields. In addition to mapping out the density-temperature phase space accessible to high energy density experiments, the report also highlighted many of the physical processes that now define current research in extreme plasma physics. These included the nonlinear optics of intense laser-plasma interactions, and the use of beam-laser collisions to probe strong-field QED processes such as nonlinear Compton scattering and multiphoton pair production. Together, these ideas helped shape the multidisciplinary research agenda that has since driven the development of extreme plasma physics [14].

Figure (1.2), adapted from that report, illustrates how the anticipated capabilities of experimental platforms like OMEGA, Z-pinch, and the National Ignition Facility could begin to overlap with the conditions found in astrophysical systems, such as stellar interiors, giant planets, and GRBs. Since then, a series of key experimental advances have begun to fulfill that vision, demonstrating that the extreme conditions outlined in the report are now within reach. Platforms such as OMEGA and NIF have not only accessed high energy density regimes but are beginning to probe fundamental plasma processes under conditions directly relevant to astrophysics [58].

Collisionless shocks, long thought to power cosmic-ray acceleration in supernova remnants, have become a major target for laboratory astrophysics [59]. Experiments at OMEGA have shown that counter-streaming plasma flows can reach the collisionless regime and generate strong, self-organized magnetic fields via Weibel instability. While these setups did not yet form true shocks, they found key processes such as electron drag heating and electrostatic instabilities [58] More recently, experiments at NIF succeeded in forming fully developed, high-Mach number collisionless shocks, demonstrating MG-level magnetic fields and relativistic

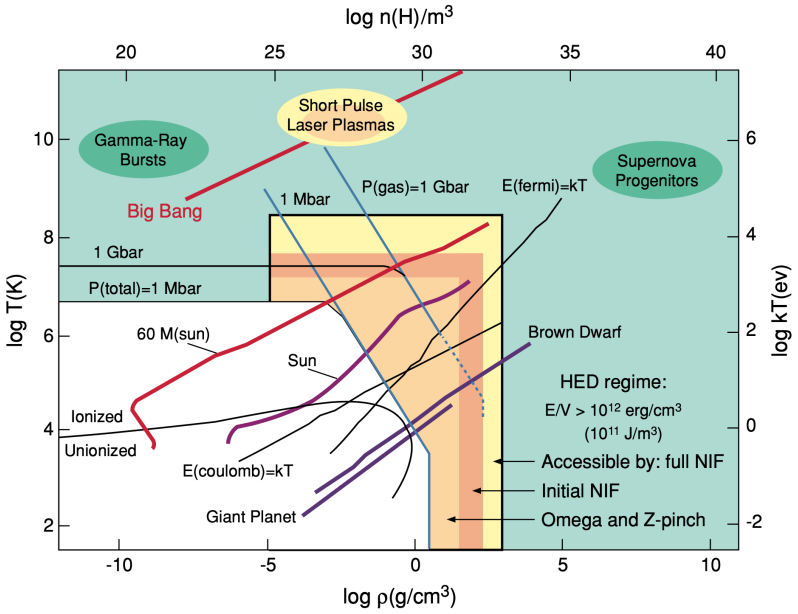

FIGURE 1.2: Density-temperature phase space showing the overlap between astrophysical environments and the high energy density regimes accessible to laboratory experiments. At the time of the report, the shaded regions outlined the reach of platforms such as OMEGA, Z-pinch, and the (then-upcoming) National Ignition Facility. Adapted from Ref. [14].

electron acceleration consistent with first-order Fermi processes [11].

Experiments at OMEGA have also confirmed the operation of the turbulent dynamo in laser-produced plasmas, showing that turbulent flows can amplify initially weak magnetic fields to strengths approaching the megagauss level on nanosecond timescales [60]. While turbulence is not unique to astrophysical systems, these experiments access regimes with properties, such as Reynolds and magnetic Prandtl numbers, comparable to those found in high-energy astrophysical environments, enabling the study of magnetized turbulence under realistic conditions [60].

These phenomena, collisionless shocks and turbulent dynamos, demonstrate that laboratory plasmas can now reach the energy densities and magnetic field strengths that characterize many astrophysical environments. While still below the Schwinger field, such fields already begin to influence radiation processes and collective dynamics. However, a parallel research direction is possible, not defined by kinetic energy density, but by the energy density of the electromagnetic fields in the particle rest frame. This opens the domain of strong-field QED.

In this regime, what matters is not the density or temperature of the plasma, but the parameter χ, which quantifies the field strength in the particle's rest frame. Strong-field QED effects become relevant when $\chi \gtrsim 0.1$, and nonlinear processes dominate once $\chi \sim 1$ [18, 19]. This threshold can be crossed by either increasing the background field or, in a more accesible manner, by boosting particles to ultra-relativistic energies, thus effectively amplifying the field in their rest frame. Consequently, GeV-class electron beams and ultra-intense lasers provide

complementary access to this regime within recent experimental efforts having provided the first results in such regime [61].

Previous efforts such as the SLAC's E-144 experiment demonstrated nonlinear Compton scattering and multiphoton Breit-Wheeler pair production [62]. More recently, experiments at Apollon, Gemini, and ELI have explored quantum radiation reaction and high-energy photon emission from laser-solid interactions at intensities exceeding $10^{21}\,\mathrm{W/cm^2}$ [63, 64]. In these conditions, relativistic electrons experience rest-frame fields near or beyond the QED critical field, enabling not only pair production but also dense, transient pair plasmas. While these systems have not yet produced macroscopic, collective, ideal pair plasmas, they provide important access to the strong-field, quantum radiative regime.

Moreover, beam-driven platforms are also advancing the frontier of strong-field QED. Experiments at SLAC and FACET-II employ GeV-class electron beams to explore quantum radiation reaction and beam, plasma instabilities [65, 66]. As will be discussed in Chapter 4, platforms, like FACET-II, offer a promising avenue for testing new theoretical ideas developed in this thesis, particularly those involving the interplay between relativistic beams, strong betatron cooling, and collective plasma dynamics. Similarly, upcoming laser-electron beam collision experiments at facilities like the Zettawatt-Equivalent Ultrashort pulse laser System (ZEUS) aim to reach Lorentz factors and field strengths comparable to those in high-energy astrophysical sources [67].

This experimental frontier has been guided by theory. Quantum-corrected synchrotron models and Monte Carlo simulations have established the limits of classical theory and clarified the onset of stochastic photon emission and pair production at $\chi \gtrsim 1$ [68, 69]. Studies have also revealed that QED effects can couple back to the plasma: compressing distribution functions and triggering QED cascades that in theory can evolve into relativistically overdense pair plasmas with $n_{e^\pm} \gtrsim 10^{23}\ \mathrm{cm}^{-3}$ [22, 28, 70]. These cascades lead to relativistic critical layers that reflect laser light and radiate efficiently in the gamma-ray regime [25, 71], marking the emergence of a genuinely collective QED regime, this is still ot be realised in a laser-plasma experimental platform.

While QED cascades offer one route to dense pair plasmas, an alternative approach has been realized through the production of relativistic electron-positron beams using a beam target configuration. This long-standing goal in laboratory astrophysics was achieved at CERN's HiRadMat facility, where the Fireball experiment produced the first quasi-neutral, relativistic pair plasma beams with transverse sizes and densities exceeding the Debye length and skin depth [72]. This created the conditions necessary for the development of beam-plasma instabilities and collective properties to emerge in pair plasmas. These experiments were made possible by foundational theory. Kinetic models and particle-in-cell simulations characterised the minimum conditions for these modes to arise, *i.e.*, that the radius satisfies $r_b \gtrsim c/\omega_p$ and the normalized emittance remains below $\epsilon_N/(\gamma\beta) \lesssim 0.1\lambda_p$ [73]. Under such conditions, instabilities such as the current filamentation can grow with rate of comparable timescle to the experimental setup.

These platforms are now probing regimes where collective behavior of beam-plasma instabilities can begin to be studied [66, 72, 74, 75]. While achieving fully QED-coupled, radiatively

cooled pair plasmas remains an ambitious goal, the direction is clear. With the advent of petawatt-class lasers and multi-GeV accelerators, the energy and field thresholds necessary to produce such systems are now within reach.

This convergence marks a turning point. Historically, astrophysics and laboratory plasma physics have progressed in parallel, shaped by distinct goals and constraints. Today, they are beginning to merge. The shared physics of relativistic energies, collective dynamics, and strong radiation now links black-hole coronae and laser-solid interactions, pulsar winds and positron beams at CERN. This thesis is situated at the intersection of astrophysics, laboratory experimentation, and theoretical plasma physics. It addresses how radiation and collective plasma effects interact across both experimental and astrophysical platforms, using theory and simulation to clarify where these interactions can be relevant, what instabilities and signatures can be observed, and how they can be probed. By helping to define and understand this regime, the work contributes to a growing unified framework for extreme plasma physics.

1.2 THIS DISSERTATION

The following chapters develop this perspective in detail, outlining the specific objectives of this work, the methods used to pursue them, and the results that emerge from this approach.

1.2.1 OBJECTIVES

The goal of this thesis is to advance our understanding of kinetic plasma dynamics in regimes where extreme plasma effects, such as strong-field radiation, pair production, and QED processes, become dynamically important. These regimes are characterized by specific physical thresholds: when the quantum parameter $\chi \gtrsim 0.1$, indicating that particles experience rest-frame fields approaching the QED critical scale; when the radiation mean free path becomes comparable to or smaller than the system size; and when radiative cooling timescales τ_{cool} are on the order of, or shorter than, characteristic kinetic or instability growth timescales. The focus is placed on plasmas that remain collective, that is, whose spatial and temporal scales exceed the Debye length and plasma period, and where coherent dynamics dominate over collisional or dissipative effects.

Two main threads run through this work: the role of radiative processes in plasma dynamics and instabilities of relativistic electron-positron beams. A central focus is placed on radiative processes, specifically the recoil experienced by particles due to radiation emitted during acceleration. Though initially appearing as a straightforward effect, radiation reaction demonstrated surprisingly rich and consequential physics, uncovering a novel mechanism by which plasmas radiate not only their energy, but also their entropy.

This work, focuses on the radiative regime, where radiation reaction, pair production, and QED processes begin to shape the collective dynamics. Thus, this thesis presents, to the best of our knowledge, the first example of a kinetic plasma process in which high-field effects such as radiation reaction give rise to a collective kinetic instability.[3] Remarkably, this leads to the

[3]During the writing of this thesis, it was brought to my attention the existance of a fluid instability driven by

self-consistent formation of ring-like phase-space structures that trigger the coherent emission of radiation via the electron cyclotron maser instability (ECMI). While earlier studies began to explore aspects of this regime, our work is the first (alongside [24]) to show that radiation reaction can actively drive such an instability, and further, to pose the question of whether this process, or an analogue thereof, can be realized in laboratory conditions.

In parallel, this thesis contributes to the theoretical and simulation effort behind the Fireball experiments at CERN's HiRadMat facility, which recently achieved the production of relativistic electron-positron beams in the laboratory [72, 77]. Long considered a hallmark of extreme astrophysical environments, such as pulsar magnetospheres and relativistic jets, these beams are now within reach of controlled experimental investigation. Through large-scale kinetic simulations, this work examines the microphysical instabilities triggered as these beams interact with ambient plasmas, processes that may underlie key dissipation and emission mechanisms in astrophysical contexts.

The convergence of theory, simulation, and experiment marks a turning point: it enables the direct study of plasma instabilities and radiative processes in regimes where collective behavior and strong-field effects are coupled.

1.2.2 OUTLINE

This thesis is structured into five chapters following this introduction.

Chapter 2 focuses on the role of synchrotron radiative losses in collisionless plasmas. Using both analytical arguments and fully kinetic particle-in-cell (PIC) simulations, we show that radiative cooling inevitably reshapes the momentum distribution of the plasma, driving it toward a ring-like structure. This redistribution represents a fundamental shift from classical kinetic equilibria and sets the stage for new kinds of collective behaviour.

Chapter 3 investigates the dynamics that follow the formation of ring distributions, focusing on their intrinsic instability to the electron cyclotron maser instability. The chapter develops the corresponding linear theory, extending the kinetic framework to include the effects of radiative losses. This theoretical model is then complemented by PIC simulations that explore the instability in the nonlinear regime, highlighting the emergence of coherent radiation and the interplay between wave growth and particle dynamics.

Chapter 4 broadens the scope by examining a scenario that is directly relevant to laboratory experiments. Here, we consider relativistic particle beams undergoing radiative cooling through betatron motion in plasma channels, a configuration that can be realized with current experimental capabilities. We show that this cooling mechanism leads to the formation of ring-like phase-space distributions, providing an alternative route to maser-prone conditions. Unlike the primarily astrophysical context of Chapters 2 and 3, this chapter focuses on a setup that is both theoretically rich and experimentally accessible, offering new opportunities for controlled studies of kinetic instabilities driven by radiation-induced phase-space structure.

Chapter 5 presents large-scale kinetic simulations carried out in support of the Fireball experiments at CERN's HiRadMat facility, which successfully produced relativistic electron-

synchrotron cooling, see Ref. [76].

positron beams in 2023. These simulations model the interaction of such beams with ambient plasma and explore the development of beam-plasma instabilities, with a particular focus on how these instabilities dissipate energy from the beam into electromagnetic fields. The simulation results were instrumental in interpreting data from the Fireball-I campaign and have guided the design of subsequent experimental runs. Crucially, the experiment provides a unique opportunity to observe, in a controlled laboratory setting, the very same physical processes, such as the dissipation of kinetic energy via collective plasma instabilities, that are believed to operate in high-energy astrophysical environments. These results help bridge the gap between theory, simulation, and experiment, and bring us closer to directly testing astrophysical plasma physics in the laboratory.

Finally Chapter 6, the thesis concludes with a summary of the main findings and a discussion of their broader implications for plasma physics and laboratory astrophysics. Particular attention is given to the unifying role of radiative processes and kinetic instabilities in shaping plasma dynamics across both astrophysical and experimental contexts. The conclusion also outlines possible future directions, including experimental follow-up, extensions to QED regimes, and opportunities for further theoretical exploration.

These findings are complemented by a series of Appendices that provide technical detail and theoretical extensions. They include simulation parameters, convergence tests, derivations of instability growth rates, discussions on entropy and synchrotron emission, and the initialization procedures used in the Fireball beam simulations. Together, they support and extend the main results of the thesis, and point toward further questions in theory and simulation.

1.2.3 METHODOLOGY: KINETIC THEORY

The physical phenomena explored in this thesis, radiative cooling, kinetic instabilities, and collective plasma dynamics, require a framework capable of capturing non-equilibrium behavior at the level of individual particles. Kinetic theory provides such a first-principles foundation by tracking the evolution of distribution functions in phase space under the influence of self-consistent electromagnetic fields. This approach traces back to the Vlasov equation [4] (and Klimontovich formalism [3]), developed in 1938, which governs the collisionless evolution of a plasma.

In its most general form, the kinetic nonrelativistic equation for a species s (with charge q_s and mass m_s) reads[4]

$$\frac{\partial f_s}{\partial t} + \mathbf{v} \cdot \nabla_{\mathbf{x}} f_s + \frac{q_s}{m_s} \left(\mathbf{E} + \frac{\mathbf{v}}{c} \times \mathbf{B} \right) \cdot \nabla_{\mathbf{v}} f_s = \left(\frac{\partial f_s}{\partial t} \right)_{\text{coll}}, \tag{1.2}$$

where $f_s(t, \mathbf{x}, \mathbf{v})$ is the distribution function in phase space, and the right-hand side represents a collision operator. In the limit where binary collisions are negligible compared to collective

[4]Throughout this thesis, we use CGS Gaussian units unless stated otherwise. All derived formulae are expressed in this system for internal consistency.

interactions, the collision term vanishes:

$$\left(\frac{\partial f_s}{\partial t}\right)_{\text{coll}} = 0, \tag{1.3}$$

reducing Eq. (1.2) to the Vlasov equation:

$$\frac{\partial f_s}{\partial t} + \mathbf{v} \cdot \nabla_{\mathbf{x}} f_s + \frac{q_s}{m_s}\left(\mathbf{E} + \frac{\mathbf{v}}{c} \times \mathbf{B}\right) \cdot \nabla_{\mathbf{v}} f_s = 0. \tag{1.4}$$

Unlike fluid models, which rely on moments and eventually employ a closure, kinetic theory retains the full velocity-space (momentum-space for relativistic dynamics) structure of the system. It captures key non-equilibrium processes such as velocity-space instabilities, wave-particle interactions, and phase-space trapping [78, 79].

The Vlasov-Maxwell system lies at the core of collisionless kinetic theory and is particularly suited to regimes where long-range collective effects dominate over binary collisions. It describes the self-consistent evolution of the distribution functions f_s and the electromagnetic fields $(\mathbf{E}, \mathbf{B})$, with particle motion governed by the Vlasov equation (1.4) and the fields evolving according to Maxwell's equations:

$$\nabla \cdot \mathbf{E} = 4\pi\rho, \tag{1.5}$$

$$\nabla \cdot \mathbf{B} = 0, \tag{1.6}$$

$$\nabla \times \mathbf{E} = -\frac{1}{c}\frac{\partial \mathbf{B}}{\partial t}, \tag{1.7}$$

$$\nabla \times \mathbf{B} = \frac{4\pi}{c}\mathbf{J} + \frac{1}{c}\frac{\partial \mathbf{E}}{\partial t}, \tag{1.8}$$

where the charge and current densities are obtained self-consistently from the distribution functions:

$$\rho = \sum_s q_s \int f_s \, d^3\mathbf{v}, \tag{1.9}$$

$$\mathbf{J} = \sum_s q_s \int \mathbf{v} f_s \, d^3\mathbf{v}. \tag{1.10}$$

This coupled system has been central to the understanding of many foundational plasma phenomena, including Landau damping [5], the formation of Bernstein-Greene-Kruskal (BGK) modes [80], and the growth of a wide range of micro-instabilities in both unmagnetized and magnetized plasmas.

This thesis applies kinetic theory to the study of extreme plasma environments, where the plasma is far from equilibrium and radiative processes become dynamically important. In these regimes, the classical Vlasov-Maxwell description must be extended to account for additional physics. Formally, this means departing from the collisionless assumption $(\partial f/\partial t)_{\text{coll}} = 0$, and introducing effective operators that model radiative energy loss and, more generally, QED processes. A fully general treatment would involve coupling the Vlasov equation to a set of such operators, each responsible for capturing a distinct physical process. Developing a unified kinetic framework that self-consistently incorporates all of these effects remains

an open and long-term goal. This thesis takes a small (but significant) step in that direction by including radiative losses within the kinetic description and examining how they reshape phase-space structure and influence the growth and saturation of kinetic instabilities. In the classical regime, radiative losses can be modeled by introducing a deterministic force term into the Vlasov equation. The most widely used formulation is the Landau–Lifshitz (LL) radiation reaction force, which approximates the full Lorentz–Abraham–Dirac expression and is valid when the electromagnetic fields vary smoothly over the particle trajectory. In CGS Gaussian units, the LL force expressed in terms of particle momentum $\mathbf{p} = \gamma m_e \mathbf{v}$ reads[5]

$$\mathbf{F}_{\mathrm{RR}} = -\frac{2}{3}\frac{e\alpha}{B_{\mathrm{Sc}}}\left\{\frac{\gamma\mathbf{p}}{m_e c}\left[\left(\mathbf{E}+\frac{\mathbf{p}\times\mathbf{B}}{\gamma m_e c}\right)^2-\left(\frac{\mathbf{p}\cdot\mathbf{E}}{\gamma m_e c}\right)^2\right]-\mathbf{E}\times\mathbf{B}-\frac{\mathbf{B}\times(\mathbf{B}\times\mathbf{p})+\mathbf{E}\,(\mathbf{p}\cdot\mathbf{E})}{\gamma m_e c}\right\}, \tag{1.11}$$

where e is the elementary charge (in statcoulombs), m_e the electron mass (in grams), c the speed of light (in cm/s), $\alpha = e^2/\hbar c$ the fine-structure constant, and $B_{\mathrm{Sc}} = m_e^2 c^3/(e\hbar) \approx 4.4 \times 10^{13}\,\mathrm{G}$ the Schwinger critical magnetic field in Gauss. All quantities are expressed in CGS Gaussian units. Some of the key consequences of this term are explored in Chapters 2 and 3.

Analytical methods grounded in kinetic theory offer valuable insights into the early, linear stages of plasma evolution, where perturbative techniques can be applied. However, as instabilities grow and nonlinear effects dominate, analytic approaches quickly become intractable. To fully capture the complexity of these systems, numerical simulations are essential.

1.2.4 Methodology: Particle-in-cell simulations

This work employs large-scale, first-principles, self-consistent simulations using the Particle-in-Cell (PIC) method, implemented via the state-of-the-art code OSIRIS [81]. These simulations are complemented by analytical models that inform the design of simulation setups and help interpret the complex plasma dynamics observed within them.

The standard PIC algorithm, first envisioned by Dawson and Buneman [82–85], models the self-consistent interaction between a collection of computational charged particles and the electromagnetic fields they generate. The PIC method are frequently viewed as numerical approximations of the Vlasov equation, representing an ideal, collisionless plasma. However, PIC simulations may not fully correspond to a purely collisionless description, and subtle differences exist between the PIC approach and a Vlasov system.[6] Moreover, it should be noted that all plasmas, whether computational or experimental, are never truly collisionless[88, 89].

The basic PIC cycle (schematically summarised in Fig. 1.3) consists of four main steps. Each simulation timestep begins with (i) interpolation of the electromagnetic fields $(\mathbf{E}, \mathbf{B})_i$ from the

[5] The appearance of c^2 in the denominator ensures consistency with the classical radiation reaction prefactor, when expressed in terms of α and the Schwinger field, as $\frac{2}{3}\frac{e^3}{m_e c^3} = \frac{2}{3}\frac{e\alpha}{B_{\mathrm{Sc}} c^2}$.

[6] PIC simulations more closely resemble a Klimontovich representation of the plasma, where the phase-space distribution is explicitly constructed from individual particle trajectories, with finite-size shape functions replacing Dirac delta functions; see, e.g., Refs.[86, 87]. Although this distinction is often overlooked, it implies that PIC can inherently capture certain discrete-particle effects and non-ideal plasma dynamics. Nevertheless, this nuance does not significantly affect the core findings presented in this work.

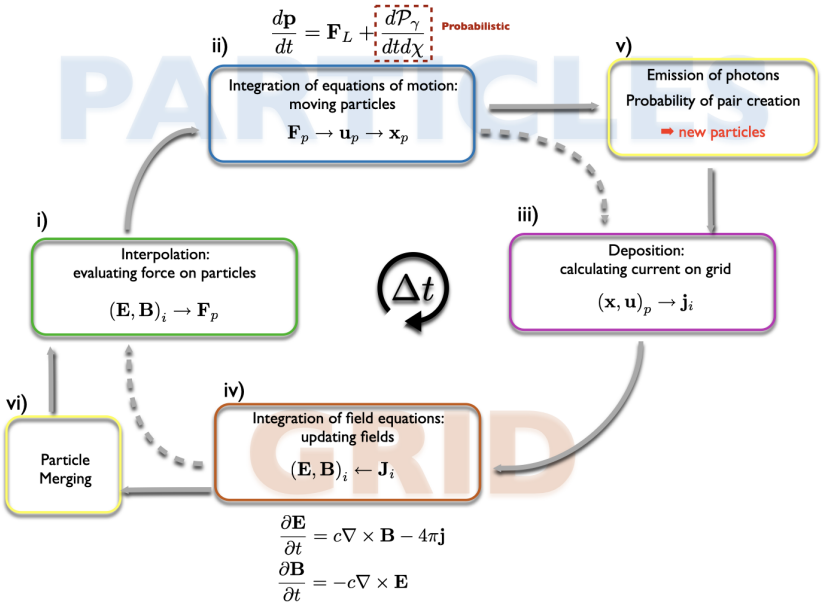

FIGURE 1.3: Simulation loop implemented in OSIRIS, including QED effects and particle merging. Grid quantities are indexed by i, and particles by subscript p. The standard particle-in-cell (PIC) cycle, comprising field interpolation i), force integration ii), current deposition iii), and field updateiv), is extended to include probabilistic QED processes (photon emission and pair production), leading to the injection of new particles v0, as well as a particle merging step vi). Figure adapted from Ref. [91].

grid to the particle positions, allowing computation of the Lorentz force $\mathbf{F}_p$. Then, in step (ii), particle positions $\mathbf{x}_p$ and momenta $\mathbf{u}_p$ are updated using the equations of motion. Following the particle push, (iii) the updated particle velocities and positions are used to deposit charge and current densities ρ_i and $\mathbf{J}_i$ onto the grid. Finally, (iv) Maxwell's equations are solved to update the electromagnetic fields, completing the self-consistent cycle.

However, the standard PIC algorithm alone is not sufficient to capture the full range of physical processes relevant to the regimes explored in this thesis. In particular, it does not explicitly account for radiative energy losses or QED effects, which play a central role in the dynamics of extreme, relativistic plasmas.[7] To study such environments, where radiation reaction alters particle trajectories and QED processes lead to photon emission and pair creation, the PIC loop must be extended. In OSIRIS, this is achieved through dedicated modules that implement both classical [90, 91] and quantum [28, 92] radiative processes.

Radiative losses are incorporated during the particle push (step ii), either through deterministic classical radiation reaction forces, modeled via the Landau-Lifshitz prescription, or via stochastic photon emission routines in the quantum regime, implemented using Monte

[7] Due to the finite-size shape functions of computational particles in standard PIC codes, one can argue that particles may experience a subtle form of self-interaction, potentially introducing signatures reminiscent of radiative damping. While this interpretation remains speculative, targeted numerical simulations could be designed to test this hypothesis systematically.

Carlo methods. When the QED module is active, an additional step (v) tracks the photons emitted by the particles as discrete computational particles. These photons can then undergo further interactions, such as nonlinear Compton scattering or Breit-Wheeler pair production, leading to the creation of new particles [28]. In high-density scenarios, step (vi) involves a particle merging algorithm to reduce computational load, while conserving key physical quantities like total charge, momentum, and energy. While reatining the correct shape of the phase-space distribution function of the plasma [92].

This extended simulation loop allows OSIRIS to evolve plasmas in regimes where nonlinear, collective, and quantum effects are coupled together. With these capabilities in place, OSIRIS provides a unique tool for first-principles studies of radiatively cooled plasmas, enabling predictive modeling for laboratory experiments and offering insight into analogous astrophysical systems.

1.2.5 ORIGINAL CONTRIBUTIONS

This PhD centers on two main lines of original contribution. The first focuses on the kinetic dynamics of plasmas in the synchrotron-dominated regime, showing that strong radiative cooling leads to ring-shaped momentum distributions, inverted populations, and the onset of kinetic instabilities. This work led to the identification of radiation-reaction-driven maser emission and established synchrotron cooling as a mechanism for triggering coherent plasma modes. The second major effort explores how similar radiative kinetic regimes can be accessed in the laboratory. In particular, it demonstrates that ion-channel (betatron) cooling can generate phase-space structured beams with the same signatures found in astrophysical contexts, opening a path to experimentally probe radiation-driven instabilities.

A third core contribution involves the Fireball collaboration at CERN, which successfully produced relativistic electron-positron beams in the laboratory. My work supported this effort through theory and simulations that guided the experimental design, helped model the generation and evolution of pair-plasma beams, and enabled the investigation of associated beam-plasma instabilities. These contributions were also central to interpreting the experimental results and connecting them to astrophysical scenarios.

In addition to these main work explictily outlined in this thesis, during this PhD I also explored the use of machine learning for efficient physics modeling in PIC simulations and contributed to collaborative work on the relaxation of collisionless plasmas with nonthermal equilibria. Alongside, work on tailoring the distribution functions of plasmas via laser ionization to study several kinetic instabilities. And I was able to contribute to the informal supervision of F. Assunçao Master's Thesis on: Particle Drifts and Radiation Reaction in Astrophysics. The cumulative impact of this PhD includes multiple publications in high-impact journals, invited talks at international conferences, and the successful acquisition of over 88 million CPU hours for large-scale simulations.

Publications

This PhD led to several publications spanning theory, simulation, and collaboration with experiment, including first-author papers on radiation-reaction-driven instabilities:

— C. Badiali, P.J. Bilbao, F. Cruz & L.O. Silva, *Machine Learning-based models in particle-in-cell codes for advanced physics extensions*, Journal of Plasma Physics 88.6: 895880602 (2022)

— P.J. Bilbao & L.O. Silva, *Radiation reaction cooling as a source of anisotropic momentum distributions with inverted populations*, Physical Review Letters 130:16, 165101 (2023)

— C.D. Arrowsmith, P. Simon, P.J. Bilbao, A.F.A. Bott *et al. Laboratory realization of relativistic pair-plasma beams*, Nature Communications 15:5029 (2023)

— P.J. Bilbao, R.J. Ewart, F. Assunçao, T. Silva & L.O. Silva, *Ring momentum distributions as a general feature of Vlasov dynamics in the synchrotron dominated regime*, Physics of Plasmas 31:5, 052112 (2024)

— R.J. Ewart, M.L. Nastac, P.J. Bilbao, T. Silva, L.O. Silva, A.A. Schekochihin, *Relaxation to universal non-Maxwellian equilibria in a collisionless plasma*, Proceedings of the National Academy of Sciences 122.17 e2417813122 (2025)

— P.J. Bilbao, T. Silva & L.O. Silva, *Radiative cooling induced coherent maser emission in relativistic plasmas*, Science Advances 11.15, eadt8912 (2025)

— P.J. Bilbao, T. Silva & L.O. Silva, *Phase-Space Shaping in Wakefield Accelerators due to betatron cooling*, (to be submitted 2025)

— T. Silva, P.J. Bilbao & L.O. Silva, *The electron cyclotron maser instability in laser-ionized plasmas*, arXiv:2412.06783 (to be submitted 2025)

— C.D. Arrowsmith, F. Miniati, P.J. Bilbao, P. Simon *et al. Suppression of pair beam instabilities in a laboratory analogue of blazar pair cascades*, submitted to Proceedings of the National Academy of Science (2025)

— J. W. D. Halliday, C. D. Arrowsmith,1, A. M. Goillot, P. J. Bilbao, *et al. First measurement of collective behavior in a relativistic pair-plasma* (in prep. 2025)

— F. Assunçao, P.J. Bilbao & L.O. Silva, *Particle Drifts and Radiation Reaction in Astrophysics*, (in prep. 2025)

Invited talks

The results of this work were presented in invited talks at several major international conferences:

— European Physics Society Plasma Physics conference, July 2024 (Salamanca, Spain), “Coherent electron cyclotron maser emission triggered by radiation reaction"

— High Energy Density Laboratory Astrophysics (HEDLA), May 2024 (Tallahassee, FL), “Laboratory analogues of astrophysical coherent maser processes".

— Fifth Purdue Workshop on Relativistic Plasma Astrophysics, May 2024 (Purdue, IN), “Radio Masers in the Synchrotron Dominated Regime".

— 65th Annual Meeting of the American Physics Society Division of Plasma Physics, November 2023 (Denver, CO), “Kinetically unstable distributions as a result of radiative damping in strong electromagnetic fields".

— LPHYS'22, June 2022 (Online), “The Impact of Radiation Reaction on the Topology of the Momentum Space".

COMPUTATIONAL ALLOCATIONS

This PhD could not have been completed without the large computational allocations that were secured. During this PhD I helped secure $\sim$ 88 million CPU hours as PI and co-PI of different projects which benefited the whole group.

— co-PI of CREPE: Coherent Radiation mechanisms in Extreme Plasma Environment LUMI (FI) via EuroHPC

— PI of MAPs: Masers in Astrophysical Plasmas 20 million CPU hours in the supercomputer DEUCALION (PT) via FCT/RNCA

— PI of MAPs 2: Masers in Astrophysical Plasmas (part 2) 30 million CPU hours in the supercomputer MareNostrum 5 (SP) via FCT/RNCA

CHAPTER 2

SYNCHROTRON COOLING AS SOURCE OF RING-SHAPED MOMENTUM DISTRIBUTIONS

This chapter is adapted from: P. J. Bilbao & L. O. Silva Phys. Rev. Lett. 130.16:165101 (2023) and P. J. Bilbao, *et al.* Phys. Plasmas 31.5 (2024).

2.1 INTRODUCTION

The interplay between quantum electrodynamics (QED) and collective plasma dynamics has recently garnered significant attention, driven by the increasing feasibility of accessing such regimes in both astrophysical and laboratory settings [20, 21, 23–25, 70, 71, 93–99].

In the presence of strong electromagnetic fields, relativistic charged particles can radiate photons with energies comparable to the rest mass of the electron $m_e c^2$ or even comparable to the kinetic energy of the particle $(\gamma - 1)m_e c^2$, where γ is the Lorentz factor and m_e is the electron mass. In these regimes, radiation reaction, i.e., the momentum recoil associated with photon emission, must be accounted for, as it fundamentally alters particle dynamics [20, 70, 100].[1]

Conditions for radiation reaction to play a central role are naturally realized in astrophysical environments such as the magnetospheres of compact objects [15, 27, 101–103], and are increasingly within reach in laboratory experiments. This progress is driven by advances in high-intensity laser systems [19, 28, 90, 104–106], magnetic-field amplification platforms [107–109], and high-energy-density or fusion plasmas [110, 111].

One of the simplest yet most consequential features of this regime is that the radiation reaction force, sometimes referred to as the radiation friction force [70], does not conserve phase-space volume. This sets it apart from the classical collsionless plasma dynamics mediated by the Lorentz force. This was hinted in recent works on runaway electrons in fusion plasmas that have shown that radiation reaction and collisional effect induce "bumps" along

[1] To be exact, radiation reaction needs to be self-consistently taken into account when the radiative cooling timescales become comparable to the plasma collective timescales.

the runaway electron tail [110, 111]. In this chapter, we show that this behavior is more general and that bunched and anisotropic momentum distributions can be produced in other regions of the momentum distribution due to the properties of the radiation reaction force, *i.e.*, its tendency to induce directional, energy-dependent cooling.

Previous works have shown that radiation reaction can produce phase-space attractors in laser-beam interactions [112], enhance anisotropic acceleration in radiatively cooled turbulent plasmas [96], and efficiently drive kinetic instabilities such as the firehose instability [24]. As we will see in Chapter 3, it also plays a key role in triggering the electron cyclotron maser instability (ECMI) [23, 113, 114]. These findings underscore the need for a first-principles kinetic approach to understand radiatively cooled plasmas, where phase-space dynamics and radiation losses are coupled.

Radiation reaction is an interesting phenomenon because it plays a fundamentally different role in plasma phase-space dynamics compared to collisional processes. While collisions tend to diffuse particles and expand the phase-space volume, radiation reaction acts to constrain it. This difference arises because radiation reaction is a non-conservative force that does not preserve phase-space volume, it violates Liouville's theorem. Conventional collisionless plasma dynamics describe an incompressible fluid in phase space, but the inclusion of radiation effectively allows the compression of the phase-space fluid.

This becomes apparent when considering the synchrotron radiative power, which scales as $P \propto \gamma^4(\mathbf{p} \times \mathbf{a})^2$, where γ, $\mathbf{p}$, and $\mathbf{a}$ are the particle's Lorentz factor, momentum, and acceleration, respectively [17, 115]. Particles experiencing stronger acceleration radiate more intensely and, as a result, cool more rapidly, leading to converging trajectories in momentum space. Moreover, this energy loss is directionally dependent, leading to anisotropic evolution of the momentum distribution [23, 24]. A clear example is synchrotron cooling in a uniform magnetic field: as particles gyrate, they emit radiation predominantly due to their perpendicular motion, gradually losing energy. In ultra-strong magnetic fields, the radiated synchrotron energy can represent a substantial fraction of the particle's initial kinetic energy.

As we will see, this process reduces the entropy of the plasma particles, as radiation reaction constricts the accessible phase-space volume. The lost entropy is carried away by the emitted synchrotron photons, driving the system away from thermodynamic equilibrium. This fundamental behavior, and its consequences for the emergence of structured, unstable distribution functions, is a central focus of this work.

In this chapter, we show how differential cooling in momentum space leads to anisotropic regions in phase space, including the formation of inverted populations, *i.e.*, regions where higher-energy states are more populated than adjacent lower-energy ones, in violation of thermal equilibrium. This effect is a general feature of radiation reaction cooling and its importance depends on the specific details of the field configuration. We focus on the simplest field configuration: a plasma immersed in a constant strong magnetic field, where synchrotron losses act preferentially on the perpendicular momentum and lead to a classical Landau-level population inversion.[2] This effect is demonstrated analytically by incorporating radiation re-

[2]Strictly speaking, Landau levels refer to discrete quantum energy levels in the perpendicular motion of a charged particle in a magnetic field. In this work, we use the term heuristically to describe classical momentum-space struc-

action into the Vlasov equation [110, 111, 116–118], yielding exact results for the evolution of the distribution function, and the relevant timescales for the resulting ring momentum distribution.

The phase-space cooling, resulting from the fact that the plasma radiates away its entropy, changes the plasma dynamics drastically, compared to the classical Lorentz force, resulting in kinetically unstable distributions in the shape of ring distributions that can be a source of magnetic-field amplification or coherent radiation. We will demonstrate that this effect is relevant for isotropic Maxwellian (or Maxwell–Jüttner) plasmas with a minimum temperature of $T > m_e c^2/\sqrt{3}$.

The resulting momentum distributions with inverted Landau populations are known to be kinetically unstable and responsible for providing the free energy for kinetic plasma instabilities and coherent radiation mechanisms such as the electron cyclotron maser instability [119–123]. Thus, radiation reaction naturally leads to the conditions required for the seeding of instabilities and coherent radiation driven by inverted Landau populations and we explore how these results are relevant for astrophysical and laboratory plasmas [49, 124–127].

Particle-in-cell (PIC) simulations confirm the theoretical results for a broad range of initial conditions spanning both the classical $\chi \ll 1$ and quantum $\chi > 1$ regimes, where χ is the Lorentz- and gauge-invariant parameter $\chi = \sqrt{-(F_{\mu\nu}p^\nu)^2}/(E_{\mathrm{Sc}} m_e c)$ [18, 19]; e is the electron charge, $F_{\mu\nu}$ the electromagnetic tensor and p^ν the 4-momentum of the particle. For a constant background magnetic field, χ reduces to $\chi = p_\perp |\mathbf{B_0}| / (m_e c B_{Sc})$, where $B_{Sc} = m_e^2 c^3/(e\hbar) \simeq 4.41 \times 10^{13}$ G is the Schwinger critical field..

2.2 SINGLE PARTICLE DYNAMICS

We will first consider the classical description of radiation reaction [100, 128–131], QED radiation reaction will be discussed later. The classical description of radiation reaction can be shown to be valid for $\chi \lesssim 1$, where the effects of quantum corrections are shown to be small compared to the classical prescription acting on a collection of synchrotron radiating particles (See Sec. B). The radiation reaction force for an electron with arbitrary momentum in a constant electromagnetic field is described by the Landau–Lifshitz expression for radiation reaction [100, 131]

$$\mathbf{F}_{\mathrm{RR}} = -\frac{2}{3}\frac{e\alpha}{B_{\mathrm{Sc}}}\left\{\frac{\gamma \mathbf{p}}{m_e c}\left[\left(\mathbf{E} + \frac{\mathbf{p}\times\mathbf{B}}{\gamma m_e c}\right)^2 - \left(\frac{\mathbf{p}\cdot\mathbf{E}}{\gamma m_e c}\right)^2\right] - \mathbf{E}\times\mathbf{B} - \frac{\mathbf{B}\times(\mathbf{B}\times\mathbf{p}) + \mathbf{E}(\mathbf{p}\cdot\mathbf{E})}{\gamma m_e c}\right\}, \tag{2.1}$$

where α is the fine-structure constant, $\gamma = \sqrt{1 + \mathbf{p}^2/m_e^2 c^2}$, and $\mathbf{E}$ and $\mathbf{B}$ are the electric and magnetic fields, expressed in CGS Gaussian units. The first term in Eq. (2.1), which dominates for relativistic particles ($\gamma \gg 1$), already shows a non-linear dependence of the radiation reaction force on the momentum of the particle $\mathbf{p}$. To study synchrotron cooling, we consider the case in which $\mathbf{E} = 0$ and constant magnetic field $\mathbf{B} = B\,\hat{e}_\parallel$, where $\hat{e}_\parallel$ is the unit vector along

turing that resembles a population inversion in perpendicular energy. There is no quantization in our treatment; the spectrum remains continuous.

the magnetic-field direction. Thus Eq. (2.1) simplifies to

$$\mathbf{F}_{RR} = -\frac{2}{3}\frac{e\alpha}{\gamma B_{\mathrm{Sc}}}\left[\frac{\mathbf{p}\,(\mathbf{p}\times\mathbf{B})^2}{m_e^2c^2} - \frac{\mathbf{B}\times(\mathbf{B}\times\mathbf{p})}{m_e c}\right]. \tag{2.2}$$

We now focus on the single-particle momentum evolution due to synchrotron cooling. Due to the symmetry perpendicular to the magnetic-field direction, it is convenient to decompose the momentum vector $\mathbf{p}$ into the parallel $p_\parallel$ and the perpendicular $p_\perp$ momentum components with respect to $\mathbf{B}$. Thus, the cross products in Eq. (2.2) simplify to $(\mathbf{p}\times\mathbf{B})^2 = p_\perp^2 B^2$ and $\mathbf{B}\times(\mathbf{B}\times\mathbf{p}) = -B^2 p_\perp \hat{e}_\perp$. From now on, momentum $\mathbf{p}$ and time t, are given in units of $m_e c$, and the inverse of the cyclotron frequency $\omega_{ce}^{-1} = m_e c/eB$, respectively. And we define $B_0 = B/B_{\mathrm{Sc}}$, unless stated otherwise we will continue to use this conventio.

The equations of motion due to synchrotron cooling are [132, 133]

$$\frac{dp_\perp}{dt} = -\frac{2}{3}\alpha B_0 \frac{p_\perp + p_\perp^3}{\gamma}, \tag{2.3}$$

$$\frac{dp_\parallel}{dt} = -\frac{2}{3}\alpha B_0 \frac{p_\parallel p_\perp^2}{\gamma}, \tag{2.4}$$

Equation (2.3) already demonstrates the nonlinear nature of synchrotron cooling, in the limit $p_\perp \gg 1$ then $dp_\parallel/dt \propto dp_\perp/dt \propto -p_\perp^2$, which implies nonlinear transport in momentum space, due to the square factor, and allows to compress momentum space trajectories. These equations can be solved exactly, yielding an analytical expression for the momentum trajectory as a function of time. The full derivation is provided in App. C.1. The result is:

$$p_\perp(t) = \frac{p_{\perp 0}}{\cosh(\tau')\left[1+\sqrt{1+p_{\perp 0}^2}\tanh(\tau')\right]}, \tag{2.5}$$

$$p_\parallel(t) = p_{\parallel 0}\frac{1+\tanh(\tau')/\sqrt{1+p_{\perp 0}^2}}{1+\tanh(\tau')\sqrt{1+p_{\perp 0}^2}}, \tag{2.6}$$

where $\tau = 2\alpha B_0 t/3$ and $\tau' = \tau\sqrt{1+p_{\perp 0}^2}/\gamma_0$, with $\gamma_0 = \sqrt{1+p_{\perp 0}^2+p_{\parallel 0}^2}$. These expressions describe the nonlinear cooling of the perpendicular and parallel components of momentum. As $t\to\infty$, all trajectories converge toward $p_\perp \to 0$ and $p_\parallel \to p_{\parallel 0}/\sqrt{1+p_{\perp 0}^2}$, reflecting the covariant nature of the radiation reaction force and is associated with a constant of motion given by

$$C_1 = \frac{p_\parallel}{\sqrt{1+p_\perp^2}}. \tag{2.7}$$

C_1 characterises the streamlines shown in Fig. 2.1. Stating that C_1 is a conserved quantity, is equivalent to stating that the parallel velocity $\beta_\parallel$ is conserved during cooling, as $\beta_\parallel = p_\parallel/\gamma = C_1/\sqrt{1+C_1^2}$. Another quantity that is conserved[3] can be obtained from Eq. (2.5) and Eq. (2.6)

$$C_2 = \tanh^{-1}\left(\frac{1}{\sqrt{1+p_\perp^2}}\right) - \frac{\gamma}{\sqrt{1+p_\perp^2}}\tau, \tag{2.8}$$

[3] C_2 is not exactly a constant of motion as it is time-dependent, yet it is a quantity that is conserved for any trajectory.

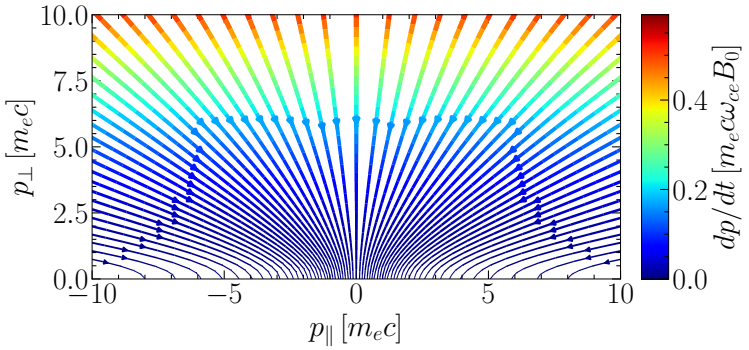

FIGURE 2.1: Streamlines of the momentum-space trajectories of particles undergoing synchrotron cooling [Eqs. (2.5) and (2.6)] demonstrating that particles in a strong magnetic field cool down anisotropically and in a non-linear fashion. This is seen by the increase in the gradient of the magnitude of the radiation force as a function of $p_\perp$ indicated by the color of the streamlines, stronger (red) at larger $p_\perp$ than at lower $p_\perp$.

which is time-dependent, since radiation reaction is a dissipative process.

We now employ the single-particle trajectories to understand the collective effect of synchrotron cooling, particularly the conditions for an initial MDF $f_0 \equiv f(t = 0)$ to develop a population inversion $\partial f/\partial p_\perp > 0$ in a finite time. As cooling is strongest in regions of $p_\perp \gg p_\parallel$, we expect that any bunching due to $dp_\perp/dt \propto -p_\perp^2$ will occur in that region of momentum space where $p_{\perp\parallel}$. Thus, we focus our study on the evolution of the MDF there, where the momentum-distribution evolution is dominated by the cooling in $p_\perp$.

2.2.1 NECESSARY CONDITION FOR THE DEVELOPMENT OF RING-SHAPED DISTRIBUTIONS

We consider the evolution of a small volume of momentum space $V_p(t)$. As radiation reaction deforms this volume, it retains the same number of particles, implying

$$\iint_{V_p(t)} dp_\parallel\, dp_\perp\, p_\perp\, f(p_\perp, p_\parallel, t) = \iint_{V_p(0)} dp_\parallel\, dp_\perp\, p_\perp\, f_0(p_\perp, p_\parallel). \tag{2.9}$$

Changing variables $\{p_\perp, p_\parallel\} \to \{p_{\perp 0}, p_{\parallel 0}\}$ on the left-hand side (method of characteristics) yields

$$f(p_\perp, p_\parallel, t) = \left|\frac{\partial(p_\perp, p_\parallel)}{\partial(p_{\perp 0}, p_{\parallel 0})}\right|^{-1} \frac{p_{\perp 0}}{p_\perp}\, f_0(p_{\perp 0}, p_{\parallel 0}). \tag{2.10}$$

At $p_\parallel = 0$, the region where the bunching will be strongest, differentiating with respect to $p_{\perp 0}$ and using Eq. (2.5) gives the condition for eventual $\partial f/\partial p_\perp > 0$:[4]

$$\frac{1}{p_\perp f_0(p_\perp)} \frac{\partial f_0(p_\perp)}{\partial p_\perp} > -\frac{2\,\tanh\tau\left(2\gamma_\perp^2 + 3\gamma_\perp \tanh\tau + 1\right)}{\gamma_\perp^2\left(\gamma_\perp + \tanh\tau\right)\left(\gamma_\perp \tanh\tau + 1\right)}, \tag{2.11}$$

[4]This compares the evolution of two neighboring phase-space elements under synchrotron cooling. A positive gradient $\partial f/\partial p_\perp > 0$ forms when the higher-$p_\perp$ element is compressed more than its lower-$p_\perp$ neighbor, after accounting for the Jacobian (phase-space contraction) and the initial particle content f_0.

with $\gamma_\perp = \sqrt{1+p_\perp^2}$ and where all quantities are evaluated from the initial condition (so we drop the 0 subscripts below). In the late-time limit $\tau \to \infty$, $\tanh\tau \to 1$, one obtains the necessary condition for developing inverted Landau populations

$$\frac{1}{f_0(p_\perp)}\frac{\partial f_0(p_\perp)}{\partial p_\perp} > -\frac{2p_\perp\left(1+2\sqrt{1+p_\perp^2}\right)}{(1+p_\perp^2)\left(1+\sqrt{1+p_\perp^2}\right)}. \tag{2.12}$$

Integrating Eq. (2.12) gives

$$f_0(p_\perp) > \frac{4\,f_0(0)}{\gamma_\perp^2\,(1+\gamma_\perp)^2}. \tag{2.13}$$

Thus, initial distributions that do not decay *faster* than the right-hand side of Eq. (2.13) at a given $p_\perp$ will develop local bunching there ($\partial f/\partial p_\perp > 0$), where Eq. (2.13) is fulfilled. In practice this requires a sufficiently broad initial spread in $p_\perp$, and a shallower power-law distribution than $f \propto \gamma_\perp^{-4}$.

For a Maxwellian MDF, $\partial f_0/\partial p_\perp = -p_\perp f_0/p_{\rm th}^2$, where $p_{\rm th} = \sqrt{\theta_e}$ and $\theta_e = k_B T/(m_e c^2)$ is the dimensionless electron temperature. Inserting this derivative into Eq. (2.12)[5] and solving in the limit $p_\perp \ll 1$ yields a condition for the minimal $p_{\rm th}$ at which a region satisfies the population inversion criterion.[6] Ring-shaped MDFs will form only when $p_{\rm th} > 1/\sqrt{3} \approx 0.577$, corresponding to $k_B T > m_e c^2/3 \simeq 170$ keV $\approx 2\times 10^9$ K. Similarly, for a Maxwell–Jüttner distribution, $\partial f_0/\partial p_\perp = -p_\perp/(\gamma\, p_{\rm th}^2)\, f_0$, and inserting this into the same equation gives the threshold $p_{\rm th} > 1/3 \approx 0.333$, i.e. $k_B T > m_e c^2/9 \simeq 57$ keV $\approx 7\times 10^8$ K.

These examples show that MDFs with inverted Landau populations naturally arise from Vlasov–Maxwell dynamics in the presence of radiation reaction for relativistic thermal plasmas. The inequality in Eq. (2.13) is satisfied by many broad distribution functions with sufficient thermal energy, such as Maxwell–Boltzmann, Maxwell–Jüttner, and power laws. We have shown that the inversion is established within a finite timescale for any initial condition satisfying Eq. (2.13). The timing and evolution of the inversion will be discussed later in this chapter. Further arguments supporting the generality of ring distributions from synchrotron cooling are given in Appendix C.4, and additional numerical tests using relativistic particle pushers and full Particle-in-Cell simulations with the OSIRIS code [28, 81, 91] corroborate these findings (see Sec. C.6).

2.3 FULL KINETIC TREATMENT

2.3.1 MODIFIED VLASOV EQUATION & 0TH ORDER SOLUTION

Generalized kinetic equations for non-conservative forces, particularly for radiation reaction, have been known for many decades [116, 134, 135]. Recent results have employed generalized kinetic equations with radiation reaction to model conditions for experimental fusion [110, 111,

[5] One can also check which values satisfy Eq. (2.13) for an arbitrary distribution function, but this often leads to a transcendental equation. For this reason, Eq. (2.12) is generally more useful.

[6] In the small $p_\perp$ limit Eq. (2.12) becomes $\partial\left(\log(f_0(p_\perp))\right)/\partial p_\perp = 3p_\perp$.

117, 136], laser-plasma interactions [118, 137], and to derive fluid descriptions that include radiation reaction effects [138]. Here, we employ the non-manifestly covariant form of the Vlasov equation with radiation reaction force term [110, 111, 116–118, 136, 139]

$$\frac{\partial f}{\partial t} + \frac{\mathbf{p}}{\gamma} \cdot \nabla_r f + \nabla_p \cdot [(\mathbf{F}_{RR} + \mathbf{F}_L) f] = 0, \tag{2.14}$$

where $f(\mathbf{p}, \mathbf{r}, t)$ is the distribution function, $\mathbf{F}_L$ is the Lorentz force, and ∇_r and ∇_p are nabla operators acting on the position and momentum coordinates, respectively. Including the radiation reaction force as the operator $\nabla_p \cdot (\mathbf{F}_{RR} f)$ guarantees the conservation of the number of particles [136]. Since $\mathbf{F}_L$ conserves the phase-space volume, but $\mathbf{F}_{RR}$ is dissipative, then $\nabla_p \cdot \mathbf{F}_{rad} \neq \nabla_p \cdot \mathbf{F}_L = 0$. Since we consider a spatially homogeneous plasma, we can neglect the term proportional to $\nabla_r f$. Equation (2.14) corresponds to Vlasov equation with the inclusion of a classical radiation reaction force.[7]

Moreover, as we are assuming gyrotropy, *i.e.* cylindrical symmetry $f = f(p_\perp, p_\parallel)$, and uniform magnetic field, the effect of the Lorentz force due to a strong magnetic field on the distribution is $\nabla_p \cdot (\mathbf{F}_L f) = 0$, even when $\mathbf{F}_L \neq 0$. Thus, Eq. (2.14) simplifies to

$$\frac{\partial f}{\partial t} + \mathbf{F}_{RR} \cdot \nabla_p f + f \nabla_p \cdot \mathbf{F}_{RR} = 0. \tag{2.15}$$

In cylindrical momentum coordinates, the operators are $\nabla_p f = \partial f / \partial p_\parallel \hat{\mathbf{e}}_\parallel + \partial f / \partial p_\perp \hat{\mathbf{e}}_\perp$ and

$$\begin{aligned} \nabla_p \cdot \mathbf{F}_{RR} &= \frac{1}{p_\perp} \frac{\partial \left(p_\perp F_{RR\perp} \right)}{\partial p_\perp} + \frac{\partial F_{RR\parallel}}{\partial p_\parallel} \\ \nabla_p \cdot \mathbf{F}_{RR} &= -\frac{2}{3} \alpha B_0 \frac{2 + 4p_\perp^2}{\gamma}, \end{aligned} \tag{2.16}$$

where $F_{RR\perp} = dp_\perp / dt$ & $F_{RR\parallel} = dp_\parallel / dt$ given by Eqs. (2.3)–(2.4). One notes that, as expected, the divergence of the radiation reaction force is negative. This demonstrates one of the key features of radiation reaction, i.e., radiation reaction compresses the momentum phase–space volume as $\nabla_p \cdot \mathbf{F}_{RR} < 0$. In doing so, it acts against collisions that have the property $\nabla_p \cdot \mathbf{F}_{col} > 0$, where $\mathbf{F}_{col}$ is an effective collisional force. Therefore, radiation reaction reduces the phase-space volume and thus, the entropy of the plasma, decreases.

The Vlasov equation for a distribution function f undergoing synchrotron cooling becomes

$$\frac{\partial f}{\partial \tau} - \frac{p_\perp^3 + p_\perp}{\gamma} \frac{\partial f}{\partial p_\perp} - \frac{p_\perp^2 p_\parallel}{\gamma} \frac{\partial f}{\partial p_\parallel} - \frac{2 + 4p_\perp^2}{\gamma} f = 0. \tag{2.17}$$

Equation (2.17) can be numerically integrated for any given initial distribution f_0. This differential equation describes the non-linear transport in momentum space where the momentum-space flow is compressible, which can exhibit momentum-space shocks analogous to hydrodynamic shocks [23, 24], resulting from $\nabla_p \cdot \mathbf{F}_{RR} < 0$ and $\nabla_p \cdot \mathbf{F}_{RR}$ not being constant along $\sim p_\perp$.

[7] We note that a quantum synchrotron equation can be recovered by coupling the QED operator for synchrotron emission with the Vlasov equation. From which one can recover Eq. (2.14) in the classical regime $\chi \lesssim 1$, this is done in Appendix B.

Our key findings apply beyond synchrotron-cooled plasmas. Other systems or electromagnetic field configurations where the dissipative power depends non-linearly on the energy level occupied will develop population inversions. In our current case of synchrotron-cooled plasmas, the radiative power $P \propto p_\perp^3/\gamma$ depends non-linearly on the Landau energy level occupied (i.e., $p_\perp$). Other radiation cooling mechanisms that exhibit analogous behavior, such as is the case of electrons undergoing betatron motion in an ion-channel, whose radiative power $P \propto r_\beta^2$, depends non-linearly on the betatron energy level occupied, i.e., the betatron oscillation amplitude r_β, and will be the subject of Chapter 4.

We note that analytical solutions to Eq. (2.17) exist. For example, one can consider a distribution function with a large spread in $p_\perp$ centered around $p_\parallel = 0$ and an infinitesimal width in $p_\parallel$. In this configuration, one can approximate $\tau' = \tau$ (since $p_\perp \gg p_\parallel$) and employ the method of characteristics to solve Eq. (2.17) for $f(p_\perp, p_\parallel = 0) = f_\perp(p_\perp)$, finding[8]

$$f_\perp(p_\perp, t) = \frac{f_{\perp 0}\left(\operatorname{csch}(a)\right)}{\left(\gamma_\perp p_\perp \sinh(a)\tanh(a)\right)^2}, \tag{2.18}$$

where $a = \log\left(p_\perp/(\gamma_\perp + 1)\right) + \tau$ and $\gamma_\perp = \sqrt{1 + p_\perp^2}$. Equation (2.18) has a singularity at $p_\perp = 1/\sinh(\tau)$. This singularity lies outside the range of valid physical values for $p_\perp$. As noted before, the whole momentum space is bounded within $p_\perp < 1/\sinh(\tau)$; therefore, Eq. (2.18) is well behaved for the range $0 < p_\perp < 1/\sinh(\tau)$, for all values of τ.[9]

The results from plotting Eq. (2.18) for different initial distributions (Maxwellian and Maxwell–Jüttner) are shown in Fig. 2.2. Regions where the curves are red in Fig. 2.2 have $\partial f/\partial p_\perp > 0$. These results validate our earlier predictions, where we examine the late-stage evolution of the distributions due to synchrotrn cooling, for Maxwellian and Maxwell–Jüttner distributions in Eq. (2.12) and Eq. (2.13). As can be seen inf Fig. 2.2, the plasma requires that $p_{\text{th}} > 0.57\, m_e c$ and $p_{\text{th}} > 0.33\, m_e c$, for Maxwellian and Maxwell–Jüttner distributions, to develop ring-shaped MDFs. As we have shown that plasmas need a minimum thermal energy to develop a population inversion, we will henceforth study Eq. (2.17) in the relativistic regime, which is also the regime relevant for astrophysical plasmas.

2.3.2 Relativistic regime

When $\gamma \gg 1$ and $p_\perp \gg 1$, the trajectories in momentum space [Eqs. (2.5) and (2.6)] and the Vlasov equation [Eq. (2.17)] become

$$p_\perp(t) = \frac{p_{\perp 0}}{1 + p_{\perp 0}^2 \tau/\gamma_0}, \tag{2.19}$$

$$p_\parallel(t) = \frac{p_{\parallel 0}}{1 + p_{\perp 0}^2 \tau/\gamma_0}, \tag{2.20}$$

$$\frac{\partial f}{\partial \tau} - \frac{p_\perp^3}{\gamma}\frac{\partial f}{\partial p_\perp} - \frac{p_\perp^2 p_\parallel}{\gamma}\frac{\partial f}{\partial p_\parallel} - \frac{4p_\perp^2}{\gamma} f = 0. \tag{2.21}$$

[8] For furhter details on this solution see Appendix C.2.

[9] This includes $\tau = 0$, when $p_\perp < \infty$ can be arbitrarily large.

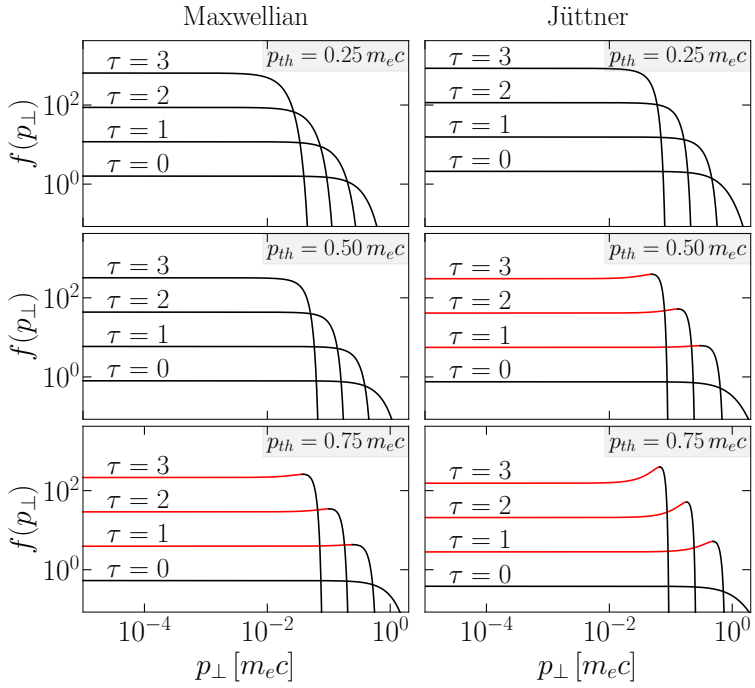

FIGURE 2.2: The time evolution of Eq. (2.18) for an initial mildly relativistic $p_{\rm th} \lesssim 1\, m_e c$, Maxwellian (left) and Maxwell–Jüttner plasma (right), demonstrating the minimum thermal energy needed to develop a region with $\partial f/\partial p_\perp > 0$, indicated in red. Different panels show initial thermal spreads $p_{\rm th} = 0.25\, m_e c$ (top), $p_{\rm th} = 0.50\, m_e c$ (middle), and $p_{\rm th} = 0.75\, m_e c$ (bottom), at normalized times $\tau = 0$, 1, 2, and 3, corresponding to unnormalized times $t = 2 m_e B_{\rm Sc} \tau/(3\alpha e B^2)$. This illustrates the minimum energy required to develop regions with $\partial f/\partial p_\perp > 0$ in the semi-relativistic regime.

These expressions accurately describe synchrotron cooling in the ultra-relativistic region of momentum space, where $p_\perp \gg 1$ and $p_\perp \gg p_\parallel$, so that $\gamma \simeq p_\perp$. At late times, as cooling proceeds and $p_\perp$ decreases to order unity, the neglected terms in order of γ are no longer small and the full equations [Eqs. (2.5) and (2.6)] should be used instead.

Equation (2.21) can be solved if one examines regions of momentum space where $p_\perp \sim \gamma$ (i.e., $p_\perp \gg p_\parallel$), corresponding to the high-$p_\perp$ limit where $\gamma \simeq p_\perp$. In this regime, Eq. (2.21) differs from Eq. (2.17) in that γ has been approximated by $p_\perp$, simplifying the advection terms. A solution for Eq. (2.21) can then be obtained using the method of characteristics[10] [23]:

$$f(p_\perp, p_\parallel, \tau) = \frac{f_0\left(\frac{p_\perp}{1-\tau p_\perp}, \frac{p_\parallel}{1-\tau p_\perp}\right)}{(1-\tau p_\perp)^4}. \tag{2.22}$$

Equation (2.22) describes the evolution of an initial momentum distribution f_0 due to synchrotron cooling in the relativistic limit. It is valid as long as the distribution retains significant weight in the high-$p_\perp$ region, which typically corresponds to $\tau \lesssim 1$ before perpendicular momentum has contracted to $p_\perp \sim 1$. Similarly to Eq. (2.18), Eq. (2.22) appears to have a singularity at $p_\perp = 1/\tau$, but this point always lies outside the range of validity. From Eq. (2.19), a particle with initial $p_{\perp 0} \to \infty$ evolves following $p_\perp(\tau) = 1/\tau$; thus all particles are bounded between $0 < p_\perp < 1/\tau$. This means f is well behaved for all physically relevant values of $p_\perp$, *i.e.*, $p_\perp < 1/\tau$. This bunching inevitably leads to a Landau population inversion, *i.e.*, a ring distribution in momentum space (see Appendix C.4). Moreover, the resulting phase-space contraction requires a decrease in plasma entropy over time, as shown in Appendix D.1.

We note that the same consistent results can be obtained if one employs the relativistic limit, *i.e.*, the dominant contribution is the leading order in γ for the Landau-Lifshiftz formula for radiation reaction as [100, 131]

$$\mathbf{F}_{rad} = -\frac{2}{3}\frac{e\alpha\gamma\mathbf{p}}{B_{Sc} m_e c}\left[\left(\mathbf{E} + \frac{\mathbf{p}}{\gamma m_e c}\times\mathbf{B}\right)^2 - \left(\frac{\mathbf{p}}{\gamma m_e c}\cdot\mathbf{E}\right)^2\right], \tag{2.23}$$

where for a constant $\mathbf{B}$ field simplifies to $\mathbf{F}_{rad} = -\frac{2}{3}\alpha B_0 \omega_{ce} p_\perp^2 \mathbf{p}/(\gamma m_e^2 c^2)$ and results in the same single particle equations of motion and modified Vlasov equation in the relativistic limit.

2.3.3 Temporal evolution of the ring distribution

As we have demonstrated (see Sec. 2.2.1 & Appedix C.4), relativistic plasmas undergoing synchrotron cooling will develop a population inversion $\partial f/\partial p_\perp > 0$. To determine the relevant timescales for forming these ring-shaped MDFs one can employ a representative initial distribution function with a large spread in $p_\perp$. We consider an isotropic Maxwellian distribution function

$$f_{0,\mathrm{MB}}(p_\perp, p_\parallel) = \frac{1}{(2\pi p_{\mathrm{th}}^2)^{3/2}} \exp\left(-\frac{p_\perp^2 + p_\parallel^2}{2p_{\mathrm{th}}^2}\right). \tag{2.24}$$

[10] See Appendix C.3.

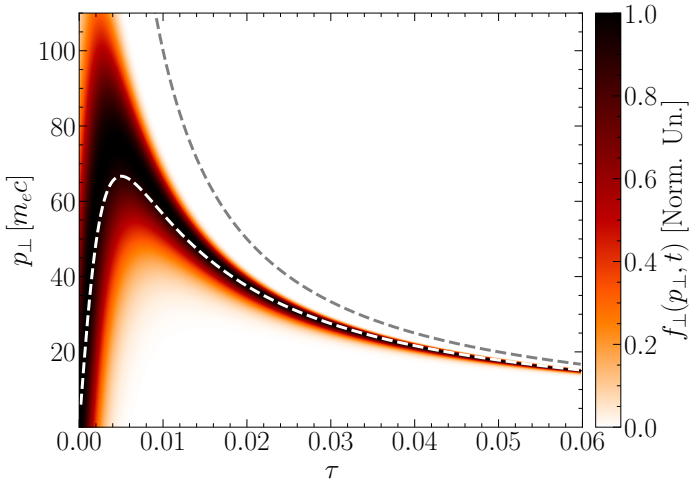

FIGURE 2.3: Evolution of an isotropic initial Maxwellian distribution, with $p_{\rm th} = 100\, m_e c$ calculated analytically from Eq. (2.22) (The distribution is normalised to its maximum value at each time). The white and gray dashed lines indicate the ring radius predicted by Eq. (2.25) and the curve that bounds the momentum space $p_\perp = \tau^{-1}$, respectively.

The resulting ring radius $p_R(t)$ in momentum space, defined as $\left|\partial_{p_\perp} f_\perp(p_\perp, t)\right|_{p_\perp = p_R(t)} = 0$, where $f_\perp(p_\perp, t) = \int_{-\infty}^{\infty} f(p_\perp, p_\parallel, t) dp_\parallel$ is the integrated distribution along $p_\parallel$. Using Eq. (2.22) to determine the temporal evolution of $f_{0,\rm MB}$, p_R evolves as

$$p_R(t) = \frac{1 + 6p_{\rm th}^2\tau^2 - \sqrt{1 + 12p_{\rm th}^2\tau^2}}{6p_{\rm th}^2\tau^3}. \tag{2.25}$$

Several conclusions about the formation and evolution of ring momentum distributions can be drawn from Eq. (2.25). Figure (2.3) shows the evolution of $f_\perp(p_\perp, t)$ for an initial isotropic Maxwellian plasma with $p_{\rm th} = 100\, m_e c$ and the ring radius evolution (white dashed line) according to Eq. (2.25). At early times $\tau = 2\alpha B_0 t/3 \ll 1$, the ring radius grows linearly with time as $p_R(t) \sim 2p_{\rm th}^2 \alpha B_0 t$; this is due to a build-up of particles in momentum space at lower $p_\perp$ first. The ring MDF results from bunching as particles with higher energies radiate strongly and slow down faster, catching up with the lower energy particles. The bunching begins at low $p_\perp$ and propagates towards higher $p_\perp$ values, eventually, it asymptotically approaches the boundary of momentum space $p_\perp < p_\perp^* = \tau^{-1}$ and $p_R(t) \sim 1/\tau = 3/(2\alpha B_0 t)$, for large τ (in Fig. 2.3 at $\tau \sim 0.05$).

Whenever the bunching direction reverses [maximum value of $p_R(t)$], the gradient of the MDF starts growing much faster, and the distribution will produce a higher contrast ring-shaped MDF. Thus, we define that time as the ring formation time normalized to cyclotron periods estimated to be

$$t_R = \frac{3}{4\alpha B_0 p_{\rm th}} = \frac{3}{4\alpha \chi_{\rm th}}, \tag{2.26}$$

where $\chi_{\rm th} = p_{\rm th} B_0$, in cgs units $t_R = 3m_e^2 c^2 B_{\rm Sc}/(4\alpha e B^2 p_{\rm th})$.

A second longer timescale can be estimated, related to the ring MDF evolution to achieve efficient conditions for the growth of kinetic instabilities, specifically the electron cyclotron maser instability. There are two relevant factors here: i) the generation of population inversion $\partial f/\partial p_\perp$ with high gradients and ii) relativistic inertial effects that slow down the instability growth. We can estimate the evolution of $\partial f/\partial p_\perp$ by noting there is a small region between the momentum-space boundary, given by $p_\perp = 1/\tau$ [gray dashed curve in Fig. 2.3], and the ring radius [white dashed curve in Fig. 2.3] of size $\delta p = 1/\tau - p_R(t)$, which can be approximated, from Eq. (2.25), for initially large $p_{\rm th}$ as $\delta p = 1/(6p_{\rm th}\tau)$. Within that region, the distribution function has the property $\partial f/\partial p_\perp < 0$; conversely, there is a region just below the ring radius of comparable width δp, where the distribution function has the property $\partial f/\partial p_\perp > 0$. Thus, the positive gradient can be approximated as $\partial f/\partial p_\perp \sim f(p_R)/\delta p$ and $f(p_R) \sim 1/4\pi p_R(t)\delta p$, leading to

$$\frac{\partial f}{\partial p_\perp} \sim \frac{9}{\pi}\frac{p_{\rm th}^2}{p_R(t)^5} = \frac{9}{\pi}p_{\rm th}^2\tau^5, \tag{2.27}$$

which shows how the gradient, at early times $\tau \ll 1$, increases slowly as a function of τ and, as $\tau \lesssim 1$, the gradient grows faster. For a fixed gradient ring MDF, the maser growth rate is maximum when $p_R \sim 1$; for $p_R \gg 1$, relativistic inertial effects decrease the growth rate [140]. Thus, a natural choice for the maximum maser onset timescale in cyclotron periods is t_i the time it takes to reach $p_R \sim 1$, which for $p_{\rm th} \gg 1$ occurs at $\tau = 1$, resulting in

$$t_i = \frac{3}{2\alpha B_0}, \tag{2.28}$$

in unnormalized units $t_i = 3m_e c B_{\rm Sc}/(2\alpha e B^2)$. Within the timescale t_i, the growth rate associated with the maser instability has grown, due to the high gradient $\partial f/\partial p_\perp \gg 1$, and the ring has cooled down enough that relativistic inertial effects have been reduced. Thus, the onset of the maser instability should occur within a shorter timescale than t_i.

Scaling engineering formulas can be obtained for both timescales t_R and t_i,

$$t_R\ [5.2\,{\rm ns}] \simeq B^{-2}\ [50\,{\rm MG}]\ T_e^{-1}\ [10\,{\rm MeV}], \tag{2.29}$$

$$t_i\ [205\,{\rm ns}] \simeq B^{-2}\ [50\,{\rm MG}]\,. \tag{2.30}$$

These scalings are compatible with magnetospheric conditions around compact objects such as pulsars and magnetars, where $B \gg 100\,{\rm MG}$. The underlying process is fundamental: any sufficiently magnetized plasma in which perpendicular cooling dominates over isotropizing processes will inevitably develop narrow momentum-space rings, regardless of how the hot population was initially generated. This applies to heating by reconnection, shocks, turbulence, or other impulsive events. As a concrete example, Sec. 3.5 considers a plasma clump propagating outward through a neutron star magnetosphere, where this cooling-driven ring formation can take place. Other scenarios such as those occuring in pair-cascades may also be capable of producing such rings. Furhter work is still needed.

Interestingly, the distribution function of the plasma is evolving away from a thermal distrbution, this means that the emitted synchrotron spectrum changes as a function of time, with an initial power that decreases as a function of time. We study the resulting spectrum in

Appendix D.2, where the resulting spectrum demonstrates features significantly different to thermal plasmas, including power-law distributions.

2.3.4 PARALLEL DISTRIBUTION FUNCTION $f(p_\parallel)$

So far, we have focused on the perpendicular dynamics of the distribution function, particularly the bunching and formation of ring-shaped momentum distributions. However, another important feature of synchrotron cooling is its anisotropic nature, as shown in Fig.2.1 and Eqs.(2.5)–(2.6). The cooling rate for a single particle depends on its location in momentum space, with higher total momentum cooling faster. In particular, the perpendicular momentum $p_\perp$ cools more rapidly than the parallel momentum $p_\parallel$. This is not simply because the particle loses momentum in all directions, as is sometimes approximated in simplified models, but because the full radiation-reaction force contains an additional term that preserves the component of velocity parallel to the magnetic field. As a result, particles radiate away all perpendicular momentum while retaining a finite $p_\parallel$ set by the constant of motion from Eq. (2.7).[11] This anisotropy leads to unequal pressure components and can give rise to kinetic instabilities, such as the firehose instability, even without requiring a population inversion [24].

In what follows we assume that the initial distribution function is separable in perpendicular and parallel momentum, i.e., $f_0(p_\perp, p_\parallel) = f_{\perp 0}(p_\perp) f_{\parallel 0}(p_\parallel)$, so that the evolution in each component can be tracked independently. In the regime $\gamma \gg 1$ and $p_\perp \gg p_\parallel$, the time evolution of f can be described by Eq.(2.22), which remains valid at early times before perpendicular cooling becomes dominant. To estimate the final spread in parallel momentum, we use the constant of motion C_1 from Eq.(2.7), which yields the final parallel momentum

$$p_\parallel^{\mathrm{f}} = C_1 = \frac{p_{\parallel 0}}{\sqrt{1 + p_{\perp 0}^2}}. \tag{2.31}$$

This allows us to express the final parallel distribution function as

$$f_\parallel^{\mathrm{f}}(p_\parallel) = \int d\mathbf{p_0}\, f_0(p_{\perp 0}, p_{\parallel 0})\, \delta\left(p_\parallel - \frac{p_{\parallel 0}}{\sqrt{1 + p_{\perp 0}^2}}\right), \tag{2.32}$$

where the Dirac delta function $\delta(x)$ enables us to perform the integral over $p_{\parallel 0}$, giving

$$f_\parallel^{\mathrm{f}}(p_\parallel) = \int_0^\infty 2\pi p_{\perp 0}\, dp_{\perp 0}\, f_0\left(p_{\perp 0}, p_\parallel \sqrt{1 + p_{\perp 0}^2}\right) \sqrt{1 + p_{\perp 0}^2}. \tag{2.33}$$

Equation (2.33) defines the asymptotic shape of the parallel distribution function, which emerges as the system cools such that $f_\perp \to \delta(p_\perp)$. Several key features follow from this expression.

[11] One way to ilustrate this is to consider two particles moving together with the same $\beta_\parallel$ along a magnetic field, one with $p_\perp = 0$ and the other with some perpendicular gyration. In the rest frame of the first particle, both have $p_\parallel = 0$, so the question becomes: what does this particle see? It observes the other electron radiating away its perpendicular momentum until $p_\perp = 0$ and $p_\parallel = 0$, leaving them both at rest relative to each other in this frame. Transforming back to the lab frame means both particles keep the same $\beta_\parallel$ they started with, which is the physical content of the constant of motion in Eq. (2.7).

First, it always converges for physical distribution functions, i.e., those that vanish at high energies. The Jacobian factor imposes that f_0 must decay faster than $p_\parallel^{-2}$, which is satisfied by any distribution with finite particle number or an eventual cutoff.

As an example, consider a thermal Gaussian distribution,

$$f_0(p_\perp, p_\parallel) = \frac{1}{2\sqrt{2}\pi^{3/2} p_{\rm th}^3} \exp\left(-\frac{p_\perp^2 + p_\parallel^2}{2p_{\rm th}^2}\right), \tag{2.34}$$

which leads to the final parallel distribution

$$f_\parallel^{\rm f}(p_\parallel) = \frac{e^{-\frac{p_\parallel^2}{2p_{\rm th}^2}}}{2\sqrt{2\pi} p_{\rm th}^3 \left(\frac{p_\parallel^2+1}{p_{\rm th}^2}\right)^{3/2}} \left[\sqrt{2\pi}\left(e^{\frac{p_\parallel^2+1}{2p_{\rm th}^2}} - e^{\frac{p_\parallel^2+1}{2p_{\rm th}^2}} \,{\rm Erf}\left(\frac{\sqrt{\frac{p_\parallel^2+1}{p_{\rm th}^2}}}{\sqrt{2}}\right)\right) + 2\sqrt{\frac{p_\parallel^2+1}{p_{\rm th}^2}}\right], \tag{2.35}$$

where ${\rm Erf}(x)$ is the error function. While this expression is cumbersome, we can simplify it by considering the limit $p_{\rm th} \to \infty$, yielding

$$f_\parallel^{\rm f}(p_\parallel) = \frac{1}{2(1+p_\parallel^2)^{3/2}}, \tag{2.36}$$

This yields a power-law decay at large $p_\parallel$, with $f_\parallel^{\rm f} \propto p_\parallel^{-3}$.

The thermal width of this distribution can be estimated via its full width at half maximum (FWHM), defined by $f_\parallel^{\rm f}(p_{\rm FWHM}) = f_\parallel^{\rm f}(0)/2$. Solving for $p_{\rm FWHM}$ gives $p_{\rm FWHM} \approx 0.76642$ in dimensionless units (normalized to $m_e c$), which sets the characteristic scale for the parallel momentum spread once perpendicular cooling is complete.

Surprisingly, performing the same calculation for a Maxwell–Jüttner distribution yields the same asymptotic result as Eq. (2.36). This suggests that both the $f_\parallel^{\rm f} \propto p_\parallel^{-3}$ decay and the characteristic width are robust, possibly universal features of synchrotron cooling. In Appendix C.5, we demonstrate that this power-law behavior arises from phase-space compression under the cooling transformation. We show that all sufficiently broad and smooth initial distributions, those with $p_{\rm th} \gg 1$, or an equivalent measure of width, converge to the same asymptotic form, regardless of the microscopic details of f_0. Moreover, we demonstrate (see Appendix C.5.1) that beam-like disitributions, these are distributions with a small momentum spread in both the parallel and perpendicular directions $p_{\rm th}$, centered at high $p_\parallel \gg p_{\rm th}$, also produce final distributions with the property $f_\parallel^{\rm f} \propto p_\parallel^{-3}$.

2.3.5 Diffusive effects

During the cooling process, other diffusive mechanisms may compete with the formation of the ring distribution. These include collisional diffusion, non-resonant wave heating, or other stochastic processes. In this section, we study the kinetic equilibrium reached when such diffusion balances synchrotron cooling. A comparison of the relevant timescales is presented in Sec. 2.5; here, we focus on the steady-state distribution emerging from their interplay. We

consider a simplified diffusive operator in perpendicular momentum space of the form

$$\left.\frac{\partial f}{\partial t}\right|_{\text{heat}} = \frac{1}{p_\perp}\frac{\partial}{\partial p_\perp}\left(p_\perp D \frac{\partial f}{\partial p_\perp}\right), \tag{2.37}$$

where D is the diffusion coefficient, which has dimensions of momentum squared per time, and may arise from collisions, stochastic heating, or turbulent fluctuations. We include both diffusion and synchrotron cooling in a Fokker–Planck-type kinetic equation:

$$\frac{\partial f}{\partial t} = \frac{1}{p_\perp}\frac{\partial}{\partial p_\perp}\left[p_\perp D \frac{\partial f}{\partial p_\perp} - p_\perp \frac{dp_\perp(t)}{dt} f\right], \tag{2.38}$$

where $p_\perp(t)$ is the momentum loss rate due to synchrotron cooling, as given in Eq. (2.3). Assuming a steady state $\partial f/\partial t = 0$, and applying boundary conditions $f(p_\perp \to \infty) = 0$ and $\partial f/\partial p_\perp|_{p_\perp\to\infty} = 0$, integration yields:

$$f_{\text{s}}(p_\perp) = \lambda e^{-\frac{2\alpha B_0 \omega_{ce} m_e^2 c^2}{9D}\left(1+(p_\perp/m_e c)^2\right)^{3/2}}, \tag{2.39}$$

where λ is a normalization constant.This expression resembles a super-Gaussian of order 3 when D is independent of $p_\perp$. If instead $D \propto p_\perp^a$, the solution becomes $f_s \propto \exp(-p_\perp^{3-a})$.

This result illustrates key features of the time evolution and steady-state behavior of the distribution function. For initially cold distributions, such as $f \propto \delta(p_\perp)$, cooling is negligible at first, and stochastic diffusion dominates, broadening the distribution. As the plasma heats up, cooling becomes increasingly effective and gradually slows the diffusive broadening. The system eventually approaches the steady state f_s, where perpendicular cooling balances the diffusive heating. On the opposite end, if the initial distribution is significantly hotter than f_s, diffusion is negligible compared to cooling. The strong radiative losses rapidly compress the distribution into a narrow ring in $p_\perp$. As the ring cools further, the cooling rate weakens at lower $p_\perp$, and diffusive effects become comparable again, gradually smoothing out the ring and driving the system toward f_s.

This steady-state solution therefore describes the asymptotic fate of the system under the combined influence of diffusion and cooling. Importantly, this outcome is largely independent of the specific origin of the diffusion, the key parameter is the ratio D/B_0. When collisions or non-resonant heating are weak, with $D \ll B_0$, the equilibrium distribution is sharply peaked, and cooling proceeds efficiently to low transverse momentum. In contrast, when $D \sim B_0$ or larger, diffusion sustains a broader distribution at higher $p_\perp$, limiting further cooling. In this case, the plasma remains hot and anisotropic until the diffusive processes cease, at which point radiative cooling can take over. This interplay governs not only the equilibrium structure but also the timing and extent of kinetic instabilities, which will be discussed in Chapter 3.

2.4 Particle-in-Cell simulations

2.4.1 Relativistic regime ring formation

In order to determine the relevant timescales for the ring formation and population inversion process, an isotropic Maxwellian distribution function is considered; more general distribution

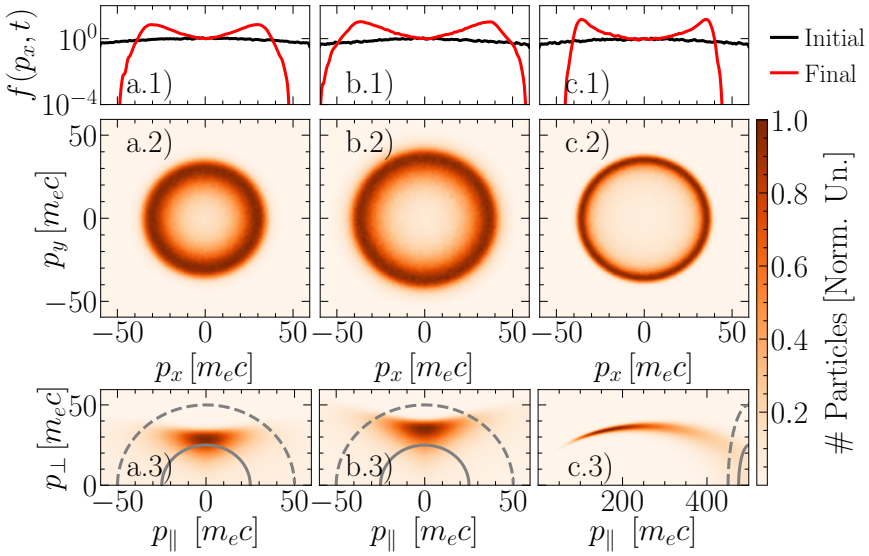

FIGURE 2.4: Particle-in-cell simulation results demonstrating the evolution of an initial isotropic Maxwellian distribution (column a), a Maxwell-Jüttner distribution (b), and a beam with bulk $\gamma_b = 500$ and isotropic Maxwellian spread (c), at $t = 3t_R$. For reference, the distribution function $f(p_x, p_y = 0)$ is shown at $t = 0$ and $t = 3t_R$ on the top row (1). The second row (row 2) shows the perpendicular plane of the momentum distribution ($f_\perp(p_x, p_y)$, where $p_\perp^2 = p_x^2 + p_y^2$) and the bottom row (3) the $f(p_\perp, p_\parallel)$ momentum distribution, at $t = 3t_R$.

functions, such as a Maxwell-Jüttner distribution function or Maxwellian beam distribution, is studied numerically.

These results can be generalized to particle beams since our calculations have considered the proper reference frame of the plasma/beam, where the fluid momentum of the beam $\overline{\mathbf{p}} = 0$. For a beam propagating parallel to the magnetic field with Lorentz factor γ_b all the previous results can be rescaled by the appropriate Lorentz transformations, $t_R = 3\gamma_b/4\,\alpha\,\chi_{\rm th}$; in these conditions, an inverse Landau population is generated and evolves into a ring-beam distribution, *i.e.* a beam with a pitch angle anisotropy.

We have performed Particle-in-Cell (PIC) simulations with the PIC code OSIRIS [81], including classical [91] and QED [91, 92] radiation reaction to confirm and to explore the theoretical findings. The full details of the simulation parameters are included in Appendix A.1. Simulations with different initial distributions show the formation of the ring at $t = 3t_R$, confirming the theoretical predictions for an initially isotropic Maxwellian distribution function $f_{0\,M}$ with $p_{th} = 50\,m_ec$ (Fig. 2.4.a). Equivalent behavior is also evident for an initially isotropic Maxwell-Jüttner distribution $f_0 \propto \exp(-\gamma/k_BT)$ with $k_BT = 50\,m_ec^2$ (Fig. 2.4.b). A beam with $\gamma_B = 500$ and a Maxwellian thermal spread $p_{th} = 50\,m_ec$ in the lab frame also evolved into a ring in the boosted timescale $t = 3\gamma_b t_R = 3\gamma_b/4\alpha\chi_{\rm th}$ (Fig.2.4.c).

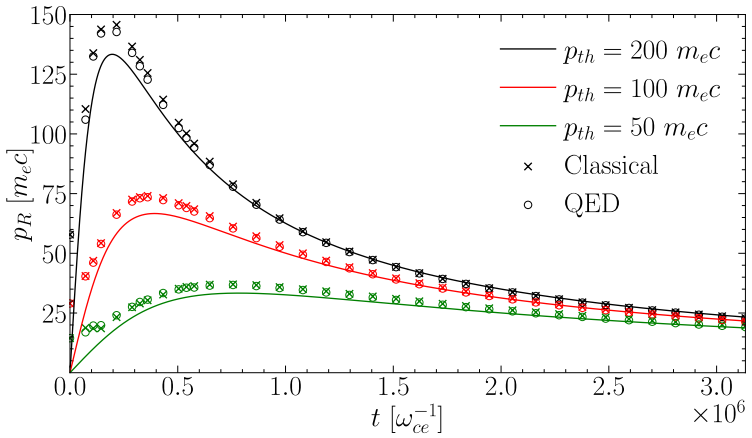

FIGURE 2.5: Temporal evolution of the ring radius p_R for different initial conditions, showing the agreement between the theoretical predictions (line Eq. (2.25)) and simulations ($\circ$ classical and $\times$ QED) for different initial Gaussian distributions with momentum spreads 200, 100, & 50 $m_e c$ (black, red, and green)

2.4.2 RING EVOLUTION TIMESCALES

This evolution is further explored in Fig. 2.5, focusing on initially Maxwellian distribution functions. The evolution of the ring radius, Eq. (2.25), shows excellent agreement with numerical simulations. Results with classical and QED radiation reaction are also shown. The average χ of the distribution function, $\bar{\chi}$, defined as $\bar{\chi}(t) = \int_0^\infty f_\perp(p_\perp, t) p_\perp^2 B_0 dp_\perp$ is a useful quantity to assess the importance of QED radiation reaction. $\bar{\chi}$ decreases as the distribution function cools down (since $\mathbf{B_0}$ is constant). Thus, the maximum $\bar{\chi}$ for this configuration is always $\bar{\chi}(t=0) = \sqrt{\pi/2}\chi_{\text{th}}$. In the simulations in Fig. 2.5, $\bar{\chi}(t=0) \sim 10^{-6} \ll 1$ and, as expected, in this regime the QED and classical results agree [28]. The discrepancy at early times in Fig. 2.5 between theory and simulations is due to the range of validity of the theoretical model ($p_\parallel \ll p_\perp$) – outside this range the evolution of the distribution function f deviates from the prediction of Eq. (2.22); at later times, due to the differential cooling, most of f is within the range of validity of the theoretical model, and a closer match between theory and simulations is observed.

2.4.3 RING FORMATION & EVOLUTION IN THE QED REGIME $\bar{\chi_0} \sim 1$

We have explored the full quantum regime through simulations with $\chi_{\text{th}} = 0.25,\ 0.5$ & 1 by increasing the magnetic field strength (shown in the supplemental material). We explored this regime with both classical and QED radiation reaction simulations. Both simulations show that the rings are formed within similar timescales, the main difference is that the simulations with quantum synchrotron emission show rings with a larger width than the rings in the classical simulations (see Fig. 2.6). Another fact to consider is that all distributions that are initially in the high $\bar{\chi}(t=0)$ regime eventually enter the classical regime $\bar{\chi} \ll 1$. This is expected, as

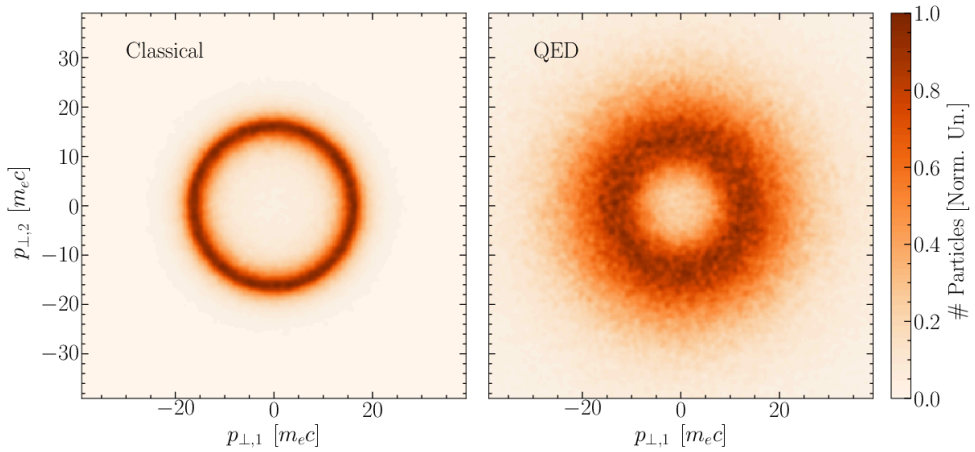

FIGURE 2.6: Evolution of an initial isotropic Maxwellian distribution with $p_{th} = 50 m_e c$ at $t = 3\, t_R$. The simulations employ a magnetic field strength $B_0 = 0.005$ (normalized to the Schwinger field). Thus, $\chi_{th} = 0.25$. The momentum distribution is shown integrated over the magnetic field direction, demonstrating the formation of the ring for both the classical and QED solver in the same timescale.

$\bar{\chi} \simeq p_R B_0$, and p_R decreases at late times as $p_R \propto t^{-1}$. The ring formation in the high χ_{th} regime and the transition to the classical regime will be studied in future work.

Simulations with $B_0 = 0.005$ (Normalised with respect to the Schwinger field B_{Sc}), for different values of p_{th}, such that $\bar{\chi}(t = 0) = 0.25,\ 0.5$ & 1 are presented here. The simulations employ the QED and classical radiation reaction solvers and develop into ring momentum distributions within similar timescales. The key difference is that the ring momentum distributions including QED synchrotron emission have a larger ring width. This numerical results align with the physical picture described in Sec. B, where the inclusion of QED effects results in a diffusive term into the vlasov equation. This is because QED radiation reaction is the result of the stochastic emission of photons, this stochasticity results in diffusion in momentum space similarly to an anomalous collisional operator.

Interestingly, the initial $\chi \propto p_\perp$ decreases with time, meaning that the diffusive effects should become smaller over time. But if the distribution is singificantly bunched up even if the diffusive effects are small, the extreme gradients in $p_\perp$ mean that the small stochasticity of QED cannot be fully neglected. In turn, in extreme cases this shall lead to a balance of bunching and diffusion, providing a minimum ring width, where both effects are balanced. This is not too different from the concept of almost collisionless plasmas where even if collisional timescales are much longer than the dynamical timescales, one cannot fully neglect their effects if there are very sharp momentum space gradients [141].

2.5 COMPETING EFFECTS

So far, our study has focused on the onset and evolution of ring-shaped MDFs within ideal magnetic-field configurations. To understand the regimes in which these ring distributions

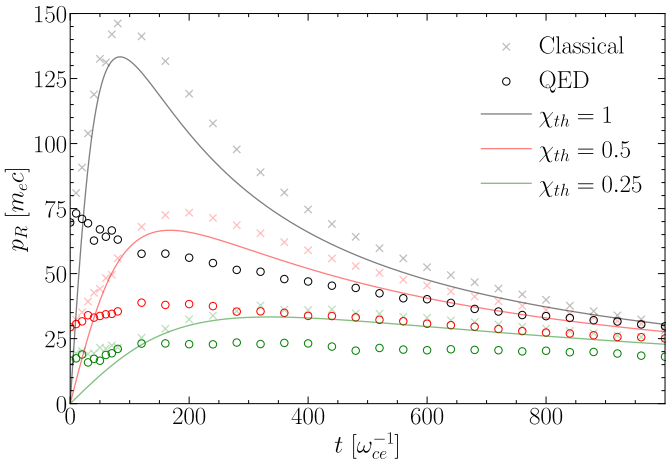

FIGURE 2.7: Particle-in-Cell simulations in the $\chi \sim 1$ regime compared with the analytical results for the ring radius evolution as predicted for the classical regime, demonstrates that the QED-dominated regime still produces the ring momentum distribution within a comparable timescale as the classical radiation reaction. The ring evolution is altered, the rings are wider and they do not grow in radius as much as in the classical case.

can emerge from synchrotron cooling, we will assess the validity of the presented model and determine the resilience of the cooling mechanism against other processes that may diffuse or alter the evolution of the radiative cooling process. We will discuss the effects of curved magnetic-field configurations; the impact of inhomogeneous magnetic fields, such as mirror fields or compressional Alfvén waves; and the diffusive effects of collisions.

2.5.1 MAGNETIC FIELD CURVATURE

Curvature effects can be relevant in a macro-scale, such as the case of a beam propagating along a curved magnetic field. As a result, beam particles will experience curvature and other drifts. A first estimate for the validity of our prediction for generating kinetically unstable MDFs [Eq. (2.30)] holds as long as that timescale is much shorter than the light crossing time of the curvature radius (r_c), leading to

$$r_c \gg \frac{3c}{2\alpha B_0 \omega_{ce}} = \frac{3 m_e c^2}{2\alpha e} \frac{B_{Sc}}{B^2}. \tag{2.40}$$

This scaling can be written as $r_c\,[\mathrm{km}] \gg 1.5/(B\,[10\,\mathrm{MG}])^2$, which is compatible with astrophysical compact objects whose scale exceeds kilometers and whose magnetic fields greatly exceed 10 MG, such as neutron stars (pulsars and magnetars), bright dwarves and black holes, which are in the order of 10 km and $B > 10\,\mathrm{MG}$. In the regime where Eq. (2.40) is not fulfilled, synchrotron cooling will still efficiently occur, and curvature may modify the distribution function. Our preliminary results of beams undergoing synchrotron cooling in curved

magnetic-field lines show that including curvature drifts leads to a spiral within a constant pitch-angle in momentum space [142], which is also an unstable distribution.

The scaling provided by Eq. (2.40) hints that synchrotron cooling might not be easily tested under current laboratory setups. Nonetheless, configurations such as betatron cooling may provide easier access to probing the properties of radiatively cooled plasmas with current technology.

2.5.2 INHOMOGENOUS MAGNETIC FIELDS: MIRRORING FIELDS

At scales smaller than the curvature radius, inhomogeneities of the guiding magnetic field can arise from magnetic turbulence or the propagation of compressional Alfvén waves, providing mirror fields that can scatter the ring-shaped MDF and diffuse it. If the mirror interaction occurs within a timescale shorter than the ring evolution t_i, we can assume that the magnetic moment $\mu = p_\perp / B$ and the Lorentz factor γ are constant during the interaction. The particles comprising ring MDF will be trapped by the mirror and scattered when its pitch angle is greater than the critical angle of the mirror given by $\sin\theta_c = \sqrt{B_0/B_A}$, where B_0 is the guiding field and B_A is the peak magnetic-field strength in the mirror field [78].

From the insights obtained from studying radiatively cooled thermal plasmas analytically and numerically [23], we know that particles in beams with a given perpendicular momentum spread $\Delta p_\perp$ and average Lorentz factor γ_b cool down towards $p_\perp = p_\parallel \simeq 0$ and cool down faster in $p_\perp$ as seen by the trajectories in Fig. 2.1. Therefore, the resulting MDF has a ring radius smaller than $\Delta p_\perp$ and an average γ lower than γ_b. This results in a beam pitch angle $\theta < \Delta p_\perp / \gamma_b$.

For such a beam propagating along a guiding field of strength B_0 to be scattered by a magnetic mirror of strength B_A, the beam pitch angle must be greater than the critical mirror angle. Thus,

$$\frac{B_0}{B_A} < \sin^2\left(\frac{\Delta p_\perp}{\gamma_b}\right). \tag{2.41}$$

For small divergences we approximate $\sin(\theta) \approx \theta$, leading to $B_A \gtrsim B_0/\theta^2$ for the ring to be scattered. For astrophysical beams such as those inferred in pulsar magnetospheres and magnetar outflows, the beam angular spread is expected to be in the milliradian range, $\theta \sim 10^{-3}$ [143]. This yields a required mirror field strength of $B_A \gtrsim 10^6 B_0$ for effective pitch-angle scattering.

Such a large enhancement of the field strength is difficult to achieve via compressional Alfvén waves or magnetohydrodynamic turbulence, especially in regions where the guiding field is already strong, e.g., $B_0 \sim 10^{12} - 10^{13}$ G near neutron star surfaces. Even further out in the magnetosphere, where B_0 may drop to $10^6 - 10^9$ G, generating mirror structures with $B_A \gtrsim 10^{12} - 10^{15}$ G remains implausible. We therefore conclude that in such astrophysical settings, synchrotron-cooled ring beams are robust against scattering by small-scale magnetic inhomogeneities and are expected to preserve their features.

2.5.3 COULOMB COLLISIONS

We have assumed a regime where the synchrotron cooling timescales and the resulting plasma physics occur on a timescale where collisional relaxation cannot return the plasma to kinetic equilibrium, i.e., in the collisionless regime. These results are valid for strong magnetic fields; however, if one considers the weak magnetic-field limit $B \to 0$, then t_R, $t_i \to \infty$, according to Eqs. (2.26) and 2.28. In this regime, collisional effects could inhibit the ring formation and evolution. We now compare the ring evolution timescale t_i to the relaxation timescales given by collisional processes. We consider three collisional processes capable of diffusing the ring momentum distribution: lepton-lepton $e^\pm + e^\pm \to e^\pm + e^\pm$, lepton-ion $e^\pm + i \to e^\pm + i$, and Compton $e^\pm + \gamma \to e^\pm + \gamma$ collisions. We note that pair production/annihilation $e^- + e^+ \rightleftharpoons \gamma + \gamma$ processes can also be relevant. However, unlike collisional processes, these will produce/evaporate the pair plasma from/to a photon gas and not necessarily destroy the ring. This will be investigated elsewhere.

For the case of lepton-lepton and lepton-ion collisions, one can employ the standard kinetic theory and obtain the relaxation timescales for lepton-lepton and lepton-ion collisions [144–146]

$$\tau_{ee} = \frac{12\pi^{3/2}}{\sqrt{2}} \frac{m_e^2 c^3}{e^4} \frac{1}{n_e \ln\Lambda}, \tag{2.42}$$

$$\tau_{ei} = \frac{12\pi^{3/2}}{\sqrt{2}} \frac{m_e^2 c^3}{e^4} \frac{1}{n_i Z^2 \ln\Lambda}, \tag{2.43}$$

where n_e is the lepton density, n_i is the ion density, $\ln\Lambda$ is the Coulomb logarithm, and, as we are dealing with relativistic plasmas, we have approximated $v_e \sim c$. Comparing both relaxation times, assuming the fastest case of $Z = 1$ against the kinetic instabilities timescale t_i, we obtain $t_i/\tau_{ee} = 10^{-6} B^{-2}\,[1\,\mathrm{G}]\, n_e\,[\mathrm{cm}^{-3}] \ln\Lambda$. Here we are emplying the classical collision rates, relativistic collisions will have an even smaller rate.

If we consider magnetic fields on the order of a gigagauss, collisional effects only become comparable to the ring evolution time for electron densities $n_e \gtrsim 10^{24}$ cm^{-3}. Such densities are extremely high and not typical of dilute magnetospheric plasmas. They might occur transiently in the deepest layers of neutron star crusts, but are well above typical densities in the outer magnetosphere where ECMI is expected to operate.

Conversely, for present-day laboratory conditions with magnetic fields $B \sim 10^7$ G and plasma densities $n_e \sim 10^{20}$ cm^{-3}, one finds $t_i/\tau_{ee} \sim \ln\Lambda$, implying that collisional effects may suppress or strongly modify ring formation. This suggests that efficient production of ring MDFs in the lab requires either lower densities, shorter formation timescales, or mitigation strategies to reduce collisional scattering.

2.5.4 EXTERNAL COMPTON COLLISIONS

The collision rate for Compton scattering is estimated as $\nu_{e\gamma} = 2\sigma c n_\gamma$ [147, 148], where σ is the Klein–Nishina cross-section and n_γ is the photon density. In the high-energy limit, and in the electron frame, the Klein–Nishina cross-section peaks for forward collisions, so it can

be approximated as $\sigma \simeq \pi r_e^2/\epsilon'_\gamma$ [149], where r_e is the classical electron radius and ϵ'_γ is the photon energy in the electron frame in units of $m_e c^2$. For frontal collisions in the beam frame, the cross-section transforms to $\sigma = \pi r_e^2/(\gamma_e \epsilon_\gamma)$, where γ_e is the beam Lorentz factor and ϵ_γ is now the photon energy in the lab frame, again in units of $m_e c^2$. The corresponding relaxation time is then approximated as

$$\tau_{e\gamma} = \frac{4\hbar}{3c\sigma_T} \frac{\langle \omega_\gamma \rangle \langle \gamma_e \rangle}{n_\gamma}, \tag{2.44}$$

where σ_T is the Thomson cross-section, $\langle \gamma_e \rangle$ is the average Lorentz factor of the leptons, and we have taken $\epsilon_\gamma = \hbar \langle \omega_\gamma \rangle$, with $\langle \omega_\gamma \rangle$ the average photon frequency and $\hbar$ the reduced Planck constant. This is taken in the frame of the beam. If we assume blackbody spectrum for the photons, we obtain $\hbar \langle \omega_\gamma \rangle / n_\gamma = \pi^6 c^3 \hbar^3/(60\zeta^2(3) k_B^2 T_\gamma^2)$ [17], and therefore $\frac{t_i}{\tau_{e\gamma}} \simeq 4.6\, B^{-2}\,[\mathrm{G}]\, T_\gamma^2\,[\mathrm{eV}]\, \langle \gamma_e \rangle^{-1}$.We find that $t_i \ll \tau_{e\gamma}$ for gigagauss field strengths and photon temperatures in the X-ray range ($T_\gamma \sim$ keV), which are compatible with astrophysical plasmas [150].[12]

In the limit of weak magnetic fields $B \to 0$ according to Eq. (2.26) $t_R \to \infty$. In this scenario, effects that can inhibit the ring formation must be included in our analysis. That is the case of collisional processes (e-e, e-i collisions, pair annihilation, and Compton scattering [17, 146]). The competition with these processes (when t_R becomes comparable to their typical time scales) might inhibit the ring formation and the Landau population inversion. However, for the range of conditions in the magnetospheres of compact objects, such as magnetars and pulsars, the ring formation time (from Eq.(2.26)) $t_R \simeq \mathcal{O}(\mathrm{ps})$, considering GigaGauss field strengths and relativistic plasmas with $p_{th} \sim 100\, m_e c$, is much shorter than all of the other timescales. For laboratory experiments with 10's of MG B field strengths and relativistic $p_{th} \sim 10\, m_e c$, the ring formation occurs in the nanosecond time-scale, which hints that other configurations might be more favorable to explore this process in the laboratory.

2.6 Conclusion

2.6.1 On the pervasiveness of ring distributions

We have considered a simplified field configuration, demonstrating the role of differential cooling of radiation reaction to generate population inversion. This is a general property that should be observed for other field configurations. Other scenarios and field configurations where differential cooling can be relevant are associated with betatron oscillations in an ion channel [126, 151–153] or direct laser acceleration configurations [154]; a population inversion is also expected in those conditions and this will be explored in future publications.

In this work, we have presented the process under which an initially kinetically stable plasma undergoing synchrotron cooling will develop into a momentum ring distribution. We

[12]Here we consider the effect of *external* photons, i.e., those originating from the stellar surface or already present in the surrounding plasma. The photons emitted by the plasma itself can also undergo Compton scattering (self-scattering), which is analyzed separately in Sec. 3.4.1.

have demonstrated that the cooling process is anisotropic, and one must consider that plasmas undergoing synchrotron cooling will be characterized by transverse momentum distributions with inverted Landau populations, i.e., a ring momentum distribution or non-monotonic pitch-angle beam distribution.

The model presented in this work employed the classical formulation of radiation reaction from the Landau–Lifshiftz model. Future studies shall address the development of rings in the strong QED regime and how this description introduces a diffusive effect. Particle-in-cell simulations have shown that the LL model accurately predicts the ring radius evolution in the $\chi \sim 1$ regime [23]. Moreover, as the plasma cools down $\chi \to 0$, it transitions from QED synchrotron cooling to classical synchrotron cooling. A QED model will allow the study of the interaction between the synchrotron photons and the plasma via Compton scattering and the production of cascades or avalanches [155], where a single photon or lepton could self-generate the whole plasma and produce a ring distribution.

We have studied the timescales for the onset of ring distributions, from which we have concluded that the ring momentum distributions under the astrophysical conditions provided by compact objects must be pervasive, resulting from the short timescale under which rings are generated, in the order of picoseconds, for gigagauss magnetic-field strengths. Such short timescales make ring momentum structures highly resilient to diffusive processes such as magnetic-field curvature, guiding field inhomogeneities, and collisional effects. Conversely, for the case of laboratory conditions, the ring formation timescales and evolution are in the nanosecond timescale, and curvature or inhomogeneities in the magnetic field and the necessary plasma temperatures of $p_{\text{th}} > m_e c$ are a challenge with state-of-the-art technology. Nonetheless, we conjecture that other radiatively cooled plasmas will also develop a population inversion, namely in laboratory conditions, e.g., high-energy particle beams undergoing betatron cooling are an ideal candidate to study analogous processes [126, 151, 152]. This will be presented in Chapter 4.

2.6.2 SUBSEQUENT KINETIC INSTABILITIES

In the next chapter we examine the late time evolution of this system, where the ring momentum distribution evolved for longer times, to assess the onset of the electron cyclotron maser instability (ECMI) by the inverted Landau population, as the ring momentum distributions are well-known to be kinetically unstable [119–123].

The ring will be formed and evolve until the onset of the instability. An important fact to consider is that independently of ω_p/ω_{ce} (and even for $\omega_p/\omega_{ce} \ll 1$), the ring will continue to constrict (and $\partial f/\partial p_\perp$ to increase), to the point for the onset of the maser process and the emission of coherent radiation.

So far two distinct kinetically unstable regimes have been identified: when $\beta \gg 1$, where $\beta = 8\pi k_B T/B^2$ is the plasma pressure to magnetic-field pressure ratio, the pressure anisotropy due to the anisotropic synchrotron cooling will lead to the firehose instability [24], and, in contrast, when $\beta \ll 1$ due to $\omega_{pe} \ll \omega_{ce}$, the inverted Landau population will dominate and lead to electron cyclotron maser emission[23]. Nevertheless, preliminary results, which will

be the subject of future work, have shown that for large β and $\omega_{pe} \ll \omega_{ce}$ (relevant for low-density plasmas with initially relativistic thermal energies) the plasma transitions from $\beta \gg 1$ to $\beta \ll 1$, where the synchrotron firehose will be triggered, first followed by the electron cyclotron maser.

It is generally accepted that coherent emission processes must be at play around compact objects [124, 127]. Among these processes, the electron cyclotron maser instability requires a Landau population inversion [119–123]. Moreover, some of the other proposed coherent emission mechanisms assume strongly radiation cooled down beams where $p_\perp \ll m_e c$ [49]. We have demonstrated that in scenarios with strong radiation reaction cooling, transverse momentum distributions with inverted Landau populations are pervasive. These distributions are unstable and can drive coherent emission via kinetic plasma instabilities. Our analytical model shows excellent agreement with numerical simulations, demonstrating the relevance of this process in the classical and in the QED regimes of radiation reaction.

We will build upon this insight in Chapter 3, where we outline a concrete astrophysical model based on this mechanism. In particular, we propose a scenario in which pair plasma is injected into the magnetosphere of a neutron star, undergoes stochastic heating via perturbations in the magnetic field, and then cools radiatively to form a ring distribution. The resulting population inversion triggers the electron cyclotron maser instability and leads to coherent emission. This scenario is presented in detail in Section 3.5.

We conjecture that our findings are also valid for other field configurations, namely in laboratory conditions, e.g. the focusing field of ion-channels in laboratory conditions with betatron oscillations [126, 151, 153], also opening the way to the laboratory exploration of Landau population inversion via radiation reaction cooling. This is explored in Chap. 4.

In conclusion, the full impact of radiation reaction cooling in the collective plasma dynamics has begun to be comprehended. The current results have applications for astrophysical processes, especially coherent maser radiation and firehose magnetic-field amplification. We conjecture that these are the first examples and that further work on different electromagnetic-field configurations will find new collective plasma physics triggered under extreme plasma physics conditions in laboratory or astrophysical settings.

CHAPTER 3

SYNCHROTRON INDUCED COHERENT MASER EMISSION

This Chapter is adapted from: P. J. Bilbao, *et al.*, Sci. Adv. 11.15: eadt8912 (2025)

3.1 INTRODUCTION

Relativistic plasmas are expected to arise around neutron stars, black holes, white dwarfs and other astrophysical compact objects through various mechanisms, *e.g.*, pair cascades [30, 32, 34, 156, 157], and in laboratory experiments, *e.g.* with intense lasers or relativistic particle beams [21, 61, 66, 72, 158–160]. These highly energetic plasmas, with electron energies comparable to or higher than the electron rest mass, form in environments with intense electromagnetic fields, which can sometimes approach the magnetic Schwinger limit ($B_{\mathrm{Sc}} \simeq 4.4 \times 10^9$ T) [27, 90, 101, 104, 105]. Under these conditions, quantum electrodynamical (QED) processes, such as non-linear Breit-Wheeler, quantum Compton scattering, and quantum radiation reaction, are dominant or comparable to classical plasma processes. Therefore, phenomena such as turbulence [53, 96, 161], shock formation [48, 162], laser-plasma interactions [99, 104, 105, 160] beam-plasma interactions [95], and, as shown here, kinetic instabilities, will exhibit substantial quantitative differences from their classical plasma counterparts and also manifest qualitatively distinct behaviours and features [15].

The complex nature of plasmas in extreme electromagnetic environments has driven substantial interest in investigating their kinetic properties. Even simplified electromagnetic field configurations show rich phenomena and can yield surprising results. For instance, plasmas undergoing strong synchrotron cooling have been shown to develop an anisotropic ring-shaped momentum distribution, characterised by a population inversion over the Landau levels, $\partial f / \partial p_\perp > 0$, where f represents the plasma momentum distribution and $p_\perp$ the momentum perpendicular to the magnetic field $\mathbf{B}$, as was first demonstrated in this thesis (See Chapter 2) [23].

However, despite these advances, the collective properties of such strongly magnetised

plasmas remain underexplored, particularly regarding the self-consistent electrodynamical effects. Theoretical and experimental investigations are needed to fully understand plasmas in this extreme regime.

One major challenge is that first-principle simulations are constrained by the vast separation of relevant spatial and temporal scales, which differ by several orders of magnitude. This requires using high resolutions over large simulation domains to capture all relevant physics, both spatially and temporally. The computational resources necessary to perform such numerical simulations, including all the relevant physics, has only recently become available. Replicating these extreme conditions in laboratory experiments is also highly challenging, and only recent advancements in experimental techniques have made it possible to generate plasmas under such extreme environments [61, 66, 72].

In this study, we address this gap by conducting the first and largest scale, first-principles numerical simulations that demonstrate how relativistic plasmas embedded in strong magnetic fields can spontaneously produce linearly polarized coherent radiation via the electron cyclotron maser instability (ECMI) [120, 163–165]. We demonstrate how the instability is qualitatively modified by the inclusion of synchrotron losses. This phenomenon occurs in collisionless plasmas with relativistic temperatures, where radiation reaction plays a crucial role. Our simulations reveal that synchrotron cooling first establishes the Landau population inversion, in the shape of a ring momentum distribution, and then maintains it for longer timescales than previously thought possible [166], leading to continuous coherent amplification of radiation and a modified saturation state of the maser instability.

3.2 ELECTRON CYCLOTRON MASER INSTABILITY IN THE SYNCHROTRON COOLED REGIME

First we present an intuitive explanation of the electron cyclotron maser instability (ECMI), as it highlights key features that will later be observed in the simulations. A full analytical description will follow in the next section.

The ECMI arises from a form of Cherenkov resonance, which amplifies or damps electromagnetic waves depending on the distribution of particles near the resonance. In a magnetized plasma, this mechanism differs from the standard Cherenkov resonance found in Landau damping, which involves particle velocities parallel to the wavevector. In contrast, the ECMI operates through the particle's gyration frequency, making it inherently coupled to the magnetized, perpendicular dynamics of the plasma.

The X-mode ECMI arises from a plasma characterized by a population inversion, *i.e.* $\partial f/\partial p_\perp > 0$, and a narrow spread in $p_\parallel$. An illustration of the electron cyclotron maser instbility bunching process is shown in Fig. 3.1, where electrons gyrate in the plane perpendicular to the magnetic field, and interact with X-modes, which are linearly polarized electromagnetic waves whose wavevector and electric field are perpendicular to the guiding magnetic field, *i.e.*, $\mathbf{k} \perp \mathbf{B}$, $\mathbf{E} \perp \mathbf{B}$, and $\mathbf{k} \perp \mathbf{E}$. Depending on whether the electrons rotate slightly faster or slower than the wave phase, they are accelerated or decelerated; consequently, their gyrofrequency (ω_{ce}/γ,

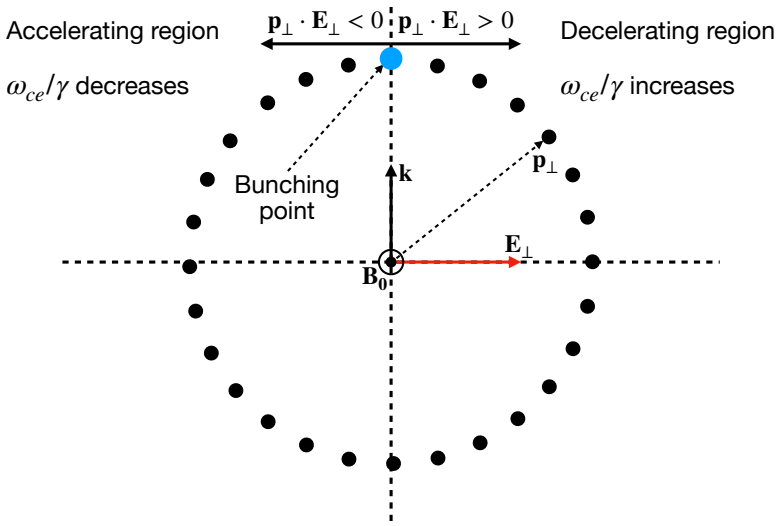

FIGURE 3.1: Qualitative illustration of the bunching process in momentum space. The circle represents the gyration of the perpendicular momentum $\mathbf{p}_\perp$ in phase space. Particles on the left (right) side satisfy $\mathbf{p}_\perp \cdot \mathbf{E}_\perp < 0$ (> 0) and accordingly gain (lose) energy from the wave. This energy exchange modifies the relativistic gyrofrequency ω_{ce}/γ, shifting the particle's phase relative to the wave. As a result, particles bunch along the direction of wave propagation $\mathbf{k}$, where the net energy exchange is minimized. As the wave propagates and the electric field reverses, the direction of bunching also reverses, leading to an oscillatory bunching pattern. When the relativistic gyrofrequency matches the wave frequency, this interaction becomes resonant: bunching reinforces the wave, and the amplified wave further enhances the bunching (Diagram inspired by Ref. [167]).

where γ is the Lorentz factor of the particle) decreases or increases, respectively. For the wave to gain energy from the particles, more electrons must have gyrofrequencies (or its harmonics) slightly below the wave frequency ($\omega \gtrsim n\omega_{ce}/\gamma$). This requires $\partial f/\partial p_\perp > 0$, ensuring that more particles transfer energy to the wave than they extract from it. The energy transfer amplifies the interacting X-mode waves at the fundamental and harmonics of the electron gyration frequency within the population inversion through phase trapping. As the wave is amplified, more electrons are phase-trapped, generating an unstable feedback [163, 167]. The ring-shaped momentum distribution is an ideal candidate to drive the X-mode ECMI, but until now there was no natural mechanism to generate a plasma with a ring momentum distribution.

3.2.1 ANALYTICAL EXTIMATES FROM KINETIC THEORY

The evolution of the synchrotron-cooled plasma, the subsequent growth rate of the X-mode, and the dynamical timescales of the instability, as will be seen in the simulations, can be directly computed from kinetic theory with the inclusion of radiative losses [23, 24, 100, 113, 116]. For a tenuous pair-plasma in a strong magnetic field, the momentum distribution of a plasma evolves as $f(p_\perp, p_\parallel, \tau) = f\left(\frac{p_\perp}{1-\tau p_\perp}, \frac{p_\parallel}{1-\tau p_\perp}\right) / (1-\tau p_\perp)^4$, where $p_\perp$ is normalised to $m_e c$, τ is a normalised time such that $\tau = (2\alpha/3) B_0 \omega_{ce} t$, where $B_0 = B/B_{\rm Sc}$ and α is the fine-structure

constant [23]. An important feature is that f is bounded between $0 < p_\perp < 3/(2\alpha B_0 \omega_{ce} t)$ and that the resulting ring radius asymptotically approaches the boundary at $p_R = 3/(2\alpha B_0 \omega_{ce} t)$ [113]. Thus, a relativistic plasma, independently of the initial shape of f, will develop into an anisotropic ring momentum distribution [23, 24, 113, 168]. This results from the nonlinear nature of synchrotron radiation, which bunches the momentum distribution in the radial momentum direction $p_\perp$. The radiation reaction force violates the conservation of phase-space volume, in contrast with the classical collisionless plasma dynamics mediated by the Lorentz force [88, 141]. Therefore, synchrotron radiation drives the plasma away from kinetic equilibrium and eventually fulfils the conditions for efficient maser emission.

We consider a relativistic pair plasma embedded in a strong background magnetic field $\boldsymbol{B}_0$, where synchrotron cooling leads to the formation of anisotropic ring momentum distributions. These non-equilibrium distributions naturally excite electromagnetic waves via the electron cyclotron maser instability. Among the possible wave modes, we focus on the X-mode, which exhibits the fastest linear growth. The X-mode corresponds to a transverse electromagnetic wave propagating nearly perpendicular to $\boldsymbol{B}_0$, with its wave vector $\boldsymbol{k} \perp \boldsymbol{B}_0$. Its electric field $\boldsymbol{E}$ lies perpendicular to both $\boldsymbol{k}$ and $\boldsymbol{B}_0$, that is, $\boldsymbol{E} \parallel \boldsymbol{B}_0 \times \boldsymbol{k}$. The group velocity points outward from the emission region, allowing for efficient energy extraction from the ring distribution through resonant interaction with the wave field.

The growth rate of X-modes,[1] Γ (obtained from first-principles kinetic theory with the inclusion of radiative losses in Appendix E), as a function of t and the wave angular frequency ω can be approximated by employing the WKB approximation, which for $\omega_{ce} \gg \omega_{pe}$ simplifies to $d\Gamma/dt \ll \omega^2$ [169], and yields

$$\Gamma(\omega, t) = 2\pi^2 \frac{\omega_{pe}^2}{\omega} \sum_{n=1}^{\infty} \left\{ p_\perp'^2 \left. \frac{\partial f_\perp(t)}{\partial p_\perp} \right|_{p_\perp = p_\perp'} \left[J_n' \left(\frac{\omega p_\perp'}{n \omega_{ce}} \right) \right]^2 \right\}, \tag{3.1}$$

where $p_\perp' = \sqrt{n^2 \omega_{ce}^2 / \omega^2 - 1}$ is the resonant momentum with the given frequency ω, $J_n'(b)$ is the first derivative of the nth order Bessel function evaluated at b, $f_\perp(p_\perp, t)$ is the perpendicular momentum distribution, *i.e.*, integrated over the parallel direction $f_\perp(p_\perp, t) \equiv \int_{-\infty}^{\infty} f(p_\perp, p_\parallel, t) dp_\parallel$.

Initially, Γ changes rapidly as the cooling process is fast due to the initial thermal spread. As the plasma cools, f changes slower, and $d\Gamma/dt \propto d\left(\partial f/\partial p_\perp\right)/dt$ decreases accordingly. This gradual slowing of the cooling process at lower values of $p_\perp$ ultimately ensures the validity of the WKB approximation.[2] This is true after the ring formation time as the gradient becomes larger and the cooling rate slows down. Therefore, the WKB approximation is valid and Eq. (3.1) provides a good approximation for the growth rate of the electronic cyclotron maser instability due to synchrotron-cooled rings. Equation (3.1) shows some of the key universal emission features characteristic of the synchrotron-induced electron cyclotron maser:

[1] We also compute the growth rate of the O-modes and electrostatic modes, which we find grow significantly slower than the X-mode (See App. E.2.3 & App. E.2.4).

[2] The WKB condition requires that the frequency of the wave varies slowly in time, i.e., $|\omega^2| \gg |\dot{\omega}|$. Since $\omega \approx \omega_{ce}$ and the variation arises from the slow evolution of the background distribution $f_0(t)$, this translates into $|\Gamma^2| \gg |\dot{\Gamma}|$ once the ring forms and the gradient becomes steep, *i.e.*, valid at late times.

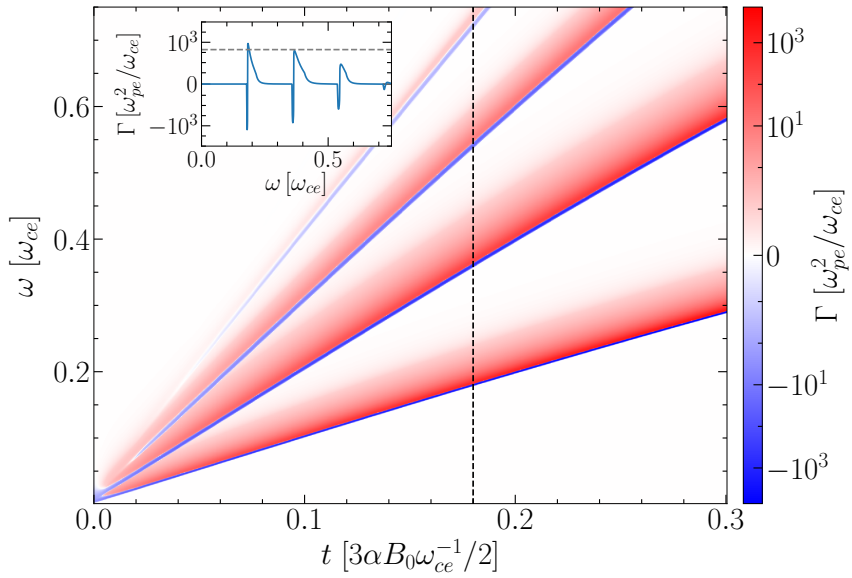

FIGURE 3.2: The key emission features of the cyclotron maser instability are demonstrated by temporal evolution of the X-mode growth rate, $\Gamma(\omega, t)$, as described by Eq. (3.1), for a typical initial distribution function, $f_\perp(p_\perp, t = 0) = e^{-p_\perp^2/(2p_{th}^2)}/p_{th}^3(2\pi)^{1/2}$, where $p_{th} = 100\ m_e c$. Since the ring distribution is a general characteristic of hot plasmas (*i.e.*, those with $p_{th} \gg m_e c$) undergoing synchrotron cooling, this initial distribution function effectively represents the qualitative behaviour of maser emission under various initial conditions [23, 113]. The figure demonstrates that the emission is evenly spaced in ω-space, as evident from the line-out of $\Gamma(\omega, t = 0.165\tau)$ shown in the inset, which highlights the emission and absorption regions, where $\Gamma > 0$ and $\Gamma < 0$, respectively. The emission predominantly occurs near the harmonics of the resonant frequency, which gradually converge towards the harmonics of ω_{ce} as the ring distribution cools down and asymptotically approaches $p_\perp = 0$.

i) the amplification rate is proportional to the plasma density $\omega_{pe}^2 \propto n_e$, ii) it occurs near the different cyclotron harmonic resonances ω_{ce}/γ, and iii) is proportional to $\partial f_\perp/\partial p_\perp$.

To illustrate the properties of the growth rate given by Eq. (3.1) we determine Γ for a typical distribution function $f_\perp(p_\perp, t = 0) = e^{-p_\perp^2/(2p_{th}^2)}/(p_{th}^3(2\pi)^{1/2})$, with $p_{th} = 100\ m_e c$. Since the ring distribution is a general feature of hot plasmas (*i.e.* those with $p_{th} \gg m_e c$) undergoing synchrotron cooling, this initial distribution function is a good representative of the qualitative properties of the maser emission for other initial conditions [23, 113]. The dashed line in Fig. (3.2), follows $p_\perp = \tau^{-1}$, *i.e.*, the boundary of the momentum distribution due to the cooling. Just below that boundary and above the ring radius p_R, the momentum distribution has a small region where $\partial f_\perp/\partial p_\perp < 0$, with a width of that can be found analytically to be $\Delta p \sim p_R^2/(\sqrt{3}p_{th}) = 1/(\sqrt{3}p_{th}\tau^2)$. For values below the ring radius, there is a region of comparable width to Δp where $\partial f_\perp/\partial p_\perp > 0$. Therefore, the momentum distribution resulting from synchrotron cooling fulfills the stringent conditions to obtain efficient maser emission, *i.e.* having a step gradient in $p_\perp$ and a small spread Δp. These conditions lead to a small emission region above the frequency $\omega_{ce}/\sqrt{1 + p_R^2}$, and a small absorption region between

$\omega_{ce}/\sqrt{1+p_R^2}$ and $\omega_{ce}/\sqrt{1+(p_R+\Delta p)^2}$.

The maximum growth rate at the fundamental frequency can be estimated by approximating $\partial f_\perp/\partial p_\perp \simeq f_\perp(p_R,\tau)/\Delta p$, $f(p_R,t) = 1/(4\pi p_R \Delta p)$ and $\omega \sim \omega_{ce}/\gamma$ in Eq. (3.1),

$$\Gamma_X \simeq \frac{3\pi}{4}\frac{\omega_{pe}^2}{\omega_{ce}}\frac{p_R\gamma_R}{\Delta p^2}\left[J_1'(1)\right]^2 \simeq \frac{3\pi}{16}\frac{\omega_{pe}^2}{\omega_{ce}}p_{th}^2\tau^2 \tag{3.2}$$

This expression approximates the value for the fastest-growing mode and frequency (the frequency in resonance with the ring radius), and demonstrates that an initial plasma with a higher p_{th} leads to a higher growth rate as it leads to a distribution function with regions of large $\partial f/\partial p_\perp$, moreover later times also increse the value of $\partial f/\partial p_\perp$, hence why Γ increases as τ^2. We show the estimate for Γ_X in the inset axis of Fig. (3.2).

3.2.2 Estimate for the onset time

Due to the dynamical evolution of f, $\Gamma > 0$ is not a sufficient condition for the efficient amplification of radiation. It is also necessary that the ring can provide several e-foldings to the interacting wave before dephasing. In other words, Γ_X^{-1}, has to be shorter than τ_r, *i.e.* the time the ring is in resonance with a given frequency ω. Given an ω there is a resonant momentum $p_\perp = \sqrt{n^2\omega_{ce}^2/\omega^2 - 1}$, when waves are in resonance with particles closer than Δp to the ring radius p_R so that they lie in a region with $\Gamma > 0$ and are amplified. This continues for a time τ_r until the ring has cooled down to the point where the resonance is now at the ring radius and $\Gamma_X = 0$ for that ω. Thus, the in-resonance time τ_r is the time it takes the ring momentum distribution to cool from a ring radius p_R to a ring radius $p_R - \Delta p$. From the equation of motion one can show that $\tau_r \simeq \Delta p/p_R^2 \simeq \tau/(\sqrt{3}p_{th})$, where τ is the time since the beginning of the cooling process. The in-resonance time τ_r is inversely proportional to the cooling rate. Thus, the in-resonance time becomes longer as the ring cools down.

Then we can compare $t_r > N\Gamma_X^{-1}$ where $t_r = 3\tau_r/2\alpha B_0$, and N is the number of e-foldings that can occur within the in-resonance time (when comparing with numerical values we take $N = 10$). This is fulfilled at a time

$$t_o = \sqrt{\frac{N}{\sqrt{3}\pi\alpha}}\frac{eB_{\rm Sc}}{m_e}\sqrt{\frac{B_0}{p_{th}}}\frac{1}{\omega_{ce}\omega_{pe}}, \tag{3.3}$$

or $t_o\,[12\,\mu{\rm s}] \simeq (B\,[{\rm MG}]\,n_e\,[10^6\,{\rm cm}^{-3}]\,p_{th}\,[100\,m_ec])^{-1/2}$ (for $N = 10$); t_o determines the time at which coherent emission begins, from the beginning of the cooling process. We note, that t_o may not be exact for any initial distribution f, or for $\omega_{pe} \lesssim \omega_{ce}$, still we argue that the scalings captured by Eq. (3.3) will hold. We note that the time until the onset of the electron cyclotron maser instability decreases as the radiation reaction effects become more relevant (at higher B_0 or p_{th}) and when the effects of the plasma become more relevant, *i.e.* higher ω_{pe}. These scalings have been confirmed with PIC simulations (See Sec. 3.3.2).

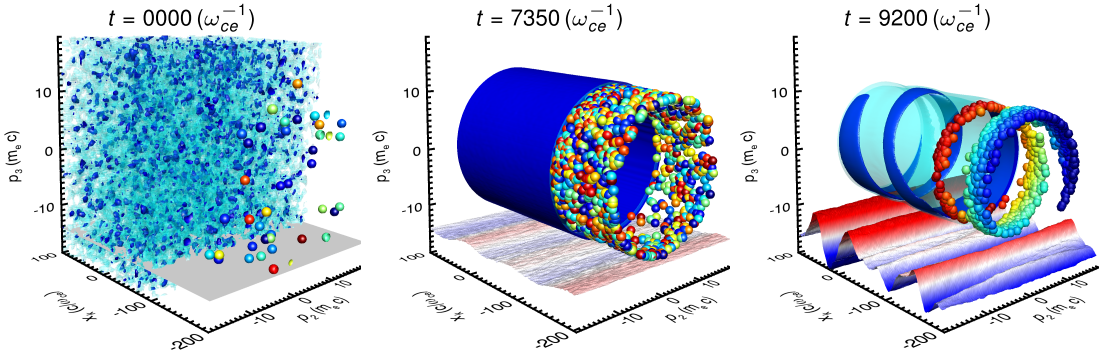

FIGURE 3.3: Self-consistent particle-in-cell simulations demonstrate the onset of electron cyclotron maser instability (ECMI) and coherent amplification of radiation. The temporal evolution (from left to right) of the plasma distribution function $f(\mathbf{r}, \mathbf{p}, t)$, shown as a 3D projection, p_2-p_3-x_k, of the 6D phase-space, where p_2 and p_3 are the momentum directions perpendicular to the B-field, with $B/B_{\mathrm{Sc}} = 0.002$, and x_k is the spatial direction along the propagation of the X mode (also perpendicular to B). Two isosurfaces of the distribution function are represented: the light blue and blue surfaces are at 0.5 and 0.8 of the peak value of the distribution function, respectively. The projection in the bottom plane (red-blue colours) represents the normalized amplitude of electric field associated with the amplified electromagnetic wave (X-mode). A sample of the plasma particles is also shown, with the colour representing their azimuthal phase (between 0 and 2π, from red to blue) with respect to the amplified electromagnetic wave. Left: Initially, the plasma consists of a Maxwellian thermal population with initial momentum distribution $f_0 \propto e^{-|\mathbf{p}|^2/(2p_{th}^2)}$, where $p_{th} = 1000\, m_e c$, and no X-mode is observed, the particles have random phases. Middle: a ring momentum distribution function has developed due to synchrotron cooling and amplification of the X-mode begins, but particles are still arranged in random phases. Right: the amplified X-mode is evident and the ring is azimuthally bunched along the direction of propagation of the X-mode, as seen by the spiral structure in phase space, and the clear phase alignment, as seen by the colour of the particles and matching of the wave phase with the phase-space structure, following the corresponding colour scale.

3.3 PARTICLE-IN-CELL SIMULATIONS

3.3.1 MASER EMISSION FEATURES

We have investigated, through large-scale, high-resolution particle-in-cell (PIC) simulations (see Appendix A.2), tenuous pair plasmas embedded in strong magnetic fields, where the cyclotron frequency $\omega_{ce} = eB/m_e$ is much higher than the plasma frequency $\omega_{pe} = \sqrt{n_e e^2/(\varepsilon_0 m_e)}$ where e and m_e are the electron charge and electron mass, respectively; n_e is the pair plasma density, ε_0 is the permittivity of free space. To the best of our knowledge, these simulations represent the most extensive study in terms of both spatial and temporal scales for this system to date. PIC simulation results, shown in Fig. 3.3, illustrate that an initial thermal population, in its proper rest frame, evolves into a ring momentum distribution characterised by steep gradients in the perpendicular momentum component $p_\perp$ with respect to the B field, and a narrow energy spread $\Delta p_\perp$. This evolution triggers the efficient onset of the ECMI, which coherently amplifies electromagnetic thermal fluctuations in the magnetised plasma, generating X-mode electromagnetic waves. This process leads to phase trapping by the amplified wave, a characteristic signature of the instability, as confirmed by the phase-space projection after the onset of the instability, shown in Fig. 3.3.

The electromagnetic spectrum of the amplified X-mode is shown in Figure 3.4.a, and demonstrates that the X-mode spectrum peaks near the regions with the highest Γ, with the first three harmonics being amplified, whereas the 4th is much weaker, as analytically predicted (see Fig. 3.2). The degree of polarisation, in Fig. 3.4.b, demonstrates that the self-consistent radiation resulting from emission is highly linearly polarised. This is a result of the X-mode being the fastest-growing mode in highly magnetized plasmas [170].

The degree of linear polarization, which can be synthetically computed, is defined as [115, 171, 172]

$$\Pi = \sqrt{Q^2 + U^2}/I. \tag{3.4}$$

Here, $I = \langle E_1^2 \rangle + \langle E_3^2 \rangle$, $Q = \langle E_1^2 \rangle - \langle E_3^2 \rangle$, and $U = \langle E_a^2 \rangle - \langle E_b^2 \rangle$, where $E_a = (E_1 + E_3)/\sqrt{2}$ and $E_b = (E_1 - E_3)/\sqrt{2}$ correspond to projections of the electric field onto a Cartesian basis rotated by 45°. These quantities form the Jones basis for characterizing linear polarization. The circular polarization basis is defined analogously with $\hat{\mathbf{l}} = (\hat{\boldsymbol{x_1}} + i\hat{\boldsymbol{x_3}})/\sqrt{2}$ and $\hat{\mathbf{r}} = (\hat{\boldsymbol{x_1}} - i\hat{\boldsymbol{x_3}})/\sqrt{2}$.

Since we use grid diagnostics, the electric field components are sampled directly from the simulation plane. For each fixed transverse position x_1, the squared field components $E_i^2(x_1, x_2, t)$ are integrated along the line-of-sight direction x_2 (denoted y) to yield the projected quantities as functions of x_1 and t. That is, $\langle E_i^2 \rangle (x_1, t) = \frac{1}{L_y} \int_0^{L_y} E_i^2(x_1, x_2, t)\, dx_2$, where L_y is the perpendicular size of the simulation domain. This defines the spatial average along x_2 at each instant of time. The resulting Stokes parameters $I(x_1, t), Q(x_1, t), U(x_1, t)$ can then be used to compute the time-resolved degree of linear polarization across the simulation domain.

In the simulation, we consider an array of synthetic observers located along the transverse direction x_1, each with a line of sight along $\hat{\mathbf{x}}_2$, perpendicular to the background magnetic field $\hat{\mathbf{x}}_1$. For each fixed x_1, the field components E_1 and E_3 are recorded along x_2, and the

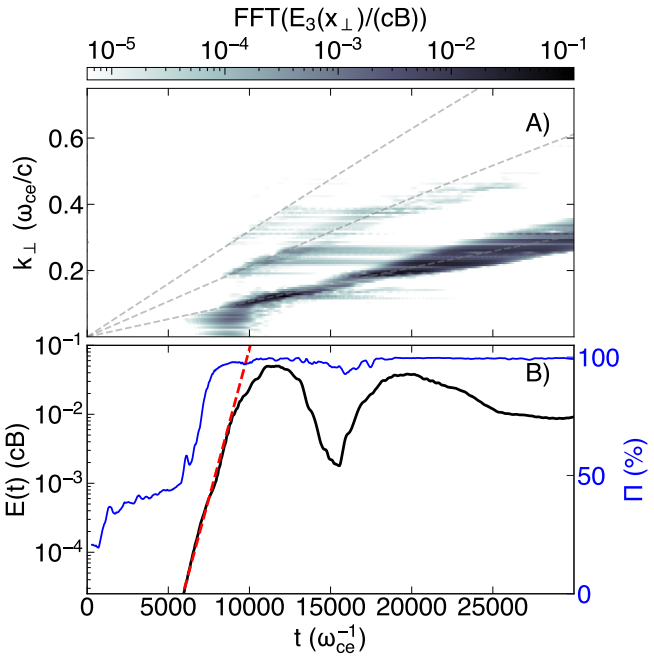

FIGURE 3.4: PIC simulations illustrate the temporal evolution of the X-mode electromagnetic spectrum and energy, which agree with the theoretical estimates, both qualitative and quantitatively. Panel a) shows the Fourier transform of the electric field component E_3 which is perpendicular to both the ambient magnetic field (of amplitude B) and the wave vector $\mathbf{k}$. This spectrum shows the ongoing evolution of the electromagnetic fields during both the linear and non-linear phases of the instability. Theoretical predictions for the maximum growth rates (i.e., the resonant frequencies) are overlaid as grey dashed lines. Panel b) shows the time evolution of the normalised electric field amplitude (black line) and the degree of polarization, derived from the Stokes parameters (blue line). The estimate for the linear growth rate Γ, obtained by numerically solving the full dispersion relation, is compared with the simulation results after the onset of the maser instability but still at early times ($t_o < t \lesssim 12000\,\omega_{ce}^{-1}$), shown as a red dashed line, which follows the relation $E_3 \propto e^{\Gamma t}$.

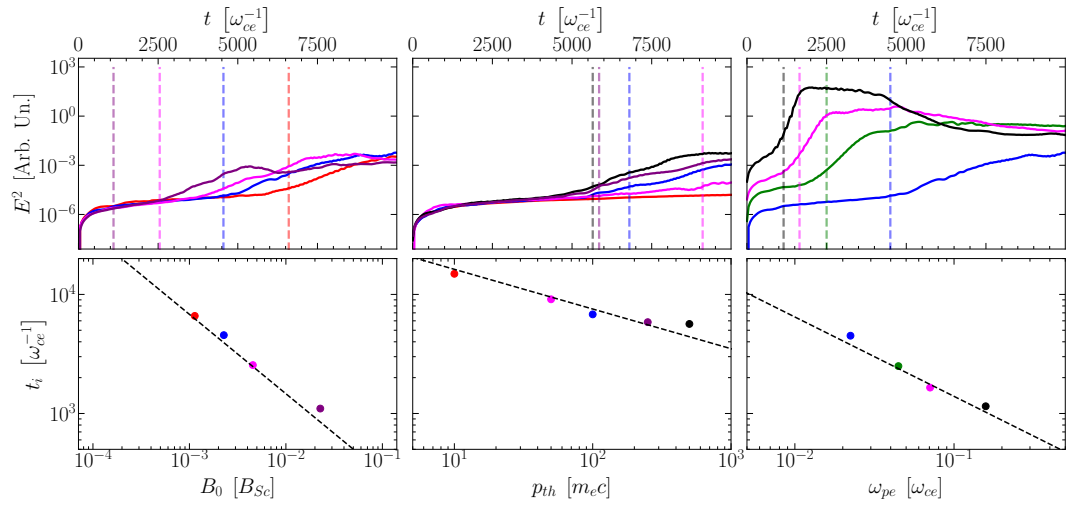

FIGURE 3.5: Particle-in-cell simulation results demonstrate the correlation between the onset of electron cyclotron maser instability and the relevant parameters. The top row depicts the field energy for different simulations, each varying a single parameter per column. In the bottom row, the onset time for each simulation is presented in a log-log scale, showcasing its dependence on the varying parameter. The first column shows the results from varying the magnetic field $B_0 = B/B_{Sc}$. The second column shows the results from a varying initial thermal spread p_{th}. The last column shows the results from varying the plasma frequency ω_{pe}. The simulation outcomes are compared against the expected dependencies from Eq. (8) in the main text. Dashed lines represent the expected dependencies on B_0, p_{th}, and ω_{pe}, which are $t_o \propto B_0^{-1/2}$ [for a fixed (ω_{pe}/ω_{ce} ratio)], and $t_o \propto p_{th}^{-1/2}\,\omega_{pe}^{-1}$, respectively.

polarization quantities $I(x_1), Q(x_1), U(x_1)$ are computed by averaging the appropriate Jones projections along the line of sight. These are then further averaged over x_1 to yield the total Stokes parameters, providing a synthetic diagnostic analogous to an unresolved far-field detector.

The result from this synthetic diagnostic for the percentile degree of polarization, in the PIC simulations, is shown in Fig. 3.4.B. Initially, the electromagnetic radiation is mostly unpolarized, later once the onset of the electron cyclotron maser instability ($t \sim 6000\,\omega_{ce}^{-1}$) the radiation becomes highly linearly polarized reaching a maximum $\Pi = 99.8\%$. This is expected due to the fact that the fastest growing linear mode is the X-mode, as demonstrated in Appedix E.

3.3.2 PARAMETER SCAN OF THE ONSET OF THE ECMI

In order to demonstrate the validity of the scaling of the onset time (*i.e.* Eq. (3.3)) a set of PIC simulations were performed while varying the key parameters. The results of this simulation campaign (displayed in Fig. 3.5) confirm our understanding of the tiemscales and onset of the instability.

The simulations performed are 1D3V, with the background magnetic field aligned perpendicular to the x_1-direction. This configuration allows the propagation of X-mode waves with

$\mathbf{k} \perp \mathbf{B}_0$. A parameter scan confirms that the onset time for the instability, expressed in cyclotron periods, scales as $t_o \propto p_{\text{th}}^{-1/2}\omega_{pe}^{-1}$. An additional scan was performed by varying the magnetic field strength while keeping the ratio ω_{ce}/ω_{pe} constant. In this case, increasing B_0 also increases ω_{pe}, and since $t_o \propto B_0^{1/2}/\omega_{pe}$, the resulting scaling becomes $t_o \propto B_0^{-1/2}$.

To extract the onset time numerically, we track the energy stored in the E_3 component of the electric field, which is the polarization direction of the X-mode. The onset of the instability is identified as the time at which the growth rate of the electromagnetic energy becomes appreciable. Specifically, we define the onset time as the earliest moment when the slope of the energy curve satisfies the condition $\Delta E^2/\Delta t > 0.001\, E^2_{\text{max}}$, where $\Delta E^2/\Delta t$ is the finite difference between successive diagnostic outputs, and E^2_{max} is the maximum electromagnetic energy recorded during the simulation. All quantities are evaluated in the normalized (simulation) units. While somewhat arbitrary, this threshold reliably captures the change in slope associated with the transition to exponential growth, and provides a consistent and robust estimate of the onset time across different parameter scans (see Fig. 3.5).

3.3.3 Non-linear dynamics of the ECMI in the synchrotron dominated regime

The classical ECMI, a collisionless plasma process, reaches saturation due to the azimuthal phase trapping of the particles by the wave. As phase-space volume is conserved, when particles are azimuthally trapped, their momentum distribution must expand radially, broadening the ring distribution and reducing its gradient $\partial f/\partial p_\perp$. This eventually stabilizes the classical ECMI. Before saturation, and for the electrons to provide energy to the wave, it is necessary that $\delta\omega = \omega - \omega_{ce}/\gamma \gtrsim 0$ [163]. At saturation ($t \sim 1.2 \times 10^4\, \omega_{ce}^{-1}$ in Fig. 3.4), particles overshoot the phase trapping condition and now $\delta\omega \lesssim 0$: particles extract energy from the previously amplified wave. This is a well-known phenomenon [163], that explains the dip in electric field amplitude at $t \sim 1.5 \times 10^4\, \omega_{ce}^{-1}$ in Fig. 3.4.b and the saturated state, as shown in devices such as Gyrotrons, FELs, and ICLs [163, 164]. PIC simulations capture the ECMI well beyond the linear regime and demonstrate that synchrotron-cooled plasmas evolve differently in the non-linear stage of the instability, as seen in Fig. 3.4.A: surprisingly, the spectrum continues to evolve with the X-mode spectrum shifting to higher frequencies and widening the spectrum. The emitted radiation is trapped in our simulation domain, mimicking an infinite plasma volume. For a finite volume plasma the X-modes escape and convert to light waves, our numerical simulations with finite plasmas confirm this picture.

The synchrotron-cooled ECMI introduces additional dynamics due to the effects of radiative losses, which do not conserve phase-space volume. As particles radiate synchrotron emission, they continue to bunch in the radial momentum direction. This creates a competition between azimuthal phase trapping, driven by the ECMI, which diffuses the gradient in $p_\perp$, and radiative losses, which continually attempt to bunch the distribution radially and sustain the gradient in $p_\perp$. The radiative losses are thus responsible for both establishing the initial ring distribution and maintaining it throughout the emission process.

PIC simulations confirm this interplay, as demonstrated by the evolution of the perpendic-

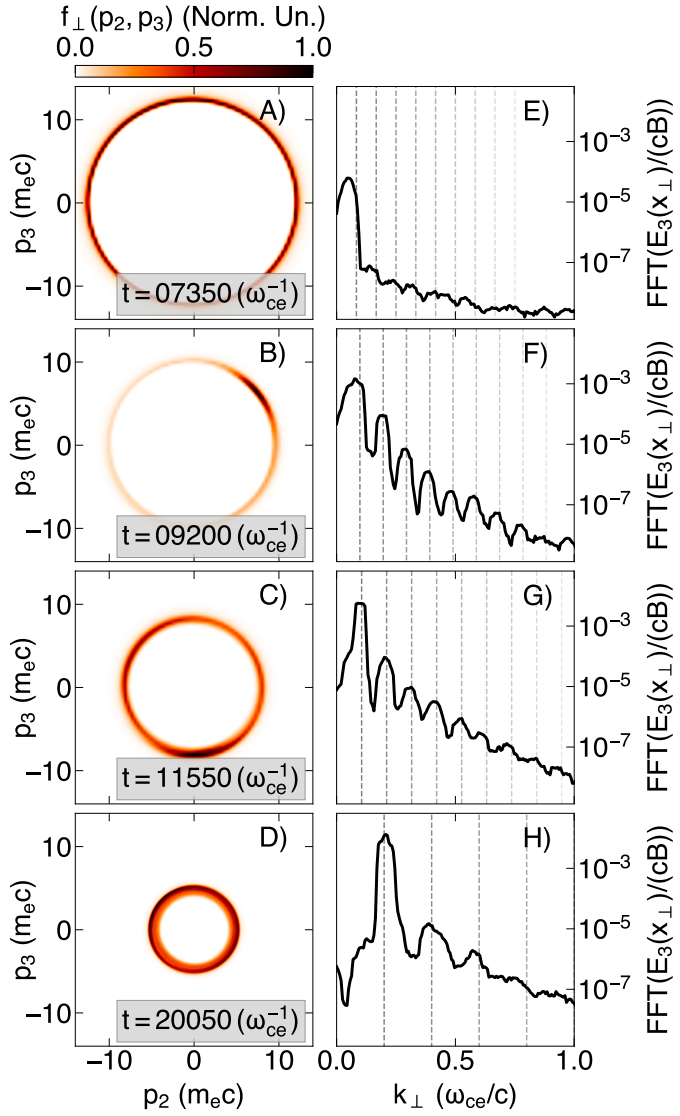

FIGURE 3.6: PIC simulations illustrate that ring distributions are sustained beyond the linear regime of the ECM instability. This is seen in the evolution of a radiatively cooled electron-positron plasma undergoing the ECMI, starting from an initial Maxwellian distribution with $p_{\rm th} = 1000\, m_e c$. Column 1 displays the electron momentum distribution integrated along the magnetic field direction $\mathbf{x_1}$, $f_\perp\,(p_2, p_3)$, while Column 2 shows the spectrum of the associated X-mode wave, with vertical dashed lines indicating the expected harmonics, as predicted by our theoretical model. Each row (a-d) corresponds to a different time in the simulation: a) shows the developed ring distribution from an initial Maxwellian plasma; b) shows the onset of the ECMI, characterised by phase trapping (the positrons, not shown here, bunch up on the opposite phase of the ring), and narrow emission observed in the spectrum; c) shows the widening of the ring distribution as the system reaches the standard ECMI saturation point; d) demonstrates further evolution of the distribution as the instability transitions to the non-linear regime, where the ring widens and the emission becomes broader.

ular momentum distribution of the plasma as it transitions from the linear to the nonlinear regime of the instability. After the establishment of the ring distribution with a narrow momentum spread (Fig. 3.6.A), the onset of the instability produces azimuthal phase trapping characteristic of ECMI (Fig. 3.6.B) and efficiently amplifies the harmonics (Fig. 3.6.F). At the point of classical saturation, the ring continues to contract and is sustained, as evidenced by the smaller radius (Fig. 3.6.C), and the frequency of each harmonic undergoes a slight upshift (evident in Fig. 3.4.A and Fig. 3.6.G).

The phase trapping caused by the amplification process radially widens the ring, but this is counterbalanced by the bunching effect of radiative cooling, leading to a broader yet still well-defined ring (Fig. 3.6.D). Consequently, the electromagnetic spectrum broadens at late times (Fig. 3.4.A and Fig. 3.6.H), indicating that the nonlinear stage does not entirely inhibit population inversion. The ring structure in momentum space remains intact, and the ECMI continues to be active well beyond the timescales presented in this work (Fig. 3.4.D).

Eventually, the ring will cool down to $T \sim m_e c^2/\sqrt{3}$, and the instability overcomes the bunching process (as the synchrotron losses which sustain the ring become less important [113]) and the ring is diffused, stopping the ECMI and emission process. This occurs when the ring cools down to a ring radius $p_R \sim m_e c/\sqrt{3}$, which determines for how long the ring structure and emission can be sustained. In the plasma proper frame that is comparable to $t_{\rm em} \simeq 2\omega_{ce}^{-1}/\sqrt{3}\alpha B_0$, or $t_{\rm em}\,[400\,\mu{\rm s}] \simeq (B\ [{\rm MG}])^{-2}$, which is independent of the plasma parameters, as it is a timescale determined solely by the cooling process when $t_{em} > t_o$.

Therefore, after the onset of the maser at t_o (Eq. (3.3)) the ring and the ECMI, will be sustained until t_{em}, producing a long pulse of radiation. This finding addresses a major criticism of the ECMI as a source of “long-lived" coherent radiation [173]. In relativistic plasmas, the onset of the maser instability does not disrupt the population inversion, allowing continued emission. Radiative effects sustain the population inversion, enabling the maser to operate over prolonged periods. Interestingly, depending on the plasma parameters, the ring can form and cool below $p_R \sim m_e c/\sqrt{3}$, before the onset of the ECMI, and in that case $t_o > t_{\rm em}$. In this scenario, the onset of the ECMI can still happen, and the ring will begin to diffuse right after saturation. Radiative losses will not be able to reform or sustain the ring, resulting in a single pulse of electromagnetic waves that escapes the plasma, resembling the classical ECMI.

3.4 Discussion

3.4.1 Competing processes

The necessary plasma parameters for relativistic plasmas to emit coherent radiation via ECMI can be determined by guaranteeing that a hierarchy of timescales is fulfilled. Firstly, the onset of the instability t_o (Eq. (3.3)) must be earlier than any diffusive process, *e.g.* Coulomb collisions, Compton collisions and pair annihilation.

For the efficient onset of the maser the ring must not collapse to the lowest Landau level before the onset of the instability. The first quantum Landau energy level is given by $E_{l,0} = \hbar eB/m_e c$, and in momentum that is $p_{l,0} = \hbar eB/m_e c^2$. This scales as $p_{l,0}\,[m_e c] \simeq B\,[B_{\rm Sc}]$. There-

fore, the time needed for the momentum space to fully collapse into the quantum levels is $t_{\rm landau} \simeq \frac{2}{3\alpha} B_0^{-2} \omega_{ce}^{-1}$. Thus, the onset time ($t_o$) must be shorter than $t_{\rm landau}$.

We consider three relevant collisional processes that could diffuse the ring distribution before the onset of the ECMI. These processes are: (i) Coulomb collisions, (ii) pair annihilation, and (iii) Compton scattering from synchrotron self-emission. The relaxation timescale for each process is defined as the inverse of its corresponding collision frequency.[3]

The relaxation timescale due to Coulomb collisions is given by [113, 144, 146]

$$t_{ee} = \frac{12\pi^{3/2}}{\sqrt{2}} \frac{\epsilon_0^2 m_e^2 c^3}{e^4} \frac{1}{n \ln \Lambda}, \tag{3.5}$$

where n is the plasma density, $\ln \Lambda$ is the Coulomb logarithm (we take it to be of order unity), and, as we are dealing with relativistic plasmas, we have approximated $v_e \sim c$.[4] Alternatively, $t_{ee} \simeq 5/(2\sigma_T c n)$ and $t_{ee}\,[\mathrm{s}] \simeq 1.25 \times 10^{14}/(n\,[\mathrm{cm}^{-3}])$, where σ_T is the Thomson cross-section.

For pair annihilation, the relaxation timescale is estimated using the cross-section for electron-positron annihilation, which can be approximated by the Thomson cross-section σ_T [17, 174]. In this case, the plasma is not simply diffused but rather "evaporates" as electron-positron pairs annihilate and are converted into high-energy photons. This process removes particles from the plasma, leading to its gradual depletion. The timescale for this "evaporation" process is $t_{eva} = 1/(2\sigma_T c n)$. We note that this timescale is comparable to t_{ee}.

The relaxation timescale due to Compton scattering, induced by synchrotron self emission, can also be estimated. For the purpose of this discussion, an overestimate of the collisional effects suffices. The collisional frequency is defined as $\nu_{e\gamma} = 2c\sigma_T n_\gamma$, where n_γ is the photon density. The photon density can be estimated as the energy budget divided by the average energy per photon, *i.e.* $n_\gamma = \Delta E/\hbar \langle\omega\rangle$, where ΔE is the change in energy of the electron population as it cools, $\langle\omega\rangle$ is the average synchrotron photon angular frequency, and $\hbar$ is the reduced Planck constant. The change in energy in the electron population is $\Delta E = p_{th}^2 n_e \tau/(1 + p_{th}\tau)$, obtained from the equations of motion [23, 113], where $\tau = \frac{2}{3}\alpha B_o t \omega_{ce}^{-1}$ with t being the time elapsed since the beginning of the cooling, and p_{th} is the initial thermal spread. We assume the average frequency $\langle\omega\rangle$ to be the critical frequency for a given ring radius at time t_o, which may underestimate the actual average frequency since electrons have higher energies earlier in the process. This overestimates the photon density at time t. This can be used to estimate the photon density and subsequently the relaxation time due to synchrotron self-emission at the onset time t_o, $t_{e\gamma} = 1/(2\sigma_T p_{\rm th}^{1/3} B_0 n_e^{1/3} n_o^{2/3})$, where $n_o \simeq 5 \times 10^5\,\mathrm{cm}^{-3}$, and $t_{e\gamma}\,[3.5 \times 10^8\,\mathrm{s}] = B_0^{-1}(n_e\,[\mathrm{cm}^{-3}]\ p_{th}\,[m_e c])^{-1/3}$. This estimate demonstrates that before the onset of the ECMI, the timescale of relaxation due to synchrotron-self-compton is much larger than Coulomb collisions.

In this estimate, we have neglected the non-linear Breit-Wheeler mechanism, where photons convert into pairs. This reduces the photon density, which would lengthen the relaxation timescale. Moreover, while the plasma is large, high-energy photons can have mean free paths

[3] Collisional processes were previously discussed in Sec. 2.5, where their timescales were compared to the ring formation time. Here, we revisit those same processes to assess whether they can inhibit the subsequent development of the ECMI, whose onset time may be significantly longer depending on plasma conditions and magnetic field strength.

[4] This strictly over estimates the collision rate, but it suffices for the purpose of this discussion.

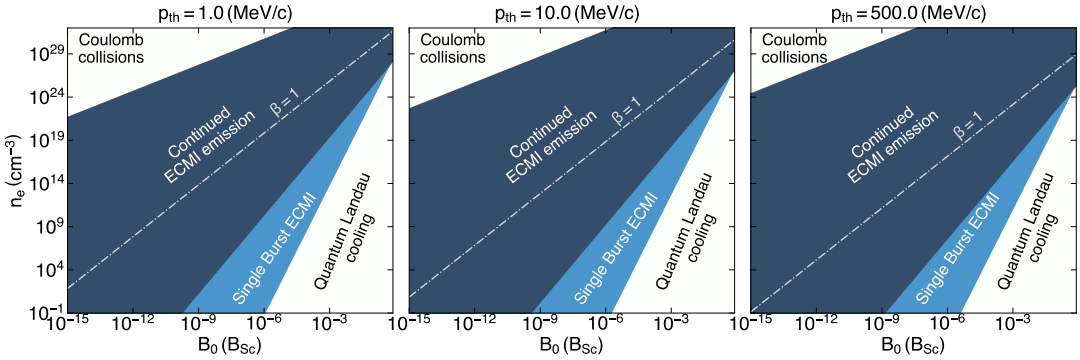

FIGURE 3.7: The comparison of relevant timescales for the onset of the synchrotron ECMI demonstrates that maser emission occurs for a wide range of plasma and magnetic field parameters. As presented across three panels, each corresponding to different initial thermal energies and defined by plasma density, magnetic field strength, and initial thermal energy. Regions in dark blue indicate where the maser instability triggers and sustains continued emission, occurring before competing processes like collisional relaxation or cooling to quantum Landau levels can interfere. The top left white region highlights conditions where collisional relaxation dominates, diffusing the ring structure and preventing efficient maser emission, while the right-hand white region shows where cooling to quantum Landau levels occurs before the maser instability can develop, rendering the plasma degenerate and preventing maser onset. A light blue region represents conditions where the maser instability triggers with a single burst produced, as the onset occurs after the ring has cooled below the threshold thermal momentum needed for sustained bunching. A white dashed line marks the boundary where the plasma beta parameter β, *i.e.* the ratio of plasma pressure to magnetic field pressure, is $\beta = 1$. Above this line, other instabilities, such as the synchrotron firehose instability can also trigger.

longer than the plasma's spatial scale, allowing some photons to escape without contributing to plasma relaxation. For further details on the balance between self-absorption and emission, refer to Ochs (2024) [168].

By comparing these timescales with the ECMI onset time, we obtain the parameter space in which the maser can operate.

There is a wide range of parameters for which the synchrotron-induced ECMI operates efficiently before (Coulomb or Compton) collisional relaxation and cooling to the quantum levels can take place, see Fig. 3.7. The parameter space increases as the plasma becomes more energetic. The ECMI will spontaneously trigger in a wide range of plasma parameters of relevance to astrophysical systems [165]. Other instabilities can also trigger due to synchrotron losses; the firehose instability can operate when $\beta > 1$, where β is the ratio of the plasma pressure to the magnetic field pressure [24]. In that regime, the firehose instability will modify the momentum distribution, but as the plasma cools down, it can transition to a $\beta < 1$ regime enabling a modified version of the "ring" ECMI to operate. Preliminary PIC simulations have confirmed this picture, see Appendix F, and will be furhter explored elsewhere.

3.4.2 Energy partition between coherent and incoherent emission

A key question is how much kinetic energy remains available for the ECMI after synchrotron cooling, *i.e.*, what fraction has already been radiated incoherently before the instability turns on. This matters for observations because FRB radio bursts are sometimes nearly simultaneous with hard X-ray activity [44, 45, 175], which can be naturally associated with the initial cooling phase.

We define the mean kinetic energy per particle at time τ as

$$E(\tau) = \int_0^\infty 2\pi p_\perp \, dp_\perp \int_{-\infty}^\infty dp_\parallel \left(\sqrt{1 + p_\perp^2 + p_\parallel^2} - 1\right) f(p_\perp, p_\parallel, \tau), \tag{3.6}$$

with f normalized to unity. For general f, the integral is not elementary. After ring formation at t_r, cooling bunches the distribution into a narrow annulus at $p_\perp \simeq p_R(\tau)$ with $p_R \simeq 1/\tau$, plus a depleted interior. A convenient approximation is

$$f(p_\perp, p_\parallel, \tau) \simeq \left[a\,\delta(p_\perp - p_R) + \Theta(p_R - p_\perp)\, f_0(p_\perp)\right] f_\parallel(p_\parallel), \tag{3.7}$$

where f_0 is the initial perpendicular profile[5] and $f_\parallel(p_\parallel)$ is the cooled parallel distribution from Sec. 2.3.4. For an initially hot, isotropic relativistic Gaussian with width $p_{\rm th}$, normalization fixes

$$a = \frac{1}{2\pi p_R}\left[1 + \frac{e^{-p_R^2/(2p_{\rm th}^2)} - 1}{\sqrt{2\pi}\, p_{\rm th}}\right]. \tag{3.8}$$

[5] We are therefore assuming that the region within the ring has slowly cooled down and the region outside the ring has collapsed into the ring structure.

Carrying out the integrals gives a closed form for the post-cooling energy (per particle, in units of $m_e c^2$),

$$\begin{aligned} E(\tau) = & -2 - e^{1/(2p_{\rm th}^2)} + 2\sqrt{1+p_R^2} - \frac{\sqrt{2/\pi}}{p_{\rm th}}\sqrt{1+p_R^2} \\ & + e^{1/(2p_{\rm th}^2)}\,\mathrm{erf}\left(\frac{\sqrt{1+p_R^2}}{\sqrt{2}\,p_{\rm th}}\right) + \frac{2\,e^{1/(2p_{\rm th}^2)}}{\sqrt{\pi}}\,\Gamma\left(\tfrac{3}{2}, \frac{1}{2p_{\rm th}^2}\right), \end{aligned} \tag{3.9}$$

where $p_R \simeq 1/\tau$. Here $\mathrm{erf}(x)$ is the Gauss error function, and and $\Gamma(s,x)$ is the upper incomplete gamma function.

For comparison, the initial mean kinetic energy for the same relativistic Gaussian is

$$E_0 = \sqrt{\frac{8}{\pi}}\,p_{\rm th}. \tag{3.10}$$

For hot beams, $p_{\rm th} \gg 1$, Eq. (3.9) simplifies to

$$E(\tau) \simeq 2\big(\sqrt{1+p_R^2} - 1\big) + \mathcal{O}\left(\frac{1}{p_{\rm th}}\right), \tag{3.11}$$

so for $p_R \gg 1$,

$$\frac{E(\tau)}{E_0} \simeq \sqrt{\frac{\pi}{2}}\,\frac{p_R}{p_{\rm th}} \simeq \sqrt{\frac{\pi}{2}}\,\frac{1}{\tau\,p_{\rm th}}. \tag{3.12}$$

This scaling is very convenient, it shows that by the time a sharp ring forms, only a fraction $\sim p_R/p_{\rm th}$ of the initial kinetic energy is left to feed the maser. For example, taking $p_R = 40$ and $p_{\rm th} = 10^3$, Eq. (3.9) gives $E/E_0 \simeq 4.9 \times 10^{-2}$, consistent with the asymptotic estimate (3.12).

Using the scaling for the maser onset time (See Eq. (3.3)),

$$\tau_o \simeq 0.02\,\left[\frac{\big(B\,[\mathrm{MG}]\big)^3}{n_e\,[10^6\,\mathrm{cm}^{-3}]\,p_{\rm th}\,[100\,m_e c]}\right]^{1/2}, \tag{3.13}$$

we have $p_R(\tau_o) \simeq 1/\tau_o$, hence combining with (3.12) gives an estimate for the available fractional energy at onset,

$$\left.\frac{E}{E_0}\right|_{\tau_o} \simeq \sqrt{\frac{\pi}{2}}\,\frac{1}{\tau_o\,p_{\rm th}} \propto \left[\frac{B^3}{n_e\,p_{\rm th}}\right]^{1/2}. \tag{3.14}$$

Stronger B and lower n_e both shorten τ_o, which increases p_R and raises the energy fraction available to the ECMI. This connects the prompt high-energy cooling signature to the delayed growth of coherent radio power in a way that can be compared with FRB plus X-ray coincidences.

The ring-plus-interior approximation is accurate once $t \gtrsim t_r$ from Eq.(2.26). Before that time, p_R is not yet sharp and the available energy is slightly larger than Eq.(3.9) predicts. Corrections from a finite ring width and from deviations of $f_\parallel$ from the Gaussian asymptote are subleading for $p_R \gg 1$ and $p_{\rm th} \gg 1$. The interplay between maser growth and synchrotron cooling makes it challenging to determine exactly how the remaining energy is partitioned between coherent maser emission and incoherent losses. A full answer would require simulations that extend over timescales orders of magnitude longer than those presented in this

chapter, and that model the escape of radiation from a finite plasma volume. The present calculation therefore provides an upper bound on the energy available to the maser when cooling becomes comparable to its growth rate, and we conjecture that it offers a reasonable order-of-magnitude estimate.

3.4.3 PROPERTIES OF THE EMITTED COHERENT RADIATION

The transmission efficiency at a sharp plasma–vacuum boundary can be estimated by comparing the *refractive index* $n = \sqrt{N^2(\omega)}$ on both sides of the interface [169]. For the extraordinary (X) mode propagating perpendicular to the magnetic field, the refractive index follows from the dispersion relation [176]

$$N^2 = \varepsilon_{yy} - \frac{\varepsilon_{xy}^2}{\varepsilon_{yy}}, \tag{3.15}$$

where the dielectric tensor elements ε_{ij} are given in Eq. (E.11). The corresponding polarization properties are discussed in App. E.2.2, which shows that the X-mode is elliptically polarized but becomes nearly linearly polarized along E_y when $\omega_{ce}/\gamma \sim \omega \gg \omega_{pe}$. In this strongly magnetized regime, the dielectric tensor yields

$$\varepsilon_{yy} = 1 + \mathcal{O}\left(\frac{\omega_{pe}^2}{\omega^2}\right), \qquad \varepsilon_{xy} = i\,\mathcal{O}\left(\frac{\omega_{pe}^2}{\omega\omega_{ce}}\right), \tag{3.16}$$

so that

$$N^2 = 1 + \mathcal{O}\left(\frac{\omega_{pe}^2}{\omega_{ce}^2}\right). \tag{3.17}$$

Hence, the X-mode refractive index approaches unity and the impedance mismatch at the plasma–vacuum boundary becomes small, though never vanishing entirely. The degree of matching improves with increasing magnetization, but for more moderate parameters, density gradients or inhomogeneities can reduce the escaping fraction. Preliminary numerical evaluation of the full dielectric tensor (including off-diagonal terms of the dielectric tensor) confirms this trend: transmission is high for $\omega_{pe}/\omega_{ce} \lesssim 10^{-3}$, while for larger values the impedance mismatch becomes increasingly important.

In summary, the analysis of the dielectric tensor (App. E.2.2) shows that the X-mode radiation produced in the plasma can couple to vacuum with relatively high efficiency in the strongly magnetized limit $\omega_{ce} \gg \omega_{pe}$. The refractive index approaches unity in this regime, so the impedance mismatch is reduced but never eliminated. The precise transmission depends on the degree of magnetization as well as plasma inhomogeneities and gradients, which may further limit the escaping fraction. Nevertheless, in sufficiently magnetized plasmas the conditions are favorable for X-mode emission to leave the plasma and contribute to observable radiation in the radio band.

In the proper frame of the plasma, the emitted frequencies occur at harmonics of $n\omega_{ce}/\gamma_r$, where $\gamma_r = (1 + p_r^2/m_e^2c^2)^{1/2}$ is the Lorentz factor associated with the ring radius at the onset of the maser instability. Radio emission occurs in the proper frame at $\omega\,[17\,\mathrm{THz}] \simeq B\,[\mathrm{MG}]/\gamma_r\,[1]$. Additionally, the emission maintains a constant ratio of $\Delta\omega/\omega$, where $\Delta\omega$ is the

frequency separation between different harmonics. This constant ratio is observed in sources such as the Crab pulsar [177].

Due to time dilation and the relativistic Doppler effect, the received radiation is upshifted by a factor of γ_b, where γ_b is the Lorentz factor of the beam's proper frame. Furthermore, the emission timescale becomes shorter by a factor of $1/\gamma_b$, and the intensity increases by a factor of γ_b^2 due to relativistic beaming [178].

3.4.4 COHERENCE OF THE EMITTED RADIATION

Although the ECMI does not operate within a resonant cavity, it exhibits the essential features of Amplified Spontaneous Emission (ASE) and functions analogously to a *mirrorless laser amplifier* [172]. In such systems, coherence arises not through optical feedback, but through the exponential amplification of spontaneous fluctuations as they propagate through a medium with population inversion. This behavior is well established in theoretical models of high-gain, saturating amplifiers, which show that even in the absence of mirrors, these systems can exhibit intensity buildup, spectral narrowing, and threshold-like behavior similar to conventional lasers [179]. In the case of the ECMI, the synchrotron-cooled ring distribution supplies the population inversion, while the exponentially unstable X-mode acts as the dominant mode undergoing amplification. The result is coherent, directional emission, even though the system lacks an optical cavity. The maser thus behaves as a single-pass, cavity-free, *mirrorless maser*, driven by a collective instability in a non-equilibrium plasma.

Quantifying coherence is a subtle and often context-dependent task, as "no general agreement exists on the precise meaning of the term..."[6]. In its most general sense, coherence reflects correlations in the fluctuations of a field, both in space and time [171, 172]. Formally, one would assess this through detailed phase relationships or autocorrelation functions of the emitted radiation. However, in astrophysics, a more pragmatic and indirect measure is often employed: the *brightness temperature*.

Brightness temperature is defined as the temperature a blackbody would require to produce the same specific intensity at a given frequency. It is given by:

$$T_B = \frac{c^2}{2\nu^2 k_B} I_\nu, \tag{3.18}$$

where ν is the observed frequency, k_B is Boltzmann's constant, and I_ν is the specific intensity. The latter can be estimated as:

$$I_\nu \approx \frac{P}{\Delta\nu\,\Omega\,A}, \tag{3.19}$$

with P the emitted power, $\Delta\nu$ the bandwidth, Ω the solid angle of emission, and A the emitting area.

While this metric is not a rigorous definition of coherence in the optical or laser physics sense, it offers a valuable diagnostic: when the inferred T_B far exceeds the physical limits for incoherent emission (e.g., the inverse Compton limit of $\sim 10^{12}$ K), it is widely interpreted

[6] Quote from L. Mandel & E. Wolf 1996 [171]

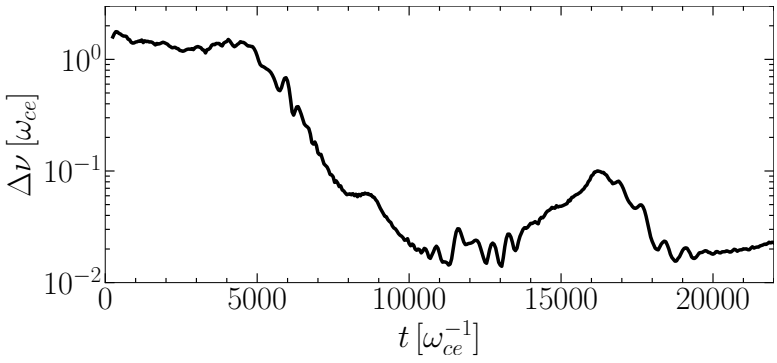

FIGURE 3.8: Bandwidth of the maser emission computed from the spectrum shown in Fig. 3.4. As the instability develops, the spectrum becomes increasingly narrow, with a marked drop in bandwidth around $t \sim 6000\,\omega_{ce}^{-1}$. During the period of coherent emission, the bandwidth remains approximately $\Delta\nu \sim 0.01\,\omega_{ce}$.

as evidence for coherent amplification processes [115]. Despite its limitations, this criterion serves as an effective and widely adopted proxy in astrophysical settings.

In this spirit, we now estimate the brightness temperature associated with ECMI emission driven by synchrotron cooling. Equation (3.19) can be recast using the relation $P/A = c\,\mathcal{E}$, where $\mathcal{E}$ is the energy density of the emitted radiation. This can be interpreted as the saturation level of the maser. Empirically, we find that the amplitude of the wave at saturation is between 1 and 10^{-2} times the amplitude of the background magnetic field, as shown in Fig. 3.4(B) and Fig. 3.5. That is, the wave energy is a small fraction of the local field energy.

This estimate refers to the plasma rest frame. In the observer's frame, Lorentz contraction reduces the emission volume by a factor of γ_b, while the energy density increases by γ_b, resulting in a net boost of $I_\nu \propto \gamma_b$.

The definition of bandwidth for complex spectral density functions, such as those arising from laboratory masers, is given by [171]

$$\Delta\nu = \frac{1}{2\pi}\left[\int_0^\infty g_\omega^2(\omega')\,d\omega'\right]^{-1}, \tag{3.20}$$

where $g_\omega(\omega)$ is the normalized spectral density of the emitted radiation. Although the emission spectrum spans a broad frequency range, the radiation is sharply peaked near harmonics of the cyclotron frequency, as shown in Fig. 3.4.[7] To quantify this, we numerically compute the bandwidth $\Delta\nu$ as a function of time using the full multidimensional PIC simulation presented in this work. The resulting time evolution is shown in Fig. 3.8.

The computed bandwidth remains of order $\Delta\nu \sim 0.01\,\omega_{ce}$ throughout the emission window. This estimate includes all active harmonics of the ECMI and therefore slightly overestimates the spectral width of each individual harmonic. An analytical estimate can also be

[7] Figure 3.4 spans the range $0 < \omega < \omega_{ce}$, but the sharp peaks evident in logarithmic scale indicate that most of the energy is narrowly concentrated around specific frequencies.

obtained by linking the spectral spread to the momentum spread of the ring distribution. Using the relation $\Delta p \sim p_R^2/(\sqrt{3}\, p_{\rm th})$, the associated frequency spread is

$$\Delta\nu \sim \frac{\Delta p}{m_e c} \cdot \frac{\omega_{ce}}{2\pi}. \tag{3.21}$$

For a typical ring radius $p_R \sim 10\, m_e c$ and thermal spread $p_{\rm th} \sim 10^3\, m_e c$, this yields $\Delta\nu \sim 0.01\, \omega_{ce}$, in agreement with both the spectral features in Fig. 3.4(B) and the time-resolved numerical evaluation shown in Fig. 3.8. In the observer frame, this bandwidth is further Doppler-broadened to $\Delta\nu \to \gamma_b\, \Delta\nu$, where γ_b is the bulk Lorentz factor of the emitting plasma.

Relativistic beaming also concentrates the radiation into a narrow solid angle $\Omega \sim 1/\gamma_b^2$ [178]. Collecting all these scalings, we arrive at a simplified expression for the observed specific intensity:

$$I_\nu \simeq \frac{\eta\, B_0^2\, \gamma_b^2}{\Delta\nu}, \tag{3.22}$$

where $\eta \ll 1$ is the fractional wave energy relative to the background field energy.

Substituting into Eq. (3.18) yields:

$$T_B \left[5 \times 10^{30}\,\mathrm{K}\right] \simeq \frac{\eta\, \left(\gamma_b \left[10^6\right]\right)^2}{\Delta p\, [0.01\, m_e c]\; B\, [10^3\,\mathrm{G}]}. \tag{3.23}$$

Therefore, this model predicts a direct connection between the brightness temperature and the local magnetic field strength at the emission site, which also sets the characteristic emission frequency via $\omega \propto \omega_{ce} \propto B$. Higher magnetic fields, corresponding to higher emission frequencies, lead to proportionally lower brightness temperatures for fixed beam parameters, since $T_B \propto 1/B$. The brightness temperature thus depends sensitively on the interplay between magnetic field strength, beam Lorentz factor, and the ring width Δp, which determine the efficiency of synchrotron cooling and the initial thermal spread of the plasma.

At $B \sim 10^3\,\mathrm{G}$, the electron cyclotron frequency falls in the tens of gigahertz range, consistent with the observed GHz frequencies of FRBs. The ECMI driven by synchrotron-cooled ring distributions can therefore plausibly account for both the high brightness temperatures and the narrow spectral features associated with these fast radio transients, which often exhibit $T_B \sim 10^{30}\,\mathrm{K}$ or higher. Similarly, pulsar radio emission is also known to reach brightness temperatures in excess of 10^{25}–$10^{28}\,\mathrm{K}$, reinforcing the idea that coherent mechanisms are at play across a range of magnetized astrophysical environments.

These considerations establish that synchrotron-induced ECMI can generate brightness temperatures and spectral features consistent with those observed in FRBs[8]. The key ingredients, strong magnetic fields, relativistic pair beams, and radiative cooling, are all expected in magnetar magnetospheres. This motivates a closer look at how such conditions can arise and evolve in a realistic astrophysical setting. In what follows, we outline a concrete scenario in which this mechanism operates within a neutron star magnetosphere, identifying the distinct spatial regions and physical processes that lead to coherent maser emission.

[8]To the best of our knowledge, this is the only known mechanism capable of generating such extreme brightness temperatures without fine tuned conditions [43].

An important condition for efficient amplification is that the background magnetic field remains approximately constant over the spatial scale of the amplification process. Amplification occurs on the timescale set by the growth rate of the instability, Γ_X^{-1}, which depends on local plasma parameters, magnetic field strength, cooling rate, and thermal spread. we know that the maser becomes active once the ring distribution stays sufficiently long in resonance, this occurs when $\tau \lesssim 1$, as confirmed in simulations. This leads to a timescale of order $\Gamma_X^{-1} \sim \frac{\omega_{ce}}{\omega_{pe}^2} \frac{m_e^2 c^2}{p_{\rm th}^2}$ (See Sec. 3.2.2).

For large thermal spreads $p_{\rm th} \sim 10^{2-3}\, m_e c$, and typical ratios $\omega_{ce}/\omega_{pe} \sim 10^{2-3}$, the growth rate is $\Gamma_X \sim \omega_{pe}$. In compact objects, this corresponds to the Goldreich–Julian density, which varies across sources. For example, a pulsar with surface field $B_s \sim 10^9$ G and spin period of 1 second yields $n_{GJ} \sim 10^7\,{\rm cm}^{-3}$, while for a magnetar with $B_s \sim 10^{13}$ G, the value increases to $\sim 10^{11}\,{\rm cm}^{-3}$ [156]. Taking $n_e \sim 10^7\,{\rm cm}^{-3}$, we find $\Gamma_X^{-1} \sim 5.6$ ns, corresponding to a propagation length $L_p \sim c\,\Gamma_X^{-1} \sim$ meters. Over this length, the magnetic field must remain sufficiently uniform, i.e., $\left|\frac{1}{B(r)}\frac{dB(r)}{dr}\right| < 1/L_p$. Assuming a dipolar field $B(r) \propto 1/r^3$, where r is the distance from the star. The condition implies $L_p < r$, which is trivially satisfied at radial distances $r \gtrsim 10$ km, *i.e.* the size of the neutron star. Therefore, the assumption of a constant background field over the amplification length is justified in this context.

3.5 Coherent astrophysical emission via Synchrotron-induced ECMI

The mechanism described above, synchrotron cooling leading to the formation of ring momentum distributions and the triggering of the electron cyclotron maser instability (ECMI), offers a compelling mechanism for the generation of coherent radio bursts in the magnetospheres of neutron stars. Given its ability to naturally reach brightness temperatures on the order of 10^{30} K, it provides a viable explanation for the observed properties of fast radio bursts (FRBs), including their GHz frequencies, and strong polarization signatures. Crucially, the conditions required for this mechanism are not confined to isolated or finely tuned regions of the magnetosphere. Rather, the ECMI can arise generically during the outward propagation of a radiatively cooled relativistic beam through a magnetized, perturbed environment.

Figure 3.9 illustrates a concrete astrophysical scenario. We emphasize that this figure is a schematic cartoon and not drawn to scale. In reality, the distances separating regions A, B, and C are very large. For emission to occur in the GHz band, the beam must propagate to radii where the magnetic field has decreased to kilogauss values ($r \sim 10^9$ cm), far from the stellar surface. This propagation distance is many orders of magnitude larger than the microscopic timescales of synchrotron cooling or ECMI growth, ensuring that there is sufficient time for the processes described below to develop. The process begins near the neutron star surface, in a region labeled A, where a high-energy electron-positron beam is injected along a magnetic field line. This injection may be triggered by a violent event such as a starquake, magnetic reconnection, or a pair cascade in a polar gap [34]. In this inner region, the magnetic field is so intense that synchrotron cooling dominates all other timescales. The beam cools quickly, and

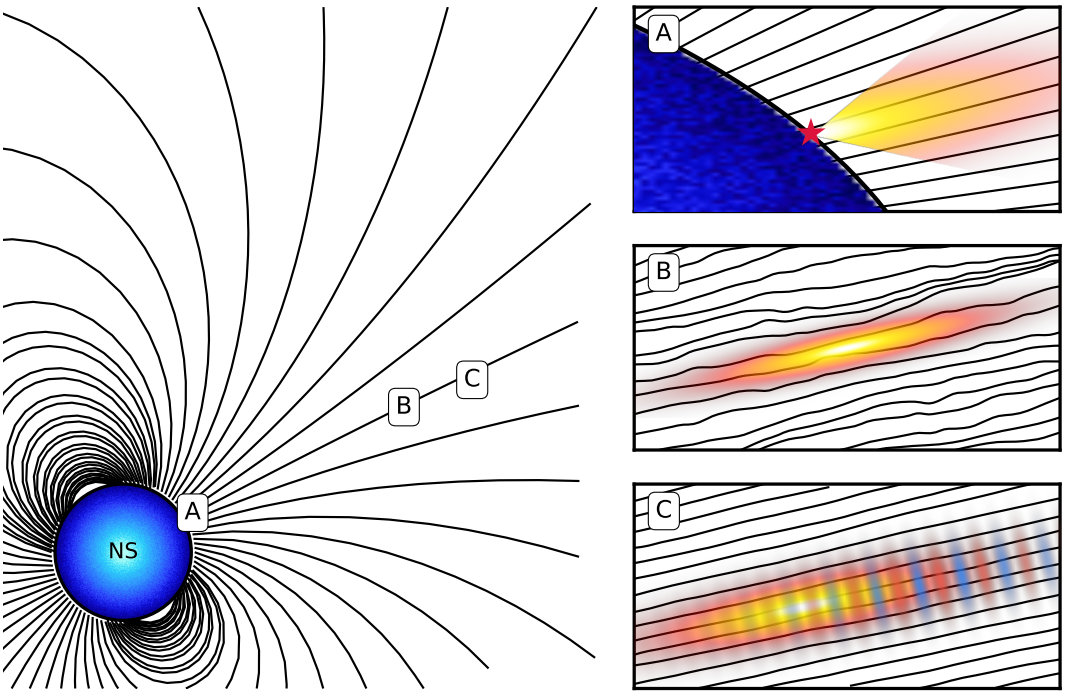

FIGURE 3.9: Illustration of the proposed mechanism for triggering the ECMI in neutron star magnetospheres. The sequence involves three key stages, labeled A, B, and C in the main diagram. In stage A, energetic plasma is injected along magnetic field lines, potentially triggered by violent events such as starquakes or magnetic reconnection near the neutron star surface (inset A). In this region, the magnetic field is so strong that synchrotron cooling dominates over other timescales. Although ring distributions and instabilities may begin to form at this stage, we do not focus on their early development here. The cooled plasma beam then propagates outward along the field line. In stage B, the beam enters a region strongly perturbed by Alfvén waves ($\epsilon \sim 10^{-4}$), leading to a balance between stochastic heating and radiative cooling. Finally, in stage C, the beam reaches a region where perturbations weaken ($\epsilon \ll 10^{-4}$), and synchrotron cooling once again dominates. This cooling drives the formation of ring momentum distributions that trigger the ECMI, resulting in coherent radiation beamed along the field-aligned direction.

its distribution becomes sharply peaked along the field direction, with negligible transverse momentum, approximated by $f = \delta(p_\perp)\delta(p_\parallel - p_{\parallel 0})$.

As the beam propagates outward into region B (within the inner region of the magnetosphere), it encounters magnetic perturbations transverse to the guiding field. These may arise from ambient Alfvén waves or be generated self-consistently via beam instabilities such as the firehose [49]. In the frame of the beam, the perturbations resemble transverse electromagnetic waves, with electric fields $\mathbf{E}'_\perp = \beta\gamma_0\delta\mathbf{B}_\perp$, where $|\delta\mathbf{B}_\perp| = \epsilon B$, with B the guiding field and $\epsilon \ll 1$ the relative perturbation strength. These fields induce stochastic heating, modeled as perpendicular momentum diffusion with diffusion coefficient

$$D = \frac{d}{dt}\left\langle p_\perp^2 \right\rangle = e^2\beta^2\gamma_0\,\delta\mathbf{B}_\perp^2\,\tau_c, \tag{3.24}$$

where τ_c is the correlation time of the perturbations, defined through the autocorrelation of the fluctuating magnetic field.

The value of τ_c is not exactly known, but it can be estimated from the local Alfvén wavelength, which sets the minimal scale over which perturbations remain coherent. The Alfvén speed in a teneous pair plasma, i.e., $\omega_{ce} \gg \omega_{pe}$ is $v_A \sim c$ [176]. The corresponding Alfvén frequency and wavelength are

$$\omega_A = \frac{v_A}{\lambda_A}, \qquad \lambda_A \sim \frac{c}{\omega_{pe}} = c\sqrt{\frac{m_e}{4\pi n e^2}}, \tag{3.25}$$

where ω_{pe} is the plasma frequency. This identifies the minimal wavelength of Alfvénic perturbations with the plasma skin depth, and the associated correlation time as

$$\tau_c \sim \frac{\lambda_A}{v_A}. \tag{3.26}$$

Near the stellar surface, at $r \sim 10^6$ cm, typical Goldreich–Julian densities are $n \sim 10^{11} - 10^{14}$ cm^{-3} and magnetic fields reach $B \sim 10^{14}$ G. Substituting into the above expressions gives Alfvén wavelengths of order a few centimeters and correlation times in the range $\tau_c \sim 0.3 - 3$ ns. Further out in the magnetosphere, at $r \sim 10^8$ cm, both n and B decrease as r^{-3}. The corresponding Alfvén wavelength then increases to tens of centimeters, with correlation lengths of tens of meters, giving correlation times $\tau_c \sim 3 - 30$ ns. These estimates are only order-of-magnitude, but they illustrate how the characteristic coherence scale of Alfvénic perturbations grows with distance from the star.

Using the results from Sec. 2.3.5, where the competition between synchrotron cooling and stochastic heating was analyzed, we now include an explicit expression for the diffusion coefficient D. This yields an estimate for the equilibrium transverse momentum spread:

$$\sigma_\perp = 3\epsilon\beta m_e c\sqrt{\omega_{\rm Cr}\tau_c\gamma_0}, \tag{3.27}$$

where $\omega_{\rm Cr} = eB_{\rm Sc}/(\alpha m_e c) \simeq 1.06 \times 10^{23}$ s^{-1} is the classical synchrotron critical frequency. Remarkably, this expression shows that the equilibrium spread depends only on the relative

perturbation strength ϵ and the correlation time τ_c, and not on the absolute value of the magnetic field. These expression scales as

$$\sigma_\perp \, [m_e c] \simeq 3 \times 10^3 \, \epsilon \, [10^{-4}] \, \sqrt{\gamma_0 \, \tau_c \, [\mathrm{ns}]}, \tag{3.28}$$

highlighting how even weak perturbations with nanosecond-scale coherence are sufficient to generate substantial transverse momentum spreads.

Eventually, the beam reaches the outer region of the magnetosphere, region C, where the perturbations weaken significantly ($\epsilon \ll 10^{-4}$) and synchrotron cooling once again dominates. The transverse momentum distribution compresses, and a narrow ring forms in momentum space. As the beam continues to propagate outward, both cooling and diffusive heating become less effective due to the decreasing magnetic field and perturbation amplitude. This leads to a progressive freezing of the distribution function: the ring no longer evolves significantly and remains imprinted in phase space. The beam continues outward until it reaches a region where the local plasma frequency becomes comparable to the cyclotron frequency, $\omega_{pe} \lesssim \omega_{ce}$, rather than deep in the underdense regime. This condition marks the point where the electron cyclotron maser becomes efficient, and the ring distribution becomes unstable. The resulting radiation is emitted in the X-mode, propagating perpendicular to the magnetic field in the beam frame. In the lab frame, the emission is relativistically beamed along the magnetic field direction and appears as GHz-frequency, circularly polarized radiation.

To illustrate the full process, we now consider a concrete example. Suppose a magnetar has radius $R_\star = 10^6$ cm, surface magnetic field $B = 10^{13}$ G, and spin period $P = 1$ s, corresponding to a light-cylinder radius $R_{\mathrm{LC}} \approx 4.8 \times 10^9$ cm. A relativistic electron-positron beam is injected from the surface with Lorentz factor $\gamma = 100$ and density $n \sim 10^9$ cm^{-3}, comparable to the local Goldreich–Julian density. Near the star, synchrotron cooling dominates and the beam rapidly loses its transverse momentum, suppressing any early instabilities.

As the beam moves outward into region B, it encounters perturbations with relative strength $\epsilon \sim 10^{-4}$ and correlation time $\tau_c \sim 1$ ns. The resulting stochastic heating leads to a transverse temperature of $p_{\mathrm{th}} \sim 10^3 \, m_e c$, sustained over the heating region. Later, in region C, the perturbations weaken to $\epsilon \sim 10^{-6}$, and synchrotron cooling once again dominates. The beam cools and compresses into a ring with width $\sigma_\perp \sim 10 \, m_e c$, after which the distribution becomes effectively frozen due to the drop in both $\delta \mathbf{B}_\perp$ and B.

The beam continues to propagate outward until it reaches a region where the local plasma frequency becomes comparable to the cyclotron frequency, $\omega_{pe} \lesssim \omega_{ce}$. For typical parameters, this condition is met when the magnetic field has decreased to $B \sim 10^3$ G, corresponding to a radial distance of $r \sim 2700 \, R_\star \sim 0.5 \, R_{\mathrm{LC}}$. At this location, the cyclotron frequency $\omega_{ce} = eB/m_e c$ matches the GHz band, and the ECMI can efficiently trigger coherent radio emission. This emission is strongly beamed along the magnetic field and appears in the observer frame as a highly polarized, GHz-frequency burst. The radiation is expected to be circularly polarized due to the Lorentz-boosted X-mode structure, consistent with the polarimetry of several observed FRBs. Finally, we can estimate that the emission will have a brightness temperature $\mathcal{O}(T_B) \sim 5 \times 10^{29}$ K,[9] based on the scaling provided by Eq. (3.23). Moreover, we

[9] For beam and B-field parameters: $\gamma_b = 100$, $\Delta p = p_R/\sqrt{3} p_{\mathrm{th}}$ ($p_R \sim 10 \, m_e c$, $p_{\mathrm{th}} \sim 3000 \, m_e c$) & $B = 1000$ G.

can estimate the ratio of energy emitted in the coherent component to the available energy for maser emission based on Eq. (3.12) we obtain that the maser will consist of $\sim$ 1% of the emitted radiation, accompanied by an incoherent burst of high frequency radiation due to the cooling. Altogether, this mechanism provides a self-consistent, first-principles explanation of FRB-like emission from neutron star magnetospheres based on kinetic processes alone.

3.6 CONCLUSION

Using the largest PIC simulations to date for tenuous, synchrotron-cooled plasmas, we have demonstrated that these plasmas can spontaneously produce coherent radiation when self-consistent electrodynamical radiative effects are considered. This radiation is driven by the onset of the ring-driven electron cyclotron maser instability. Importantly, our results reveal that this emission process can persist for substantially longer periods than previously thought, due to the interplay between the instability and synchrotron losses. This finding challenges the classical understanding of ECMI, which has traditionally been seen as resulting in only short bursts of radiation due to rapid saturation, and demonstrates the relevance of ECMI in synchrotron cooled relativistic plasmas.

Our findings suggests the synchrotron driven ECMI is relevant beyond the specific plasma conditions explored in our simulations, having also a broader applicability across various plasma and magnetic field parameters. The timescales and properties of this fundamental plasma process were estimated using an idealized electromagnetic field configuration, applicable to a plasma at rest in a constant magnetic field, or in the proper frame of an arbitrary beam. Previous work has explored the limiting conditions for ring formation in curved and inhomogeneous magnetic fields [113] and found them to remain compatible with astrophysical conditions, including the curved or inhomogeneous fields expected near astrophysical objects, such as neutron stars and black holes, as well as modest thermal spreads. Future work will incorporate these more realistic electromagnetic field configurations into self-consistent simulations, which may modify emission properties and, in extreme cases, partially or fully suppress emission. Nonetheless, preliminary estimates suggest that ring formation remains robust under such conditions [113].

This implies that this mechanism can operate in a wide range of astrophysical environments. Notably, this mechanism appears to align with several key features observed in pulsar and magnetar emissions [180], offering a potential explanation for certain characteristics of Fast Radio Bursts (FRBs) and pulsar emission [181, 182]. The observed connection between FRBs and magnetars, particularly the detection of FRBs coinciding with magnetar glitches, suggests a model where pair plasmas in a low-twist magnetar magnetosphere generate these bursts [34, 44, 45]. Our findings demonstrate that synchrotron losses combined with the ECMI can sustain coherent emission over longer durations, which may explain the observed coherence, radio emission range, linear polarisation, repetition, and similarities across diverse astronomical objects. This mechanism is a result of the unique qualitative properties of extreme plasmas. The resulting synchrotron-induced ECMI mechanism has implications that extend beyond the specific case of FRBs to a broader spectrum of astrophysical phenomena and future

astro-laboratory experiments.

CHAPTER 4

RADIATIVE COOLING AND PHASE-SPACE SHAPING IN WAKEFIELD ACCELERATION

This Chapter is adapted from: P. J. Bilbao, *et al.* to be submitted (2025).

4.1 INTRODUCTION

Plasma wakefield accelerators have demonstrated accelerating gradients on the order of 10-100 GV/m [183–186]. These gradients arise from the high densities of the background plasma and have enabled energy gains in the multi-GeV range [185, 186]. As higher-intensity lasers, tighter and higher-charge driver beams, and denser background plasmas are explored, even greater accelerating gradients are being achieved [187]. However, these gradients are not limited to the accelerating direction, they also generate strong focusing fields. Electrons displaced from the axis experience transverse betatron oscillations as they are accelerated [188]. These oscillations have been extensively studied as a source of intense radiation in both laser-driven and beam-driven schemes [164, 189, 190], and are also central to direct laser acceleration [188, 191–194].

The combination of intense electromagnetic fields and high-energy beams allows relativistic electrons undergoing betatron oscillations to radiate a significant fraction of their energy, at a rate comparable to the acceleration rate [188, 195], and radiative losses must be self-consistently incorporated into the kinetic description of the beam dynamics. Previous studies have addressed effects such as emittance damping and energy loss [196, 197].

It is well known that betatron radiation leads to energy loss and emittance damping, reducing both the beam energy and its transverse spread [196, 197]. The amplitude of each electron's oscillation depends on its initial position and transverse momentum, and the radiated power scales with the square of the oscillation amplitude. This suggests that different regions of phase space cool at different rates, as the cooling process is nonlinear with respect to betatron amplitude. In a manner similar to what has been demonstrated for synchrotron radiation in magnetized plasmas [23, 114, 198], this nonlinear cooling modifies the kinetic properties of the

beam, leading to distinct phase-space structures. However, whereas synchrotron cooling leads to momentum-space bunching in Landau levels, betatron cooling in ion-channel or blowout regimes leads to phase-space bunching, forming structured "donut" beams with both spatial and angular anisotropies. This process fundamentally alters beam dynamics and may enable coherent betatron emission from population-inverted beams.

In this chapter, we demonstrate that high-energy beams undergoing betatron emission in high-density wakefield accelerators naturally develop such bunching. We derive the timescales for this process analytically and confirm the results through fully 3D particle-in-cell simulations. The resulting "donut" beams display pitch-angle anisotropies and ring-shaped structures that are robust features of betatron-cooled dynamics in plasma accelerators.

4.1.1 Betatron cooling as an analogue of Synchrotron cooling

These structured beams not only exhibit properties relevant to advanced accelerator applications, such as positron wakefield drivers [199] or ion-channel laser concepts, but also offer a platform for laboratory astrophysics. In particular, they serve as analogues of synchrotron-cooled, magnetized astrophysical plasmas, where radiation reaction drives the formation of ring momentum distributions and triggers kinetic instabilities such as the electron cyclotron maser instability (ECMI) [114]. Whereas synchrotron cooling shapes plasmas near pulsars and black holes through strong magnetic fields, betatron cooling in laboratory setups provides a complementary mechanism driven by strong electric focusing fields.

This analogy is not coincidental, ion-channel and magnetized plasma dynamics are deeply related, as shown in the unified framework developed in [164], where both ion-channel laser and magnetized maser instabilities were described within the same theoretical structure. Remarkably, the phase-space bunching we describe, resulting from nonlinear radiative cooling, has not been observed in any plasma system to date. This makes high-density wakefield accelerators the first experimental platform capable of realizing and studying radiatively induced phase-space structuring, opening the door to controlled studies of radiation-driven dynamics in extreme plasma environments.

4.2 Analytical theory

4.2.1 Single particle dynamics

We consider the dynamics of an electron beam with Lorentz factor γ_b propagating within a plasma of background density n_0, corresponding to a plasma frequency $\omega_p = (4\pi n_0 e^2/m_e)^{1/2}$, where e is the elementary charge and m_e is the electron mass. The beam propagates in a blowout (or bubble) structure that is excited by either a beam or a laser driver [200]. The dynamics presented in this work are independent of the specific driver, making the results equally applicable to both PWFA, LWFA, and ion-channel scenarios [201, 202]. Inside the

bubble, the fields are given by [203]

$$E_r = \frac{1}{4}\frac{m_e\omega_p^2}{e}r, \tag{4.1}$$

$$B_\phi = -\frac{1}{4}\frac{m_e\omega_p^2}{e}r, \tag{4.2}$$

$$E_z = \frac{1}{2}\frac{m_e\omega_p^2}{e}\xi, \tag{4.3}$$

where r is the radial distance from the bubble axis and $\xi = z - z_0$ is the longitudinal displacement from the bubble center. The resulting Lorentz force on an electron with $v_z \simeq c$ is [203]

$$\mathbf{F}_\mathrm{L} = -e\left(\mathbf{E} + \frac{\mathbf{v}}{c}\times\mathbf{B}\right) = -\frac{1}{2}m_e\omega_p^2\Delta\mathbf{r}, \tag{4.4}$$

where $\Delta\mathbf{r} = \mathbf{r} - \mathbf{r_0}$ is the displacement from the bubble center $\mathbf{r_0}$. As a result, electrons within the bubble experience both longitudinal acceleration and transverse betatron oscillations driven by this linear restoring force.

Furthermore, particles also experience radiative losses due to the strong acceleration. To estimate radiative losses, we employ the classical description of radiation reaction. The radiative force acting on an electron with relativistic momentum is described, to first order in γ, by the Landau–Lifshitz formulation [100, 131]

$$\mathbf{F}_\mathrm{RR} = -\frac{2}{3}\frac{e\alpha}{E_\mathrm{Sc}}\frac{\gamma\mathbf{p}}{m_e c}\left[\left(\mathbf{E} + \frac{\mathbf{p}\times\mathbf{B}}{\gamma m_e c}\right)^2 - \left(\frac{\mathbf{p}\cdot\mathbf{E}}{\gamma m_e c}\right)^2\right], \tag{4.5}$$

where α is the fine-structure constant, c is the speed of light, $E_\mathrm{Sc} \simeq 1.32\times10^{18}$ V/m is the Schwinger field, and $\mathbf{E}$ and $\mathbf{B}$ are the electric and magnetic field, respectively.

This chapter formulates the theory of phase-space evolution of betatron cooled beams in the classical regime, radiative quantum effects will introduce a diffusive effect in phase-space (See Sec. 2.4.3 & App. B). Thus, the conclusions of this work are valid for both the classical regime $\chi \ll 1$ and quantum radiative regime $\chi \sim 1$, where χ is the Lorentz- and Gauge-invariant parameter $\chi = e\sqrt{-(F_{\mu\nu}p^\nu)^2}/E_\mathrm{Sc}m_e^3$ [18, 19]; $F_{\mu\nu}$ the electromagnetic tensor and p^ν the 4-momentum of the particle.

We consider relativistic beams such that $\gamma \gg 1$ and $p_\parallel \gg p_\perp$, where parallel ($\parallel$) and perpendicular ($\perp$) with respect to the direction of the beam propagation. For these beams, the radiation reaction force does not depend on the parallel electric field, and solely on the perpendicular displacement from the center of the bubble $\Delta r_\perp$. The radiation reaction force in the laboratory frame simplifies to $\mathbf{F}_\mathrm{RR} = -(2\alpha e/3m_e)\chi^2 E_\mathrm{Sc}\mathbf{v}/c$, where $\chi = m_e\omega_p^2\Delta r_\perp\gamma/2eE_\mathrm{Sc}$, scales as $\chi \simeq 0.1\, n_0\,[10^{20}\,\mathrm{cm}^{-3}]\ \Delta r_\perp\,[10\,\mu\mathrm{m}]\ E\,[10\,\mathrm{GeV}]$.

The betatron cooling rate depends in a non-linear manner on the amplitude of the betatron oscillation $\propto \Delta r_\perp^2$, akin to the energy level of the oscillating electron. This draws the parallel with synchrotron cooled plasmas, where the nonlinear cooling with respect to the Landau levels results in bunching over these levels [23, 114]. Here for betatron cooling, it will lead to bunching of the amplitude of oscillation in phase-space.

By taking into account the radiation reaction force into the equations of motion, the dynamics of a betatron damped electron are determined by

$$\frac{d\mathbf{r}}{dt} = \mathbf{p}/m_e\gamma, \tag{4.6}$$

$$\frac{d\mathbf{p}}{dt} = -\frac{m_e}{2}\omega_{p0}^2\Delta\mathbf{r} - \frac{1}{6}\frac{\alpha m_e}{ecE_{\mathrm{Sc}}}\omega_{p0}^4\gamma\Delta r_\perp^2\,\mathbf{p}. \tag{4.7}$$

Thus, the electron undergoes damped harmonic oscillations and radiates its perpendicular momentum, *i.e.* emittance damping, as well as a significant portion of its parallel momentum. Notably, there exists a position within the blowout structure where particles do not lose parallel momentum averaged for a betatron oscillation. That is at $\Delta r_\parallel = -\frac{\alpha}{3ecE_{\mathrm{Sc}}}\omega_{p0}^2\gamma_\parallel p_\parallel \left\langle \Delta r_\perp^2 \right\rangle_\beta$. This means that particles lagging behind the center of the bubble by more than $-\Delta r_\parallel$ will on average throughout a betatron period gain parallel momentum, *i.e.* be accelerated, whereas particles ahead of that point will radiate more than they are accelerated. Making them oscillate around that equilibrium point. Moreover, future high density and high energy wakefield accelerators will necessitate a large enough bubble structure, such that the bubble radius $r_b > \Delta r_\parallel$, for efficient acceleration. Regarding the perpendicular betatron cooling which we will concern ourselves with, we will assume for the sake of analytical work that the beams are positioned around that equilibrium point such that $\dot{p}_\parallel \sim 0$.

Therefore, the dynamics of an electron undergoing betatron cooling will be described by the following non-linear differential equation

$$\frac{d^2\Delta r_\perp}{dt^2} = -\omega_\beta^2\Delta r_\perp - \frac{1}{6}\frac{\alpha m_e\omega_{p0}^4\gamma_\parallel(t)}{ecE_{\mathrm{Sc}}}\frac{d\Delta r_\perp}{dt}\Delta r_\perp^2, \tag{4.8}$$

where $\omega_\beta = \omega_{p0}/\sqrt{2\gamma_\parallel}$ is the betatron frequency. While $\gamma_\parallel$ evolves over time, this primarily leads to a gradual rescaling of the dynamics in time. In fact, continued acceleration enhances betatron cooling by increasing the radiation rate, and thus promotes faster bunching. The general (and still exact) solution to the transverse displacement equation with radiation reaction is

$$\Delta r_\perp(t) = A(t)\sin\left(\omega_\beta t + \phi_0(t)\right), \tag{4.9}$$

where $A(t)$ and $\phi_0(t)$ vary with time. While obtaining the exact forms of $A(t)$ and $\phi_0(t)$ is generally not feasible, the Krylov-Bogoliubov (KB) averaging method can be employed when the radiative cooling rate is smaller than the betatron frequency [204].

This condition holds for oscillation amplitudes satisfying $A < \sqrt{3\sqrt{2}\frac{ecE_{\mathrm{Sc}}}{\alpha m_e}}\gamma_\parallel^{-3/4}\omega_{p0}^{-3/2}$, a regime relevant to laboratory beam-plasma experiments. For example, in a plasma with density $10^{19}\,\mathrm{cm}^{-3}$, a 10 GeV beam must have a transverse size exceeding 50 μm for the approximation to break down. Within the approximation, however, the KB averaging method provides an effective approach to determine phase-space trajectories averaged over a betatron period [204].

The solution to Eq. (4.8) assuming a small amplitude of oscillation[1]

$$\dot{A}(t) = -\frac{\frac{1}{6}\frac{\alpha m_e \omega_{p0}^4 \gamma(t)}{ecE_{\rm Sc}}}{2\pi}\int_0^{2\pi} A^3 \sin^2\theta\cos^2\theta d\theta = -\frac{1}{48}\frac{\alpha m_e \omega_{p0}^4 \gamma(t)}{ecE_{\rm Sc}}A^3 \tag{4.10}$$

$$\dot{\phi}(t) = -\frac{\frac{1}{6}\frac{\alpha m_e \omega_{p0}^4 \gamma(t)}{ecE_{\rm Sc}}}{2\pi}\int_0^{2\pi} A^2 \sin^3\theta\ \cos\theta d\theta = 0. \tag{4.11}$$

$$A(t) = \frac{A_0}{\sqrt{1 + A_0^2\tau}} \tag{4.12}$$

and $\dot{\phi}_0(t) = 0$, where A_0 is the initial amplitude of oscillation and $\tau = \frac{1}{48}\frac{\alpha m_e}{E_{\rm Sc}ce}\omega_{p0}^4\int_0^t \gamma_\parallel(t')dt'$ is a normalized time.[2] As noticed before, the change in $\gamma_\parallel$ leads to a rescaling of the dynamics. For the analytical treatment that follows, we focus on the limit where the beam is near the equilibrium point $-\Delta r_\parallel$ and the longitudinal momentum is approximately constant, $\dot{p}_\parallel \sim 0$. This allows us to simplify $\tau = \frac{1}{48}\frac{\alpha m_e}{E_{\rm Sc}ce}\omega_{p0}^4\gamma_\parallel t$ and obtain analytical solutions that still capture the essential features of the bunching dynamics. Interestingly, a particle with initial $A_0 \to \infty$ will follow $A_\infty = \tau^{-1/2}$. This trajectory corresponds to the upper bound of phase-space, thus, all physically relevant trajectories remain below it. This demonstrates that the whole phase-space volume is constricted into a region between $\frac{2p_\perp^2}{\gamma_\parallel m_e^2\omega_{p0}^2} + r_\perp^2 < A_\infty^2$, a key feature that will modify the dynamics of beams in blowout structures. In fact, the boundary at $A = A_\infty$ is a limit-cycle orbit that all physically relevant trajectories are attracted towards [205]. This boundary is the betatron equivalent of the momentum-space boundary p_∞ discussed for synchrotron-cooled plasmas in Sec. (2).

Interstingly, there exist a second regime for betatron cooling, one where initially the radiative force is much larger than the Lorentz force, *i.e.*, the betatron oscillation amplitude is larger than $A > \sqrt{3\sqrt{2}\frac{ecE_{\rm Sc}}{\alpha m_e}}\gamma_\parallel^{-3/4}\omega_{p0}^{-3/2}$. This results in an initial overdamping of the betatron oscillations.

This overdamping rapidly stops as the amplitude is suddenly reduced within less than a betatron oscillation and then it eneters the slow damping regime. This is seen in Fig. 4.1, where both regimes are shown. Top demonstrates the trajectories of slow cooling particles. The bottom panel of Fig. 4.1 shows how particles with large amplitudes all converge and collapse to regions of lower amplitude betatron oscillations.

This regime rapidly establishes phase-space bunches. In contrast, the slow cooling regime, more relevant for current laboratory platforms, requires several betatron oscillations for bunching to develop. Accessing the fast cooling regime would, for example, require that in a plasma with density $1 \times 10^{19}\,\mathrm{cm}^{-3}$, a 10 GeV beam have a transverse size exceeding 50 μm, so that the radiation reaction force exceeds the perpendicular Lorentz force and bunching occurs in less than a single betatron period. Since such high-density bubbles are not yet achievable experimentally, we focus here on the slow cooling regime, which is accessible to current accelerators.

[1] Full derivation and explanation of this result is shown in App. G.1.

[2] We note that A_0 has units of length and τ has units of inverse squared length.

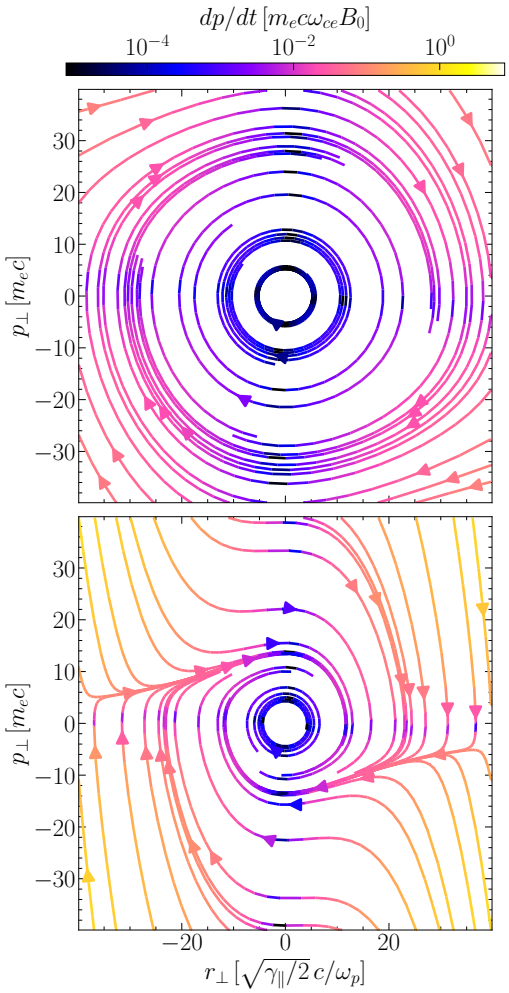

FIGURE 4.1: Phase-space stream plots, obtained from numerically integrating Eqs. (4.6 & 4.7) (for constant $\gamma_\parallel$) demonstrate the bunching in phase-space as a result of betatron cooling and showcase the different regions of phase-space where the particles undergo either underdamped osicllations or overdamped oscillations. The darker regions of the streamlines, show regions where no radiation occurs, *i.e.*, the center of the oscillation where there is no focusing **E** field and the highest point in $r_\perp$ as at that point the perpendicular velocity is 0. The top plot shows the slow cooling regime, where radiative losses are small compared with the cooling. The bottom plot shows streamlines where the radiative losses are strong and rapidly collapse the phase-space if the amplitude of oscillation is too large. This occurs when particles are falling back into the center of oscillation, under strong fields the particles radiate more than they gain as they fall in the potential and collapse the phase-space.

However, future higher-energy and higher-density wakefield accelerators will enter the fast cooling regime, where sudden betatron cooling becomes important, this will be explored in future work.

4.2.2 Dynamics of the distribution function of wakefield accelerated beams

Therefore, from the characteristic equation (Vlasov $df/dt = 0$) we obtain the advection equation in phase space

$$\frac{df}{dt} = \frac{\partial f}{\partial t} + \nabla_r \cdot \left(\frac{\mathbf{p}}{\gamma m_e c} f \right) + \nabla_p \cdot \left[\left(\mathbf{F}_L + \mathbf{F}_{RR} \right) f \right] = 0. \tag{4.13}$$

To effectively describe the kinetic properties of these beams, we introduce the distribution function $f(A, \phi)$ in the phase-space coordinates A and ϕ, akin to action-angle coordinates [205]. As explained before, we assumed that $\dot{\gamma}_{\parallel} \sim 0$ Doing this, allows us to recast the kinetic equation

$$\frac{\partial f}{\partial t} + \frac{1}{A}\frac{\partial}{\partial A}\left[A \frac{dA(t)}{dt} f \right] + \frac{\omega_\beta}{A}\frac{\partial f}{\partial \phi} = 0, \tag{4.14}$$

where A & ϕ corresponds to the amplitude and angle coordinate, whereas $A(t)$ corresponds to the single particle trajectory ($dA(t)/dt = -A^3/2$), and recall $\tau = \frac{\pi}{2}\frac{\alpha m_e}{E_{\mathrm{Sc}} c e}\omega_{p0}^4 \gamma_{\parallel} t$. Equation (4.14) is a result of combining the Lorentz force, that provides advection in ϕ coordinate and the radiation reaction which changes the amplitude of oscillation. A general solution exists for Eq. (4.14) via the method of characteristics[3]

$$f(A, \phi, t) = \frac{f_0\left(\frac{A}{\sqrt{1 - A^2\tau}}, \phi - \frac{t\omega_\beta}{A} \right)}{\left(1 - A^2\tau\right)^2}. \tag{4.15}$$

The close similarity of the form of Eq. (4.15) with the equation of a synchrotron cooled plasma (See [23, 113]) demonstrates the key insight that betatron cooled beams will also develop an energy population inversion in a similar manner to synchrotron cooled plasmas. Where synchrotron cooled plasmas develop a Landau population inversion *i.e.* $\partial f/\partial p_\perp > 0$, betatron cooled beams develop a population inversion in the amplitude of betatron oscillations, *i.e.* a region that satisfies $\partial f/\partial A > 0$. This is demonstrated for both an emittance matched beam and non-emittance matched beam in Fig. 4.2, where both develop bunching in phase-space, radially, *i.e.* in amplitude. The non-emittance matched shows how the bunching is less efficient but clear signatures are observed both spatially and in momentum.

The close similarity of the form of Eq. (4.15) with the equation of a synchrotron cooled plasma (See [23, 113]) demonstrates the key insight that betatron cooled beams will also develop an energy population inversion in a similar manner to synchrotron cooled plasmas. Where synchrotron cooled plasmas develop a Landau population inversion, betatron cooled beams develop a population inversion in the amplitude of betatron oscillations, *i.e.* a region that satisfies $\partial f/\partial A > 0$.

[3] Details of this calculation are shown in App. G.2.

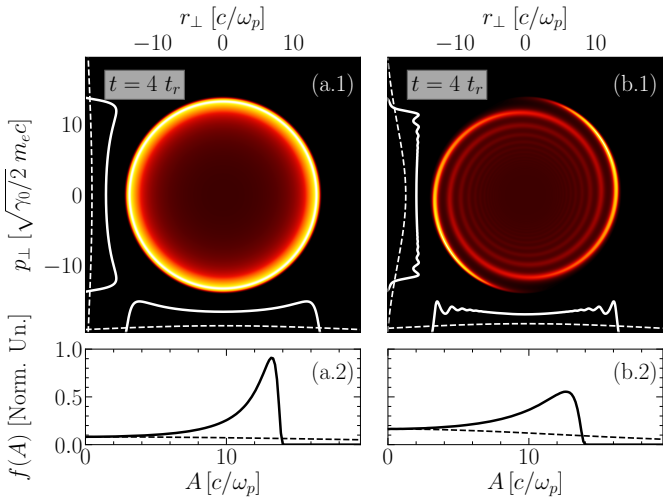

FIGURE 4.2: Analytical results at $t = 3t_r$ show how an initially smooth distribution evolves into a bunched structure in amplitude space due to radiative cooling. Column (a) shows an emittance-matched initial distribution, which preserves symmetry and develops a sharp ring in phase space. Column (b) shows a non-emittance-matched case, where asymmetries emerge. Top row (1): full transverse phase-space distribution $f(r_\perp, p_\perp)$; white lines correspond to the perpendicular momentum (vertical) and radial (horizontal) distributions. Dashed lines show the initial state at $t = 0$. Bottom row (2): distribution of the oscillation amplitude $f(A)$ (where A is proportional to the maximum $r_\perp$ a particle undergoes, *i.e.*, $A^2 = 2(p_\perp/m_e\omega_p)^2/\gamma_0 + r_\perp^2$), highlighting the emergence of a narrow peak (solid) compared to the initial distribution (dashed)

Equation (4.15) describes the general evolution of any given beam in the blowout structure. We focus our study on the population inversion process for Gaussian beam profiles, such that $f \propto e^{-A^2/2\sigma_\perp^2}$, where $\sigma_\perp$ is the transverse waist of the electron beam. A ring-beam is characterized by a spatial ring radius $r_r(t)$ at which the distribution satisfies $\partial_A f|_{A=r_r(t)} = 0$. This occurs when the amplitude evolution matches

$$r_r(\tau) = \frac{\sqrt{4\tau\sigma_\perp^2 - 1}}{2\tau\sigma_\perp}. \tag{4.16}$$

From Eq. (4.16), it is evident that the square root becomes real only after a finite time. This defines the onset of the bunching process: bunching becomes physically observable only when $\tau > (4\sigma_\perp^2)^{-1}$. Below this threshold, the distribution remains monotonic and no population inversion can occur. After this point, the ring radius increases with time until it reaches a maximum. This maximum occurs when the derivative of $r_r(\tau)$ with respect to τ vanishes:

$$\left.\frac{dr_r(\tau)}{d\tau}\right|_{\tau=\tau_r} = 0. \tag{4.17}$$

Solving this condition gives $\tau_r = (2\sigma_\perp^2)^{-1}$, the time at which the ring reaches its largest spatial extent. Evaluating Eq. (4.16) at this point yields

$$r_r(\tau_r) = \sigma_\perp, \tag{4.18}$$

indicating that the ring structure becomes comparable to the beam waist. Therefore, we define τ_r as the characteristic timescale at which the ring-beam is clearly formed and most distinguishable from the background.

$$t_r = \frac{E_{\mathrm{Sc}} ce}{\alpha \pi m_e} \frac{1}{\gamma_{\parallel} \sigma_{\perp}^2 \omega_{p0}^4}, \tag{4.19}$$

that is a propagation length $L_r \ [15\,\mathrm{mm}] \simeq n_0^{-2} \ [10^{19}\,\mathrm{cm}^{-3}] \ E^{-1} \ [10\,\mathrm{GeV}] \ \sigma_{\perp}^{-2} \ [5\,\mu\mathrm{m}]$, which is realizable in current and future laboratory facilities such as LCLS. We note that the bunching begins from $t = 0$, and that signatures of the bunching process are present throught the propagation timescale. t_r provides a scaling to understand the timescale of this process and when the rings will be clearly observable.

4.3 PARTICLE-IN-CELL SIMULATIONS

We use two complementary simulation approaches: (i) an *idealised parameter-scan configuration* designed to isolate the essential physics of ring formation and test theoretical scalings Sec. 4.3.1, and (ii) a realistic beam-plasma configuration based on FACET-II parameters Sec. 4.3.2, demonstrating the effect in an experimentally relevant regime. Both are modeled with the OSIRIS particle-in-cell code [81] including classical and quantum radiative losses [28, 91], with simulation parameters given in Appendix A.3.

4.3.1 IDEALISED SETUPS: PARAMETER SCANS

In the idealised case, a high-density plasma is driven by a tailored driver beam that produces a clean blowout structure, allowing direct comparison with our theoretical model. This setup isolates the essential physics behind ring formation and enables parameter scans to test the model predictions. A witness beam propagates through the blowout cavity, which is large enough to sustain acceleration and capture radiation-induced dynamics. We vary the beam energy, waist, and background plasma density.

The simulation results, shown in Fig. 4.3, exhibit excellent agreement with the theoretical prediction for the evolution of the distribution function [Eq. (4.15)] and the ring-formation radius [Eq. (4.16)]. In particular, the characteristic formation time t_r extracted from the simulations follows the scaling derived in Eq. (4.19), decreasing with increasing plasma density and beam waist, and with beam energy. These parameter scans therefore confirm the central theoretical conclusion: betatron-cooled beams undergo a population inversion in oscillation amplitude that leads to ring-beam formation on a timescale $t_r \propto n^{-2} \sigma_{\perp}^{-2} E^{-1}$, in quantitative agreement with the analytical model.

Having established these scalings in an idealised blowout configuration, we now turn to more realistic laboratory conditions. In such setups, the driver beam itself depletes as it excites the plasma cavity, and the bubble size can become comparable to the beam dimensions, modifying the ideal assumptions of the theory. Nonetheless, the confirmed scaling laws predict

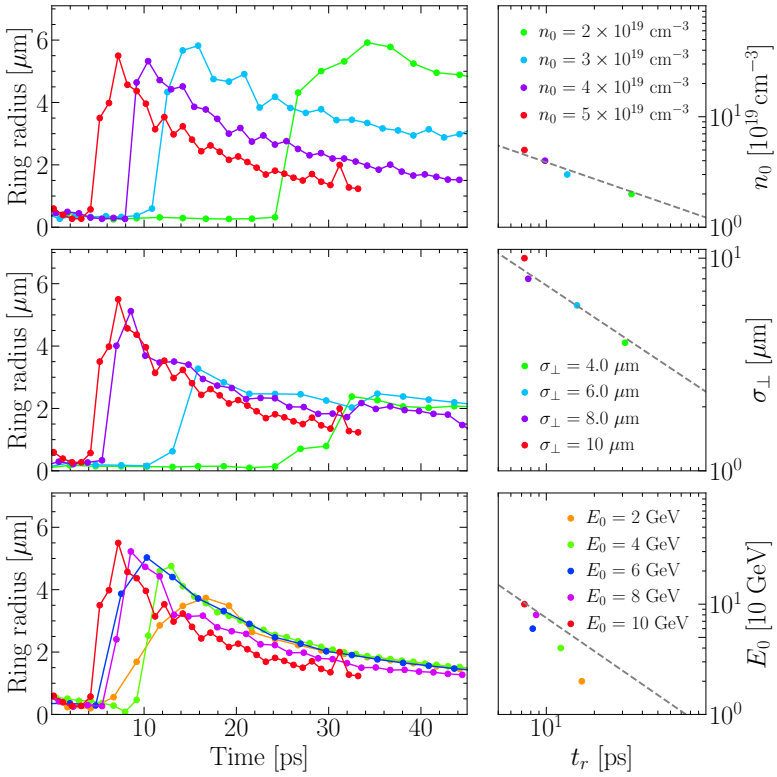

FIGURE 4.3: Parameter scan showing the formation and evolution of ring structures in PIC simulations of ion-channel beams undergoing betatron cooling. Each row corresponds to a scan over a single parameter: initial beam energy (top), background plasma density (middle), and initial transverse width (bottom). The left column shows the temporal evolution of the ring radius for each case. The right column displays the ring formation time as a function of the scanned parameter in log-log scale, allowing direct comparison with theoretical scalings. The observed trends confirm the model predictions: $t_r \propto n^{-2}$ (top), $t_r \propto \sigma_\perp^{-2}$ (middle), and $t_r \propto E^{-1}$ (bottom), as indicated by the overlaid reference slopes.

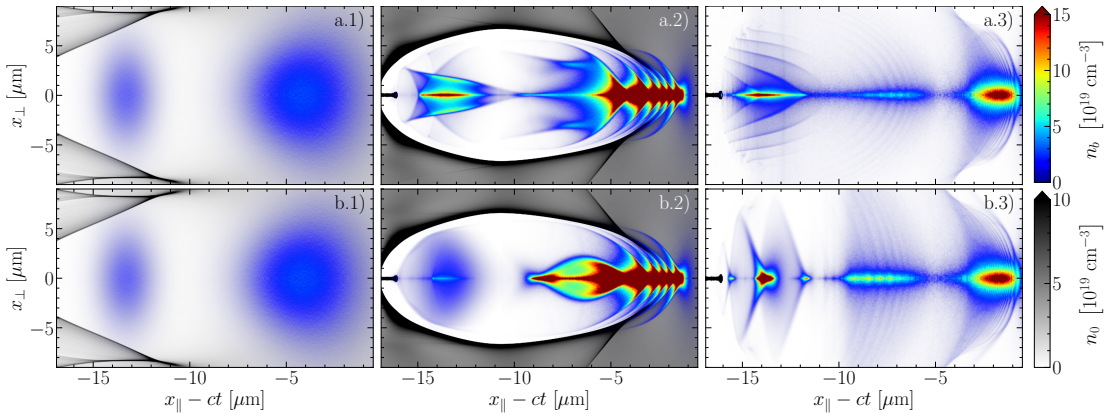

FIGURE 4.4: PIC simulations demonstrate that FACET-II, like electron beams propagating through high-density plasma develop a ring-shaped, phase-bunched profile when radiation reaction is included. A dense driver generates a blowout cavity, while a trailing witness beam undergoes acceleration. Row a includes radiation reaction; row b does not. Columns correspond to different stages of propagation: upramp (1), inside the plasma (2), and downramp (3). With radiation reaction (a), the witness beam exhibits transverse bunching due to betatron cooling. Without it (b), the beam remains featureless.

that ring formation should remain observable within experimental parameters, motivating simulations with realistic driver, witness beam configurations.

4.3.2 REALISTIC LABORATORY SETUP: DRIVER AND WITNESS BEAM CONFIGURATION

We further study this process with the help of Quasi-3D PIC simulations based on realistic configurations based on beam parameters compatible with FACET-II [65, 187]. The driver beam had a charge of 0.3 nC, a waist size of 5 μm, and a length of 2 μm. The witness beam had a total charge of approximately 0.1 nC, a longitudinal FWHM of $\sim$ 1 μm, and the same radial width as the driver. They both have a a normalized emittance of 300 mm mrad. They propagate through a plasma with a peak density of 5×10^{19} cm^{-3}, configured with a 1 mm up-ramp, a 5 mm flat-top region, and a 1 mm down-ramp. Further details of the simulation parameters are shown in the App. A.3.

Figure 4.4 shows two simulation results with identical initial conditions: the top row includes radiation reaction, while the bottom does not. Initially, the driver beam produces a blowout in the upramp region [Fig. 4.4.a.1], undergoing self-focusing and forming a stable ion cavity that persists through the flat-top region. The trailing witness beam, injected near the back of the cavity, experiences strong transverse oscillations due to the ion channel field. In the presence of radiation reaction [Fig. 4.4.a.2], these betatron oscillations induce rapid synchrotron cooling, which acts nonlinearly on the transverse momentum. As predicted by the theoretical analysis in Sec. 4.2, this cooling compresses phase-space volume and leads to the formation of a narrow ring in $p_\perp$, resulting in a sharply defined annular structure in the transverse spatial density. The radius of this ring is consistent with the amplitude derived from

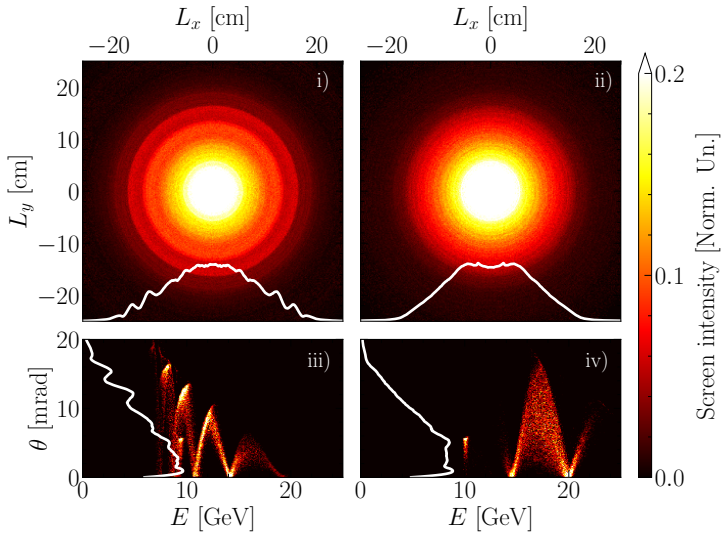

FIGURE 4.5: Synthetic diagnostics of the simulated screen (100 cm downstream from the plasma) and spectrometer analysis demonstrate that phase-space bunching features are observable under experimental conditions. (i) Screen image with radiation reaction enabled shows visible ring structures. (ii) Screen image without radiation reaction shows no ring formation. (iii) Divergence versus energy with radiation reaction demonstrates clear correlation with ring features. (iv) Divergence versus energy without radiation reaction shows no such structure.

Eq. (4.16), and its formation occurs over a propagation distance $ct_r \simeq 0.6\,\mathrm{mm}$, in good agreement with the estimate from Eq. (4.19). Indeed, ring features begin to appear in the simulations at this distance into the flat-top region. In contrast, when radiation reaction is not included [Fig. 4.4.b.2], the same witness beam exhibits no sign of transverse structuring and retains a broad, featureless profile throughout propagation, confirming that the observed ring is a direct consequence of betatron cooling.

To determine whether these ring features, resulting from phase-space bunching, can be detected experimentally, we simulate the beam as it exits the down-ramp region. As the beam exits the plasma, several bunches are observed in the witness beam Fig. 4.4.a.3 as modulations of the radial beam profile, as predicted by Eq. (4.15) for a non-emittance matched beam and as shown in Fig. 4.2 where the radial profile also shows multiple radial bunches. For comparison, we performed identical simulations with radiation reaction disabled Fig. 4.4.b. In this case, no bunching or ring formation is observed throughout the beam's propagation, confirming that the witness profile results from betatron radiation losses.

The radial bunches are a result of the phase-space bunched structured due to betatron cooling, therefore, this structures also have a momentum component as seen in Fig. 4.2, which should exhibit signatures as a pitch-angle anisotropies, which could be easily observable with diagnostic studying the propagation of such beams. We thus, simulate a downstream luminescent screen placed 100 cm from the plasma exit. As shown in Fig. 4.5.i, the ring structures

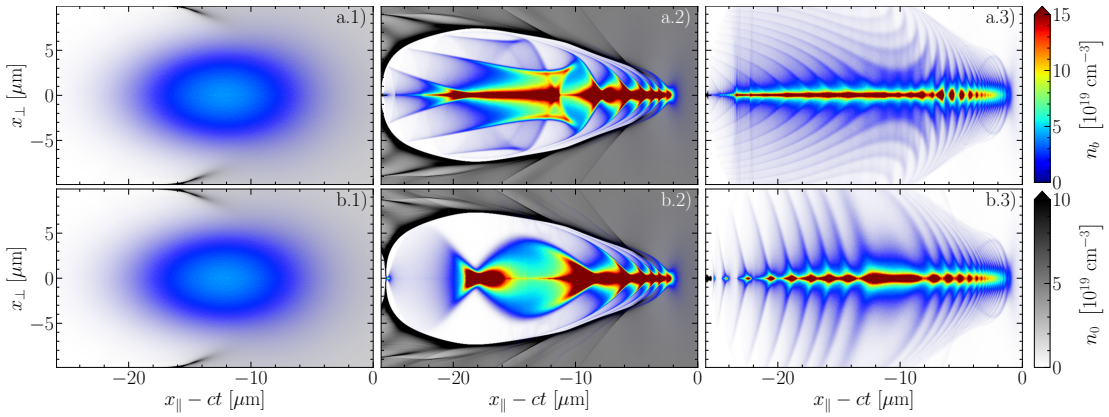

FIGURE 4.6: PIC simulations showing the formation of ring-shaped, phase-bunched profiles in a single FACET-II, like electron beam propagating through high-density plasma. The front of the beam drives the blowout cavity, while the rear undergoes betatron cooling. Row (a) includes radiation reaction; row (b) does not. Columns correspond to different propagation stages: upramp (1), uniform plasma (2), and downramp (3). Ring formation occurs only when radiation reaction is included.

(now due to bunching in propagation angle) are clearly visible on the screen.[4] Furthermore, because of their different positions in the accelerating structure and their energy loss due to betatron losses, the rings also differ in energy. This implies that spectrometers could also detect these features. By estimating the divergence as a function of energy Fig. 4.5.iii, we observe that each ring has a distinct emittance. Notably, the highest-emittance ring corresponds to the lowest-energy structure, which has undergone the most cooling. In contrast, lower-emittance structures, which radiated less, are able to accelerate beyond the initial 10 GeV beam energy.

Comparing the same analysis without radiation reaction Fig.(4.5.ii & 4.5.iv), we find no observable ring structures on the screen and a no signature of bunching in the synthetic spectrometer. This absence further confirms that the observed phase-space structures are a result of betatron cooling.

4.3.3 REALISTIC LABORATORY SETUP: SINGLE DRIVER BEAM CONFIGURATION

Interestingly, the rear of the driver beam also exhibits similar ring-shaped beams when radiation reaction is included. A comparison of the density profiles in Fig. 4.4.a shows clear signatures of bunching in both the witness and the tail of the driver. This suggests that a simpler experimental configuration is possible: a single electron beam could drive the blowout with its rear experiencing betatron cooling and forming rings. Motivated by this, we explored a simpler configuration where a single beam simultaneously drives the blowout structure and experiences betatron cooling.

We conducted a Quasi-3D PIC simulation using a single electron beam with parameters consistent with FACET-II: total charge of 3 nC, energy of 10 GeV, normalized emittance of

[4] Details on how the screen was synthetically reconstructed from PIC simulation data are outlined in App. A.3.1.

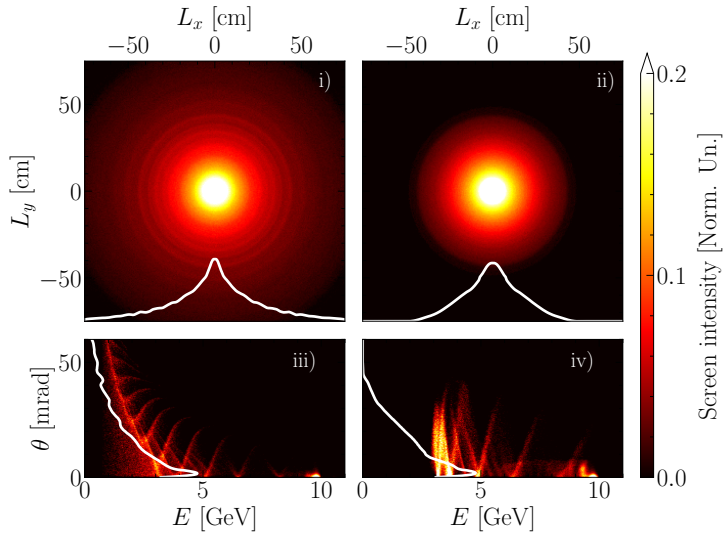

FIGURE 4.7: Synthetic diagnostics for the single-beam configuration. (i) Downstream screen (100 cm from plasma exit) with radiation reaction shows visible ring structures. (ii) Without radiation reaction, the screen shows no ring formation. (iii) Divergence versus energy plot with radiation reaction demonstrates distinct ring-associated features. (iv) Without radiation reaction, the divergence spectrum is smooth and unstructured.

300 mm mrad, waist of 5 μm, and a length of 10 μm. The beam propagates through a plasma with peak density 5×10^{19} cm^{-3}. These parameters match those used in the two-beam scenario to allow direct comparison.

The simulation results, shown in Fig. 4.6, confirm that the beam drives a blowout cavity in the upramp region (a.1), while the rear of the beam develops a clear ring-shaped structure as it propagates through the uniform-density plasma (a.2). These features persist as the beam exits into the downramp region (a.3), confirming the robustness of the phase-space bunching. In contrast, when radiation reaction is disabled (row b), the beam remains smooth and featureless throughout propagation.

To assess the experimental observability of these structures, we simulated downstream diagnostics analogous to those presented in the main text. A synthetic screen placed 100 cm downstream from the plasma exit (Fig.4.7.i) clearly shows ring-shaped intensity patterns in the presence of radiation reaction. The corresponding energy-resolved divergence plot (Fig.4.7.iii) shows that each ring possesses distinct energy and emittance characteristics, again confirming the presence of phase-space bunching. In contrast, simulations without radiation reaction produce neither ring structures nor energy-dependent features, see Figs. (4.7.ii & 4.7.iv).

These results demonstrate that ring-shaped, phase-structured beams can emerge naturally in single-beam setups and are robust against diagnostic and propagation effects. This provides a more accessible experimental configuration, requiring only a single high-energy beam to observe the effects of betatron cooling.

4.4 COHERENT BETATRON EMISSION VIA ION-CHANNEL LASER AMPLIFICATION

Since ring-like beams can drive the Ion Channel Laser (ICL) [126, 189], we explore the possibility that betatron-cooled, phase-space, bunched beams may emit coherent betatron radiation, offering an additional pathway for their detection. For the ICL to operate, two key criteria must be satisfied: (i) the relative energy spread must remain below the threshold $\Delta\gamma/\gamma < 2\rho/3$, where ρ is the Pierce parameter, estimated as $\rho = (I/2I_A\gamma)^{1/3}$, with I the beam current and $I_A = 17\,\mathrm{kA}$ the Alfvén current [126]; and (ii) the spread in the dimensionless wiggler parameter K must satisfy $\Delta K/K < \rho' = 2^{-2/3}\rho$. The Pierce parameter ρ quantifies the beam, wave coupling strength, determining both the gain length and the tolerable energy and amplitude spreads for coherent radiation; it depends on the beam current, energy, and focusing strength of the channel.

Condition (i) is naturally satisfied over time: betatron cooling causes the oscillation amplitudes of different electrons to converge, reducing the energy spread and promoting synchronous emission. To assess condition (ii), K characterizes the average transverse oscillation amplitude in units of the betatron wavelength, i.e., $K \equiv \langle A\rangle\sqrt{\gamma/2}\,\omega_p/c$. As the beam cools, the amplitude distribution sharpens around a ring radius $r_r(\tau)$, given by Eq. (4.16).[5] We approximate

$$\frac{K}{\Delta K} \approx \frac{1}{2}\frac{r_r(\tau)}{\tau^{-1/2} - r_r(\tau)}, \tag{4.20}$$

which slightly overestimates $\Delta K/K$, yielding a condition for when the beam satisfies the wiggler coherence threshold:

$$\tau_c > \frac{(2+\rho')^2}{4\rho'\,\sigma_\perp^2(4+\rho')}. \tag{4.21}$$

For representative parameters (such as those possible at FACET-II [65, 187]): plasma density $n_0 = 5\times10^{19}\,\mathrm{cm}^{-3}$, beam charge $q_b \sim 1\,\mathrm{nC}$, bunch length $\sigma_z \sim 5\,\mu\mathrm{m}$, transverse size $\sigma_\perp = 5\,\mu\mathrm{m}$, and energy $E \sim 10\,\mathrm{GeV}$, we estimate $\rho \sim 0.05$. This gives a critical propagation length $c\tau_c \simeq 0.7\,\mathrm{mm}$, beyond which $\Delta K/K$ continues to decrease. The gain length in this regime is [126]

$$L_G = \frac{2}{\sqrt{3}\rho}\frac{c}{\omega_\beta} \simeq 20\frac{c}{\omega_\beta} \simeq 3\,\mathrm{mm}. \tag{4.22}$$

These results suggest that betatron-cooled beams can satisfy the conditions for coherent amplification of betatron radiation within experimentally accessible lengths. Continued cooling of the beam also reduces K. If the beam initially satisfies $K > 1$, it will eventually transition from the wiggler regime ($K > 1$) to the undulator regime ($K < 1$). In the undulator limit, radiation becomes concentrated on-axis and dominated by the fundamental frequency, in contrast to the broad angular and harmonic spread of the wiggler regime. The transition occurs when

[5] Furhter details on the approximations for the fulfillment of these condtions and exact equations for their evolution are shown in App. G.3.

$r_r(\tau_u) = \sqrt{2/\gamma}\, c/\omega_p$, yielding the (beam-independent) time:

$$t_{\mathrm{u}} = \frac{eE_{\mathrm{Sc}}}{\pi\alpha m_e c\omega_p^2}. \tag{4.23}$$

The corresponding propagation length is

$$ct_{\mathrm{u}}\,[320\,\mathrm{cm}] \simeq \left(n_e\,[10^{21}\,\mathrm{cm}^{-3}]\right)^{-1}, \tag{4.24}$$

indicating that access to the undulator regime may require a staged setup: initial ring formation at high density, followed by propagation in a lower-density plasma to allow $K < 1$ to be reached.

These findings highlight the potential of betatron-cooled beams not only for studying nonlinear radiation reaction dynamics but also for generating coherent betatron emission through self-structured phase-space distributions. The fact that such coherence conditions are naturally met by the beams shaped via radiation losses suggests a new path for producing high-brightness, narrow-band radiation sources and for exploring analogues of astrophysical maser processes in the laboratory.

4.5 CONLUSION

Here we have shown that in the presence of strong radiative losses, betatron cooling induces a population inversion in the amplitude of betatron oscillations, leading to phase-space bunching and the formation of ring-shaped, or "donut" structures in both position and momentum space. This effect arises from the nonlinear nature of radiation reaction in focusing fields and, to the best of our knowledge, represents a fundamentally new kinetic phenomenon in beam, plasma systems. Our analytical model, validated by Q3D particle-in-cell simulations, demonstrates that this structuring occurs on experimentally accessible timescales using currently available high-energy beams and plasma densities.

We also conjecture that experiments operating in high-density ($\gtrsim 10^{20}$ cm^{-3}) and high-energy beams ($\gtrsim 10$ GeV) will access the fast cooling regime, where strong radiative losses collapse momentum space within a single betatron oscillation, further enhancing bunching. This will be further studied in future work.

While this Chapter has focused on PWFA, the underlying mechanism is not limited to this configuration. In fact, LWFA platforms offer a high degree of control over the injection process, which could be harnessed to tailor the initial phase-space properties of injected beams in high-density plasmas [206, 207]. This tunability makes LWFA an attractive pathway for experimentally realizing and controlling betatron-cooled phase-space structures. Moreover, the emergence of petawatt-class laser systems [208, 209] opens the door to driving wakefields in near-solid-density plasmas, such as ion channels, where radiative losses become extreme. These next-generation facilities will make it straightforward to access regimes of strong betatron cooling, enabling precise studies of phase-space dynamics and coherent radiation processes under extreme conditions.

Finally, the betatron-cooled process described in this chapter serves as analogous process to synchrotron-cooled plasmas in astrophysical environments, which can drive maser instabilities via Landau population inversion [23, 113, 114], these findings establish betatron cooling as a laboratory pathway to tailoring beam phase space and potentially enabling coherent betatron emission via ion-channel, driven instabilities [126, 164, 189] and may allow to study analogous systems to coherent radiation emission in astrophysical plasmas.

CHAPTER 5

FIREBALL BEAMS: PAIR PLASMA INSTABILITIES

Portions of this Chapter are adapted from: C. D. Arrowsmith, P. Simon, P. J. Bilbao *et al.*, "Laboratory realization of relativistic pair-plasma beams." Nat. Comms. 15.1 (2024): 5029.; C. D. Arrowsmith, F. Miniati, P. J. Bilbao *et al.*, Under consideration in Proceedings of the National Academy of Science (2025) & future publications from the Fireball collaboration.

5.1 INTRODUCTION

Electron–positron plasmas are ubiquitous in high-energy astrophysical phenomena. From the magnetospheres of neutron stars and black holes to the collimated jets launched from active galactic nuclei [32, 156, 157], these plasmas are not only relativistic and collisionless, but often dominated by radiation and quantum electrodynamic (QED) effects. In particular, astrophysical jets, such as those from blazars, may propagate over cosmological distances through the intergalactic medium, where inverse-Compton and pair-production cascades shape their observable spectra [210, 211]. These phenomena offer a platform for investigating the collective dynamics of relativistic pair plasmas.

One of the most generic configurations arising in these environments is that of a relativistic pair beam streaming through an ambient plasma [212]. Such beams can form as part of electromagnetic cascades triggered by high-energy gamma rays [157] or as structured components within larger-scale jets [212]. In all these cases, the interaction between the fast-moving beam and the background plasma can give rise to a range of kinetic instabilities, seeded by anisotropies in the momentum distribution or by relative streaming between populations [213, 214]. These instabilities act on microscopic length- and timescales, and their dynamics are governed by the kinetic properties of the system: energy spread, beam divergence, density ratio, and dimensionality.

Laboratory *Fireball beams* are designed to replicate this astrophysical scenario under controlled conditions. Ideally, they consist of quasi-neutral, ultra-relativistic electron–positron

beams propagating through an ambient electron–ion plasma, reproducing the essential ingredients of pair-beam interactions in pulsar winds, gamma-ray burst afterglows, and relativistic jets [66]. In the CERN experiment used in this work, a 440 GeV/c SPS proton bunch strikes a composite graphite–tantalum target, producing a hadronic cascade whose secondary photons undergo pair production in the converter, yielding a high-flux $e^{\pm}$ beam with near-equal charge densities [72]. This beam, with Lorentz factors $\gamma \gg 1$ and transverse dimensions much larger than the plasma skin depth, is injected into a background plasma to study beam-plasma instabilities on kinetic scales. A complementary approach proposed at SLAC's FACET-II facility uses magnetic chicanes to overlap separate ultra-relativistic e^- and e^+ bunches in space and time [215]. Both platforms bridge laboratory and astrophysical regimes, enabling direct study of kinetic instabilities relevant to extreme environments.

However, the importance of beam–plasma instabilities extends further than any one astrophysical scenario. The fundamental mechanism, free energy stored in anisotropic distribution functions being converted into electromagnetic fields, is expected to operate wherever relativistic particle beams propagate through an ambient plasma. In this sense, the presence (or absence) of kinetic instabilities such as the current filamentation or oblique mode is not just a technical detail, but a diagnostic of the underlying plasma state. If such instabilities are observed, they can rapidly mediate energy transfer, generate magnetic fields, and shape the radiation emitted by the system [216]. If they are suppressed, it implies that the plasma possesses structure, such as finite transverse temperature, beam divergence, or spatial inhomogeneity, that fundamentally alters its kinetic response [217]. Understanding the conditions under which these instabilities are active or quenched is essential to building a predictive theory of extreme plasma dynamics.

Despite their fundamental importance, kinetic beam–plasma instabilities in relativistic pair plasmas are still not fully understood in realistic conditions. While linear theory captures the essential features of instability growth in idealized scenarios, such as cold, monoenergetic, and collimated beams, these assumptions rarely hold in practice. Finite temperature, energy spread, beam divergence, and partial pair purity all impact the evolution of instabilities, yet their combined effect remains difficult to treat analytically [213, 214, 218]. As a result, there is a clear need to study how these instabilities behave under experimentally relevant conditions, where deviations from ideality play a critical role in determining their growth and nonlinear saturation.

5.1.1 Current Filamentation instability in pair-plasmas

In this chapter, we focus on the study of beam-plasma instabilities where the beam is composed of electron-positron pairs and the background plasma consists of electron-ion components. This configuration is analogous to the interaction of a relativistic jet, such as those emitted by blazars, propagating through the intergalactic medium.

In astrophysical contexts, the exact form of the particle distribution functions is often unknown due to the impossibility of in-situ measurements. For example, it is possible to send probes and directly characterize the properties of the solar wind or magnetospheric plasmas around solar system bodies [12]. Such luxuries are not possible in the case of high-energy as-

trophysical phenomena. Consequently, significant assumptions must be made regarding the distribution functions of such plasmas, and hence the role and nature of plasma instabilities in these environments remain somewhat uncertain.

A key instability in this context is the so-called current filamentation instability (CFI). This arises when a beam propagates through a plasma and self-consistently generates transverse magnetic fields which leads to the filamentation of currents within the plasma [217], in the nonlinear stage this will lead to separation of the species for electron-positron plasmas [73].

The outcomes of plasma instabilities can differ dramatically depending on the assumed properties of the plasma. For instance, we highlight the role of the divergence of the beam, as the dynamics of a collimated beam differs significantly from that of a divergent or warm beam [217]. A useful estimate involves the typical filament scale $\sigma \sim k_{\max}^{-1}$, where the cutoff of the growth rate occurs, *i.e.*, the minimum scale of the filaments formed. Each filament carries a current of magnitude $I = en_b\sigma^2 c\beta$, where n_b is the density of the beam and $c\beta$ is the spatial velocity, producing a pinching force $F_{max} \simeq 2e^2 n_b \sigma$. In the presence of a perpendicular temperature, there is a counteracting thermal pressure force given by $F_p \simeq k_B T_\perp / \sigma$. For the instability to grow, the pinching force must overcome the thermal pressure, *i.e.*, $F_{\max} > F_p$. This leads to the scaling $k_{max} \propto T_\perp^{-1/2} \propto p_{\perp th}^{-1}$. This simple estimate helps illustrate how transverse temperature can suppress CFI. As increasing the divergence of the beam $p_{\perp th}$ increases the minimum size of the filaments and their growth rate [217]. The implications are far-reaching: one can support or rule out certain astrophysical mechanisms based on the plasma parameters chosen, which in turn determines which instabilities are excited.

A more formal treatment starts from the Vlasov equation, Eq. (1.4), which can be linearized along with Maxwell's equations to derive the dielectric tensor for an arbitrary distribution function [169, 219]. Still, the linear regime poses significant challenges, especially for realistic, non-trivial forms of f_s, for which the exact solution of the dispersion relation might not have an analytical expression

In the following, we consider the transverse electromagnetic mode associated with the current filamentation instability. The coordinate system is chosen such that the beam propagates along the z-axis and the wavevector $\mathbf{k}$ is along the x-axis (transverse to the beam). In this configuration, the dominant magnetic perturbation δB_y points out of the x–z plane. By Faradays law, this implies an inductive electric field δE_z aligned with the beam propagation direction, as well as a smaller transverse electric component δE_x arising from charge-separation effects. The δB_y component is responsible for the transverse deflection of beam particles according to their longitudinal velocity, driving the formation of current filaments. This is the same field geometry as in the classical Weibel mode: a purely transverse wave ($\mathbf{k} \perp \mathbf{v}_b$) with magnetic perturbations perpendicular to both $\mathbf{k}$ and $\mathbf{v}_b$, and an inductive electric field parallel to the beam.

With this configuration in mind, the dispersion relation for waves propagating along x-perpendicular to the bulk momentum along z, can be written, normalized to the background plasma frequency ω_{pe}, as [169, 219]

$$0 = \Lambda_{zz} = -c^2k^2 + \omega^2\varepsilon_{zz}, \tag{5.1}$$

by normalizing the plasma frquency $\omega_{pe} = 1$, speed of light $c = 1$, and the electron mass $m = 1$, the permittiviy tensor is given by

$$\varepsilon_{ij} = \delta_{ij} + \sum_s \frac{4\pi e_s^2}{\omega} \int \frac{d\mathbf{p}}{\omega - \mathbf{k}\cdot\mathbf{p}/\gamma} \frac{\mathbf{p}}{\gamma} \frac{\partial f_{0s}}{\partial p_l} \left[\left(1 - \frac{\mathbf{k}\cdot\mathbf{p}/\gamma}{\omega} \right) \delta_{lj} + \frac{k_l \mathbf{p}}{\gamma\omega} \right], \tag{5.2}$$

which expanded out, including contributions from the plasma electrons and beam electron positrons,[1] is

$$0 = \omega^2 - k^2 - \left\langle \gamma_0^{-1} \right\rangle + \left\langle p_{z0}^2/\gamma_0^3 \right\rangle + \alpha \left\langle \gamma^{-1} \right\rangle + \alpha \left\langle p_z^2/\gamma^3 \right\rangle + \alpha \int d^3\mathbf{p} \frac{p_z^2}{\gamma^2} \frac{k \frac{\partial f_0(\mathbf{p})}{\partial p_x}}{\omega - k p_x/\gamma}, \tag{5.3}$$

where the brackets $\langle Q \rangle$ denote averages over the corresponding distribution function,

$$\langle Q \rangle = \int d^3\mathbf{p}\, f(\mathbf{p})\, Q, \tag{5.4}$$

and all frequencies are normalized to the background plasma frequency ω_{pe}. Here ω is the wave frequency, k is the wave wavenumber, γ (γ_0) is the Lorentz factor of the beam (background plasma) particles, $\alpha = n_b/n_0$ pair-beam to background plasma density, p_i is the momentum in the i-th direction, and the brackets represent the averaged quantity. We consider a background electron-ion plasma whose temperature is negligible, i.e., $p_z = 0$ and $p_x = 0$, and focus on beam distribution functions relevant to electron-positron beams, the full distribution function is outline in Appendix H.1, notably the beam distribution function can be decomposed into $f(p_x, p_z) = f_z(p_z) f_x(p_x, p_z)$, along the propagation direction $f_z(p_z)$ and a thermal spread in the perpendicular direction ($f_x \propto e^{-p_x^2/(2p_{th}^2(p_z))}$), where the thermal spread $p_{th} = \Delta\theta\, p_z$. Approximating $\gamma \simeq p_z$ then one can write the dispersion relation in the following form

$$0 = \omega^2 - k^2 - 1 - \alpha \left[1 - \frac{1}{\Delta\theta^2} + \frac{\omega}{k\sqrt{2}\Delta\theta^3} Z\left(\frac{\omega}{k\sqrt{2}\Delta\theta} \right) \right] \left\langle \gamma^{-1} \right\rangle + \alpha \left\langle p_z^2/\gamma^3 \right\rangle. \tag{5.5}$$

where $Z(x)$ is the plasma dispersion function [220].

Analytical expressions for the plasma dispersion function Z exist in asymptotic regimes: as a Maclaurin series for small arguments and as a Laurent series for large arguments. These expansions are fundamental in deriving solutions such as Landau damping [5]. In the limit of small transverse thermal spread $\Delta\theta$, one can approximate the Z function as $Z\left(\omega/(k\sqrt{2}\Delta\theta)\right) \simeq i\sqrt{\pi}\exp\left(-\omega^2/(2k^2\Delta\theta^2)\right)$, which holds when $\omega/(\sqrt{2}k) \gg \Delta\theta$ [220]. Even with this approximation, however, the dispersion relation Eq. (5.5) remains transcendental, and must therefore be solved numerically.

Numerical solutions confirm that increasing the transverse thermal spread suppresses the growth of the instability, as shown in Fig. 5.1. These results validate the intuitive scaling derived earlier: as the transverse temperature increases, the associated thermal pressure counteracts the magnetic pinching force, reducing the instability's growth rate. Specifically, the cutoff

[1] We note the system is charge and current neutral, the beam electron positron components neutralize each other and for the background plasma we have considered mobile electron on a neutralising background of high mass to charge ratio ions, such that their dynamical contribution can be neglected in ε_{ij}

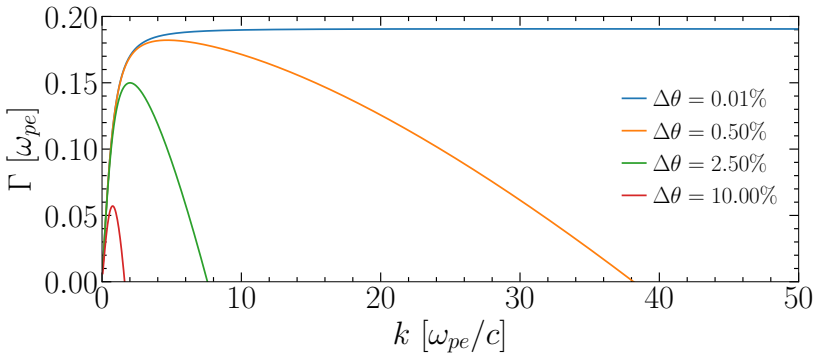

FIGURE 5.1: Theoretical growth rate for an electron-positron Fireball beam, with realistic momentum distribution function (see Appendix H.1) propagating in an electron-ion plasma, obtained from the linear dispersion relation Eq. (5.5), demonstrates how the divergence of the beam $\Delta\theta$ affects the growth rate of the different modes. The beam has density ratio $\alpha = 1$ and varying divergence $\Delta\theta$, while maintining the longitudinal momentum distrbution constant.

wavenumber shifts to lower values of k, corresponding to wider filaments, consistent with the estimate $k_{\max} \propto T_{\perp}^{-1/2}$.

This agreement between a simple force-balance argument and the full kinetic solution highlights the underlying physical mechanism. It demonstrates that the beam's kinetic properties, particularly perpendicular thermal pressure, play a critical role in shaping both the growth rate and dominant scale of the instability. Cold-beam models, while useful as a first approximation, can significantly mischaracterize energy transfer efficiency, magnetic field generation, and particle isotropization in realistic astrophysical conditions [221]. This underscores the importance of employing a more careful and quantitative kinetic treatment when modeling beam-plasma instabilities in such environments.

In this context, the possibility of generating relativistic electron-positron beams in the laboratory opens an exciting opportunity: for the first time, it becomes feasible to directly measure the onset and growth of these instabilities under controlled conditions, and to test how sensitive they are to beam properties such as divergence, temperature, and density. In an electron-positron beam, the underlying driver, a momentum-space anisotropy between the beam and the background, is the same as in the pure electron case. However, a pure electron beam is not current neutral, so the background plasma responds by establishing a return current. This return current alters the subsequent dynamics substantially,[2] and in addition, charged beams can drive wakefields and modify the instability through the electrostatic potential they generate.

In contrast, the absence of a large net current in a quasi-neutral $e^{\pm}$ beam means that no strong return current is established in the background plasma. This suppresses large-scale

[2]In astrophysical environments, this distinction can be critical: pair plasmas in pulsar winds or AGN jets may be close to current neutral, whereas cosmic-ray electron beams streaming through the interstellar medium are not, leading to different instability hierarchies.

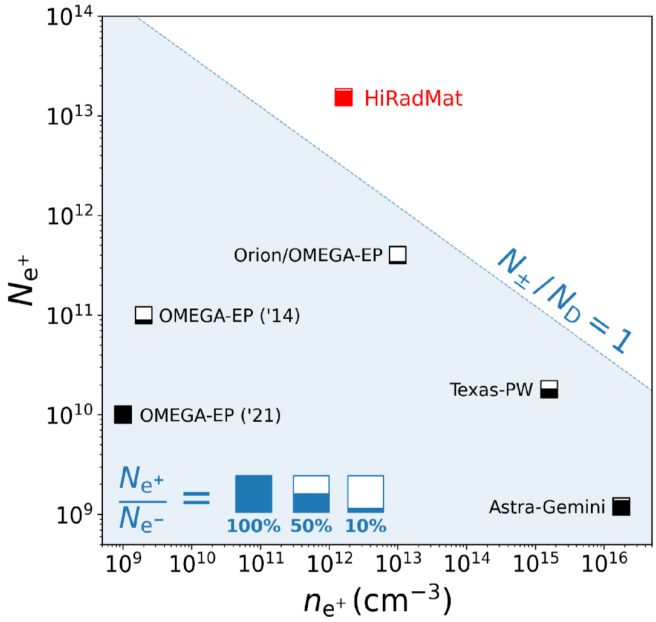

FIGURE 5.2: Comparison of laboratory-produced high-density pair beams (adapted from Ref. [72, 75]): Peak pair number and density from the Fireball-I experiment at CERN's HiRadMat facility (red square) are shown alongside results from previous high-power laser experiments (black squares): Orion/OMEGA-EP, Texas-PW, Astra-Gemini, and OMEGA-EP (2014 and 2021). Each marker is labelled by facility, with the fill fraction indicating the positron-to-electron ratio. The blue-shaded region corresponds to the boundary demarking more than one pair per Debye sphere.

electrostatic fields and makes the instability more purely magnetic in character, while also changing the seeding: in perfectly neutral beams, the Weibel/CFI grows from noise-level fluctuations, whereas in non-neutral beams, the return current can provide a finite initial B-field that accelerates onset.[3]

5.1.2 FIREBALL EXPERIMENT: STUDYING BEAM-PLASMA INSTABILITIES AT CERN

This breakthrough would not have been possible without recent experimental advances. Experiments at the HiRadMat facility at CERN have successfully produced the first laboratory-generated electron-positron pair-plasma beam, characterized by transverse and longitudinal sizes exceeding the relevant plasma length scales, namely the skin depth and the Debye length [72]. A summary of the experimental parameters and how they compare with previous laser-based efforts is shown in Fig. 5.2.

[3]Because a neutral $e^{\pm}$ beam is itself a plasma, it can in principle sustain collective instabilities even without a background plasma, provided it has sufficient internal anisotropy. This self-interaction channel is absent in single-species beams. Preliminary simulations of Fireball beams indicate that such self-driven instabilities can indeed occur even in vacuum, although these results are still at an early stage.

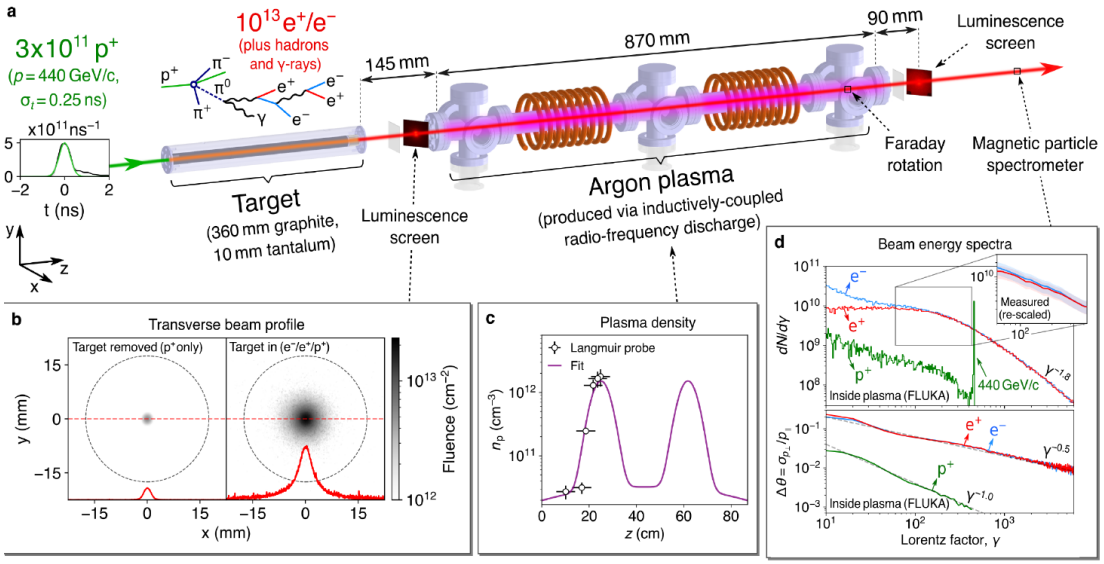

FIGURE 5.3: Experimental setup (adapted from Ref. [75, 77]): (a) An electron-positron pair beam, produced by irradiating a graphite-tantalum target with 440 GeV/c protons (temporal profile shown in the inset), propagates through a meter-long argon plasma generated by an RF discharge. (b) The transverse beam profile is measured upstream of the plasma using luminescence screens and digital cameras. (c) The plasma density is diagnosed using probes and optical spectroscopy.[5] Filamentation due to the beam-plasma instability is measured with a downstream luminescence screen, and magnetic-field growth is inferred from Faraday rotation. (d) Electron and positron energy spectra are measured using a magnetic spectrometer, corrected for the collection geometry.

The key feature of this new regime is that the beams are sufficiently dense and extended to support collective plasma behavior. In particular, the beam occupies a volume that spans multiple skin depths and Debye lengths, and contains more than one pair per Debye sphere, ensuring it behaves close to a collisionless plasma. Under these conditions, the onset of collective modes, including beam-plasma instabilities analogous to those expected in astrophysical environments, becomes possible.[4]

For the parameters measured in Fireball-I [72], the beam full-width-half-maximum dimensions are $\ell_{\parallel} \simeq 17.7$ cm and $\ell_{\perp} \simeq 0.40$ cm, with a peak pair density $n_{\pm} \simeq 1.6 \times 10^{12}$ cm^{-3} and a bulk Lorentz factor $\Gamma_{\rm bulk} \simeq 8$. In the co-moving frame, the transverse and longitudinal temperature parameters are $\Theta_{\perp} \simeq 3.5$ and $\Theta_{\parallel} \simeq 6.5$, giving an effective $\Theta \simeq 5.0 \pm 1.5$. This yields a collisionless skin depth $\lambda_s^{\rm c.f.} \simeq 0.10$ cm and a Debye screening length $\lambda_D^{\rm c.f.} \simeq 0.20$ cm. The beam thus spans ~ 40 skin depths in length and ~ 20 Debye lengths transversely in the co-moving frame [72]. The number of pairs per Debye sphere, $N_D^{\rm c.f.} \simeq 7 \times 10^{12}$, and per skin-depth volume, $N_s^{\rm c.f.} \simeq 10^{12}$, are both orders of magnitude above unity, confirming that the beam is deep in the collective regime. Based on this analysis Fig. 5.2 demonstrates the num-

[4]The closeness to an idealized plasma is key to scale provide a lenght and time independance scale to the Vlasov system, if a collisional term is present it fixes the scales of the system.

ber, yield, and beam neutrality of the $e^{\pm}$ pairs. These are compared against results from previous experiments at high-power laser facilities. It is clear that the presented scheme achieves pair yields and densities in a quasi-neutral beam that will not be attainable at laser facilities without increases in laser energy by several orders of magnitude. Given that $(N_{\pm}/N_D) \gtrsim 1$, $(N_{\pm}/N_s) \gtrsim 1$, and N_D, $N_s \gg 1$ in the co-moving frame, it becomes possible for the first time to perform laboratory studies of the collective plasma behavior of relativistic electron-positron pair plasmas.

This breakthrough was achieved using the 440 GeV proton beam from the Super Proton Synchrotron, which delivered approximately 3×10^{11} protons[6] onto a high-Z particle converter composed of carbon and tantalum as seen on the left of Fig. 5.3. Through electromagnetic cascade and pair-production processes, the resulting particle shower yielded a total of 1.5×10^{13} electron-positron pairs, representing the highest positron yield achieved in a laboratory to date [72, 75]. The resulting beam exhibits relativistic energies and pair quasi-symmetry, and enters a parameter regime where laboratory-scaled analogues of astrophysical, collisionless plasma processes become experimentally accessible.

For this reason, one of the objectives of the Fireball-I experiment was to produce an electron-positron pair plasma and to propagate it through a background plasma of comparable density in order to see the onset of the beam-plasma instabilities often invoked in astrophysical models. In order to design an experimental platform and to interpret the outcome of experimental results of pair-plasma beams, it is necessary to employ kinetic theory and to employ models and simulations that correspond one-to-one to the experimental parameters.

5.2 PARTICLE-IN-CELL SIMULATIONS

The Fireball-I experiment is part of a large, international collaboration involving several institutions across Europe, including our team at IST. Our contribution focused on the theoretical and numerical modeling of beam-plasma instabilities, helping to design and interpret the experiments. In particular, we performed large-scale particle-in-cell simulations aimed at reproducing the key features of the experiments and testing the expected instability growth rates under realistic beam and plasma conditions.

We performed full 3D simulations with as close as possible to initial conditions to the experimental conditions. The initial conditions were estimated via FLUKA simulations, performed by the team in Oxford, these provided the initial conditions of the Fireball beam that would be initialized in our simulation setup. The initialisation of these beams necessitates a careful initialisation in momentum space, this is described in Appendix H.2 alongside the momentum properties of the beams in Appendix H.

5.2.1 ONE-TO-ONE EXPERIMENTAL SIMULATIONS

Our first set of 3D simulations (see parameters in Appendix A.4.1) was carried out after a thorough convergence study in 2D3V (see Appendix A.4.2). These simulations showcase the

[6]The beam delivered an approximate energy of 7 KJ, or around 2 grams of TNT.

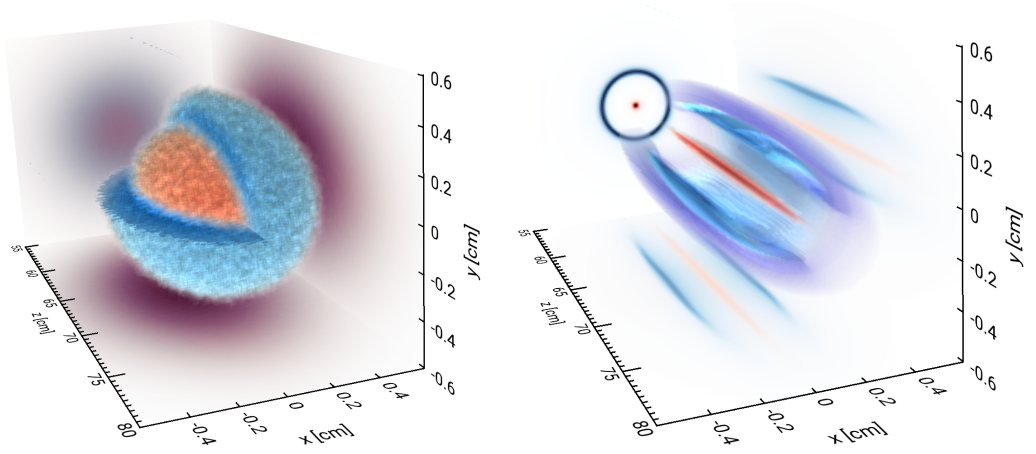

FIGURE 5.4: 3D PIC simulations demonstrate the importance of beam divergence in determining the onset of beam-plasma instabilities. The plots show volume renderings of positron density (orange) and electron density (blue). Left: a divergent beam produces diffuse, overlapping electron and positron distributions, with no clear filamentation, electron density is cut open to show the interior positron structure. Right: a collimated beam develops a distinct positron filament surrounded by a thin electron filament, a clear signature of an instability.

critical role of beam emittance in enabling or suppressing instability growth. As shown in Fig. 5.4, the realistic beam configuration, represented by the left panel, displays no clear signs of filamentation, whereas the collimated beam on the right develops a pronounced filamentary structure, consistent with the onset of the current filamentation instability (CFI). This highlights how transverse momentum spread, or beam divergence, acts to stabilize the system and inhibit the growth of instabilities, as discussed in Sec. 5.1.1.

We initially expected that beam-plasma instabilities would efficiently transfer energy from the beam into electromagnetic fields. For the experimental case, however, the instability is significantly suppressed. Only weak magnetic amplification is observed, with a growth rate of $\Gamma \sim 0.2$ ns^{-1}. In contrast, the idealized collimated case exhibits a much stronger initial growth rate of $\Gamma \sim 2.1$ ns^{-1} (Fig. 5.5).

While the linear growth rates of the current filamentation instability can, in principle, be estimated from analytic theory, existing models rely on idealized assumptions, such as monoenergetic or waterbag energy distributions [217], perfectly neutral and current-neutral beams, and spatially homogeneous conditions, that do not reflect the measured Fireball beam parameters. In our case, the full experimental energy distribution is neither monoenergetic nor waterbag-like, and the beam is close but not fully quasi-neutral, with a residual proton component whose influence is difficult to capture analytically, and as we will see has an important effect on the seeding of the instability in Sec. 5.2.2. Moreover, theory alone cannot determine whether growth in the experimental regime proceeds into the nonlinear stage within the available plasma length, especially when divergence, density gradients, and finite beam size are important. The 3D simulations presented here incorporate all measured beam properties, the

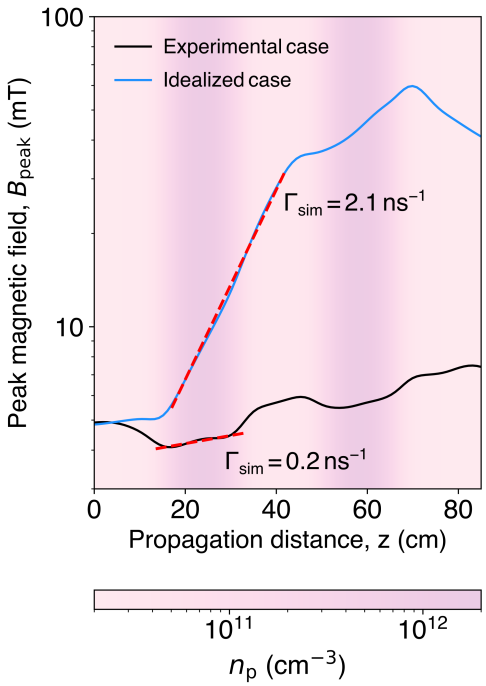

FIGURE 5.5: Peak magnetic field as a function of propagation distance, obtained from PIC simulations. The degree of field amplification depends strongly on the divergence of the beam. Shading corresponds to the local background plasma density.

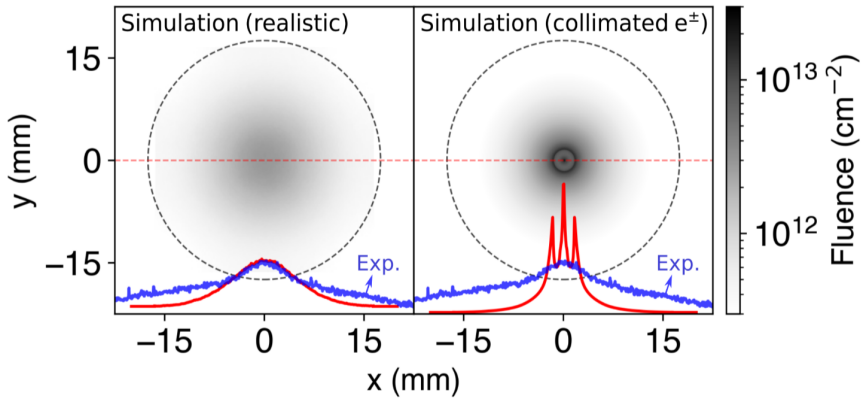

FIGURE 5.6: PIC simulations reproduce the experimental measurements from the Fireball-I luminescence screen. Shown are synthetic transverse beam profiles at the screen location for two cases: (i) the 'experimental' divergent beam (left), and (ii) the 'idealized' collimated beam (right), as defined in Fig. 5.4. The grey dashed circle marks the edge of the plasma column. Red lineouts (simulations) are compared with the experimental data (blue), showing good agreement in the divergent case and highlighting the absence of filamentation under realistic beam conditions.

realistic plasma profile, and the proton fraction, allowing us to assess the actual onset and saturation behavior under experimental conditions. Beyond their predictive role, these simulations also serve as a diagnostic complement: the limited set of experimental measurements (perpendicular imaging before and after the plasma plates and a single Faraday probe) cannot resolve the full spatiotemporal evolution of the beam-plasma system. The simulations therefore fill in the gaps, enabling both interpretation of existing diagnostics and guidance for future measurements.

A direct comparison with the Fireball-I experimental data was carried out by Charles Arrowsmith, who also led the design and execution of the experiment. For further details, see Ref. [75]. The PIC simulations performed in this thesis closely match the experimental configuration and reproduce its key diagnostic results: no evidence of filamentation was observed in the downstream luminescence screen, and no significant magnetic field amplification was measured. Additionally, no signal above noise level was observed in the Faraday rotation diagnostic. This implies that the magnetic fields remained below the probe's sensitivity, which was estimated to be $\langle B \rangle < 5$ mT. The magnetic field calculated in the simulation, corresponding to a virtual probe placed at the same location, yields an average of $\langle B \rangle \simeq 1.7$ mT, consistent with the experimental non-detection [75].

5.2.2 QUASI-CHARGE-NEUTRAL BEAM DYNAMICS

The simulation results of the idealized case, shown in the right panel of Fig. 5.4, demonstrated some unexpected but physically interesting dynamics. Our simulations did not produce multiple filaments, often observed in PIC simulations studying CFI in symmetric pair plasmas [73], instead we observed the formation of a single positron filament, surrounded by a cylin-

drically symmetric distribution of electrons. This stark difference suggests that other effects are at play during the experiment.

This behavior can be traced back to the composition of the beam. Our setup begins with a beam that is not exactly charge neutral. First, the positron content is slightly reduced due to reabsorption in the converter target, meaning the peak electron density n_- is approximately 1.21 the positron density n_+. Second, a fraction of the initial 440 GeV proton beam remains and propagates downstream with the pair beam, with density $n_p = 0.5n_-$. As a result, the simulations include a small but non-negligible component of the original proton beam and still a small imbalance in the electron-positron density. While pure electron-beam filamentation has been extensively studied [73, 74, 215, 221, 222], the dynamics in the intermediate regime, neither fully charge neutral nor purely electron, remains relatively unexplored [215, 223].[7] In particular, it is unclear how instabilities behave in a plasma that includes multiple species and lacks full current neutrality. The interplay between beam-driven instabilities and large-scale background fields generated by charge imbalance is still an open question.

We suggest that the residual electromagnetic field of the proton beam can provide a seed magnetic structure that the filamentation instability grows from. These seed fields arise from the initial current imbalance and may influence which modes are preferentially amplified by the current filamentation instability.

An estimate of the initial azimuthal magnetic field and its spectral content, based on Gaussian fits to the beam profiles obtained from FLUKA simulations, is presented in Appendix H.3. This calculation shows that the seed field peaks at wavelengths of $\sim$2-3 mm, consistent with the observed filament spacing in the collimated simulation. Comparison with the theoretical growth rate confirms that modes seeded at this scale are within the range of maximum instability, supporting the idea that beam charge imbalance can help determine the dominant filament structure, see full details in Appendix H.3.

QUASI-CHARGE-NEUTRAL BEAM DYNAMICS: ROLE OF THE PROTON COMPONENT

We performed a series of 2D PIC simulations to investigate how quasi-neutrality and the presence of a residual proton beam influence the development of beam-plasma instabilities in the Fireball-I configuration.

Figure 5.7 summarizes the results. The top row shows fully QN cases with equal numbers of electrons and positrons and no proton beam. The bottom row includes the proton component and an electron excess, matching experimental conditions. In the QN case, the collimated beam exhibits clear current filaments typical of the CFI, while no instability signatures are seen for the divergent beam or for the case without plasma. When protons are included, the results reproduce the trends of the 3D simulations in the main text: collimated beams develop strong structure, while divergent beams show reduced growth. The no-plasma case confirms that structure formation is a beam-plasma effect rather than a self-modulation in vacuum.

[7] Even a small departure from perfect charge or current neutrality can substantially influence the instability's onset and evolution, as will become clear in the discussion below. Understanding what instability is being probed is key to be able to correctly scale the findings to astrophysical objects.

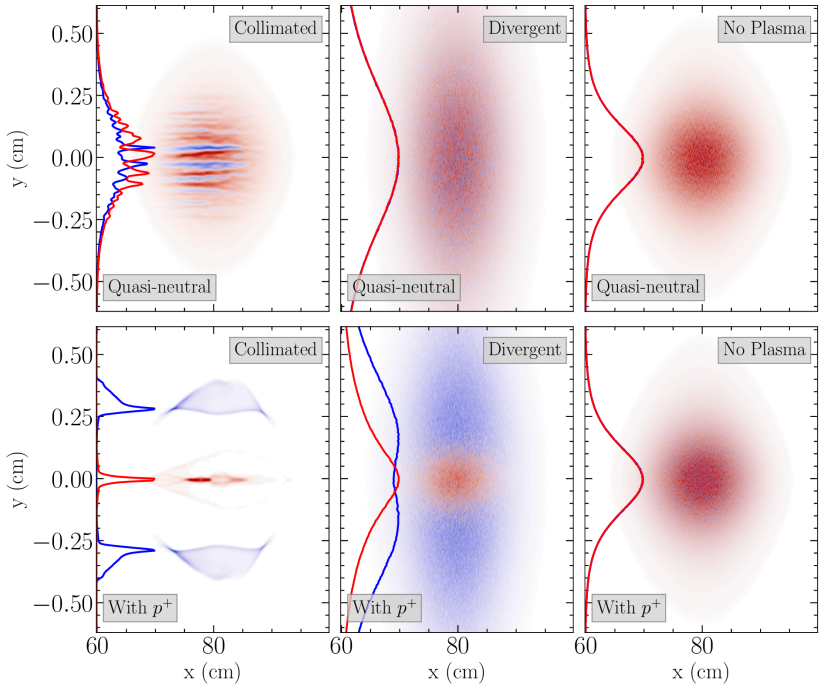

FIGURE 5.7: 2D PIC simulations comparing quasi-neutral (QN, top row) and imbalanced beams with a residual proton component (bottom row) in the Fireball-I configuration. Columns show: (1) collimated beam, (2) divergent beam with FLUKA-estimated divergence, and (3) beam in vacuum without background plasma. Snapshots are taken near the Faraday probe location. In the QN case, clear CFI filaments appear only for the collimated beam. With protons included, collimated beams reproduce the 3D simulation trends, while the no-plasma case confirms that structure formation is a beam-plasma effect.

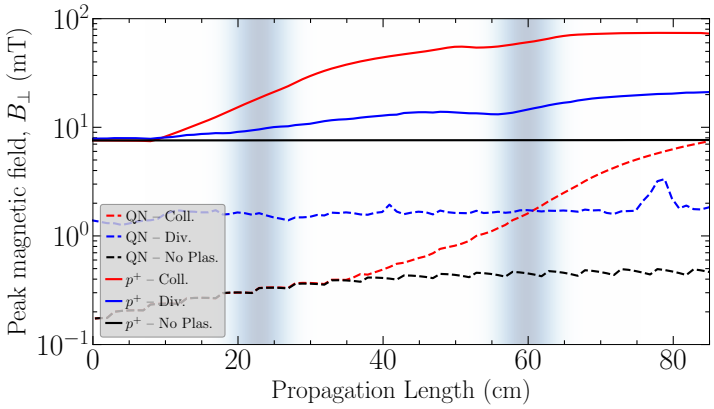

FIGURE 5.8: Peak transverse magnetic field B_3 versus propagation distance L (with $L = 0$ at the plasma entrance). Solid lines: simulations with proton beam. Dashed lines: quasi-neutral beams. Collimated beams show the fastest growth, while divergent beams grow weakly or not at all. The no-plasma cases remain at constant B_3, representing the seed field from the initial current imbalance. The darker blue regions indicate where the plasma density is highest.

To quantify these trends, we track the peak transverse magnetic field B_3 as a function of propagation distance, with $L = 0$ defined at the plasma entrance (Fig. 5.8). Simulations with protons (solid lines) display the same hierarchy as in the 3D runs: the collimated case grows fastest, while the no-plasma case remains at a constant B-field amplitude, representing the seed field from the proton beam. In QN cases, the divergent beam shows little or no growth, likely masked by noise from its high temperature, while the cold collimated beam eventually grows from noise at a rate comparable to the proton-beam case, but from a much lower initial amplitude. This indicates that the proton component primarily sets the initial B-field level while leaving the intrinsic growth rate similar to the QN case.

The electromagnetic character of the instability is illustrated in Fig. 5.9, which shows the total E- and B-field energy normalized to the initial beam energy. In QN simulations, the divergent case exhibits only noise-level growth, with occasional E-field spikes caused by incomplete plasma screening. The collimated case begins with $E > B$; when the instability develops, B surpasses E, indicating a magnetically dominated (Weibel) regime where a frame exists with $E = 0$ [224]. In the divergent case, the initial normalized field energy is smaller due to the higher kinetic energy of the hotter beam. In both proton cases, the E-field is quickly screened upon entering the plasma, followed by a dip in B as the background return current is established. Growth of B due to the instability then follows, accompanied by a later increase in E in the lower-density central region of the plasma cell, where screening is less effective. At the plasma exit, both cases end with $B > E$, indicating net beam magnetization seeded by the proton beam.

These results show that the residual proton component in the experimental beam does not qualitatively alter the instability under study, but it does provide an initial magnetic seed that

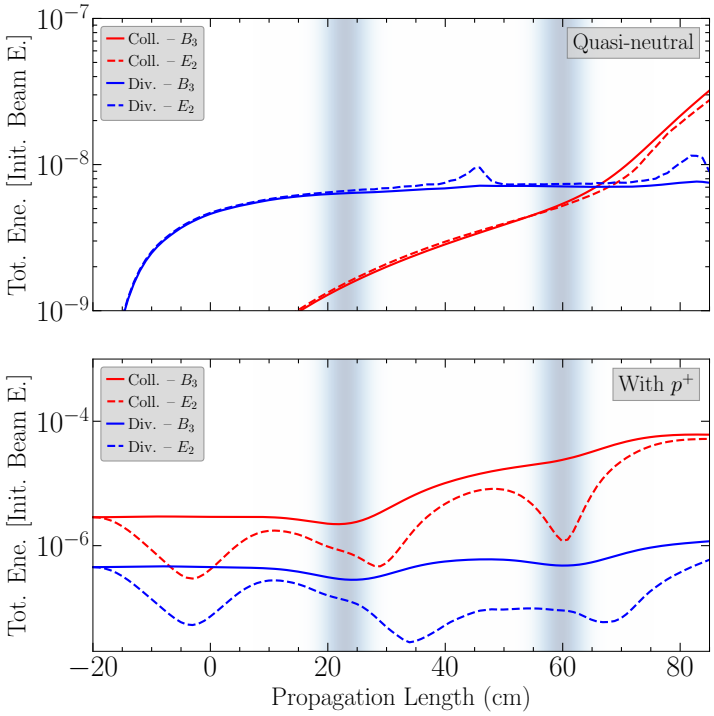

FIGURE 5.9: Evolution of total electric- and magnetic-field energy, normalized to the initial beam energy, for quasi-neutral (top) and proton-beam (bottom) simulations. In QN collimated beams, B overtakes E once the instability develops, indicating a magnetically dominated (Weibel) regime. In proton-beam cases, E is rapidly screened on entering the plasma; B dips as the return current is established, then grows due to the instability. Both collimated cases exit the plasma with $B > E$, showing net beam magnetization seeded by the proton component. The darker blue regions indicate where the plasma density is highest.

sets the starting amplitude of the growing mode. This offers a useful avenue for interpreting experimental data from beams that are not perfectly quasi-neutral, as complete neutrality of electron-positron beams is extremely difficult to achieve. In practice, positrons tend to interact with the converter and annihilate, so the electron yield is consistently higher in experimental results [72], and the original beam composition is never fully suppressed. Establishing the role of non-neutral beams, and determining how they can be meaningfully compared to astrophysical beams, is therefore key for connecting laboratory and astrophysical regimes. Moreover, this result points to a broader role of heavy species: beyond their kinetic involvement in processes such as the ion-Weibel instability (where the growth rate is modified), their spatial profiles, which has not been considered in theoretical analyses thus far, can imprint preferred spectral modes onto lighter species, thereby controlling the structure and scale of the resulting instability.

QUASI-CHARGE-NEUTRAL BEAM DYNAMICS: SEEDING THE INSTABILITY

To investigate how heavier species can seed instabilities in lighter ones, we performed a series of PIC simulations in a periodic plasma box containing a homogeneous electron-positron beam ($n_{e^-} = n_{e^+} = n_0/2$) and a proton component of equal total density ($n_p = n_0/2$). The proton beam was modulated with a weak transverse density perturbation of the form $\delta n_p/n_p = 10^{-4}$, with varying wavelength. All species were initialized with a realistic Fireball-like momentum distribution, including an angular spread of $\Delta\theta = 0.025$, as in Sec. 5.2.1. Since the beams are relativistic, space-charge effects are reduced by a factor γ^{-1} [225], and the proton modulation provides a small but well-defined initial current seed. The goal of this setup is to test whether the filamentation observed in the full simulations (Sec. 5.2.1) can be efficiently seeded when the perturbation wavelength matches the natural scale of the instability.

A theoretical estimate of the CFI growth rate for this beam configuration is shown in Fig. 5.1. For $\Delta\theta = 0.025$, the fastest growing mode occurs at $k_{\max} \simeq 3, \omega_{p0}/c$, corresponding to a wavelength $\lambda_{\max} \simeq 2, c/\omega_{p0}$. The unstable spectrum extends up to a cutoff at $k_{\rm cut} \simeq 9, \omega_{p0}/c$ ($\lambda_{\rm cut} \simeq 0.69, c/\omega_{p0}$), beyond which small-scale perturbations are suppressed. Toward longer wavelengths, the growth rate decays rapidly and becomes negligible for $k \lesssim 0.5, \omega_{p0}/c$ (i.e., $\lambda \gtrsim 12.5, c/\omega_{p0}$). This defines a well-bounded spectral window for effective seeding.

The simulation results, shown in Fig. 5.10, reflect this behavior in detail. Row (a) shows the electron density for four simulations with increasing proton modulation wavelength. Row (b) presents the corresponding transverse Fourier spectra, with vertical lines marking the seeded wavenumber $k_{\rm seed}$ and its first harmonic. In column (1), the imposed wavelength $\lambda_{\rm seed} = 0.1, c/\omega_{p0}$ corresponds to $k_{\rm seed} = 10, \omega_{p0}/c$, well beyond the cutoff. As expected, no dominant spectral response is observed, and the instability evolves as in the unseeded case. In column (2), $\lambda_{\rm seed} = 2.5, c/\omega_{p0}$ lies near $k_{\max}$, leading to efficient seeding with rapid amplification of both the fundamental and its harmonic. Column (3), with $\lambda_{\rm seed} = 10, c/\omega_{p0}$, corresponds to a slower-growing mode that still seeds the instability, albeit less efficiently. In column (4), $\lambda_{\rm seed} = 25, c/\omega_{p0}$ lies in the regime of very weak growth, and the modulation fails to imprint a dominant spectral signature.

These results confirm that efficient seeding requires alignment between the imposed mod-

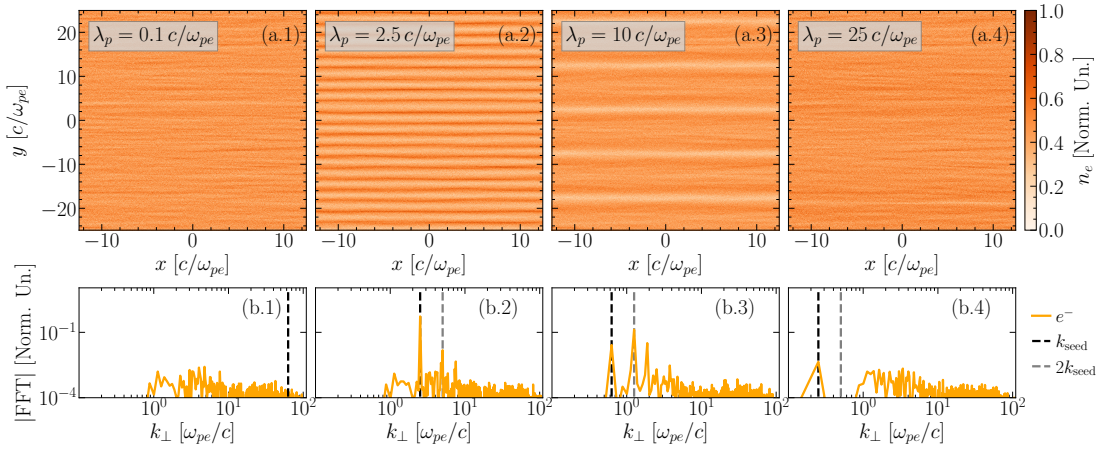

FIGURE 5.10: PIC simulations showing the seeding of the current filamentation instability (CFI) by weak transverse density modulations in the proton beam. Each column (1-4) corresponds to a different modulation wavelength: (1) $\lambda_p = 0.1\,c/\omega_{pe}$, (2) $2.5\,c/\omega_{pe}$, (3) $10\,c/\omega_{pe}$, and (4) $25\,c/\omega_{pe}$. **(a)** Electron density profiles at the time of strongest filamentation, showing how the imposed proton modulation affects the resulting structure. **(b)** Corresponding transverse Fourier spectra of the electron density. The seeded wavenumber $k_{\rm seed}$ and its first harmonic are marked, allowing direct comparison between the input modulation and the spectral response. Efficient seeding occurs when the imposed wavelength lies near the peak of the theoretical growth rate spectrum (columns 2-3), while wavelengths that are too short or too long (columns 1 and 4) fail to imprint a dominant mode.

ulation and the natural scale of the instability. Importantly, the CFI is fundamentally a current-driven process: it grows from transverse modulations in the net beam current, which generate azimuthal magnetic fields that reinforce the current perturbations. The familiar density filaments observed in PIC simulations emerge only later, as beam particles are deflected and pinched by these evolving fields. In this context, the proton modulation acts by seeding a transverse current structure through quasi-static electromagnetic fields. This seeding imprints its modulation and triggers the instability in the more responsive light species. This cross-species coupling is especially striking given that the characteristic scale of the instability is much smaller than the proton skin depth, highlighting that seeding is mediated through field structures, not direct dynamical interaction. This is analogous to the failure of electrons to respond to proton-scale perturbations in the long-wavelength case of Fig. 5.10.

While seeding via transverse velocity modulations is also a promising route, our focus here is on isolating the effect of density-driven seeding, which is directly relevant to experimental configurations. Exploring the role of velocity-space seeding remains an interesting direction for future work. Finally, these results raise an important question that echoes our earlier discussion of exotic beams: as the filaments formed by the light species grow and merge in the nonlinear regime, could they eventually reach a scale where their self-generated fields begin to influence heavier species that initially acted only as passive backgrounds?[8]

[8]This will be outlined in Sec. 5.3.3.

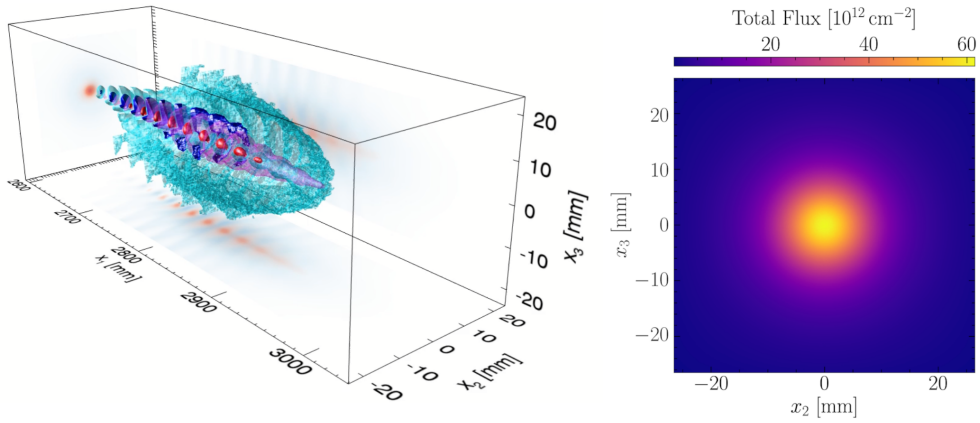

FIGURE 5.11: Three-dimensional PIC simulation results for a Fireball-I beam propagating through a 3 m plasma. **Left:** Isosurfaces of electron (blue/cyan) and positron (red/magenta) densities. Light shades (cyan, magenta) correspond to 20% of the species' peak density, while darker shades (blue, red) correspond to 60%. The distribution shows mild structuring and limited magnetic pinching, due to high angular divergence and residual proton content. **Right:** The resulting fluence map reveals a lower peak intensity and a more diffuse profile, consistent with suppressed instability growth under these initial conditions.

5.3 FOLLOW-UP EXPERIMENTS: FURTHER WORK

5.3.1 FIREBALL-III

The upcoming Fireball-III experiment, scheduled for June 2025, will introduce two major experimental upgrades: a redesigned particle converter and a longer plasma cell. The new converter features an extended iron section, which is expected to absorb most of the residual proton content from the initial particle shower [226]. As a result, the generated electron-positron beam will closer to charge-neutral, minimizing background contributions from heavy positive particles. This improvement is essential for isolating the intrinsic dynamics of beam-plasma instabilities in symmetric pair plasmas, without the asymmetries and seeding effects introduced by proton contamination.

In addition to the improved converter, Fireball-III will employ a significantly longer plasma cell, extending up to 3 meters [226]. While the plasma density remains comparable to Fireball-I, *i.e.*, $n = 2 \times 10^{12}$ cm^{-3}. The longer propagation distance brings the system closer to the regime where collective plasma effects, such as filamentation, magnetic field generation, and energy redistribution, can fully develop over several e-foldings, as we will see for original beam converter will provide 2 e-foldings and $\sim$ 12 e-foldings with a new converter.

To understand the role of propagation length in the development of instabilities, we first simulate the same beam as in Section 5.2.1, i.e., the realistic, divergent beam ($\Delta\theta = 0.025$) from Fireball-I generated using the original converter. Only the background plasma is modified, replacing the original cell with the new 3-meter-long configuration.

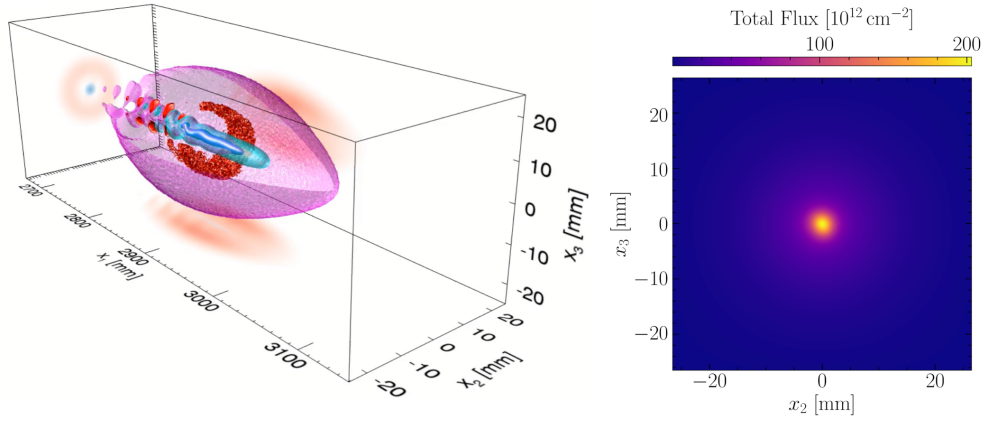

FIGURE 5.12: Three-dimensional PIC simulation results for a Fireball-III beam propagating through a 3 m plasma. **Left:** Isosurfaces of electron (blue/cyan) and positron (orange/yellow) densities. Light shades (cyan, yellow) correspond to 20% of the species' peak density, while darker shades (blue, orange) correspond to 60%. The reduced beam emittance results in stronger magnetic pinching, with electrons focused toward the axis and positrons expelled outward, driven by reversed seed magnetic fields. **Right:** Synthetic fluence map at the downstream screen shows enhanced peak intensity and tighter beam confinement, consistent with increased magnetic self-focusing compared to the Fireball-I case.

Figure 5.11 shows isosurfaces of electron and positron densities after propagation through the extended plasma. Despite the beam's significant divergence, positrons are again pinched toward the center of the beam, indicating that a longer plasma cell allows instability-driven dynamics to develop even for realistic, high-emittance beams (like Fireball-I with $\Delta\theta = 0.025$). This behavior is reminiscent of the idealized collimated case, albeit more diffuse.

However, the observed structuring does not correspond to clean transverse current filamentation as in canonical current filamentation instability (CFI) scenarios [73, 215]. Instead, the beam appears to undergo a more complex streaming-type instability, potentially seeded by residual charge imbalance and modified by the presence of the proton component. The resulting modulation resembles a self-modulation instability (See Ref. [227]) rather than pure filamentation (as seen by the longitudinal bunching of the positrons along the beam propagation direction in Fig. 5.11), which demonstrates the interplay between the CFI and other beam plasma instabilities.

To isolate the effect of beam composition, we next simulate the setup expected for Fireball-III using the new converter and updated beam parameters. While the overall number density of electrons and positrons is reduced, from $n_{e^-} = 0.339\, n_0$, $n_{e^+} = 0.264\, n_0$ to $n_{e^-} = 0.30\, n_0$, $n_{e^+} = 0.25\, n_0$ in normalized units, the proton component is strongly suppressed, dropping from $n_p = 0.15\, n_0$ to $n_p = 0.03\, n_0$. The electron-positron divergence is also reduced, with the angular spread decreasing from $\Delta\theta = 0.025$ to $\Delta\theta \approx 0.008$, corresponding to nearly a threefold reduction in transverse emittance. The simulation reflects this cleaner and more collimated beam composition while retaining the same 3-meter plasma length. For further details on this simulation paramters, see Appendix A.4.3.

Figure 5.12 shows the resulting dynamics. In contrast to the previous case, we now observe

a reversed structure: positrons are pushed outward, while electrons are pinched inward. This inversion reflects a change in the initial current distribution that seeds the instability. In the previous setup, the central beam region carried a net positive current density, with $n_{e^+} + n_p = 0.414 > n_{e^-} = 0.339$, meaning the majority of the current was carried by positively charged species. This configuration seeded magnetic fields that acted to focus positrons toward the axis and deflect electrons outward. In the new configuration, the proton contribution is strongly reduced and the balance reverses: $n_{e^+} + n_p = 0.28 < n_{e^-} = 0.30$, leading to a net negative current density in the beam core. As a result, the seed magnetic fields now focus electrons and expel positrons, inverting the instability structure.

Moreover, the new converter leads to reduced beam emittance, corresponding to a lower transverse temperature and narrower angular spread $\Delta\theta$ [226]. This allows the beam to pinch more effectively, resulting in stronger magnetic field amplification and increased local fluence. The right-hand panel of Fig. 5.12 shows a sharper and more intense filamentary structure compared to the previous case, consistent with a lower-temperature beam entering a more nonlinear regime. These trends are in agreement with the theoretical predictions shown in Fig. 5.1, where a decrease in $\Delta\theta$ leads to both an increase in the peak growth rate and an upshift in the most unstable wavenumber $k_{\max}$, enhancing both the strength and signatures of the instability, as seen in the stark difference between the flux measured in Fig. 5.11 compared against Fig. 5.12.

This highlights how the new Fireball-III configuration enables seeding and more efficient amplification of magnetic fields. It may thus offer the first experimental opportunity to observe kinetic beam-plasma instabilities in relativistic pair plasmas,[9] within a regime where the onset of the instability can be systematically controlled.

In the previous case, we observed the onset of the self-modulation instability. Now with the new beam parameters one observes the onset of the hosing instability [227], as seen by the perpendicular offset of the centroid of the electron beam component in Fig. 5.12. This highliths the interplay of streaming instabilities, *i.e.*, CFI oblique and two-stream, with whole beam instabilities. The dynamics are a result of the non fully charge neutral beams; we hypothesise that similar interplay will be observed in fully charge-neutral beams. Therefore, we can conjecture (and shall be further explored in the future) that charge neutral beams are proned to self-modulation and hosing instabilities; mediated by the non-linear stage of streaming instabilities, which drive modulations that in turn drive the background plasma wakes responsible for self-modulation and hosing.

5.3.2 FIREBALL ELECTRON CYCLOTRON MASER INSTABILITY

The next stage in the Fireball experimental program will take place at the Beam Test Facility (BTF) in Frascati. This experiment is motivated by the goal of exploring electron cyclotron maser (ECM) emission as a viable mechanism for producing the coherent, highly polarized radiation observed in extreme astrophysical transients, such as Fast Radio Bursts (FRBs) [42].

[9] Analysis of the Fireball-II experiment is still underway. An improved Faraday rotation diagnostic was fielded to enhance magnetic field sensitivity. Preliminary results indicate a signal consistent with the amplified magnetic fields observed in simulations [228].

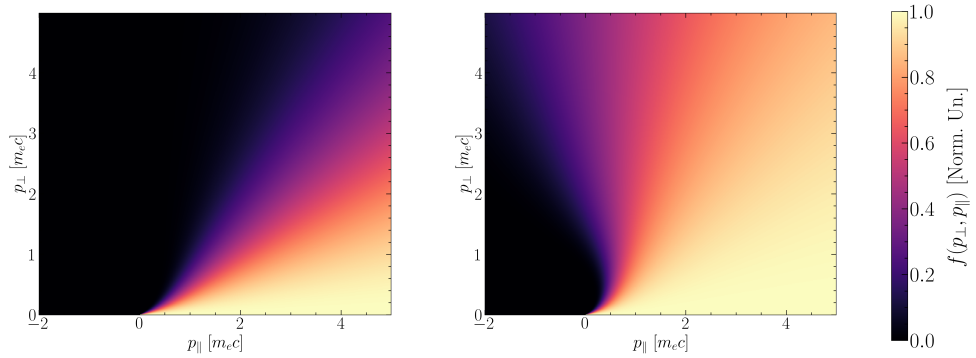

FIGURE 5.13: Numerical evolution of the beam distribution as it enters a 4 T magnetic mirror, shows how a horseshoe-shaped distribution is obtained. Left: Initial distribution at the mirror entrance ($z = 0$ cm). Right: Distribution after propagation to $z = 100$ cm, showing a clear population inversion in $p_\perp$, a key condition for ECM emission.

As discussed in Chapter 3, ECM emission is a leading candidate for coherent radiation in astrophysical environments. Unlike conventional synchrotron emission, which is fundamentally incoherent and thus limited in brightness temperature, ECM emission arises from population inversion in the perpendicular momentum distribution of relativistic leptons. Such inversions naturally develop when charged particles enter regions with increasing magnetic field strength, such as those found in magnetospheres or near relativistic shocks [48, 78].

As the beam moves into the region of increasing magnetic field strength, conservation of the magnetic moment enforces a transfer of longitudinal to transverse momentum. This leads to adiabatic compression in momentum space, producing ring- or horseshoe-shaped distributions, precursors of ECM emission [121, 229, 230]. By horseshoe-shaped distribution, we refer to a momentum-space configuration in $p_\perp$–$p_\parallel$ space where particles form an incomplete ring, concentrated at large $p_\perp$ and with a gap opposite to the beam propagation direction. This geometry naturally produces a positive perpendicular gradient ($\partial f / \partial p_\perp > 0$) over part of the distribution, providing the population inversion that drives ECM emission.

This experiment will allow for a direct comparison between pure electron beams and quasi-neutral electron-positron beams within the same magnetic mirror configuration. In the electron-only case, the resulting distribution is expected to form a distinct horseshoe shape, known to trigger ECM in non-relativistic systems like Earth's auroral kilometric radiation [120, 231]. In contrast, the dynamics of quasi-neutral beams are more symmetric and relativistic, and have never been studied experimentally. This side-by-side comparison represents an opportunity to test the onset of ECM emission in both charge-asymmetric and charge-symmetric systems.

Preliminary theoretical results, based on the parameters of the beams and magnetic mirror strenghts available at BTF in Frascati, confirm that magnetic mirrors can indeed produce the required population inversions in both cases. In particular, the evolution of the beam distribution can be derived from conservation laws. Assuming constant energy and magnetic

moment, $\dot{\gamma} = 0$ and $\dot{\mu} = 0$, the pitch angle θ (where $\sin\theta = p_\perp / p_\parallel$) evolves according to[10]

$$\frac{\partial \theta}{\partial t} = \sin\theta \, \frac{\sqrt{\gamma^2 - 1}}{\gamma} \, \frac{c}{2B(z)} \frac{dB(z)}{dz}. \tag{5.6}$$

Equation (5.6) can be numerically integrated to track the evolution of the distribution function as the beam enters the mirror. Figure 5.13 shows an example for a beam entering a magnetic mirror with $B_{\max} = 4$ T, following the profile $B(z) = \frac{B_{\max}}{1 - g(z-d)}$, where $g = 90\ \mathrm{m}^{-1}$ is the taper parameter and $d = 100$ cm is the location of the field maximum,[11] these parameters are based on the "Flux Concentrator" available at BTF [232, 233]. The initial distrbution is modelled after preliminary results of Fireball beams that can be produced in INFN's BTF, this were obtained via FLUKA simulations performed by the Oxford team [233]. After evolving the propagation of the beam, the resulting distribution at the center of the mirror clearly shows a region with $df/dp_\perp > 0$, in the shape of a horseshoe distribution, indicating local instability to the oblique (mixed) and purely perpendicular (X-mode) maser [167].

Using the evolved distribution function $f_0(p_\perp, p_z)$, we compute the growth rate Γ of the EM modes propagating oblique and purely perpendicular to the magnetic field by numerically evaluating the growthrate of the ECMI [163, 169, 234]

$$\Gamma = \frac{\pi \omega_{pb}^2}{\omega} \sum_{n=1}^{\infty} \int d\mathbf{p} \frac{\delta\left(\omega - \frac{n\Omega}{\gamma} - \frac{k_z p_z}{\gamma}\right)}{\gamma} \left[\left(\omega - \frac{k_z p_z}{\gamma}\right) \frac{\partial f_0}{\partial p_\perp} + \frac{k_z p_\perp}{\gamma} \frac{\partial f_0}{\partial p_z}\right] \left[J_n'(b_\perp)\right]^2. \tag{5.7}$$

In this context, "purely perpendicular" emission refers to electromagnetic waves with wave vector $\mathbf{k}$ exactly perpendicular to the background magnetic field $\mathbf{B}$, corresponding to the canonical X-mode. "Oblique" emission denotes wave propagation at an angle $0 < \theta_k < 90^\circ$ with respect to $\mathbf{B}$, in which case the mode has mixed polarization (both transverse electromagnetic and electrostatic components) and can interpolate continuously between the X- and O-mode branches [169]. In the present calculation we have neglected the effects of magnetic field curvature, which would couple to the particle drifts and alter the resonance condition. This approximation is justified by the fact that including curvature in a full kinetic ECMI treatment is technically challenging and beyond the scope of this work. The beam consists of an electron–positron pair plasma, so both species contribute equally to the instability. In the notation of Eq. (5.7), the plasma frequency is thus written as $\omega_{pb}^2 = 4\pi e^2(n_e + n_p)/m = 4\pi e^2(2n_e)/m$, giving $\omega_{pb} = \sqrt{2}, \omega_{pe}$ for equal densities $n_e = n_p$. While the presence of multiple species in this case does not modify the growth rate Γ (since both species resonate in the same way), it does affect the polarization properties of the emitted radiation.

The numerically computed growth rate is shown in Fig. 5.14. Emission peaks just below the first harmonic ($\omega_{ce} \approx 0.8$ THz), with maximum growth at an angle of approximately 45° off-axis (with respect to the beam propagation direction). Higher harmonics are also observed, as well as a backward-propagating wave mode, consistent with long-standing theoretical predictions but never before confirmed experimentally [235]. While the growth rate depends sen-

[10] The derivation of this equation is detailed in App. H.4.

[11] This corresponds to a mirror ratio of $B_{\max}/B(0) = 1 + (90\,\mathrm{m}^{-1} \times 100\,\mathrm{cm}) = 91$.

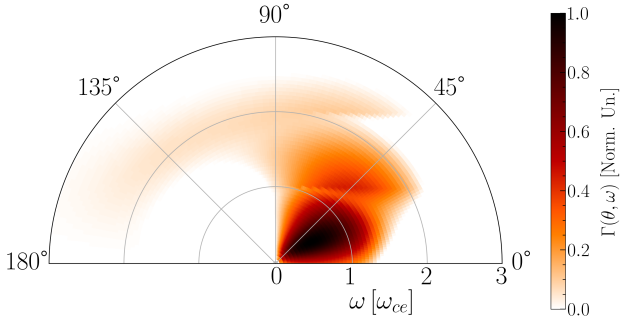

FIGURE 5.14: Numerically integrated growth rate of the ECMI (Eq. 5.7) for the beam electron-positron beam distrbutions in the a magnetic mirror (Fig. 5.13), demonstrate the angular distribution of the maser radiation, showing a peak near 45° and frequency close to the first cyclotron harmonic ($\omega_{ce} = 0.8$ THz). Backward wave modes are also visible. We note that the growth rate for the single-species plasma and pair-plasma will differ by a factor of 2 in the density component, but the shape of the emission will remain the same

sitively on the achievable beam and plasma densities near the flux concentrator center, these preliminary results already show that the magnetic mirror configuration can generate sufficient pitch-angle evolution and reflection to form unstable distributions, for both pure and quasi-neutral beams. This establishes that the planned geometry is capable of producing the basic conditions required for ECM generation, even though detailed predictions will require further studies of the densities and initial beam parameters attainable in the experiment. These findings support the feasibility of observing ECM emission in the laboratory and underscore the critical role of beam composition in shaping the momentum-space dynamics that lead to coherent emission.

One of the key questions this experimental platform can address is the polarization of the resulting maser radiation. Previous studies have shown that electron-only beams produce circularly polarized emission along the direction of propagation and magnetic field [121, 163, 167, 236, 237], while positron beams yield opposite-handed circular polarization. In contrast, electron-positron pair plasmas are expected to emit unpolarized radiation in this configuration, due to the cancellation of contributions from oppositely charged species. However, in strongly magnetized regimes where $\omega_{ce} \gg \omega_{pe}$, the most unstable modes are predominantly perpendicular to the magnetic field. In this case, the linearly polarized X-mode dominates [114, 163], and the electron and positron contributions to wave amplification add in phase, enhancing rather than cancelling the emission. By enabling a direct comparison between charge-asymmetric and pair-symmetric beams under controlled conditions, this platform offers a novel opportunity to investigate how plasma composition and field geometry shape the polarization properties of coherent emission.

5.3.3 EXOTIC FIREBALL BEAMS

The results of the previous section, Sec. 5.2.2, showed how small-scale modulations in a heavier species (protons) can seed instabilities in a lighter, more responsive plasma component (electrons and positrons). This raises an intriguing complementary question: can the reverse occur? That is, as nonlinear filamentation progresses and larger spatial structures emerge, can light species begin to drive instabilities in heavier, initially passive species?

In the context of hadronic cascades generated by the SPS proton beam, the particle spectrum is not limited to electrons and positrons. Secondary species such as muons, pions, and photons are also produced in significant numbers [74]. While these heavier particles are often neglected in modeling, their presence opens the possibility of multi-species coupling within relativistic plasmas. Due to their large inertia, muons and pions are less responsive on short timescales, but may become increasingly relevant as instabilities evolve and the dominant spatial scales grow.

Previous studies have explored related dynamics in background or streaming ion populations. For instance, Ref.[222] examined how background ions respond to electron-driven space-charge fields by slowly forming filaments that screen the charge separation, albeit too sluggishly to maintain full neutrality. Similarly, Ref. [238] showed that streaming ions modify the initial CFI growth rate and eventually amplify a secondary, ion-driven Weibel instability after electron-scale filamentation saturates. In both cases, heavier species evolve on longer timescales and larger spatial scales, aligning with and amplifying pre-existing structures seeded by lighter, faster particles. These behaviors exemplify a key physical idea: that lighter species can seed the instability of heavier ones bridging the scales between both species.

To investigate the possibility of cross-species seeding in the Fireball context, we performed PIC simulations including multiple beam species, as detailed in Appendix A.4.5. The composite beam consisted of electrons, positrons, and a third, heavier species with charge-to-mass ratio $e/264, m_e$, representative of pions. All species were initialized with realistic Fireball-like momentum distributions, including an angular divergence of $\Delta\theta = 0.025$, and propagated through a background electron-ion plasma.

At early times, the electron-positron component dominates the dynamics, driving the current filamentation instability at scales comparable to $k^{(e)} \simeq 3, \omega_{pe}/c$, as predicted in Fig. 5.1. As the instability enters the nonlinear regime, filaments begin to merge and grow in scale [213]. Once this transverse scale approaches the skin depth of the heavier species, the electromagnetic fields generated by the light species begin to modulate the heavier component, triggering secondary filamentation, an effect also observed in electron-proton systems [238]. Based on the mass ratio, the dominant wavenumber for the heavier species is expected to scale comparable to $k^{(\pi)} \sim k^{(e)}/\sqrt{264} \simeq 0.2, \omega_{pe}/c$, which is what we observe in the simulations in Fig. 5.15.

Figure 5.15 captures this process in detail. The electron density (row a) shows the emergence and subsequent merging of current filaments. In the multi-species case (row b), the pion density remains smooth at early times but later develops clear structure at the same transverse wavenumber as the electrons. The corresponding Fourier spectra (row d) confirm that both

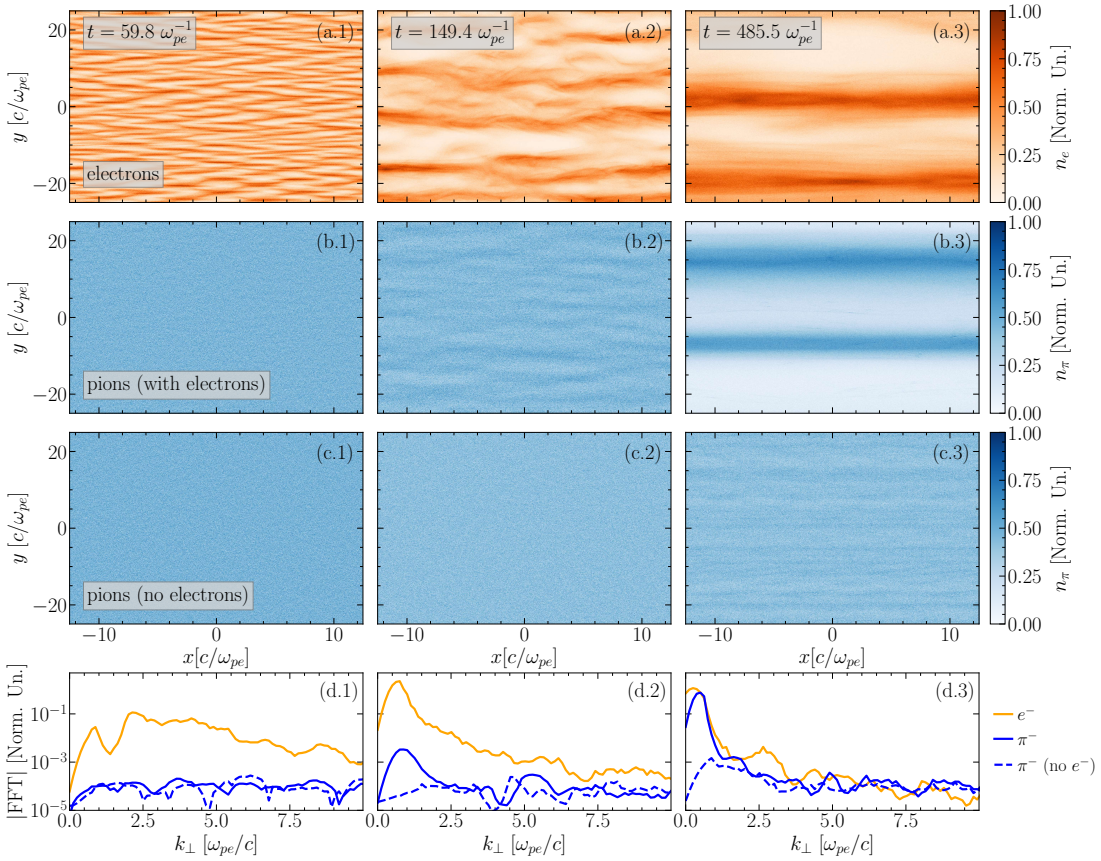

FIGURE 5.15: PIC simulations of a multi-species beam demonstrating the sequential onset of filamentation across species. Each column corresponds to a different time: (1) after the electrons develop density modulations ($t = 59.8\ \omega_{pe}^{-1}$), (2) when pions begin to debelop density modulations ($t = 149.4\ \omega_{pe}^{-1}$), and (3) late time ($t = 485.5\ \omega_{pe}^{-1}$). Rows show: **(a)** electron density, **(b)** pion density from a simulation including electrons and positrons, **(c)** pion density from a control simulation without electrons (pion-only case), and **(d)** the corresponding transverse spatial Fourier spectra. In the full multi-species case (b), the pion distribution remains initially unstructured but develops filaments at later times that mirror the electron structure in (a), consistent with a scale-dependent seeding process. In contrast, the control case (c) shows no significant modulation, confirming that the observed pion filamentation in (b) arises from coupling to the electron-driven dynamics. The Fourier spectra (d) further highlight the emergence of shared spectral features between electrons and pions at late times.

species share a dominant spectral peak at $k \simeq 0.5, \omega_{pe}/c$, comparable to $k^{(\pi)}$. In contrast, the control simulation (row c), which includes only pions, shows no such structure, and its only beginning to develop its own weak modulations, confirming that the observed filamentation arises from coupling to the lighter species.

What is new here relative to linear growth-rate arguments is the causal, nonlinear seeding mechanism we observe. In the full multi-species run, heavy-species (pion) filamentation does not develop until after electron filaments nonlinearly merge and the dominant transverse scale grows to $k \sim k^{(e)}/\sqrt{m_\pi/m_e}$. At that point, the pion spectrum acquires a peak at the same k and with phase alignment to the electron pattern, whereas a pion-only control remains unstructured over the same interval. This demonstrates that heavy-species filamentation is seeded by the finite-amplitude electromagnetic fields and pre-formed current channels produced by the light species, rather than arising from its own linear growth, thus accelerating the onset of the pion filamentation. The result is a scale-bridging instability cascade, from electron to pion scales, with a measurable delay Δt_{seed} and wavenumber inheritance $k^{(\pi)} \simeq k^{(e)}/\sqrt{m_\pi/m_e}$ that go beyond what can be inferred from side-by-side growth-rate estimates.

In short, the novelty is not that heavier species are more unstable in when including elctropns, linear theory already predicts that like the ion-electrn-weibel instability [238], but that light-species nonlinear structure onset the heavy-species instability, with phase-locked, scale-inherited filaments that a linear growth-rate comparison cannot predict.

While the role of muons and pions may be negligible under current experimental conditions, these results highlight a potentially important mechanism in future high-density or long-propagation scenarios. They point to the possibility of multi-scale instability cascades in relativistic plasmas, where light species initiate processes that are subsequently taken over by heavier ones. A full theoretical treatment of such nonlinear, cross-species coupling remains an open challenge, but our results suggest that relativistic exotic beams offer a promising platform to explore this new regime of plasma dynamics. e

5.4 CONCLUSIONS

In this chapter, we have presented a comprehensive theoretical and numerical investigation of kinetic instabilities in relativistic electron-positron beams, with a focus on the current filamentation instability (CFI) and its relevance to both astrophysical scenarios and recent laboratory experiments.

We began by outlining the importance of beam-plasma instabilities in high-energy environments, such as blazar jets and gamma-ray bursts, where relativistic pair plasmas are thought to interact with ambient backgrounds. In such systems, the interplay between anisotropic distribution functions and collective electromagnetic modes governs energy redistribution, field generation, and potentially even radiation emission. Using both analytical theory and linear kinetic modeling, we explored how key parameters, such as transverse temperature and beam divergence, determine the onset and growth of instabilities.

We then turned to large-scale particle-in-cell simulations performed in the context of the Fireball-I experiment at CERN. These simulations closely reproduced the experimental condi-

tions, validating the suppression of filamentation in realistic, divergent beams and highlighting the sensitivity of instability growth to beam emittance and composition. In particular, we identified a novel role for residual proton content in seeding specific filamentary modes, even when the overall system is nearly charge-neutral.

Extending these results, we examined follow-up scenarios relevant to the upcoming Fireball-III experiment. Our simulations show that the use of a new converter, designed to suppress the proton component, and a longer plasma cell may enable the controlled excitation of kinetic instabilities. By tuning beam parameters and observing the resulting magnetic structure, this configuration may allow the first direct measurement of nonlinear beam-plasma dynamics in relativistic pair plasmas.

We also presented preliminary theoretical and numerical results for the study of electron cyclotron maser (ECM) emission in magnetic mirror fields, relevant to a new experiment at the Beam Test Facility in Frascati. For the first time, this setup enables a systematic comparison between pure electron beams and quasi-neutral pair beams in identical magnetic geometries. Simulations show that both cases can develop population-inverted, horseshoe-shaped distributions capable of triggering ECM emission, a mechanism increasingly favored to explain the brightness and polarization of fast radio bursts.

Finally, we explored an outlook on "exotic" Fireball beams: multi-species plasmas containing not only leptons but also heavier hadronic products such as muons and pions. While these components are often ignored in conventional modeling, our analysis suggests that nonlinear beam evolution may eventually seed instabilities in heavier species, initiating a cascade across mass scales. This presents a promising direction for future theoretical and experimental efforts.

Taken together, the results presented here mark a significant step toward bridging laboratory plasma experiments with open problems in high-energy astrophysics. They also emphasize the critical role of theory and simulation in guiding experimental design, interpreting measurements, and uncovering the underlying physics of collective plasma behavior in relativistic regimes.

CHAPTER 6

CONCLUSION

> Philosophy, as the thought of the world, does not appear until reality has completed its formative process, and made itself ready ... When philosophy paints its grey in grey, one form of life has become old, and by means of grey, it cannot be rejuvenated but only known. The owl of Minerva takes its flight only with the coming of dusk.
>
> *Georg W. F. Hegel – Preface to the Elements of the Philosophy of Right [239]*

6.1 SUMMARY

This doctoral work began with the goal of studying Compton-driven plasma processes in both laboratory and astrophysical settings. However, the focus of the thesis shifted early on due to the unexpected results outlined in Chapter 2. These findings, which emerged from PIC simulations, found a phenomenon that was surprising yet welcome, and ultimately set the direction for the rest of the thesis.

Chapter 2 presents original contributions that show how tenuous, highly magnetized, relativistically hot plasmas undergo significant radiative cooling. This process leads not only to substantial losses in kinetic energy but also in entropy, rendering the plasma unstable. Notably, the local momentum distribution function of the cooling plasma develops a ring-like structure in the plane perpendicular to the magnetic field. This marks the first instance of such a ring distribution arising naturally through radiative processes, suggesting that ring distribution plasmas may be a common feature in highly magnetized environments such as those around compact astrophysical objects.

Chapter 3 presents the first demonstration that coherent maser emission can be spontaneously triggered and sustained in radiatively cooled, strongly magnetized relativistic plasmas. This process, driven by the electron cyclotron maser instability (ECMI), emerges from

synchrotron-induced ring momentum distributions, established in Chapter 2, and develops in a regime where radiation reaction qualitatively alters the instability dynamics. Using large-scale PIC simulations and kinetic theory, it is shown that ultra-strong fields not only trigger the ECMI but also sustain population inversion well into the non-linear regime, enabling long-lived, linearly polarized, multi-harmonic radiation. This mechanism represents a new class of plasma instability, one intrinsically shaped by radiative effects, and defines a clear hallmark of extreme plasma conditions with direct relevance to pulsars and Fast Radio Bursts, as the resulting emission naturally produces high brightness comparable to that observed in astronomical observations.

Chapter 4 builds on the general principle established in Chapters 2 and 3, that nonlinear radiative cooling drives phase-space compression and population inversion, by demonstrating its manifestation in unmagnetized, beam-plasma systems. Specifically, it shows that relativistic electron beams undergoing betatron oscillations in plasma wakefield accelerators naturally develop ring-shaped phase-space structures as a result of radiation reaction. This process, driven by the amplitude-dependent nature of betatron cooling, mirrors the synchrotron-induced bunching seen in magnetized plasmas but arises purely from electric focusing fields. Using analytical theory and large-scale 3D PIC simulations, this chapter provides the first demonstration of radiatively induced phase-space structuring in accelerator beams, revealing a broader class of kinetic phenomena governed by extreme-field-induced cooling. These results establish high-density wakefield accelerators as a promising experimental platform for studying the fundamental dynamics of extreme plasmas.

Chapter 5 concerns itself with a distinct facet of extreme plasma physics, the dynamics of relativistic electron-positron plasmas and their associated kinetic instabilities. Unlike the radiatively structured electron-ion systems studied in previous chapters, pair plasmas exhibit unique symmetry properties and instability behavior, particularly in beam-plasma configurations. This chapter is based on our work within the Fireball experimental program at CERN, where I led the PIC simulation effort to interpret and model the first laboratory-generated pair plasma beams. These large-scale simulations were essential to understanding why the current filamentation instability was not observed in Fireball-I, showing that beam divergence and charge imbalance were key suppressing factors. By exploring a wide parameter space of beam composition, divergence, and neutrality, our results identified the conditions required for instability growth and informed the design of future campaigns. In particular, they helped motivate the use of a longer plasma cell and improved beam converter in Fireball-III, which is expected to enter the nonlinear regime. The chapter also investigates how small-scale modulations in heavier species can seed instabilities in relativistic leptons, and outlines ongoing work on coherent emission from magnetized pair beams via the electron cyclotron maser instability. Finally, it explores multi-species effects, showing how nonlinear structures generated by light particles can trigger filamentation in heavier, initially passive components.

6.2 FUTURE PERSPECTIVES & CLOSING REMARKS

This thesis represents one of the first steps toward a kinetic theory of extreme plasmas. It has shown that incorporating even a single physical ingredient, radiative cooling, can lead to qualitatively new behaviors: phase-space compression, population inversion, and the spontaneous onset of coherent emission. These findings suggest a much richer landscape of plasma dynamics, where strong fields, radiation, and collective effects are tightly coupled.

In studying the emergence of ring distribution functions in the magnetospheres of compact objects, we considered an initially hot plasma in a uniform magnetic field. However, several important extensions remain. How do realistic field geometries alter this behavior? What role do curvature drifts play? These questions are currently being addressed by F. Assunção in forthcoming work [142], which includes radiation reaction and particle drifts in curved fields. The influence of general relativity in such settings is also unclear, will it suppress or enhance ring formation? Moreover, while we assumed a pre-heated plasma, the physical mechanisms that generate such nonthermal initial states are still poorly understood. Preliminary PIC simulations suggest that high-energy gamma-ray beams may produce high-density plasmas via shower-like processes (rather than self-sustaining avalanches), potentially converting gamma-ray energy into a ring-shaped pair plasma [240]. This raises the intriguing possibility of realizing full pair cascades in aligned **E** and **B** configurations, reminiscent of those expected during pair-cascade events in compact object magnetospheres.

Beyond the formation of ring distributions, their nonlinear evolution remains an open problem. For instance, instabilities like the firehose instability may reshape these structures under certain conditions, as discussed in Appendix F. A full mapping of the relevant parameter space, including plasma β, ω_{pe}/ω_{ce}, and normalized magnetic field B/B_{Sc}, will be needed to understand this interplay. Extending these studies to more complex, turbulent environments such as collisionless shocks or realistic pair-cascade scenarios may help bridge theoretical models with observed FRB features.

Chapter 4 opens a promising experimental avenue: the observation of radiatively induced phase-space bunching in accelerator beams. Simulations using FACET-II parameters show that such bunching should be observable with current technology. If achieved experimentally, this could serve as a platform for generating coherent betatron emission via the ion-channel laser instability, a mechanism that parallels the ECMI in magnetized plasmas. Further theoretical and numerical work will be required to assess the viability of this scheme and its potential as a laboratory analogue for coherent astrophysical phenomena.

In parallel, the Fireball experiment, discussed in Chapter 5, offers a complementary approach to studying pair plasmas. With Fireball-II currently under analysis and Fireball-III on the horizon, the next generation of experiments will benefit from improved beam converters and extended plasma cells. These upgrades will allow for greater control over beam composition, charge neutrality, and divergence, all of which were shown in Chapter 5 to influence instability growth. The PIC simulations performed in this thesis helped explain the suppression of the current filamentation instability in Fireball-I, identifying beam divergence and residual proton content as key factors. Fireball-III will allow us to test these predictions directly. Addi-

tionally, upcoming magnetized configurations, such as those proposed for Frascati, may allow for the direct observation of maser instabilities in pair plasmas. These experiments, designed to probe coherent emission in magnetic mirror setups, offer a concrete laboratory analogue to conditions near pulsars and black holes.

Looking ahead, a complete theory of extreme kinetic plasma physics remains to be developed. Key open questions include: What other instabilities or nonlinear structures arise when radiation, pair production, and QED effects are fully coupled? How is the radiation emitted by unstable plasmas absorbed, scattered, or reprocessed, and what signatures does it carry? Do such systems relax at all, or do they settle into quasi-stationary states shaped by radiative and entropic constraints? Each of these questions opens a new direction of research.

Progress will require more than theoretical development. Experimental access to extreme regimes remains limited, making large-scale simulations indispensable. These simulations not only bridge theory and experiment, but often provide the only practical means of exploring nonlinear plasma dynamics. The work presented in this thesis represents a small contribution to that effort. The radiative structures uncovered in Chapters 2 through 4, and the instability conditions identified in Chapter 5, mark the first steps into a broader, still largely unexplored region of phase space.

More broadly, this work has shown that extreme plasmas fundamentally expand the scope of kinetic theory. In these regimes, radiation is not a perturbation, it reshapes phase space, sustains population inversion, and drives coherent emission. Instabilities and radiation become entangled, leading to dynamics that co-evolve with dissipation. While radiation has not yet played a central role in the Fireball experiments, the program offers a unique opportunity to explore relativistic pair plasmas in the laboratory for the first time. These systems differ fundamentally from traditional electron-ion plasmas, not only due to their symmetry but also because they may host distinct instability behavior and nonlinear evolution. The early results from Fireball have underscored the importance of kinetic modeling in capturing these effects, especially as standard assumptions break down in the presence of charge imbalance and beam divergence. Together, these developments point toward the need for a more complete kinetic framework, one that treats radiation, quantum effects, and collective dynamics on equal footing.

There is still much to explore. But if this thesis has shown anything, it is that these regimes are no longer remote curiosities. They are within reach, both theoretically and experimentally, and they are extraordinarily rich. The time is ripe for a full kinetic description of extreme plasma physics.

APPENDIX A

SIMULATIONS PARAMETERS

A.1 CHAPTER 2

For the simulations, we have considered the same physical scenario examined analytically. There is in the x_1 direction a strong magnetic field $B_0 = 2.2 \times 10^{-6}$ (Normalized with respect to the Schwinger field B_{sc}) with an associated cyclotron frequency $\omega_{ce} = |e|B_{sc}B_0/m_e$, where e is the electron charge and m_e the electron mass. We normalised timescales and spatial dimensions with respect to the gyrofrequency ω_{ce} and c/ω_{ce}, respectively. And momentum with respect to $m_e c$. The simulations employ a temporal resolution that guarantees the gyromotion is accurately resolved $\Delta t \sim 0.0099\ \omega_{ce}^{-1}$. The typical simulation is performed in one spatial dimension (and three momentum dimensions), using 5000 cells and 1024 particles per cell, with a spatial domain length along the x_1 direction of $L_x = 50\ c\omega_{ce}^{-1}$ with periodic boundary conditions. This yields a grid resolution of $\Delta x = 0.01\ c/\omega_{ce} = 0.99 c\Delta t$, which verifies the Courant condition $\Delta x > c\Delta t$. A low-density electron plasma with plasma frequency $\omega_p = 10^{-4}\ \omega_{ce}$ fills the whole simulation domain with a background of immobile ions. Three different momentum distributions are initialized. A Maxwellian distribution $f_{0\,M} \propto e^{-(p_\parallel + p_\perp)^2/(2p_{th}^2)}$, with an isotropic momentum spread $p_{th} = 50\ m_e c$, a Maxwell-Jüttner distribution $f_{0\,MJ} \propto e^{-\gamma m_e c/p_{th}}$ and a Maxwellian beam distribution $f_{0\,Mb} \propto e^{-((p_\parallel - \gamma_b m_e c)^2 + p_\perp^2)/(2p_{th}^2)}$, where γ_b is the bulk Lorentz factor of the beam, which was chosen to be $\gamma_b = 500$.

The macro-particles employ a cubic interpolation. We tested and compared different current smoothing filters, it was found that smoothing did not significantly affect the ring formation under these simulation conditions, for this reason, the final simulation setup employed a first-order binomial smoothing. The OSIRIS PIC code employs the reduced Landau-Lifshitz model (LLR) for classical radiation reaction, which includes the two leading orders of the full Landau-Lifshitz formulation, as described in [91].

For the parameters scan we kept all parameters constant and only changed the p_{th} for the initial Maxwellian distribution. Employing $p_{th} = 50,\ 100$ & $200 m_e c$.

A.1.1 ENERGY CONSERVATION

To confirm that the numerical heating/energy conservation is addressed properly we have compared energy conservation with and without radiation reaction for the same set of numerical parameters and calculated the radiated energy for all the runs presented in this study. This is shown in Fig. (A.1), which accounts for the energy of the plasma particles, the energy radiated through synchrotron cooling and the expected kinetic energy of the plasma particles as predicted from our analytical results. In the bottom row of Fig. (A.1) we show the evolution of the percentile change of the total energy, *i.e.* the sum of the plasma and synchrotron radiated energy. Both plots demonstrate that energy is accurately conserved throughout the simulations, even for many time steps.

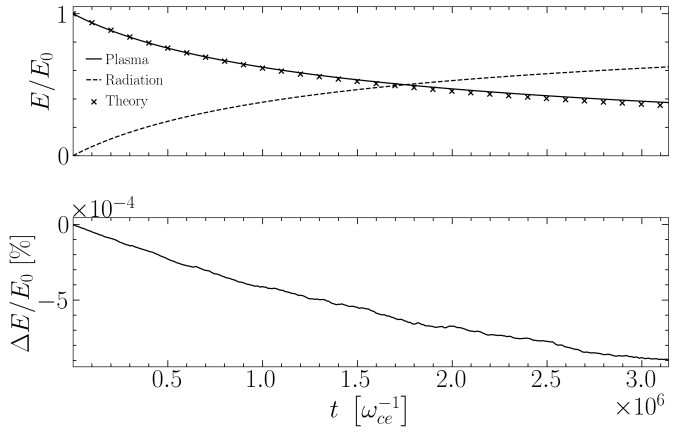

FIGURE A.1: Top: Simulation results for the total energy for an initial isotropic Maxwellian plasma with $p_{th} = 50\ m_e c$ and initial energy E_0 as a function of simulation time t. The plot shows plasma energy (continuous line), the energy from the synchrotron radiation diagnostic (dashed line) and the evolution of the energy of the plasma according to the theoretical calculation $E = \int d\mathbf{p} f(p_\perp, p_\parallel, t)(\gamma - 1)$ (crosses), where $f(p_\perp, p_\parallel, t)$ is given by Eq. (2.22). Bottom: Percentual change of the total simulation energy (sum of plasma energy and synchrotron radiation) over time.

A.2 CHAPTER 3

We study radiatively cooled rings and the subsequent ECMI via particle-in-cell (PIC) simulations with OSIRIS [81], including classical [91] and QED [28] radiation reaction. The PIC method is widely used in plasma physics to model the behaviour of plasmas by solving the equations of motion for charged particles and the self-consistent evolution of electromagnetic fields. The plasma is represented by a large number of particles, which move according to the Lorentz force (with Landau-Lifshiftz force to account for semi-classical radiative losses [91, 100], and QED Monte Carlo module to account for QED processes [28]) in response to the electromagnetic fields. These fields, in turn, are computed on a grid using Maxwell's equations,

with the particle motions and fields updated iteratively.

PIC simulations are well-suited for studying kinetic instabilities in plasmas, such as the electron cyclotron maser instability (ECMI), because they capture the full range of particle interactions and non-linear effects. The massively parallel nature of these simulations allows for the handling of large-scale problems, making it possible to explore complex phenomena in tenuous, synchrotron-cooled plasmas with high fidelity and at unprecedented scales.

For the simulations presented in this work, we have considered the setup described analytically. The ECMI is a kinetic instability for which the relevant dynamics occur in momentum space, and the resulting excited wave modes propagate either parallel or perpendicular to the magnetic field. Therefore, our simulations employ a 2D configuration space and full 3D momentum space. This guarantees that all the relevant physics of the ECMI and cooling dynamics are captured in our setup. There is a magnetic field aligned along the x_1-direction of strength $B = 100$ GG, *i.e.* $B_0 \simeq 0.002$ normalized to the Schwinger field ($B_{Sc} = 4.4 \times 10^1 3$ Gauss). The magnetic field has a cyclotron frequency $\omega_{ce} = |e|B/m_e = 1.75 \times 10^{18}$ s^{-1}. All relevant timescales and lengths are normalized to the cyclotron period ω_{ce}^{-1} and c/ω_{ce}. The simulations utilize a small timestep such that the cyclotron period is accurately resolved $\Delta t = 0.014\,\omega_{ce}^{-1}$ and a spatial resolution of $\Delta x = 0.02\,c/\omega_{ce}$ (in both directions), which fulfils the 2D Courant condition $\Delta x > 2^{-1/2} c\Delta t$. This resolution resolves the gyromotion of all electrons with at least ~ 70 temporal steps, with higher energy particles being resolved with even more spatial and temporal points. The simulation window has a size of $L_1 = 200\,c/\omega_{ce}$ and $L_2 = 1000\,c/\omega_{ce}$, this yields a simulation grid of size 10000×50000 and we employ 16 particles per cell, *i.e.* a total of 16 billion computational particles.

The dimensions of the simulation box were carefully chosen, the x_2-direction utilises a larger domain to capture the theoretically predicted modes that propagate perpendicular and almost perpendicular to the magnetic field (a 1D3V PIC simulation would solely capture the the wave dynamics propagating perfectly parallel to the simulation domain, but not those at small angles).

The simulations were run for $40000\,\omega_{ce}^{-1}$, this is $\sim 2.8 \times 10^6$ time iterations. Due to the size of each simulation, the high-resolution runs were performed in LUMI-C (Finland) and had an average cost of 1 million CPU hours. Smaller simulations were performed in Deucalion (Portugal).

The plasma was initialized with a plasma frequency ratio of $\omega_{pe}/\omega_{ce} \simeq 0.00223$ for each species. This value was carefully chosen to model a low-density electron-positron pair plasma in a strong magnetic field, where $\omega_{pe}/\omega_{ce} \ll 1$ is characteristic of tenuous astrophysical environments. From a computational standpoint, this ratio corresponds to a total normalized density of $n = 0.1$ (i.e., 0.05 per species), which is the lowest density that still allows resolving multiple plasma skin depths within the simulation domain. Specifically, with $p_{th} = 1000\,m_e c$, this density ensures that $c/\omega_{pe} \ll L \sim 1000\,c/\omega_{ce}$, while maintaining numerical accuracy and avoiding excessive computational cost. Simulations at lower densities would require prohibitively large box sizes or cell counts to adequately resolve the relevant kinetic scales. The pair plasma is initialized from a relativistic Maxwellian distribution $f\left(p_\perp, p_\parallel\right) \propto$

$e^{-\left(p_\perp^2+p_\parallel^2\right)/(2p_{th}^2)}$, with additional runs using a Maxwell-Jüttner distribution confirming the same results, as expected in the ultra-relativistic regime.

The macro-particles employ cubic interpolation. Different current smoothing filters were tested, and we found that first-order binomial smoothing was sufficient to reduce the computational collisionality, for the large number of time steps in the simulations. For the simulations shown in this work, OSIRIS employed the Landau-Lifshitz model for classical radiation reaction as described by [91]. Moreover, QED simulations which employ a Monte Carlo method to model quantum synchrotron emission [28], were also used, QED simulations agree with simulations employing the Landau-Lifshitz pusher with the inclusion of stochastic diffusion, as expected as $\chi = pB_0/(m_e c)$ decreases rapidly during the cooling process. These effects will be explored elsewhere at higher energies, where diffusive effects are expected to be dominant.

Convergence studies were performed to determine the computational parameters and to ensure energy conservation accounting for synchrotron losses.

It is important to note that all results, both numerical and analytical, are presented in the proper frame of the plasma or beam. This means that the results can be directly applied to beam-plasma systems in other reference frames through the appropriate Lorentz transformation.

A.3 CHAPTER 4

The simulations were performed using the OSIRIS Particle-In-Cell code in a quasi-3D (cylindrical coordinates with azimuthal mode decomposition) geometry, retaining only the $m = 0$ azimuthal mode. The simulation domain spanned $L_x \times L_r = 30 \times 60\ (c/\omega_{pe})^2$, discretized using 2500×5000 cells, yielding a grid spacing of $\Delta x = 0.012\ c/\omega_{pe}$. The simulation employed a moving window propagating along the longitudinal direction at the speed of light. The radial extent of the simulation box was chosen to be twice the longitudinal size to avoid boundary effects that might modify the blowout structure; this was verified through convergence testing. The plasma had a peak density of $n_0 = 5 \times 10^{19}$ cm^{-3}, corresponding to a plasma frequency $\omega_p \simeq 3.98 \times 10^{14}$ s^{-1}. Time was normalized to ω_p^{-1}, and the timestep was set to $\Delta t = 0.0069\ \omega_p^{-1}$, satisfying the Courant condition $\Delta t < \Delta x/(c\sqrt{3})$.

The beam configuration consisted of a high-density driver beam and a lower-density witness beam, both initialized with Gaussian density profiles in the longitudinal and radial directions. The driver beam had a charge of 0.3 nC, a waist size of 5 ¯m, and a length of 2 ¯m. The witness beam had a total charge of approximately 0.1 nC, a longitudinal FWHM of ~ 1 ţm, and the same radial width as the driver. Each species was initialized with a 3D momentum distribution. Both beams were initialized with a bulk energy of 10 GeV, a relative energy spread of 1%, and a transverse thermal spread of $\Delta p_{2,3} \sim 6\ m_e c$, corresponding to a normalized emittance of 300 mm mrad.

The background plasma consisted of cold electrons ($T_e = 0$) and immobile ions. Its density profile featured a 1 mm linear up-ramp, a 5 mm flattop region, and a 1 mm down-ramp. Macroparticles employed cubic interpolation, with 64 particles per cell used for both the driver and

witness beams, and 25 particles per cell for the background plasma. Fields were evolved using a second-order finite-difference time-domain Maxwell solver. Several current smoothing filters were tested, and it was found that smoothing did not significantly affect the formation of ring structures under these simulation conditions. A first-order binomial filter was therefore used in the final setup. Radiation reaction was included using the reduced Landau-Lifshitz (LLR) model for classical radiation losses, which retains the two leading-order terms of the full Landau-Lifshitz equation. Companion simulations with radiation reaction disabled were carried out for direct comparison.

A.3.1 Synthetic screen and spectrometer diagnostics from PIC simulations

We export the full macroparticle data at the final simulation iteration, i.e., positions $\mathbf{r}_i$, momenta $\mathbf{p}_i$, and weights w_i. Since the plasma has transitioned to vacuum, particles are propagated ballistically to a detection plane placed 100 cm downstream. For each particle, the intersection time is $t_i^* = (z_{\mathrm{scr}} - z_i)/v_{z,i}$, after which $x_i^* = x_i + v_{x,i}t_i^*$ and $y_i^* = y_i + v_{y,i}t_i^*$ are recorded (constant momentum throughout). All particles that reach the plane are included; no acceptance cuts are applied beyond the field of view. The screen image is formed by depositing the particle weights w_i onto a regular (x, y) grid at (x_i^*, y_i^*); intensities are normalized to the peak, and we display the central window $x, y \in [-25, 25]$ (cm in the figures).

For the synthetic spectrometer, we compute for each particle the divergence $\theta_i = \tan^{-1}(p_{\perp,i}/p_{\parallel,i})$ and energy $E_i = \gamma_i m_e c^2$, then accumulate w_i on a regular grid in (θ, E). No instrumental response, filtering, or resolution broadening is applied; the maps reflect direct projections of the exported simulation data. To isolate the witness signal, particles tagged as driver are excluded prior to both projections. Experimentally, this corresponds to subtracting driver-only background shots from shots containing both driver and witness.

A.4 Chapter 5

A.4.1 3D runs: Fireball-I

Three-dimensional (3D3V) PIC simulations were performed using the OSIRIS code at the exascale LUMI supercomputer (Finland). Simulations use a moving window travelling at c along the z-direction that follows relativistic electrons, positrons and protons in the secondary beam as they propagate through the ambient plasma. The electron-positron-proton beam is initialised before entrance of the plasma, centred at $z = -20\,\mathrm{cm}$ and $x = y = 0$. The density and momentum phase-space distributions are accurately modelled by fitting analytical forms to the distributions at the entrance of the plasma cell, after the glassy carbon window, obtained from a FLUKA simulation. The longitudinal density profile of the plasma is chosen to match closely the measured electron density profile of the plasma discharge: double peaked with maximum plasma density $n_0 = 1.78 \times 10^{12}\,\mathrm{cm}^{-3}$, see Appendix H. All quantities in the simulations are normalized to the peak plasma density n_0 (associated plasma period

$\omega_{\mathrm{pe}}^{-1} = 13.29\,\mathrm{ps}$, and plasma skin-depth $c/\omega_{\mathrm{pe}} = 3.98\,\mathrm{mm}$). The moving window has absorbing boundary conditions and dimensions $L_x \times L_y \times L_z = 3.5\,\mathrm{cm} \times 3.5\,\mathrm{cm} \times 40\,\mathrm{cm}$, discretised into $879 \times 879 \times 10050$ cells. This yields a spatial resolution $\Delta x = 0.01\, c/\omega_{\mathrm{pe}} = 0.096\,\mathrm{mm}$. The simulations employ a time resolution $\Delta t = 0.0057\,\omega_{\mathrm{pe}}^{-1} = 43.7\,\mathrm{fs}$, fulfilling the 3D Courant-Friedrichs-Lewy condition: $c\Delta t < \Delta x/\sqrt{3}$. We employ 8 macro-particles per cell (for each species), and utilize quadratic interpolation with first-order binomial current smoothing. The numerical parameters were carefully chosen after a convergence study with 2D3V PIC simulations.

A.4.2 Convergence study: Fireball-I

Table 1: Particles per Skin-Depth Area

#PPC \ Δx	1 [c/ω_{pe}]	0.64 [c/ω_{pe}]	0.32 [c/ω_{pe}]	0.16 [c/ω_{pe}]	0.04 [c/ω_{pe}]	0.02 [c/ω_{pe}]	0.01 [c/ω_{pe}]
1	1.0	2.44141	9.76562	39.0625	625.0	2500.0	10000.0
2	2.0	4.88281	19.53125	78.125	1250.0	5000.0	20000.0
4	4.0	9.76562	39.0625	156.25	2500.0	10000.0	40000.0
8	8.0	19.53125	78.125	312.5	5000.0	20000.0	80000.0
16	16.0	39.0625	156.25	625.0	10000.0	40000.0	160000.0
32	32.0	78.125	312.5	1250.0	20000.0	80000.0	320000.0
64	64.0	156.25	625.0	2500.0	40000.0	160000.0	640000.0
128	128.0	312.5	1250.0	5000.0	80000.0	320000.0	1280000.0
256	256.0	625.0	2500.0	10000.0	160000.0	640000.0	2560000.0

Table 2: Energy Conservation [0.01%]

#PPC \ Δx	1 [c/ω_{pe}]	0.64 [c/ω_{pe}]	0.32 [c/ω_{pe}]	0.16 [c/ω_{pe}]	0.04 [c/ω_{pe}]	0.02 [c/ω_{pe}]	0.01 [c/ω_{pe}]
1	6.04128	4.03424	1.91417	0.95637	0.23584	0.1173	0.05839
2	6.35353	3.98504	1.93813	0.9499	0.23546	0.1173	0.0584
4	6.3554	3.98465	1.93873	0.94975	0.23544	0.1173	0.0584
8	6.34466	3.989	1.9311	0.95315	0.23554	0.11736	0.05839
16	6.30996	3.98949	1.93178	0.95316	0.23556	0.11735	0.0584
32	6.35589	3.96281	1.93184	0.95317	0.23555	0.11735	0.0584
64	6.35684	3.96281	1.93172	0.95317	0.23555	0.11735	0.0584
128	6.3567	3.96597	1.93172	0.95277	0.23555	0.11735	0.0584
256	6.35642	3.96598	1.93172	0.95278	0.23555	0.11735	0.0584

Table 3: B-Field Magnitude [$m_e c\omega_{pe}/e$]

#PPC \ Δx	1 [c/ω_{pe}]	0.64 [c/ω_{pe}]	0.32 [c/ω_{pe}]	0.16 [c/ω_{pe}]	0.04 [c/ω_{pe}]	0.02 [c/ω_{pe}]	0.01 [c/ω_{pe}]
1	0.10066	0.09297	0.129	0.16863	0.17279	0.17233	0.17085
2	0.05271	0.05804	0.129	0.15145	0.16893	0.17059	0.17024
4	0.05244	0.05696	0.13054	0.15125	0.16879	0.17032	0.16985
8	0.03513	0.07037	0.12966	0.15371	0.16757	0.16972	0.1696
16	0.03529	0.071	0.12941	0.15395	0.16747	0.16913	0.16962
32	0.03573	0.07142	0.12964	0.15415	0.16743	0.16914	0.16962
64	0.03595	0.07117	0.12976	0.15409	0.16731	0.1691	0.16954
128	0.0362	0.07116	0.12983	0.15388	0.16744	0.16906	0.1696
256	0.03615	0.07094	0.1297	0.15388	0.1674	0.16898	0.16952

To ensure numerical accuracy, we conducted a resolution study with 2D3V PIC simulations, using the same parameters later employed in the 3D simulations presented in the main text. The grid resolution Δx was varied from $1 \times c/\omega_{pe}$ to $10^{-2} \times c/\omega_{pe}$, and the number of particles per cell (PPC) from 1 to 256. The timestep Δt was adjusted accordingly to satisfy the CFL condition. The number of computational particles per skin-depth area spans six orders of magnitude, with the largest 2D run reaching 2.56×10^6 particles per skin-depth area. For

the 3D simulation, we scaled this by a factor of ~ 4, achieving approximately 8×10^6 particles per skin-depth cube. Achieving this level of numerical resolution in 3D is typically challenging, but our approach ensures accuracy and reliability. Energy conservation was also carefully evaluated, with errors ranging from 0.06% (lowest resolution) to 0.0005% (highest resolution), confirming the numerical stability of our results (see Table 2).

To demonstrate that the observed magnetic field amplification arises from physical processes rather than numerical artifacts, we examined the field's dependence on computational parameters. Table 3 shows that increasing the resolution leads to stronger field growth, asymptotically approaching $B \sim 0.1695\, m_e c\omega_{pe}/e$. Meanwhile, increasing the PPC slightly reduces the growth rate, consistent with expectations, since the convergence study assumes a cold plasma, the process is fluid-like rather than kinetic. Low-PPC PIC simulations resemble fluid simulations, which tend to overestimate magnetic field growth. However, as PPC increases, the field strength converges asymptotically.

We further analyzed the time evolution of the magnetic field as a function of beam propagation length, considering two cases: (i) fixed PPC (256) with varying resolution and (ii) fixed resolution ($\Delta x = 0.01\, c/\omega_{pe}$) with varying PPC (Figure A.2). The left panel shows that the B-field evolution asymptotically converges, with minimal changes when increasing the resolution from $0.02\, c/\omega_{pe}$ to $0.01\, c/\omega_{pe}$, demonstrating that $\Delta x = 0.01\, c/\omega_{pe}$ is sufficient to resolve the relevant scales. Similarly, the right panel shows that increasing PPC leads to convergence, with little difference between 128 and 256 PPC.

We also studied the effects of particle interpolation (particle shape function). Figure A.3 shows that increasing the interpolation order leads to convergence, with negligible differences between quadratic and cubic interpolation. Thus, quadratic interpolation is sufficient to accurately model the experimental setup.

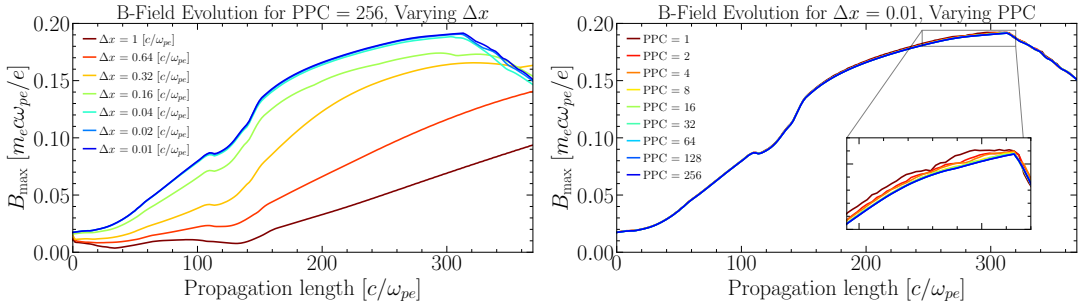

FIGURE A.2: B-field strength as a function of beam propagation distance, demonstrating convergence for both spatial resolution (left) and PPC (right).

Finally, it is important to highlight that the fully 3D simulations used to study the experimental setup employed a comparable spatial resolution and four times the number of computational particles per skin-depth volume. Achieving this level of resolution in 3D is rare, setting a new standard for simulations of beam-plasma interactions.

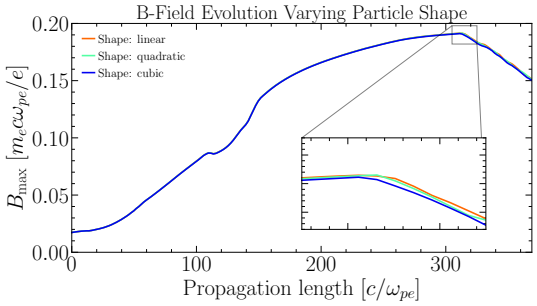

FIGURE A.3: B-field strength as a function of beam propagation distance for different particle shapes, showing that quadratic interpolation is sufficient.

A.4.3 FIREBALL-III BEAM PARAMETERS

Three-dimensional (3D3V) PIC simulations were performed using OSIRIS to model the Fireball beam produced with a new converter geometry. All computational and numerical parameters were kept identical to the baseline configuration used for previous simulations: spatial resolution $\Delta x = 0.02, c/\omega_{\rm pe}$, timestep $\Delta t = 0.01152, \omega_{\rm pe}^{-1}$, quadratic interpolation, and binomial current smoothing. Similarly, the plasma profile and normalization remain unchanged. The main physical modification is the extension of the plasma cell, which now spans 3 m, allowing significantly longer beam propagation and enabling the onset of late-time kinetic instabilities.

Compared to the previous converter setup, the new beam is significantly more collimated and energetic. The bulk longitudinal momentum increased from $p_1 \approx 205, m_e c$ to $p_1 \approx 614, m_e c$, while the angular spread decreased from $\Delta\theta \approx 0.025$ to $\Delta\theta \approx 0.008$, yielding a beam that is roughly three times more collimated. Transversely, the electron-positron beam broadened from $r_\perp \approx 0.80$ mm to $r_\perp \approx 1.60$ mm, while the proton beam remained tightly focused, with a slight reduction from $r_\perp \approx 0.28$ mm to $r_\perp \approx 0.27$ mm.

In terms of composition, the relative densities of electrons and positrons remain similar, with $n_{e^-}/n_{e^+} \approx 0.3/0.25$, but the proton content has been significantly reduced, from $n_p = 0.15$ in the original setup to $n_p = 0.03$, yielding a more pair-dominated beam. These updates reflect improved spectral selection and reduced background contamination in the revised converter geometry, leading to cleaner and more representative initial conditions for studying beam-plasma interactions over meter-scale propagation.

A.4.4 PROTON-MODULATED SEEDING SIMULATIONS

The simulations presented in Fig. 5.10 were performed using 2D3V Particle-in-Cell simulations with periodic boundary conditions in both transverse directions. The simulation domain covered $L_x = 25\ c/\omega_{pe}$ and $L_y = 50\ c/\omega_{pe}$, discretized into 1000×2000 cells, with a timestep of $\Delta t = 0.009\ \omega_{pe}^{-1}$. The plasma consisted of electrons, positrons, and protons with initial densities $n_{e^-} = n_{e^+} = n_0/2$ and $n_p = n_0/2$, ensuring overall charge neutrality.

All species were initialized with the same momentum distribution as in the main simulations, reflecting realistic beam spectra with an angular divergence of $\theta = 0.025$. To investigate seeding, the proton beam was modulated with a weak transverse density perturbation of the form $\delta n_p/n_p = 0.005 \sin(2\pi y/\lambda)$, with the wavelength λ varied across simulations to assess resonant enhancement of the instability. This imposed spatial modulation imprints a seed electromagnetic field structure that can selectively trigger the current filamentation instability at specific scales.

A five-pass smoothing filter was applied to suppress high-frequency numerical noise. These simulations enabled controlled studies of how initial background structure in a heavy species can modulate and seed instabilities in relativistic pair plasmas.

A.4.5 Simulation parameters for exotic species

The simulations shown in Fig. 5.15 were performed using the same 2D3V periodic PIC setup as in Fig. 5.10 in Appendix A.4.4, with the same spatial resolution, box size ($L_x = 25\ c/\omega_{pe}$, $L_y = 50\ c/\omega_{pe}$), and timestep ($\Delta t = 0.009\ \omega_{pe}^{-1}$). The setup was extended to include additional heavy species: pions and antipions, each with charge-to-mass ratio $q/m = \pm 1/264$. These were initialized with densities of $0.5\ n_0$ and sampled from realistic energy distributions based on the secondary particle spectrum of the hadronic cascade. Their longitudinal momentum distribution matched that of the primary pair beam, and their transverse spread was set equal to that of the positrons. All species were injected with homogeneous spatial profiles, ensuring overall charge neutrality. Diagnostics and smoothing settings remained unchanged. This configuration enabled the study of delayed filamentation in the pion component, triggered by nonlinear structures in the lighter electron-positron beam.

APPENDIX B

JUSTIFICATION OF THE RADIATIVE OPERATOR IN THE KINETIC EQUATION

In this appendix, we derive an effective synchrotron cooling operator suitable for use in the Vlasov equation. Starting from the quantum description of radiation reaction as a stochastic process, we follow a standard kinetic-theory procedure to derive a Fokker–Planck operator that captures photon emission in strong fields. This approach makes it possible to study the interplay between radiation reaction and collective plasma effects, while allowing a smooth transition between quantum and classical regimes.

Our goal is twofold: first, to establish the form of the radiative operator under quantum synchrotron emission; and second, to show that in the classical limit $\hbar \to 0$, this operator reduces to a purely advective form that matches the relativistic Landau–Lifshitz force (shown previously in Eq. (2.2)). In this limit, radiation reaction enters the Vlasov equation as a classical drift force, supplementing the Lorentz force. We demonstrate this reduction explicitly, thus validating the use of the classical radiation reaction force in regimes where quantum corrections become negligible.

To study the effects of quantum synchrotron cooling on a distribution of particles, we can construct a radiative operator. The master equation models the evolution of a distribution function due to stochastic synchrotron emission [28, 241, 242]

$$\left.\frac{\partial f}{\partial t}\right|_{RR} = \int d\mathbf{p}_\gamma \mathcal{W}\left(\mathbf{p}+\mathbf{p}_\gamma, \mathbf{p}_\gamma\right) f(\mathbf{p}+\mathbf{p}_\gamma, t) - f(\mathbf{p}) \int d\mathbf{p}_\gamma \mathcal{W}\left(\mathbf{p}, \mathbf{p}_\gamma\right), \tag{B.1}$$

where $\mathcal{W}\left(\mathbf{p}, \mathbf{p}_\gamma\right)$ is the emission rate of a photon with momentum $\mathbf{p}_\gamma$ by an electron with momentum $\mathbf{p}$, W has units of momentum per unit of time. From now on we normalize time per cyclotron period such that, the emission rate is in units of $m_e c$. If we assume that photon

emission occurs parallel to the particle momentum, is given by [18, 28]

$$\mathcal{W}(\mathbf{p},\mathbf{p}_\gamma) = \frac{1}{\sqrt{3}\pi}\frac{\alpha B_0 m_e c}{\gamma^2}\delta(\hat{\mathbf{p}}_\gamma - \hat{\mathbf{p}}) \times \left[\int_\nu^\infty K_{5/3}(x)dx + \frac{(\mathcal{E}_\gamma/\gamma)^2}{1-\mathcal{E}_\gamma/\gamma}K_{2/3}(\nu)\right], \tag{B.2}$$

where $K_n(x)$ is the modified n-th order Bessel function of second-kind (or Basset function), $\mathcal{E}_\gamma$ is the energy of the emitted photon in $m_e c^2$, γ is the Lorentz factor of the electron, $B0 = B/B_{Sc}$, and $\nu = 2(\mathcal{E}_\gamma/\gamma)/[3\chi(1-\mathcal{E}_\gamma/\gamma)]$. Recall that χ is the Lorentz invariant quantity $\chi = p_\perp |\mathbf{B}|/(m_e c B_{\mathrm{Sc}})$, that for a constant magnetic field simplifies to $\chi = p_\perp B/(m_e c B_{Sc})$. One notes that in the classical limit when the photon energy is much smaller than the kinetic energy of the electron, *i.e.*, $(\mathcal{E}_\gamma/\gamma)^2 \ll 1$, one recovers the classical radiation rate from the classical synchrotron, which can be derived from classical electrodynamics [17, 243–245]

$$\mathcal{W}(\mathbf{p},\mathbf{p}_\gamma) = \frac{\sqrt{3}}{2\pi}\alpha B_0 m_e c\frac{\delta(\hat{\mathbf{p}}_\gamma - \hat{\mathbf{p}})\,\omega_{ce}}{\omega_c}\int_{\omega/\omega_c}^\infty K_{5/3}(x)dx, \tag{B.3}$$

as $\nu = 2\omega/(3\omega_{ce}\gamma^2)$, *i.e.*, $\nu = \omega/\omega_c$ the ratio between the emitted frequency and critical frequency. This hints that the term proportional to $K_{2/3}(\nu)$ is of quantum nature.

To make analytical progress, we approximate the integro-differential collision operator in Eq. (B.1) using a Kramers–Moyal expansion [242, 246, 247], which systematically expands the integral in terms of the moments of the momentum change per emission event. Physically, this corresponds to assuming that the cumulative effect of many small photon emissions can be treated as a continuous stochastic process. Truncating the expansion at second order yields a Fokker–Planck-type operator, which captures both deterministic drift (mean radiation reaction force) and stochastic diffusion (energy spread due to quantum fluctuations). The resulting transport-diffusion form is:

$$\left.\frac{\partial f}{\partial t}\right|_{RR} = \nabla_p\cdot[\mathbf{F}f] + \frac{1}{2}\nabla_p^2[Df], \tag{B.4}$$

where

$$\mathbf{F} = \frac{2}{3}\frac{9\sqrt{3}}{8\pi}\alpha B_0\chi^2\hat{\mathbf{p}}\int_0^\infty d\nu\left[\frac{2\nu^2K_{5/2}(\nu)}{(2+3\nu\chi)^2} + \frac{36\nu^3\chi^2K_{2/3}(\nu)}{(2+3\nu\chi)^4}\right] \tag{B.5}$$

represents the average radiative drag, and

$$D = \frac{2}{3}\alpha B_0 m_e^2 c^2\chi^3\gamma\int_0^\infty d\nu\left[\frac{2\nu^3K_{5/2}(\nu)}{(2+3\nu\chi)^3} + \frac{54\nu^4\chi^5K_{2/3}(\nu)}{(2+3\nu\chi)^5}\right] \tag{B.6}$$

the momentum diffusion coefficient associated with stochastic photon emission.

In the limit $\chi \ll 1$, the integrands in Eqs. (B.5) and (B.6) simplify considerably. Specifically, terms proportional to higher powers of χ in the numerator and denominator can be neglected. This allows us to keep only the leading-order contributions:

$$\mathbf{F} \approx \frac{2}{3}\frac{9\sqrt{3}}{8\pi}\alpha B_0\chi^2\hat{\mathbf{p}}\int_0^\infty\frac{2\nu^2K_{5/2}(\nu)}{4}\,d\nu = \frac{2}{3}\frac{9\sqrt{3}}{8\pi}\alpha B_0\chi^2\hat{\mathbf{p}}, \tag{B.7}$$

$$D \approx \frac{2}{3}\alpha B_0 m_e^2 c^2\chi^3\gamma\int_0^\infty\frac{2\nu^3K_{5/2}(\nu)}{8}\,d\nu = \frac{55}{24\sqrt{3}}\alpha B_0 m_e^2 c^2\chi^3\gamma. \tag{B.8}$$

The resulting integrals are known from synchrotron radiation theory [245]:

$$\int_0^\infty \nu^2 K_{5/2}(\nu)\, d\nu = \frac{3\pi}{8\sqrt{3}}, \qquad \int_0^\infty \nu^3 K_{5/2}(\nu)\, d\nu = \frac{55\pi}{16\sqrt{3}}. \tag{B.9}$$

This yields the following effective operator for radiation reaction:

$$\left.\frac{\partial f}{\partial t}\right|_{RR} = -\nabla_p \cdot [\mathbf{F}_{RR} f] + \frac{55}{48\sqrt{3}} \alpha B_0 m_e^2 c^2 \nabla_p^2 \left[\chi^3 \gamma f\right], \tag{B.10}$$

where $\mathbf{F}_{RR}$ is the classical radiation reaction force from Eq. (2.2), valid in the relativistic limit $\gamma \gg 1$.

Combining this with the Vlasov equation, we obtain a "semi-classical" kinetic model for synchrotron-cooled plasmas, in which quantum effects enter as a momentum-space diffusion operator:

$$\frac{\partial f}{\partial t} + \frac{\mathbf{p}}{\gamma} \cdot \nabla_r f + \nabla_p \cdot [(\mathbf{F}_{RR} + \mathbf{F}_L) f] = \frac{55}{48\sqrt{3}} \alpha B_0 m_e^2 c^2 \nabla_p^2 \left[\chi^3 \gamma f\right]. \tag{B.11}$$

The only remaining quantum correction appears on the right-hand side of Eq. (B.11). This becomes evident by expressing $\chi = (B/B_{\mathrm{Sc}})(p_\perp/m_e c) = (\hbar B e p_\perp)/(m_e^2 c^3)$, and noting that $\alpha/B_{\mathrm{Sc}} = 1/B_c$, where B_c is the classical critical field. This implies that the quantum diffusion term scales as $\chi^3 \propto \hbar^3$, and thus vanishes in the classical limit $\hbar \to 0$, recovering the Vlasov equation with only classical radiation reaction.

In summary, we have derived a quantum-corrected kinetic equation for synchrotron-cooled plasmas by expanding the master equation for stochastic photon emission in the small-χ limit. This yields a semi-classical Vlasov equation with a classical radiation reaction force and a quantum-induced momentum diffusion term. In the limit $\hbar \to 0$, the diffusion vanishes, recovering the classical Landau-Lifshitz form. This framework provides incorporates leading-order QED corrections in kinetic models, an explains the observed features of quantum particle-in-cell simulations in regimes where $\chi \sim 1$.

APPENDIX C

INVERTED LANDAU POPULATIONS DUE TO SYNCHROTRON COOLING

C.1 ANALYTIC SOLUTION OF SYNCHROTRON COOLING TRAJECTORIES

The equations of motion for a relativistic particle under synchrotron radiation reaction in a constant magnetic field are given by [132, 133]:

$$\frac{dp_\perp}{dt} = -\frac{2}{3}\alpha B_0 \frac{p_\perp + p_\perp^3}{\gamma}, \tag{C.1}$$

$$\frac{dp_\parallel}{dt} = -\frac{2}{3}\alpha B_0 \frac{p_\parallel p_\perp^2}{\gamma}, \tag{C.2}$$

where $\gamma = \sqrt{1 + p_\parallel^2 + p_\perp^2}$ and α is the fine-structure constant. To simplify, define the dimensionless time $\tau = \frac{2}{3}\alpha B_0 t$.

We use the chain rule:

$$\frac{dp_\perp}{dp_\parallel} = \frac{1 + p_\perp^2}{p_\parallel p_\perp}, \tag{C.3}$$

which integrates to:

$$\frac{p_\parallel}{\sqrt{1 + p_\perp^2}} = \frac{p_{\parallel 0}}{\sqrt{1 + p_{\perp 0}^2}} = \text{const} = C_1, \tag{C.4}$$

where $p_{\parallel 0}$ and $p_{\perp 0}$ correspond to the initial parallel and perpendicular momentum, respectively.

Using this constant of motion, the perpendicular equation becomes:

$$\frac{dp_\perp}{d\tau} = -\frac{p_\perp \sqrt{1 + p_\perp^2}}{\sqrt{1 + C_1^2}}. \tag{C.5}$$

This can be separated and integrated:

$$\int \frac{dp_\perp}{p_\perp\sqrt{1+p_\perp^2}} = -\frac{\tau}{\sqrt{1+C_1^2}} + \text{const}$$

Solving the integral and exponentiating, one obtains:

$$p_\perp^2(\tau) = \left(\frac{1+Ae^{-2\tau/\sqrt{1+C_1^2}}}{1-Ae^{-2\tau/\sqrt{1+C_1^2}}}\right)^2 - 1, \tag{C.6}$$

with

$$A = \frac{\sqrt{1+p_{\perp 0}^2}-1}{\sqrt{1+p_{\perp 0}^2}+1}.$$

Using the identity:

$$\tanh(x) = \frac{1-e^{-2x}}{1+e^{-2x}}, \quad \text{so} \quad e^{-2x} = \frac{1-\tanh x}{1+\tanh x},$$

we rewrite the solution in closed form:

$$p_\perp(\tau) = \frac{p_{\perp 0}}{\cosh(\tau')\left[1+\sqrt{1+p_{\perp 0}^2}\tanh(\tau')\right]}, \tag{C.7}$$

with

$$\tau' = \tau\cdot\frac{\sqrt{1+p_{\perp 0}^2}}{\gamma_0}, \quad \gamma_0 = \sqrt{1+p_{\perp 0}^2+p_{\parallel 0}^2}.$$

Using the constant of motion $C_1 = p_{\parallel 0}/\sqrt{1+p_{\perp 0}^2}$, we can reconstruct the parallel momentum as:

$$p_\parallel(\tau) = p_{\parallel 0}\cdot\frac{1+\tanh(\tau')/\sqrt{1+p_{\perp 0}^2}}{1+\sqrt{1+p_{\perp 0}^2}\tanh(\tau')} \tag{C.8}$$

These expressions fully describe the exact radiative cooling trajectories in momentum space. Notably, as $t\to\infty$, $p_\perp\to 0$ and $p_\parallel\to C_1$, preserving the quantity $p_\parallel/\sqrt{1+p_\perp^2}$, consistent with the covariant nature of the Landau–Lifshitz radiation reaction formulation.

C.2 Solution to the kinetic synchrotron cooling equation (Eq. (2.17))

We now solve the kinetic equation governing synchrotron cooling in relativistic plasmas. As introduced in Eq. (2.17), the Vlasov equation for a distribution function f undergoing classical synchrotron cooling reads

$$\frac{\partial f}{\partial\tau} - \frac{p_\perp^3+p_\perp}{\gamma}\frac{\partial f}{\partial p_\perp} - \frac{p_\perp^2 p_\parallel}{\gamma}\frac{\partial f}{\partial p_\parallel} - \frac{2+4p_\perp^2}{\gamma}f = 0, \tag{C.9}$$

where τ is a dimensionless time and $\gamma = \sqrt{1 + p_\perp^2 + p_\parallel^2}$ is the Lorentz factor.

In regions where $p_\perp \gg p_\parallel$, we approximate $\gamma \simeq \sqrt{1 + p_\perp^2}$ and neglect the term proportional to $\partial f / \partial p_\parallel$, yielding the reduced form

$$\frac{\partial f}{\partial \tau} - \frac{p_\perp^3 + p_\perp}{\gamma} \frac{\partial f}{\partial p_\perp} - \frac{2 + 4p_\perp^2}{\gamma} f = 0. \tag{C.10}$$

We solve this equation using the method of characteristics. The characteristic system reads:

$$\frac{dp_\perp}{d\tau} = -\frac{p_\perp^3 + p_\perp}{\gamma}, \tag{C.11}$$

$$\frac{df}{d\tau} = \frac{2 + 4p_\perp^2}{\gamma} f. \tag{C.12}$$

Equation (C.11) corresponds to the single-particle perpendicular equation of motion under synchrotron cooling (cf. Eq. (2.3) with $p_\parallel = 0$). Its solution is

$$p_\perp(\tau) = \frac{p_{\perp 0}}{\cosh(\tau) \left[1 + \sqrt{1 + p_{\perp 0}^2} \tanh(\tau)\right]}, \tag{C.13}$$

where $p_{\perp 0} \equiv p_\perp(\tau = 0)$ is the initial perpendicular momentum.

To invert this expression and solve for $p_{\perp 0}$, define the auxiliary variable

$$a \equiv \log\left(\frac{p_\perp}{\sqrt{1 + p_\perp^2} + 1}\right). \tag{C.14}$$

We recall the identity for the hyperbolic cosecant of a sum:

$$\operatorname{csch}(a + \tau) = \frac{1}{\sinh(a)\cosh(\tau) + \cosh(a)\sinh(\tau)}. \tag{C.15}$$

Using this identity, and substituting $\sinh(a)$ and $\cosh(a)$ in terms of $p_\perp$, one can show that

$$\frac{p_\perp \operatorname{sech}(\tau) \left(1 + \sqrt{1 + p_\perp^2} \tanh(\tau)\right)}{\operatorname{sech}^2(\tau) - p_\perp^2 \tanh^2(\tau)} = -\operatorname{csch}\left(\log\left(\frac{p_\perp}{\sqrt{1 + p_\perp^2} + 1}\right) + \tau\right), \tag{C.16}$$

which yields the inverse solution:

$$p_{\perp 0} = -\operatorname{csch}\left(\log\left(\frac{p_\perp}{\sqrt{1 + p_\perp^2} + 1}\right) + \tau\right). \tag{C.17}$$

This identity is useful for evaluating the distribution function at any later time by tracing the solution backward along characteristics. Specifically, Eq. (C.12) integrates to

$$f(p_\perp, \tau) = f_0(p_{\perp 0}) \cdot \exp\left[\int_0^\tau \frac{2 + 4p_\perp^2(\tau')}{\gamma(\tau')} d\tau'\right], \tag{C.18}$$

with $p_\perp(\tau')$ given by Eq. (C.13) and $p_{\perp 0}$ as in Eq. (C.17).

The final closed-form expression for the distribution function at time τ is

$$f_\perp(p_\perp, \tau) = \frac{f_{\perp 0}\left(-\mathrm{csch}(a)\right)}{\left[\gamma_\perp \, p_\perp \, \sinh(a) \, \tanh(a)\right]^2}, \tag{C.19}$$

where

$$a = \log\left(\frac{p_\perp}{\gamma_\perp + 1}\right) + \tau, \qquad \gamma_\perp = \sqrt{1 + p_\perp^2}. \tag{C.20}$$

Equation (C.19) displays a formal singularity at $a = 0$, which occurs when $p_\perp = 1/\sinh(\tau)$. However, this lies outside the physically allowed domain of the solution. As discussed in the main text, synchrotron cooling confines the momentum-space support to

$$p_\perp < \frac{1}{\sinh(\tau)}, \tag{C.21}$$

ensuring that Eq. (C.19) remains well-behaved for all $\tau \geq 0$. At $\tau = 0$, the distribution is unconstrained and recovers its original support $p_\perp < \infty$.[1]

C.3 Solution to the relativistic kinetic synchrotron cooling equation (Eq. (2.21))

In the ultra-relativistic limit $\gamma \gg 1$ and $p_\perp \gg 1$, the single-particle trajectories and kinetic equation simplify considerably. Using the asymptotic expressions derived in Eqs. (2.5) and (2.6), the momentum evolution becomes

$$p_\perp(\tau) = \frac{p_{\perp 0}}{1 + \left(p_{\perp 0}^2/\gamma_0\right)\tau}, \tag{C.22}$$

$$p_\parallel(\tau) = \frac{p_{\parallel 0}}{1 + \left(p_{\perp 0}^2/\gamma_0\right)\tau}, \tag{C.23}$$

where $\gamma_0 = \sqrt{p_{\perp 0}^2 + p_{\parallel 0}^2}$ is the initial Lorentz factor.

In this regime, the Vlasov equation governing the distribution function $f(p_\perp, p_\parallel, \tau)$ simplifies to

$$\frac{\partial f}{\partial \tau} - \frac{p_\perp^3}{\gamma}\frac{\partial f}{\partial p_\perp} - \frac{p_\perp^2 p_\parallel}{\gamma}\frac{\partial f}{\partial p_\parallel} - \frac{4p_\perp^2}{\gamma} f = 0. \tag{C.24}$$

We solve Eq. (C.24) using the method of characteristics. The characteristic equations read

$$\frac{dp_\perp}{d\tau} = -\frac{p_\perp^3}{\gamma}, \tag{C.25}$$

$$\frac{dp_\parallel}{d\tau} = -\frac{p_\perp^2 p_\parallel}{\gamma}, \tag{C.26}$$

$$\frac{df}{d\tau} = \frac{4p_\perp^2}{\gamma} f. \tag{C.27}$$

[1] We note that at $t = \tau = 0$, Eq. (C.19) simplifies to $f(p_\perp, \tau = 0) = f_0(p_\perp)$, as expected.

Assuming $\gamma \approx p_\perp$ as is appropriate in the $p_\perp \gg p_\parallel$ limit, the characteristic equations can be solved analytically. Integrating Eq. (C.25) yields

$$p_\perp(\tau) = \frac{p_{\perp 0}}{1 + \tau p_{\perp 0}}, \tag{C.28}$$

which implies

$$p_{\perp 0} = \frac{p_\perp}{1 - \tau p_\perp}. \tag{C.29}$$

Using this, the longitudinal momentum evolves as

$$p_\parallel(\tau) = \frac{p_{\parallel 0}}{1 - \tau p_\perp}. \tag{C.30}$$

Solving the final characteristic equation for f, and substituting the above relations, we obtain the general solution:

$$f(p_\perp, p_\parallel, \tau) = \frac{f_0\left(\frac{p_\perp}{1-\tau p_\perp}, \frac{p_\parallel}{1-\tau p_\perp}\right)}{(1 - \tau p_\perp)^4}. \tag{C.31}$$

Equation (C.31) describes the evolution of an initial momentum distribution f_0 under synchrotron cooling in the relativistic regime. This expression features a formal singularity at $p_\perp = 1/\tau$, corresponding to $p_{\perp 0} \to \infty$. However, this singularity is never reached physically. As can be seen from Eq. (C.28), a particle with infinite initial momentum asymptotes toward $p_\perp = 1/\tau$. Therefore, all finite-momentum particles are constrained to

$$0 < p_\perp < \frac{1}{\tau}, \tag{C.32}$$

which ensures the solution remains regular and finite for all physical values of τ.

C.4 Arguments demonstrating the pervasiveness of ring distirbutions

Sec. 2.2.1 present the necessary condition for the any arbitrary initial distribution f_0 to develop into a ring distribution within a finite time. Now we present two weaker arguments that further support our conjecture that any initial relativistic plasma eventually develops momentum space bunching and an inverted Landau population in the shape of $\partial f/\partial p_\perp > 0$.

As Eq. (2.22) fully determines the temporal evolution for any given initial distribution f_0, and demonstrates several conclusions regarding the general evolution of momentum distributions undergoing synchrotron cooling. Firstly, The solution domain decreases with time, with an upper bound at $p_\perp^* = \tau^{-1}$ (such that $p_\perp \tau < 1$). Therefore, the distribution function is compressed within $p_\perp \leq p_\perp^*$, where $p_\perp^*$ describes the trajectory of a particle that $p_\perp(\tau = 0) = \infty$.

Argument 1: From Eq. (2.22) we can conjecture that a Landau population inversion, characterized by $\partial f/\partial p_\perp > 0$, develops in a finite time for a wide variety of initial momentum

distributions. This can be shown by rearranging $\partial f/\partial p_\perp > 0$ and considering $p_\parallel = 0$

$$4\epsilon f_0\left(p'_\perp, 0\right) > -p'_\perp \frac{\partial f_0}{\partial p'_\perp}\left(p'_\perp, 0\right), \tag{C.33}$$

where $p'_\perp = p_\perp/(1 - p_\perp\tau)$ and we have used the fact that $0 < p_\perp < p^*_\perp$ to write $p_\perp = \epsilon p^*_\perp = \epsilon/\tau$, with $0 \leq \epsilon < 1$. For an initially stable distribution f_0 all terms in Eq. (C.33) are positive because $f_0 > 0$ and $\partial f_0/\partial p_\perp \leq 0$, everywhere. Equation (C.33) illustrates a very simple condition for the development of unstable distributions. From this inequality, one can obtain the range of $p_\perp$ where the unstable region is developed. Moreover, furthering our conjecture, we have checked that a wide variety of momentum distributions fulfil Eq. (C.33), including Maxwellian, Maxwell-Jüttner, constant negative slope distributions, power-laws up to the power of 4, *etc*. For all of these distributions, or combinations a population inversion *i.e.* a ring momentum distribution, will be formed.

ARGUMENT 2: The radiation reaction force for a relativistic particle in a constant magnetic field **B** is

$$\frac{d\mathbf{p}}{d\tau} = -\frac{p_\perp^2}{\gamma}\mathbf{p}, \tag{C.34}$$

where $\tau = 2\alpha B_0/3$, as defined in the main text. We focus on particle trajectories with $p_\parallel = 0$ as the population inversion is expected to develop in that region of the distribution. We can calculate the trajectory of a particle in the perpendicular momentum space:

$$p_\perp(\tau, p_{\perp 0}) = \frac{p_{\perp 0}}{1 + p_{\perp 0}\tau}, \tag{C.35}$$

where $p_{\perp 0}$ is the initial perpendicular momentum. For a particle at $p_{\perp 0} = \infty$ the trajectory simplifies to

$$p^*_\perp(\tau) = \frac{1}{\tau}, \tag{C.36}$$

Eq. (C.36) describes the trajectory of a particle cooling from $p_{\perp 0} = \infty$ at $\tau = 0$ to $p_\perp = 0$ at $\tau = \infty$. Therefore, for any distribution function cooling due to synchrotron radiation, its domain lies within $0 < p_\perp < p^*_\perp$. Moreover, a momentum distribution undergoing synchrotron cooling also obeys $\partial f/\partial\tau|_{p_\perp=0} = 0$ because particles with no perpendicular momentum will not cool down, and the momentum distribution at $p_\perp = 0$ remains constant over time, as shown in the simulations (Chapter 2.

Due to the conservation of the number of particles, the distribution function obeys

$$N = \int_0^\infty f(p_\perp, \tau = 0)2\pi p_\perp dp_\perp = \int_0^{p^*_\perp(\tau)} f(p_\perp, \tau)2\pi p_\perp dp_\perp, \tag{C.37}$$

where N is the total number of particles. We can rewrite the right-hand side as

$$N = \int_0^{p^*_\perp(\tau)} f(p_\perp, \tau)2\pi p_\perp dp_\perp = p^*_\perp f_{avg}(\tau), \tag{C.38}$$

where f_{avg} is the average f within $0 < p_\perp < p^*_\perp$. Thus, using Eq. (C.36),

$$f_{avg} = \tau\int_0^\infty f(p_\perp, \tau)2\pi p_\perp dp_\perp = \tau N. \tag{C.39}$$

If the average of the distribution becomes larger than the value of the distribution at $p_\perp = 0$ this implies a region where $\partial f/\partial p_\perp > 0$. Thus,

$$f(p_\perp = 0, \tau) < f_{avg} = \tau N. \tag{C.40}$$

As $f(p_\perp = 0, \tau)$ is constant over time, and finite valued, there is a finite time at which this inequality becomes true. Therefore, a population inversion, i.e. a region where $\partial f/\partial p_\perp > 0$ occurs within a finite time.

C.5 Geometric origin of the universal tail in $f_{\parallel}^{\mathrm{f}}(p_{\parallel})$

In the main text, we derived the asymptotic expression for the final parallel distribution function after synchrotron cooling (Eq. (2.33)), given by

$$f_{\parallel}^{\mathrm{f}}(p_{\parallel}) = \int 2\pi p_{\perp 0}\, dp_{\perp 0}\, f_0\left(p_{\perp 0}, p_{\parallel}\sqrt{1+p_{\perp 0}^2}\right)\sqrt{1+p_{\perp 0}^2}. \tag{C.41}$$

This expression follows from the cooling-induced constant of motion (Eq. (2.7) in the main text),

$$p_{\parallel}^{\mathrm{f}} = \frac{p_{\parallel 0}}{\sqrt{1+p_{\perp 0}^2}}, \tag{C.42}$$

which defines a one-to-one mapping from the initial momentum space $(p_{\perp 0}, p_{\parallel 0})$ onto the final parallel momentum $p_{\parallel}$.

To isolate the origin of the universal decay observed in Eq. (2.36), we analyze the structure of this mapping. The key observation is that a fixed interval $dp_{\parallel}$ in the final distribution arises from a region in the initial phase space whose area *decreases* as $p_{\parallel}$ increases. This geometric contraction leads directly to the emergence of a power-law tail in $f_{\parallel}^{\mathrm{f}}(p_{\parallel})$.

The limits of integration in Eq. (C.41) are controlled by the support of the initial distribution f_0. We assume that f_0 is localized within a finite domain, characterized by a typical thermal momentum spread $p_{\mathrm{th}} \gg 1$, such that

$$f_0(p_{\perp 0}, p_{\parallel 0}) \approx 0 \quad \text{for} \quad p_{\perp 0} > p_{\perp 0}^{\max}, \quad p_{\parallel 0} > p_{\parallel 0}^{\max}. \tag{C.43}$$

These cutoff scales are not strict boundaries but represent the effective range over which f_0 remains appreciable. For example, in a Gaussian or Maxwell–Jüttner distribution, one may take $p_{\perp 0}^{\max} \sim p_{\parallel 0}^{\max} \sim \epsilon$, where $\epsilon \gg 1$ defines the broad-distribution limit.

We now estimate how this upper bound in $p_{\parallel 0}$ restricts the range of $p_{\perp 0}$ that contributes to a given value of $p_{\parallel}$. Inverting Eq. (C.42), we obtain

$$p_{\perp 0,\max}(p_{\parallel}) = \sqrt{\left(\frac{p_{\parallel 0}^{\max}}{p_{\parallel}}\right)^2 - 1} = \frac{p_{\parallel 0}^{\max}}{p_{\parallel}} \cdot \sqrt{1 - \left(\frac{p_{\parallel}}{p_{\parallel 0}^{\max}}\right)^2}. \tag{C.44}$$

In the regime $p_{\parallel} \ll p_{\parallel 0}^{\max}$, this reduces to

$$p_{\perp 0,\max}(p_{\parallel}) \sim \frac{p_{\parallel 0}^{\max}}{p_{\parallel}}, \tag{C.45}$$

indicating that higher final momenta are sourced from increasingly smaller domains in the initial momentum space.

To evaluate how much of the initial phase space contributes to a fixed interval $dp_\parallel$, we analyze the structure of the cooling map. For fixed $p_{\perp 0}$, the transformation $p_{\parallel 0} = p_\parallel \sqrt{1 + p_{\perp 0}^2}$ implies

$$dp_{\parallel 0} = \sqrt{1 + p_{\perp 0}^2}\, dp_\parallel. \tag{C.46}$$

The corresponding infinitesimal area element in the $(p_{\perp 0}, p_{\parallel 0})$ plane is

$$dA = dp_{\perp 0} \cdot dp_{\parallel 0} = \sqrt{1 + p_{\perp 0}^2}\, dp_{\perp 0} \cdot dp_\parallel. \tag{C.47}$$

The total area contributing to a given $dp_\parallel$ is thus

$$A(p_\parallel) = dp_\parallel \int_0^{p_{\perp 0,\max}} \sqrt{1 + p_{\perp 0}^2}\, dp_{\perp 0} \sim dp_\parallel \cdot \frac{p_{\parallel 0}^{\max}}{p_\parallel}, \tag{C.48}$$

which decreases as $1/p_\parallel$. This shrinking of the contributing momentum-space area directly explains the suppression of $f_\parallel^{\mathrm{f}}(p_\parallel)$ at large $p_\parallel$.

To compute the resulting scaling, we return to Eq. (C.41). In the broad-distribution limit, we may approximate

$$f_0(p_{\perp 0}, p_{\parallel 0}) \sim \epsilon^{-3} g(p_{\perp 0}/\epsilon, p_{\parallel 0}/\epsilon), \tag{C.49}$$

with g smooth and normalized. For $\epsilon \gg 1$, the function f_0 varies slowly over the narrow region contributing to a fixed $p_\parallel$, and the integral becomes dominated by geometric factors that come from the Jacobian:

$$f_\parallel^{\mathrm{f}}(p_\parallel) \sim \int_0^{p_{\perp 0,\max}} p_{\perp 0} \sqrt{1 + p_{\perp 0}^2}\, dp_{\perp 0}. \tag{C.50}$$

For $p_{\perp 0,\max} \gg 1$, valid when $p_\parallel \ll p_{\parallel 0}^{\max}$, the integrand scales as $p_{\perp 0}^2$, so

$$f_\parallel^{\mathrm{f}}(p_\parallel) \sim \int_0^{p_{\perp 0,\max}} p_{\perp 0}^2\, dp_{\perp 0} \sim p_{\perp 0,\max}^3 \sim \frac{(p_{\parallel 0}^{\max})^3}{p_\parallel^3}. \tag{C.51}$$

This recovers the universal asymptotic form presented in Eq. (2.36).

Finally, the resulting distribution is normalizable:

$$\int f_\parallel^{\mathrm{f}}(p_\parallel)\, dp_\parallel \sim \int \frac{dp_\parallel}{(1 + p_\parallel^2)^{3/2}} < \infty. \tag{C.52}$$

This analysis confirms that the power-law tail $f_\parallel^{\mathrm{f}}(p_\parallel) \propto p_\parallel^{-3}$ arises directly from the geometry of the synchrotron cooling transformation. The shrinking of the contributing momentum-space area with increasing $p_\parallel$, combined with the broad and smooth nature of the initial distribution, determines the final scaling behavior independently of the detailed form of f_0.

C.5.1 BEAM-LIKE DISTRIBUTIONS

To illustrate the geometric origin of the universal decay from a different perspective, we now consider a beam-like initial distribution with small momentum spread and finite drift velocity. Specifically, we take the initial distribution $f_0(p_\perp, p_\parallel)$ to be a uniform "waterbag" in cylindrical momentum space, centered at $p_\parallel = u \gg 1$ and $p_\perp = 0$, with width $p_{\mathrm{th}} \ll u$:

$$f_0(p_\perp, p_\parallel) = \begin{cases} \dfrac{1}{2\pi p_{\mathrm{th}}^3}, & \text{if } 0 \le p_\perp \le p_{\mathrm{th}}, \quad u - p_{\mathrm{th}} \le p_\parallel \le u + p_{\mathrm{th}}, \\ 0, & \text{otherwise,} \end{cases} \tag{C.53}$$

where the normalization ensures unit integral over phase space.

Substituting this into Eq. (C.41), the final parallel distribution becomes

$$f_\parallel^{\mathrm{f}}(p_\parallel) = \frac{1}{p_{\mathrm{th}}^3} \int_0^{p_{\mathrm{th}}} p_{\perp 0} \sqrt{1 + p_{\perp 0}^2}\, \Theta\left(p_\parallel \sqrt{1 + p_{\perp 0}^2} \in [u - p_{\mathrm{th}}, u + p_{\mathrm{th}}] \right) dp_{\perp 0}. \tag{C.54}$$

The Heaviside function restricts the integration to values of $p_{\perp 0}$ such that

$$u - p_{\mathrm{th}} \le p_\parallel \sqrt{1 + p_{\perp 0}^2} \le u + p_{\mathrm{th}}. \tag{C.55}$$

Solving for the corresponding bounds on $p_{\perp 0}$, we obtain

$$p_{\perp 0} \in \left[\sqrt{\left(\frac{u - p_{\mathrm{th}}}{p_\parallel} \right)^2 - 1},\ \sqrt{\left(\frac{u + p_{\mathrm{th}}}{p_\parallel} \right)^2 - 1} \right], \tag{C.56}$$

provided this interval lies within the physical support $[0, p_{\mathrm{th}}]$.

The resulting expression for the final distribution is

$$f_\parallel^{\mathrm{f}}(p_\parallel) = \begin{cases} \dfrac{1}{3 p_{\mathrm{th}}^3 p_\parallel^3} \left[(u + p_{\mathrm{th}})^3 - (u - p_{\mathrm{th}})^3 \right], & \text{if } p_\parallel \in \left(\dfrac{u - p_{\mathrm{th}}}{\sqrt{1 + p_{\mathrm{th}}^2}},\ u + p_{\mathrm{th}} \right), \\ 0, & \text{otherwise,} \end{cases} \tag{C.57}$$

demonstrating the power-law dependence $p_\parallel^{-3}$ explicitly for beams undergoing cooling.

The parallel momentum spread is

$$\Delta p_\parallel = (u + p_{\mathrm{th}}) - \left(\frac{u - p_{\mathrm{th}}}{\sqrt{1 + p_{\mathrm{th}}^2}} \right), \tag{C.58}$$

which simplifies in the limit $p_{\mathrm{th}} \ll 1$ to

$$\Delta p_\parallel \simeq p_{\mathrm{th}} + \frac{p_{\mathrm{th}}}{\sqrt{1 + p_{\mathrm{th}}^2}} \simeq 2 p_{\mathrm{th}}. \tag{C.59}$$

Thus, the beam remains narrow in $p_\parallel$ after cooling, but the distribution acquires an algebraic tail over a finite window.

Finally, expanding the exact expression in Eq. (C.57) in the limit $p_{\text{th}} \ll u$, we find

$$f_{\parallel}^{\text{f}}(p_{\parallel}) \simeq \frac{6up_{\text{th}}^2}{p_{\parallel}^3}, \tag{C.60}$$

which exhibits the same asymptotic decay as the broad thermal distributions considered earlier.

To estimate the spread, we compute the standard deviation $\sigma_{p_{\parallel}}$ of the final distribution. Introducing the small-angle parameter $\theta \ll 1$ via $p_{\text{th}} = u\theta$, the expression for the standard deviation becomes a function of θ alone. Expanding the exact expression in powers of θ, we obtain

$$\sigma_{p_{\parallel}} = u \cdot \frac{\theta}{\sqrt{3}} - \mathcal{O}(\theta^2), \tag{C.61}$$

where the leading-order term reflects the maximum achievable fractional spread from synchrotron cooling.

This expansion shows that the maximum spread of the final distribution is bounded by

$$\sigma_{p_{\parallel}}^{\max} \simeq \frac{p_{\text{th}}}{\sqrt{3}}, \tag{C.62}$$

and that increasing the initial momentum spread p_{th} (or angle θ) beyond this point leads to a decrease in the final spread.

This example illustrates two central geometric consequences of synchrotron cooling. First, the emergence of a $p_{\parallel}^{-3}$ tail in the final parallel distribution is not limited to broad or symmetric initial conditions: it arises generically from the phase-space compression induced by the cooling map, even in the case of narrow, drifting beams. Second, the width of the resulting distribution exhibits non-monotonic behavior as a function of the initial momentum spread. For small angular spreads, the standard deviation of the final distribution reaches a maximum of $\sigma_{p_{\parallel}}^{\max} = p_{\text{th}}/\sqrt{3}$. Further initial broadening of the initial distribution leads to a narrowing of the final one, as large-angle particles are strongly compressed. Together, these features highlight the universal nature of synchrotron-cooled momentum-space distributions.

C.6 Weakly-relativistic regime ($p_{th} = m_e c$) ring formation

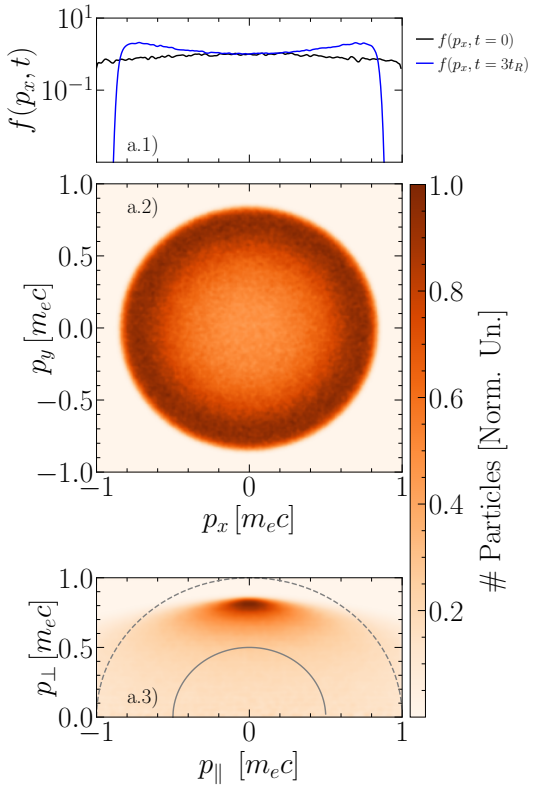

FIGURE C.1: Particle-in-cell simulation results demonstrating the evolution of a mildly-relativisitc initial isotropic Maxwellian distribution. For reference, the distribution function $f(p_x, p_y = 0)$ is shown at $t = 0$ and $t = 3t_R$ on the top row (1). The second row (row 2) shows the perpendicular plane of the momentum distribution ($f_\perp(p_x, p_y)$, where $p_\perp^2 = p_x^2 + p_y^2$) and the bottom row (3) the $f(p_\perp, p_\parallel)$ momentum distribution, at $t \sim t_R$.

To demonstrate the ring formation in the weakly-relativistic regime, simulations with $p_{th} \sim 1\ m_e c$ were also performed, the results are shown in Fig. C.1. Here we show the simulation results for an isotropic Maxwellian distribution with $p_{th} = m_e c$, Most of the distribution lies in the region where $\gamma \simeq 1$, simulations with smaller p_{th} significantly increase the timescale for the onset of the ring distribution. This result illustrates the development of the ring distribution as expected because even if the thermal energy is mildly-relativisitc it still produces a ring because it is above the threshold estimated previously in Sec. 2.2.1.

APPENDIX D

PROPERTIES OF THE SYNCHROTRON RADIATION

D.1 RADIATION OF ENTROPY

The definition of entropy is subtle and often context-dependent. Still, it remains a cornerstone of statistical physics and, by extension, plasma physics. In systems close to classical thermodynamic equilibrium, where collisional processes dominate locally, the Boltzmann-Gibbs-Shannon (BGS) entropy provides a well-established framework. Defined as [248]

$$S_{\mathrm{BGS}} = -k_B \int d\mathbf{p} d\mathbf{r}\, f(\mathbf{p},\mathbf{r}) \log\left(f(\mathbf{p},\mathbf{r})\right), \tag{D.1}$$

it quantifies disorder in terms of the distribution function f(p,r)f(p,r), and its maximization leads naturally to a Maxwellian distribution (or Jüttner in the relativistic case), characteristic of equilibrium. However, recent studies have shown that BGS entropy is not always sufficient to capture the dynamics of collisionless systems governed by long-range interactions [89]. Alternative, more nuanced entropy measures have been explored to better describe such regimes [88, 89, 249].

Still, even in the absence of collisions, and in particular under conditions of synchrotron cooling, it remains an intriguing question how entropy, under any definition, evolves. While BGS entropy may not be the definitive measure in these regimes, it remains a useful diagnostic. Tracking it provides insight into the irreversible processes and potential loss of phase-space volume induced by radiative effects.

For a system described by a Vlasov equation coupled with a collision operator or radiative operator the change in entropy dS/dt depends on the nature of the operators [250]

$$\frac{dS}{dt} = -k_B \int d\mathbf{p} d\mathbf{r}\, \left(\frac{df}{dt}\right) \log\left(f(\mathbf{p},\mathbf{r})\right), \tag{D.2}$$

where $\left(\frac{df}{dt}\right)$ refers to the operators. For a collisionless system there are no collisions and therefore $dS/dt = 0$. The inclusion of collisions one finds that $dS/dt \geq 0$ [250].

Interestingly, when a radiative operator is introduced, such as one modeling synchrotron cooling, the system's entropy can decrease. Using Eq. (D.2) together with the radiative operator

$$\left(\frac{df}{dt}\right)_{\text{rad}} = -\nabla_p \cdot (\mathbf{F}_{\text{rad}} f)\,, \tag{D.3}$$

or equivalently, the full solution of f in Eq. (2.22), one obtains

$$\frac{dS}{d\tau} = -k_B \int d\mathbf{p}\, \frac{p_\perp \left(p_\parallel t \frac{dg_0}{dp_\parallel} + \frac{dg_0}{dp_\perp} - 4t(p_\perp t - 1) g_0\right) \log\left(\frac{g_0}{(1-p_\perp t)^4}\right)}{(p_\perp t - 1)^6}, \tag{D.4}$$

where $g_0 = f_0\left(\frac{p_\perp}{1-p_\perp \tau}, \frac{p_\parallel}{1-p_\perp \tau}\right)$ is the rescaled initial distribution, note that we are now writing $dS/d\tau$, where $\tau = 2\alpha B_0 \omega_{ce} t/3$, and t is in cgs. Thus, $dS/dt \propto B^2 dS/d\tau$, and the entropy radiation rate in cgs units is proportional to the magnetic field intesity squared.

Without loss of generality we can set $t = 0$ ($\tau = 0$), which simply redefines the initial condition and yields the instantaneous entropy change:

$$\frac{dS}{d\tau} = -k_B \int d\mathbf{p}\; p_\perp \log\left(f_0(p_\perp)\right) \frac{df_0}{dp_\perp}. \tag{D.5}$$

It is nontrivial to show that any arbitrary distribution f_0 will result in $dS/dt < 0$. However, Eq. (D.5) provides more than just a diagnostic, it tells us which shapes of distribution functions radiate entropy, and at what rate. While it is not necessary to prove this explicitly for all possible forms of f_0, we have verified that a wide range of physically relevant distributions do satisfy $dS/dt < 0$ under the action of the synchrotron cooling operator. This supports the broader conclusion that synchrotron cooling acts as a compressive, entropy-reducing mechanism in phase space.

As a concrete example, consider a Maxwellian distribution of the form given in Eq. (2.24). In this case, we find

$$\frac{dS}{d\tau} = -\left(5 + \log\left(8\pi^3\right) + 6\log\left(p_{\text{th}}\right)\right) k_B < 0. \tag{D.6}$$

That is, the entropy of the plasma decreases for synchrotron cooled plasmas (Note that this was obtained in the relativistic limit, *i.e.*, $p_{\text{th}} \gg 1$). Physically, this lost entropy is carried away by the emitted synchrotron radiation, transferring entropy from the particle distribution into the photon distribution. Notably, the rate of entropy loss scales with p_{th} meaning that broader (i.e., higher-temperature) distributions radiate more strongly and lose entropy more rapidly, as expected.

D.2 SYNCHROTRON SPECTRUM FROM RING DISTRIBUTIONS

We have demonstrated that plasmas undergoing strong synchrotron cooling will modify their kinetic properties. And we have self-consistently modelled how that is modified as the synchrotron radiation escapes. Still how does the synchrotron spectrum change over time instantaneously or how will the total spectrum be changed needs to be answered.

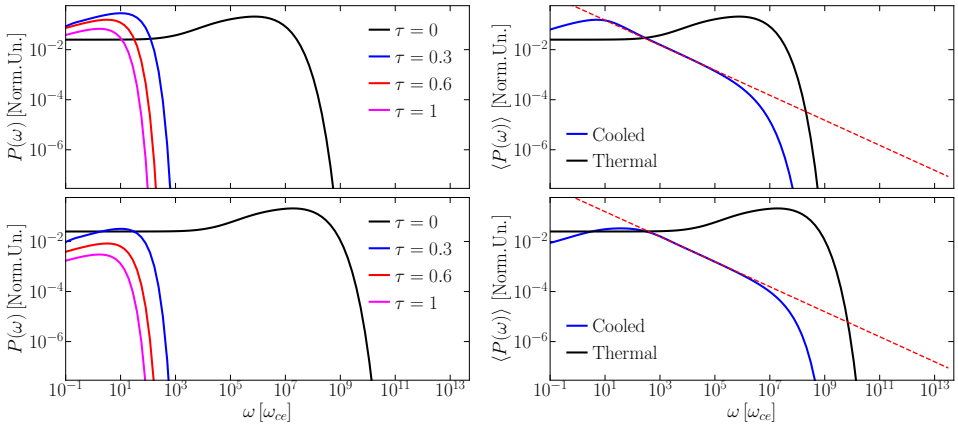

FIGURE D.1: Analytical results show that synchrotron cooling modifies the emitted spectrum over time and the averaged synchrotron spectrum during the cooling process. The spectrum is normalized to $m_e c^2 \omega_{ce}$ per particle and the time averaged spectrum is normalized to $m_e c^2 \omega_{ce}^2$. Left columns demonstrate the evolution of the instantaneous synchrotron power spectrum at different times. Right column shows the time integrated spectrum (blue) against the synchrotron emission spectrum of a static thermal plasma, *i.e.* a plasma distribution that is not undergoing synchrotron cooling. Two different initial thermal spreads are initialised: Top row the initial $p_{th} = 1000\, m_e c$, and Bottom row $p_{th} = 5000\, m_e c$. Both time averaged spectrums demonstrate the appearance of a power-law distribution with index $\alpha = -1/2$, where $\langle P(\omega)\rangle \propto \omega^{\alpha}$.

The spectrum for any given distribution can be obtained from integrating the single-particle instantaneous synchrotron spectrum with the distribution function of particle $f_\perp(p_\perp, t)$ [115, 245]

$$P_s(\omega, t) = \int_0^\infty p_\perp \partial p_\perp \frac{\sqrt{3} B_0}{m_e} \omega_{ce} F\left(\frac{\omega}{\omega_c}\right) f_\perp(p_\perp, t), \tag{D.7}$$

where $F(x) = x \int_x^\infty K_{\frac{5}{2}}(x) dx$ and $K_{\frac{5}{2}}(x)$ is the modified Bessel function and ω_c is the critical frequency $\omega_c = 3\gamma^2 \omega_{ce}/2$, where ω_{ce} is the cyclotron frequency.

For a plasma undergoing synchrotron cooling $f_\perp(p_\perp, t)$ evolves as described by Eq. (4.15), the instantaneous emission spectrum at different times during the cooling can be obtained via numerical integration of Eq. (D.7). And the total emitted power during the cooling process can be obtained. In Fig. D.1 the time evolution of the instantaneous synchrotron spectrum is shown for two different initial thermal distributions. The ring formation modifies the instantaneous spectrum. Surprisngly, the time-averaged spectrum $\langle P(\omega)\rangle$ exhibits a power-law distribution $\langle P(\omega)\rangle \propto \omega^{\alpha}$, where the power-law index $\alpha = -1/2$ is independent of the initial thermal spread.

The emergence of a power-law spectrum can be understood analytically. As the plasma cools, its perpendicular momentum distribution rapidly approaches a ring-like structure. This can be approximated as $f_\perp(p_\perp, \tau) \approx \delta(p_\perp - p_r)/2\pi p_r$, where $p_r \sim 1/\tau$ describes the shrinking radius of the ring with time. In this limit, where all electrons radiate at approximately the same energy, the synchrotron emission per particle at a given time becomes equivalent to

that of a single electron. Thus, the instantaneous spectrum reflects the standard single-particle synchrotron spectrum.

To compute the time-averaged emission, we integrate this single-particle spectrum over the cooling time:

$$\langle P_s(\omega) \rangle \propto \int_0^\infty d\tau, F\left(\frac{2\omega\tau^2}{3\omega_{ce}}\right). \tag{D.8}$$

In the high-frequency limit $x \gg 1$, the kernel asymptotes as $F(x) \sim e^{-x}\sqrt{x}$ [245]. Applying this approximation to Eq. (D.8) and performing the integration yields

$$\langle P_s(\omega) \rangle \propto \omega^{-1/2}, \tag{D.9}$$

which explains the observed power-law scaling.

Physically, this time average corresponds to a scenario in which a high-field plasma region is continually replenished with hot, uncooled particles. Each population cools independently and contributes its own instantaneous single-particle-like spectrum. The superposition of these spectra, emitted at different stages of the cooling process, gives rise to the observed power-law scaling $\langle P(\omega) \rangle \propto \omega^{-1/2}$, independent of the initial thermal spread.

APPENDIX E

GROWTH RATE OF THE ECMI IN SYNCHROTRON COOLED REGIME

E.1 ZEROTH ORDER STATIONARY SOLUTION

We begin our analysis by recalling the results Sec. 2.3.2, where the evolution of the synchrotron cooled plasma where outlined to zeroth order, this is necessary to perform the first order expansion and obtain a linear theory of synchrotron cooled plasma instabilities. We onsider a time-dependent spatially homogeneous distribution function $f = f_0(p_\perp, p_\parallel, t)$ for a tenuous pair-plasma in a strong magnetic field, the momentum distribution is axi-symmetric in momentum space along the momentum direction parallel to the magnetic field. To zeroth order, there are no self-generated electromagnetic fields, therefore $\nabla_{\mathbf{p}} \cdot (\mathbf{F}_L f_0) = 0$. For this distribution function one can show that Eq. (2.14) simplifies to [23, 113]

$$\frac{\partial f_0}{\partial t} + \nabla_{\mathbf{p}} \cdot (\mathbf{F}_{rad} f_0) = 0. \tag{E.1}$$

Equation (E.1) can be solved with the method characteristics to obtain the evolution of any given initial distribution undergoing synchrotron cooling [23, 113]

$$f_0(p_\perp, p_\parallel, \tau) = \frac{f_0\left(\frac{p_\perp}{1-\tau p_\perp}, \frac{p_\parallel}{1-\tau p_\perp}, \tau = 0\right)}{(1-\tau p_\perp)^4}, \tag{E.2}$$

τ is a normalised time such that $\tau = \frac{2\alpha}{3} B_0 \omega_{ce} t$. Equation (E.2) demonstrates the evolution of the plasma purely due to synchrotron losses. One can demonstrate that any initial distribution function f_0, following Eq. (E.2) eventually develops a positive gradient in $p_\perp$, *i.e.* an inverted Landau population or ring distribution, making it unstable to the electron cyclotron maser instability [23, 113].

Thus, a relativistic plasma, independently of the initial shape of f, will develop into an anisotropic ring momentum distribution [23, 24, 113, 168]. This results from the nonlinear nature of synchrotron radiation, which bunches the momentum distribution in the radial momentum direction $p_\perp$. The radiation reaction force violates the conservation of phase-space

volume, in contrast with the classical collisionless plasma dynamics mediated by the Lorentz force [88, 141]. Therefore, synchrotron radiation drives the plasma away from kinetic equilibrium and eventually fulfils the conditions for efficient maser emission.

E.2 LINEAR PERTURBATION: DISPERSION RELATION

Now consider the effects of the self-consistent fields. To first order they will produce a small perturbation on f_0. Thus, we linearize the Vlasov equation employing

$$f(\mathbf{p}, \mathbf{r}, t) = f_0(p_\perp, p_\parallel, t)\left(1 + \delta f(p_\perp, p_\parallel, p_\phi, \mathbf{r}, t)\right), \tag{E.3}$$

such that f_0 is the resulting ring distribution from the radiative cooling process (Eq. (E.2)) and $f_0\delta f$ will capture the azimuthal perturbation that gives rise to the maser instability.[1] Thus, we can write

$$(1+\delta f)\frac{\partial f_0}{\partial t} + f_0\frac{\partial \delta f}{\partial t} + f_0\frac{\mathbf{p}}{\gamma}\cdot\nabla_{\mathbf{r}}\delta f + (1+\delta f)\nabla_{\mathbf{p}}\cdot[\mathbf{F}_{rad}f_0] = -\delta\mathbf{F}_L\cdot\nabla_{\mathbf{p}}f_0 - f_0\mathbf{F}_B\cdot\nabla_{\mathbf{p}}\delta f, \tag{E.4}$$

Equation (E.4) can be further simplified with Eq. (E.2)

$$f_0\frac{\partial \delta f}{\partial t} + f_0\frac{\mathbf{p}}{\gamma m}\cdot\nabla_{\mathbf{r}}\delta f + \nabla_{\mathbf{p}}\cdot(\mathbf{F}_L f_0) + \nabla_{\mathbf{p}}\cdot(\mathbf{F}_L f_0\delta f) = 0, \tag{E.5}$$

the Lorentz force can be decomposed to first order as $\mathbf{F}_L = \mathbf{F}_B + \delta\mathbf{F}_L$, where $\mathbf{F}_B$ is the force due to the guiding magnetic field and $\delta\mathbf{F}_L$ is the Lorentz force due to the self-generated electromagnetic fields. Notice that $\nabla_{\mathbf{p}}\cdot(\mathbf{F}_B f_0) = 0$ and to first order $\nabla_{\mathbf{p}}\cdot(\delta\mathbf{F}_L\delta f f_0) = 0$, therefore

$$f_0\frac{\partial \delta f}{\partial t} + f_0\frac{\mathbf{p}}{\gamma m}\cdot\nabla_{\mathbf{r}}\delta f + \nabla_{\mathbf{p}}\cdot(\delta\mathbf{F}_L f_0) + f_0\nabla_{\mathbf{p}}\cdot(\mathbf{F}_B\delta f) = 0. \tag{E.6}$$

Then we can follow the standard procedure and employ the ansatz $\delta f \propto e^{(-i(\omega t - \mathbf{k}\cdot\mathbf{v}))}$. We know that the underlying distribution f_0 is changing as a function of time, which means strictly that ω has a time dependence. As waves are propagating in a time-varying medium. We will employ the WKB approximation which is valid as long as $|\omega|^2 \gg |\dot{\omega}|$, *i.e.* that the change in frequency due to the change of f_0 over time is smaller than the frequency itself. This is valid once the ring is formed and a steep gradient develops, at that point the underlying distribution is slowly varying $\partial f_0/\partial t < \omega_{ce}$ and the the frequency tends to ω_{ce}, therefore the WKB is a valid approximation to estimate the linear growth rate of X-mode waves. We can then write

$$f_0\left(-i(\omega - \mathbf{k}\cdot\mathbf{v})\delta f + \nabla_{\mathbf{p}}\cdot(\mathbf{F}_B\delta f)\right) = -\nabla_{\mathbf{p}}\cdot(\delta\mathbf{F}_L f_0). \tag{E.7}$$

Following the standard procedure for magnetised plasmas one obtains that $\nabla_{\mathbf{p}}\cdot(\mathbf{F}_B\delta f) = -(\omega_{ce}/\gamma)\partial_{p\phi}\delta f$,[2] and $\nabla_{\mathbf{p}}\cdot(\delta\mathbf{F}_L f_0) = \mathbf{E}\cdot\nabla_p f_0$. We conclude that

$$-i(\omega - \mathbf{k}\cdot\mathbf{v})f_0\delta f - \frac{\omega_{ce}}{\gamma}\frac{\partial f_0\delta f}{\partial p_\phi} + \mathbf{E}\cdot\nabla_p f_0 = 0. \tag{E.8}$$

[1] While the standard linearization uses $f = f_0 + \delta f$, this would require evolving δf under radiation reaction, since both f_0 and δf cool over time. By instead writing $f = f_0(1+\delta f)$, we account for the fact that any perturbation must evolve along with the background distribution, simplifying the analysis.

[2] Where $\partial_{p\phi}$ is the partial derivative with respect to the azimuthal momentum coordinate.

One notices that the perturbed current $\mathbf{J} = \int d\mathbf{p} \frac{\mathbf{p}}{\gamma} f_0(p_\perp, p_\parallel, t)\delta f(p_\phi, \mathbf{r}, t)$ that will modify the dielectric tensor and that Eq. (E.8) has the usual form encountered throughout literature for the derivation of the dielectric tensor of a magnetised plasma. We can solve for $f_0\delta f$ using the method of characeristics and following the steps given by Ref. [169] we can obtain the time-varying dielectric tensor

$$\begin{aligned}\epsilon_{ij}(t) =& \delta_{ij} \\ &+\frac{\omega_{pe}^2}{\omega^2}\sum_{n=-\infty}^{\infty}\int d\mathbf{p}\left\{\frac{1}{\gamma}\left[\left(\omega - \frac{k_\parallel v_\parallel}{\gamma}\right)\frac{\partial f_0(t)}{\partial p_\perp} + \frac{k_\parallel v_\perp}{\gamma}\frac{\partial f_0(t)}{\partial p_\parallel}\right]\frac{\Pi_{in}^*(b)\Pi_{jn}(b)}{\omega - \frac{n\omega_{ce}}{\gamma} - \frac{k_\parallel v_\parallel}{\gamma}}\right\} \\ &+\delta_{i\parallel}\delta_{j\parallel}\frac{\omega_{pe}^2}{\omega^2}\int d\mathbf{p}\left\{\frac{p_\parallel}{\gamma}\left[\frac{\partial f_0(t)}{\partial p_\parallel} - \frac{v_\parallel}{v_\perp}\frac{\partial f_0(t)}{\partial p_\perp}\right]\right\},\end{aligned} \tag{E.9}$$

where $b = k_\perp v_\perp/\omega_{ce}$, $\Pi_{xn}(b) = \frac{n}{b}J_n(b)$, $\Pi_{yn}(b) = iJ_n'(b)$, $\Pi_{\parallel n}(b) = \frac{v_\parallel}{v_\perp}J_n(b)$, $J_n(x)$ is the nth order Bessel function of x and $J_n'(x)$ is its derivative, and $\int d\mathbf{p}$ expands to $\int_0^\infty 2\pi p_\perp dp_\perp \int_{-\infty}^\infty dp_\parallel$.

E.2.1 Growth rate of the X-mode

We consider waves propagating along k_x, i.e., the perpendicular direction to the magnetic field (z-direction parallel to $k_\parallel$). This waves have $k_\parallel = 0$. Thus, the dielectric tensor simplifies to

$$\epsilon_{ij}(t) = \delta_{ij} + \frac{2\pi\omega_{pe}^2}{\omega^2}\sum_{n=-\infty}^{\infty}\left\{\int_0^\infty p_\perp^2 dp_\perp \int_{-\infty}^\infty dp_\parallel \frac{\partial f_0(t)}{\partial p_\perp}\frac{\Pi_{in}^*(b)\Pi_{jn}(b)}{\gamma - \frac{n\omega_{ce}}{\omega}}\right\}. \tag{E.10}$$

For the sake of simplicity we will consider a distribution function such that $\int_{-\infty}^\infty f_0(p_\perp, p_\parallel, t)\partial p_\parallel = f_\perp(p_\perp, t)$, given by Eq. (E.2), then $\gamma^2 \simeq 1 + p_\perp^2$. Thus, the dielectric tensor simplifies to

$$\epsilon_{ij}(t) = \delta_{ij} + \frac{2\pi\omega_{pe}^2}{\omega^2}\sum_{n=-\infty}^{\infty}\left\{\int_0^\infty p_\perp^2 dp_\perp \frac{\partial f_\perp(t)}{\partial p_\perp}\frac{\Pi_{in}^*(b)\Pi_{jn}(b)}{\gamma - \frac{n\omega_{ce}}{\omega}}\right\}. \tag{E.11}$$

The growth rate of small perturbations can be determined from the dispersion relation is given by [169]

$$\Lambda_{ij}(\omega, \mathbf{k}, t)E_j = \left[k^2\delta_{ij} - k_i k_j - \omega^2\epsilon_{ij}(t)/c^2\right]E_j = 0. \tag{E.12}$$

which is equivalent to the condition

$$\det\left|k^2\delta_{ij} - k_i k_j - \frac{\omega^2}{c^2}\epsilon_{ij}(\omega, t)\right| = 0. \tag{E.13}$$

Under the conditions relevant here the fastest-growing branch is the X-mode. For the X-mode with dominant E_y we have $k_y = 0$ and $k_\perp = k_x$[3]. Strictly speaking, the X-mode is elliptically polarized with both E_y and E_x components, but in the strongly magnetized limit $\omega_{ce} \gg \omega_{pe}$ the off-diagonal components of the dielectric tensor are suppressed by $\mathcal{O}(\omega_{pe}^2/\omega\omega_{ce})$. This makes

[3]The O-mode also has $k_y = 0$ and $k_\perp = k_x$, the difference being that the O-mode is polarized along E_z. Its growth rate is given in App. E.2.3.

the longitudinal fraction small, $|E_x/E_y| \ll 1$ (see App. E.2.2). Neglecting these off-diagonal corrections, the relevant dispersion reduces to

$$\Lambda_{yy}(\omega, \mathbf{k}, t) = k_\perp^2 - \omega^2 \epsilon_{yy}(t)/c^2 = 0. \tag{E.14}$$

ω is a complex-valued number; from now on we write $\omega \to \omega + i\Gamma$, where Γ represents a small damping or growth rate, with $|\Gamma| \ll |\omega|$. This allows us to perform a Taylor expansion of the dispersion relation. We also assume that the imaginary part of Λ arises solely from the analytic continuation through the pole, and not from the explicit form of $\Lambda(\omega)$ when ω is real. We adopt the standard causal prescription $\omega \to \omega + i0^+$, which implies that poles are treated via the Sokhotski-Plemelj theorem.

Under this approximation, we expand the dispersion function as

$$\Lambda(\omega + i\Gamma, \mathbf{k}, t) \simeq \Lambda(\omega, \mathbf{k}, t) + i\Gamma \frac{\partial}{\partial \omega} \left[\Re \left\{\Lambda(\omega, \mathbf{k}, t)\right\}\right]. \tag{E.15}$$

Since the dispersion relation satisfies $\Lambda(\omega + i\Gamma, \mathbf{k}) = 0$, we obtain the pair of conditions:

$$\Re\{\Lambda(\omega, \mathbf{k}, t)\} = 0 \tag{E.16}$$

and

$$\Gamma = -\frac{\Im\{\Lambda(\omega, \mathbf{k}, t)\}}{\frac{\partial}{\partial \omega}\left[\Re\left\{\Lambda(\omega, \mathbf{k}, t)\right\}\right]}. \tag{E.17}$$

The function $\Lambda(\omega, \mathbf{k})$ is given by

$$\Lambda(\omega, \mathbf{k}, t) = \omega^2 - c^2 k_\perp^2 + 2\pi\omega_{pe}^2 \sum_{n=-\infty}^{\infty} \left\{ \int_0^\infty p_\perp^2 dp_\perp \frac{\partial f_\perp(t)}{\partial p_\perp} \frac{\left[J_n'\left(\frac{k_\perp v_\perp}{\omega_{ce}}\right)\right]^2}{\gamma - \frac{n\omega_{ce}}{\omega}} \right\}. \tag{E.18}$$

The integral over $p_\perp$ develops a pole at $\gamma = \frac{n\omega_{ce}}{\omega}$, and since ω is real, the pole lies on the integration path. We apply the Sokhotski-Plemelj theorem [169] to evaluate the singular contribution:

$$\begin{aligned}\int_0^\infty p_\perp^2 dp_\perp \frac{\partial f_\perp(t)}{\partial p_\perp} \frac{\left[J_n'\left(\frac{k_\perp v_\perp}{\omega_{ce}}\right)\right]^2}{\gamma - \frac{n\omega_{ce}}{\omega}} &= -i\pi p_\perp'^2 \left.\frac{\partial f_\perp(t)}{\partial p_\perp}\right|_{p_\perp = p_\perp'} \left[J_n'\left(\frac{k_\perp v_\perp}{\omega_{ce}}\right)\right]^2 \\ &\quad + \mathcal{P}\int_0^\infty p_\perp^2 dp_\perp \frac{\partial f_\perp(t)}{\partial p_\perp} \frac{\left[J_n'\left(\frac{k_\perp v_\perp}{\omega_{ce}}\right)\right]^2}{\gamma - \frac{n\omega_{ce}}{\omega}},\end{aligned} \tag{E.19}$$

where $\mathcal{P}$ denotes the Cauchy principal value, and $p_\perp' = \sqrt{n^2\omega_{ce}^2 - \omega^2}/\omega$ is the resonant momentum.

Substituting into Eqs. (E.16) and (E.17), we obtain:

$$0 = \omega^2 - c^2 k_\perp^2 + 2\pi\omega_{pe}^2 \sum_{n=-\infty}^{\infty} \left\{ \mathcal{P}\int_0^\infty p_\perp^2 dp_\perp \frac{\partial f_\perp(t)}{\partial p_\perp} \frac{\left[J_n'\left(\frac{k_\perp v_\perp}{\omega_{ce}}\right)\right]^2}{\gamma - \frac{n\omega_{ce}}{\omega}} \right\}, \tag{E.20}$$

and

$$\Gamma(\omega,t)=\frac{2\pi^2\omega_{pe}^2\sum_{n=1}^{\infty}\left\{p_\perp'^2\left.\frac{\partial f_\perp(t)}{\partial p_\perp}\right|_{p_\perp=p_\perp'}\left[J_n'\left(\frac{k_\perp p_\perp}{n\omega_{ce}}\right)\right]^2\right\}}{\omega+\frac{\partial}{\partial\omega}\left[\pi\omega_{pe}^2\sum_{n=-\infty}^{\infty}\left\{\mathcal{P}\int_0^\infty p_\perp^2 dp_\perp\frac{\partial f_\perp(t)}{\partial p_\perp}\frac{\left[J_n'\left(\frac{k_\perp v_\perp}{\omega_{ce}}\right)\right]^2}{\gamma-\frac{n\omega_{ce}}{\omega}}\right\}\right]}, \tag{E.21}$$

Where we have taken into account that $[J_n'(x)]^2=[J_{-n}'(x)]^2=[J_n'(-x)]^2$ and that the $n=0$ term in the numerator sum is equal to zero. The term proportional to ω_{pe} in Eq. (E.20) can be made arbitrarily small when compared to ω in the limit of $\omega_{ce}/\gamma\sim\omega\gg\omega_{pe}$. Therefore, the X-modes in strongly magenetised dilute plasmas have a dispersion relation close light waves, such that $\omega=ck_\perp$. In the same limit Eq. (E.21) simplifies to

$$\Gamma(t)=2\pi^2\frac{\omega_{pe}^2}{\omega}\sum_{n=1}^{\infty}\left\{p_\perp'^2\left.\frac{\partial f_\perp(t)}{\partial p_\perp}\right|_{p_\perp=p_\perp'}\left[J_n'\left(\frac{k_\perp v_\perp}{\omega_{ce}}\right)\right]^2\right\}. \tag{E.22}$$

We can check that the condition for the WKB approximation taken to derive the dispersion relation Eq. (E.9) fulfills $|\omega^2|\gg|\dot{\omega}|$. As $\Re(\omega)$ varies slowly as the distribution cools down, then the condition means that $|\Gamma^2|\gg|\dot{\Gamma}|$.

E.2.2 POLARIZATION OF THE X-MODE

For perpendicular propagation ($k_\parallel=0$), the X-mode dispersion relation is obtained from [169]

$$N^2=\varepsilon_{yy}-\frac{g^2}{\varepsilon_{yy}},\qquad \varepsilon_\perp\equiv\varepsilon_{yy},\quad g\equiv i\varepsilon_{xy}. \tag{E.23}$$

The corresponding polarization vector satisfies

$$\left(\varepsilon_{xx}-N^2\right)E_x+\varepsilon_{xy}E_y=0, \tag{E.24}$$

so that the ratio of the field components is

$$\frac{E_x}{E_y}=-\frac{\varepsilon_{xy}}{\varepsilon_{xx}-N^2}. \tag{E.25}$$

In a highly magnetized plasma, $\omega_{ce}\gg\omega_{pe}$ and $\omega\sim\omega_{ce}$, the dielectric tensor satisfies $\varepsilon_{xx}\simeq\varepsilon_{yy}\simeq1+\mathcal{O}(\omega_{pe}^2/\omega^2)$ and $\varepsilon_{xy}=i\,\mathcal{O}(\omega_{pe}^2/\omega\omega_{ce})$. Substituting into Eq. (E.25) yields

$$\left|\frac{E_x}{E_y}\right|\sim\mathcal{O}\left(\frac{\omega_{pe}^2}{\omega\omega_{ce}}\right)\ll1. \tag{E.26}$$

This shows that the X-mode is elliptically polarized but becomes nearly linearly polarized along E_y as the degree of magnetization increases. The residual longitudinal component E_x quantifies the ellipticity and vanishes in the limit $\omega_{pe}/\omega_{ce}\to0$.

E.2.3 GROWTH RATE OF THE O-MODE

The dispersion relation of the O-mode is obtained from Eq. (E.12) as

$$\Lambda_{zz}(\omega, \mathbf{k}, t) = k_\perp^2 - \omega^2 \epsilon_{zz}(t)/c^2 = 0, \tag{E.27}$$

where the longitudinal dielectric function ϵ_{zz} reads

$$\epsilon_{zz}(t) = 1 + \frac{2\pi\omega_{pe}^2}{\omega^2} \sum_{n=-\infty}^{\infty} \int_0^\infty p_\perp^2 dp_\perp \frac{\partial f_\perp(t)}{\partial p_\perp} \frac{v_\parallel^2}{v_\perp^2} \frac{\left[J_n\left(\frac{k_\perp v_\perp}{\omega_{ce}}\right)\right]^2}{\gamma - \frac{n\omega_{ce}}{\omega}}. \tag{E.28}$$

As in the case of the X-mode, the integral has a pole at $\gamma = \frac{n\omega_{ce}}{\omega}$. Applying the Sokhotski–Plemelj theorem to isolate the singular contribution, we obtain

$$\begin{aligned}\int_0^\infty p_\perp^2 dp_\perp \frac{\partial f_\perp(t)}{\partial p_\perp} \frac{v_\parallel^2}{v_\perp^2} \frac{\left[J_n\left(\frac{k_\perp v_\perp}{\omega_{ce}}\right)\right]^2}{\gamma - \frac{n\omega_{ce}}{\omega}} &= -i\pi p_\perp'^2 \frac{\partial f_\perp(t)}{\partial p_\perp} \frac{v_\parallel^2}{v_\perp^2} \left[J_n\left(\frac{k_\perp v_\perp}{\omega_{ce}}\right)\right]^2 \Big|_{p_\perp = p_\perp'} \\ &\quad + \mathcal{P} \int_0^\infty p_\perp^2 dp_\perp \frac{\partial f_\perp(t)}{\partial p_\perp} \frac{v_\parallel^2}{v_\perp^2} \frac{\left[J_n\left(\frac{k_\perp v_\perp}{\omega_{ce}}\right)\right]^2}{\gamma - \frac{n\omega_{ce}}{\omega}},\end{aligned} \tag{E.29}$$

where again $\mathcal{P}$ denotes the Cauchy principal value and $p_\perp' = \sqrt{n^2\omega_{ce}^2 - \omega^2}/\omega$.

This yields the real and imaginary parts of the dispersion relation:

$$0 = c^2 k_\perp^2 - \omega^2 + 2\pi\omega_{pe}^2 \sum_{n=-\infty}^{\infty} \mathcal{P} \int_0^\infty p_\perp^2 dp_\perp \frac{\partial f_\perp(t)}{\partial p_\perp} \frac{v_\parallel^2}{v_\perp^2} \frac{\left[J_n\left(\frac{k_\perp v_\perp}{\omega_{ce}}\right)\right]^2}{\gamma - \frac{n\omega_{ce}}{\omega}}, \tag{E.30}$$

$$\Gamma(t) = \frac{2\pi^2\omega_{pe}^2}{\omega} \sum_{n=1}^{\infty} \left\{ p_\perp'^2 \frac{\partial f_\perp(t)}{\partial p_\perp} \frac{v_\parallel^2}{v_\perp^2} \left[J_n\left(\frac{k_\perp v_\perp}{\omega_{ce}}\right)\right]^2 \Big|_{p_\perp = p_\perp'} \right\}. \tag{E.31}$$

While the sign of $\partial f_\perp/\partial p_\perp$ can be positive (which would normally favor growth), the accompanying suppression by $v_\parallel^2/v_\perp^2 \ll 1$ near the ring effectively quenches the instability. Thus, the O-mode remains damped or weakly amplified in narrow ring distributions, in contrast with the X-mode, which exhibits strong growth in this regime.

As with the X-mode, the background distribution $f_0(t)$ evolves slowly once the ring has formed. Therefore, the frequency ω and growth rate Γ vary adiabatically in time. The WKB approximation used to derive Eqs. (E.30)–(E.31) remains valid as long as $|\omega^2| \gg |\dot{\omega}|$, which is satisfied in the strongly magnetized, slowly cooling regime considered here.

E.2.4 GROWTH RATE OF ELECTROSTATIC MODES

For electrostatic modes propagating along the magnetic field direction, we consider $\mathbf{k} = k_z\hat{z}$ and $\mathbf{E} = E_z\hat{z}$, so the only relevant component is $\Lambda_{zz} = 0$, yielding the scalar dispersion relation:

$$k_z^2 - \frac{\omega^2}{c^2}\epsilon_{zz}(t) = 0. \tag{E.32}$$

We now evaluate the zz component of the dielectric tensor from Eq. (E.9), setting $k_\perp = 0$ so that $b = 0$ and only the $n = 0$ harmonic contributes:

$$\epsilon_{zz}(t) = 1 + \frac{\omega_{pe}^2}{\omega^2} \int d\mathbf{p} \left\{ \frac{1}{\gamma} \left[\left(\omega - \frac{k_z v_z}{\gamma} \right) \frac{\partial f_0(t)}{\partial p_\perp} + \frac{k_z v_\perp}{\gamma} \frac{\partial f_0(t)}{\partial p_z} \right] \cdot \frac{(v_z/v_\perp)^2}{\omega - \frac{k_z v_z}{\gamma}} \right\} + \frac{\omega_{pe}^2}{\omega^2} \int d\mathbf{p} \left\{ \frac{p_z}{\gamma} \left[\frac{\partial f_0(t)}{\partial p_z} - \frac{v_z}{v_\perp} \frac{\partial f_0(t)}{\partial p_\perp} \right] \right\}. \tag{E.33}$$

We now take the limit $v_\parallel \ll v_\perp$, appropriate for synchrotron-cooled ring distributions. In this regime, the parallel velocity is much smaller than the perpendicular velocity, such that $(v_z/v_\perp)^2 \ll 1$. Additionally, the longitudinal momentum p_z is small compared to $p_\perp$, making the longitudinal pressure correction negligible. Since the distribution is strongly anisotropic, the derivative $\partial f_0(t)/\partial p_z$ is also subdominant compared to $\partial f_0(t)/\partial p_\perp$, allowing further simplification of the dielectric response.

Using the approximation $\omega - \frac{k_z v_z}{\gamma} \approx \omega$ in the denominator, the leading contribution to ϵ_{zz} becomes

$$\epsilon_{zz}(t) \approx 1 + \frac{\omega_{pe}^2}{\omega^3} \int d\mathbf{p} \left(\frac{v_z^2}{\gamma^2 v_\perp^2} \frac{\partial f_0(t)}{\partial p_\perp} \right) + \mathcal{O}(v_z), \tag{E.34}$$

which vanishes in the limit $v_z \to 0$. However, keeping the leading finite contribution that survives when the distribution is strictly perpendicular ($v_z = 0$), the non-resonant denominator can be treated as constant, giving

$$\epsilon_{zz}(t) \approx 1 + \frac{\omega_{pe}^2}{\omega^2} \int d\mathbf{p} \left(\frac{1}{\gamma^2} \frac{\partial f_0(t)}{\partial p_\perp} \right). \tag{E.35}$$

This expression shows that longitudinal electrostatic waves can become unstable if the distribution exhibits a positive gradient in perpendicular momentum, such that $\partial f_0(t)/\partial p_\perp > 0$, which leads to $\epsilon_{zz}(t) < 0$, and thus to an unstable mode.

Both the electrostatic and X-mode instabilities are driven by the same source of free energy: a positive gradient in perpendicular momentum, $\partial f_\perp(t)/\partial p_\perp > 0$, characteristic of synchrotron-cooled ring distributions. However, their coupling to the plasma differs significantly. The electrostatic mode, described by the scalar dielectric function $\epsilon_{zz}(t)$ in Eq. (E.35), responds to the global integral of this gradient and is non-resonant, with growth suppressed by relativistic factors $1/\gamma^2$. In contrast, the X-mode couples resonantly through the full form of $\epsilon_{ij}(t)$, as shown in Eq. (E.11), selectively amplifying waves at cyclotron harmonics where the gradient is steepest. As a result, the X-mode typically exhibits stronger and sharper growth, making it the dominant channel for instability and coherent emission in this regime.

APPENDIX F

INTERPLAY BETWEEN THE FIREHOSE AND ELECTRON CYCLOTRON MASER INSTABILITY

As pointed out by V. Zhdankin et al. (2022) [24], synchrotron cooling is inherently anisotropic. This has also been highlighted in P. J. Bilbao et al. (2023) [23]. Specifically, particles are preferentially cooled in the direction perpendicular to the magnetic field, leading to anisotropic momentum distributions. Such distributions are known to be unstable to Weibel and Firehose instabilities due to their pressure anisotropy.

This becomes particularly relevant when the parallel plasma beta, defined as

$$\beta_{\parallel} = \frac{8\pi n \left\langle p_{\parallel}^2 \right\rangle}{B^2}, \tag{F.1}$$

exceeds unity. In this regime, the parallel kinetic pressure dominates over the magnetic pressure. Anisotropic distributions with $P_{\parallel} > P_{\perp}$ can then drive the Firehose instability, provided the anisotropy satisfies the threshold condition

$$P_{\parallel} - P_{\perp} > \frac{B^2}{4\pi}, \tag{F.2}$$

or, in terms of momentum moments,

$$\left\langle p_{\parallel}^2 \right\rangle - \left\langle p_{\perp}^2 \right\rangle > \frac{B^2}{4\pi n}. \tag{F.3}$$

This instability is characterized by perturbations with wavevector $\mathbf{k} \parallel \mathbf{B}$, which induce transverse magnetic fluctuations that "wiggle" the field lines. The growth rate scales with the strength of the anisotropy and the Alfvén speed, and it saturates by scattering particles along constant-energy contours, promoting isotropization. This isotropization is key, and occurs along lines of constant energy, *i.e.*, $p_{\perp}^2 + p_{\parallel}^2 = \text{const.}$, transferring particles from lower $p_{\perp}$ to higher $p_{\perp}$, and vice versa for $p_{\parallel}$.

At the same time, as discussed in Ref. [23], the electron cyclotron maser instability (ECMI) becomes active when $\omega_{pe}/\omega_{ce} < 1$, which is a distinct condition from $\beta_{\parallel} < 1$, since $\beta_{\parallel}$ also

depends on the plasma temperature. The ECMI relies on perpendicular momentum inversion, typically associated with ring distributions, and favors wavevectors $\mathbf{k} \perp \mathbf{B}$, leading to emission of X-mode radiation.

The Firehose instability and ECMI are both seeded by synchrotron cooling, but they arise on different timescales in different regions of parameter space, depending primarily on B, n, and $p_{\rm th}$. The Firehose instability is triggered when sufficient perpendicular cooling lowers $P_\perp$ such that $P_\parallel - P_\perp > B^2/4\pi$. This occurs rapidly, and its onset time can be estimated analytically from [24] as

$$\tau_{\rm FH} = \frac{5\,C_{\rm thr}}{16}\left(\theta_{e0}^2\,\sigma_T\,n_0\,c\right)^{-1}, \tag{F.4}$$

where $\theta_{e0} = k_B T/m_e c^2$ is the initial dimensionless temperature. Expressing this in terms of thermal momentum $p_{\rm th} = \theta_{e0}\,m_e c$, we find the scaling

$$\tau_{\rm onset}^{\rm FH}\,[15\ {\rm s}] \simeq \frac{1}{\left(p_{\rm th}\,[100\,m_e c]\right)^2\,n\,[10^6\ {\rm cm}^{-3}]} \tag{F.5}$$

Notably, this timescale does not depend on the magnetic field strength: stronger B fields increase the synchrotron cooling rate but also stabilize the instability, and these effects cancel out in the threshold condition.

In contrast, the onset of the ECMI requires the development of a perpendicular population inversion, which occurs on a longer cooling scale. As estimated by Eq. (3.3), the ECMI onset time is

$$\tau_{\rm onset}^{\rm ECMI}\ \left[12\times10^{-4}\ \mu{\rm s}\right] \simeq \left(B\,[{\rm MG}]\,n\,[10^6\ {\rm cm}^{-3}]\,p_{\rm th}\,[100\,m_e c]\right)^{-1/2} \tag{F.6}$$

Comparing both timescales gives the ratio

$$\frac{\tau_{\rm onset}^{\rm ECMI}}{\tau_{\rm onset}^{\rm FH}} \simeq 4\times10^{-6}\,\left(\beta_0\,[1]\,B\,[{\rm MG}]\,p_{\rm th}\,[100\,m_e c]\right)^{1/2}, \tag{F.7}$$

where β_0 is the initial plasma beta. This scaling shows that, for fixed β, increasing either B or $p_{\rm th}$ reduces the Firehose onset time relative to the maser. This occurs because increasing B or $p_{\rm th}$ at fixed β implies a larger density n, which shortens the firehose timescale while leaving the maser onset time relatively unaffected. This expression demonstrates the importance of the different parameters to determine what instability will occur first.

This separation of thresholds opens the possibility of a regime where both instabilities coexist: a hot plasma with strong pressure anisotropy (high $\beta_\parallel$) and low density-to-field ratio (small ω_{pe}/ω_{ce}). In this work, we explore this joint regime using 2D3V particle-in-cell simulations of a relativistic pair plasma, initially isotropic, with thermal momentum $p_{\rm th} = 100\,m_e c$ and parameters set such that $\omega_{pe} = 1\,\omega_{ce}$, corresponding to $\beta \approx 100$.

To explore this, we performed two-dimensional, three-velocity (2D3V) particle-in-cell simulations of an initially isotropic, relativistic electron-positron plasma with a Maxwellian distribution characterized by $p_{\rm th} = 100\,m_e c$. The background magnetic field is oriented along the x_1 direction, and the plasma parameters are set such that $\omega_{pe} = 0.2\,\omega_{ce}$, yielding an initial plasma beta of $\beta = 4$.

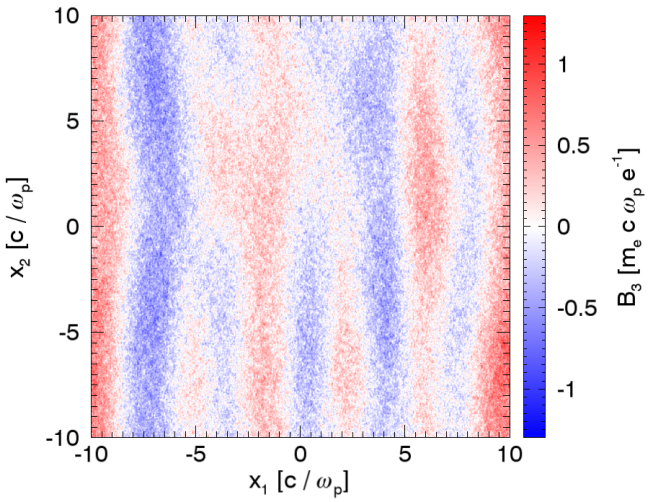

FIGURE F.1: Particle-in-cell simulations demonstrate the onset of the Firehose instability in a pair plasma, as indicated by the emergence of perpendicular magnetic-field fluctuations with k along the guide field.

We normalize the simulation such that $B = 10^{14}\,\mathrm{G}$, which implies a ratio $\tau_{\mathrm{onset}}^{\mathrm{ECMI}}/\tau_{\mathrm{onset}}^{\mathrm{FH}} \simeq 0.4$. This places the system in a regime where both instabilities become comparable in timescale and can potentially interplay dynamically.

As shown in Fig. F.1, the simulation clearly demonstrates the onset of the synchrotron-driven Firehose instability. This is evidenced by the growth of magnetic field fluctuations in the out-of-plane component B_3, with a characteristic wavevector aligned along the magnetic field.

Following the development of the Firehose instability, the distribution function undergoes significant deformation. Allowing the plasma to continue cooling radiatively after the onset of the instability reveals that the distribution does not relax into a simple ring. Instead, two distinct rings form. This bifurcation results from the saturation of the Firehose instability under continuous radiative cooling. The instability works to isotropize the plasma by scattering particles along resonant momentum-space paths of constant γ, effectively redistributing them from high $p_\parallel$, low $p_\perp$ to lower $p_\parallel$, higher $p_\perp$ values. This behavior is reminiscent of adiabatic motion in magnetic mirrors, where the magnetic moment is conserved, although here it is not stricly conserved due to radiative losses. Synchrotron losses, which remain stronger in the perpendicular direction, then cause particles to accumulate at an intermediate angle, approximately $\sim 45^\circ$, where perpendicular and parallel pressures are critically balanced, reaching saturation and no further growth of the firehose instability.

This emergent double-ring structure is still unstable to the electron cyclotron maser instability, as it exhibits regions with $\partial f/\partial p_\perp > 0$. Once the Firehose instability saturates, these rings generate coherent emission. Importantly, because the rings are tilted, the wave vector associated with the emitted radiation is no longer purely perpendicular to the magnetic field. Instead, Doppler-shifted emission appears at a characteristic angle of approximately 45°, as confirmed by a Fourier analysis of the out-of-plane electric field component E_3 shown

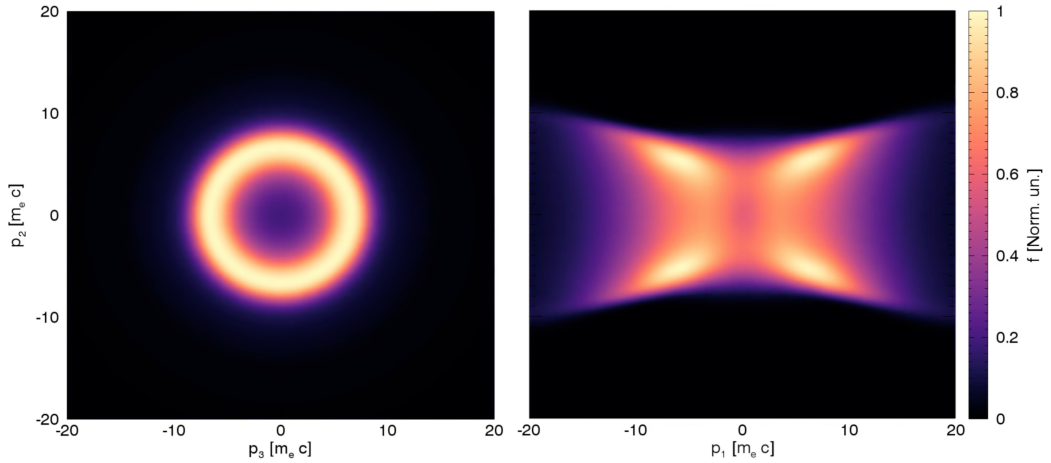

FIGURE F.2: The distribution function evolves into a double-ring structure, where the peak density occurs at $\sim 45°$. Left: f integrated along the magnetic field. Right: f integrated along the out-of-plane direction.

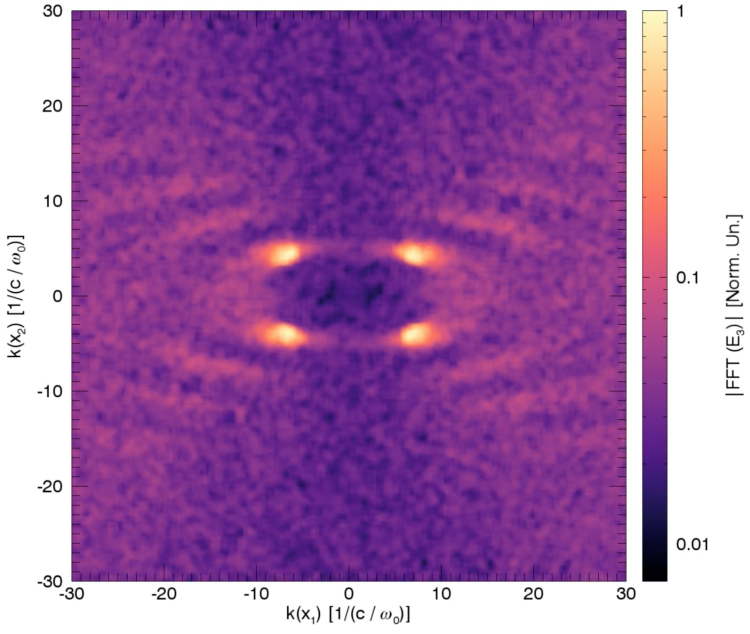

FIGURE F.3: Spectral analysis (FFT) of the out-of-plane electric field E_3 demonstrates coherent maser emission and its harmonics emitted at $\sim 45°$, following the saturation of the Firehose instability.

in Fig. F.3.

At this oblique angle, the emitted waves are elliptically polarized. The modes no longer correspond to the canonical X-mode, which are strictly defined for perpendicular propagation [176]. Instead, they arise from the oblique branches of the plasma dispersion relation, which smoothly interpolate between the linear polarization of perpendicular modes and the circular polarization of parallel ones. This elliptical character reflects both the oblique emission geometry and the plasma's mixed-mode response at intermediate angles [169].

These results suggest a non-trivial interplay between the Firehose instability and the ECMI in relativistically hot, radiatively cooled pair plasmas. Synchrotron cooling not only drives the pressure anisotropy that seeds the Firehose instability but also shapes the final distribution function into configurations favorable for coherent maser emission.

APPENDIX G

BETATRON COOLING IN THE ION–CHANEL

G.1 KRYLOV–BOGOLIUBOV AVERAGED SOLUTION TO BETATRON COOLING

In order to solve the non-linear differential Eq. (4.8), describing the dynamics of an electron undergoing betatron cooling,

$$\frac{d^2\Delta r_\perp}{dt^2} = -\omega_\beta^2 \Delta r_\perp - \frac{1}{6}\frac{\alpha m_e \omega_{p0}^4 \gamma_\parallel}{ecE_{\mathrm{Sc}}}\frac{d\Delta r_\perp}{dt}\Delta r_\perp^2, \tag{G.1}$$

where $\omega_\beta = \omega_{p0}/\sqrt{2\gamma_\parallel}$ is the betatron frequency. The general (and still exact) solution to the transverse displacement equation with radiation reaction is

$$\Delta r_\perp(t) = A(t)\sin\left(\omega_\beta t + \phi_0(t)\right), \tag{G.2}$$

where $A(t)$ and $\phi_0(t)$ vary with time. While obtaining the exact forms of $A(t)$ and $\phi_0(t)$ is generally not feasible, the Krylov–Bogoliubov (KB) averaging method can be employed when the radiative cooling rate is smaller than the betatron frequency [204]. Here we outline how this method is derived (Following Ref. [204]) and applied to this differential equation.

This method can be employed to solve differential equations of the form

$$\frac{d^2 g}{dt^2} + k^2 g = a + \varepsilon f\left(g, \frac{dg}{dt}\right), \tag{G.3}$$

assuming that f is a smooth function and that $k \gg \varepsilon$ [204]. The exact solution for $\varepsilon = 0$ is

$$g(t) = \frac{a}{k^2} + A\sin\left(kt + B\right), \tag{G.4}$$

where A and B are chosen based on the initial conditions. When $\varepsilon \neq 0$, the solution is assumed to take the same form, but with slowly varying amplitude and phase, $A \to A(t)$ and $B \to B(t)$. It is further assumed that

$$\frac{dg}{dt} \approx kA\cos\left(kt + B\right), \tag{G.5}$$

neglecting terms of order $\mathcal{O}(\varepsilon)$.

We now substitute the ansatz into the original equation and collect the $\mathcal{O}(\varepsilon)$ residual:

$$\frac{d^2g}{dt^2} + k^2 g - a = \varepsilon f\left(\frac{a}{k^2} + A\sin\phi,\, kA\cos\phi\right), \tag{G.6}$$

where we define $\phi = kt + B(t)$. This residual includes contributions from the time derivatives of $A(t)$ and $B(t)$. To extract evolution equations for these variables, we project the residual onto the basis functions $\cos\phi$ and $\sin\phi$ and average over one period:

$$\dot{A} = \frac{\varepsilon}{k}\left\langle f\left(\frac{a}{k^2} + A\sin\phi,\, kA\cos\phi\right)\cos\phi\right\rangle, \tag{G.7}$$

$$\dot{B} = -\frac{\varepsilon}{kA}\left\langle f\left(\frac{a}{k^2} + A\sin\phi,\, kA\cos\phi\right)\sin\phi\right\rangle, \tag{G.8}$$

where the angle brackets denote averaging over $\phi \in [0, 2\pi]$.

Equivalently, one can define the slowly varying components $A_0(t)$ and $B_0(t)$ as the averages over the fast oscillatory timescale. Their evolution equations take the form

$$\begin{aligned}
\frac{dA_0}{dt} &= \frac{\varepsilon}{2\pi k}\int_0^{2\pi} f\left(\frac{a}{k^2} + A_0\sin\theta,\, kA_0\cos\theta\right)\cos\theta\, d\theta, \\
\frac{dB_0}{dt} &= -\frac{\varepsilon}{2\pi k A_0}\int_0^{2\pi} f\left(\frac{a}{k^2} + A_0\sin\theta,\, kA_0\cos\theta\right)\sin\theta\, d\theta,
\end{aligned} \tag{G.9}$$

which correspond to the Krylov–Bogoliubov averaged dynamics of the amplitude and phase.

Applying the Krylov–Bogoliubov averaging method to Eq. (G.1), we identify the perturbation function as

$$f\left(g, \frac{dg}{dt}\right) = -\frac{1}{6}\frac{\alpha m_e \omega_{pc}^4 \gamma}{ecE_{\mathrm{Sc}}}\frac{dg}{dt}\, g^2, \tag{G.10}$$

with $k = \omega_\beta = \omega_{pc}/\sqrt{2\gamma}$ and $a = 0$. Substituting into the averaged evolution equations, we obtain

$$\begin{aligned}
\dot{A}(t) &= -\frac{1}{2\pi k}\int_0^{2\pi}\left[\frac{1}{6}\frac{\alpha m_e \omega_{pc}^4 \gamma(t)}{ecE_{\mathrm{Sc}}}\,(kA\cos\theta)(A\sin\theta)^2\right]\cos\theta\, d\theta \\
&= -\frac{\frac{1}{6}\frac{\alpha m_e \omega_{pc}^4 \gamma(t)}{ecE_{\mathrm{Sc}}}}{2\pi}\int_0^{2\pi} A^3\sin^2\theta\cos^2\theta\, d\theta \\
&= -\frac{1}{48}\frac{\alpha m_e \omega_{pc}^4 \gamma(t)}{ecE_{\mathrm{Sc}}}A^3,
\end{aligned} \tag{G.11}$$

and

$$\begin{aligned}
\dot{\phi}(t) &= -\frac{1}{2\pi kA}\int_0^{2\pi}\left[\frac{1}{6}\frac{\alpha m_e \omega_{pc}^4 \gamma(t)}{ecE_{\mathrm{Sc}}}\,(kA\cos\theta)(A\sin\theta)^2\right]\sin\theta\, d\theta \\
&= -\frac{\frac{2}{3}\frac{e\alpha\omega_{pc}^2\gamma(t)}{E_{\mathrm{Sc}}m_e c}}{2\pi}\int_0^{2\pi} A^2\sin^3\theta\cos\theta\, d\theta = 0.
\end{aligned} \tag{G.12}$$

The vanishing of the phase evolution $\dot{\phi} = 0$ reflects the symmetric structure of the cooling term and the absence of any resonant frequency shift at this order.

G.2 Solution to Eq. (4.14) via the method of characteristics

We consider the evolution of the distribution function under the Vlasov equation:

$$\frac{\partial f}{\partial t} + \frac{1}{A}\frac{\partial}{\partial A}\left[A\frac{dA(t)}{dt}f\right] + \frac{\omega_\beta}{A}\frac{\partial f}{\partial \phi} = 0, \tag{G.13}$$

where A is the betatron amplitude and ϕ is the betatron phase. The solution to Eq. (G.13) can be obtained via the method of characteristics.

To proceed, we introduce a normalized cooling time $\tau = \lambda t$, where

$$\lambda = \frac{\pi}{2}\frac{\alpha m_e}{E_{\mathrm{Sc}} ce}\omega_{p0}^4 \gamma_\parallel, \tag{G.14}$$

This separates the slow cooling timescale from the fast betatron oscillations. As a result, the characteristic equations involve derivatives with respect to different time variables: the cooling is governed by τ, while the phase evolves on the faster timescale t. The full set of characteristic equations reads:

$$\frac{dA}{d\tau} = -\frac{A^3}{2}, \tag{G.15}$$

$$\frac{d\phi}{dt} = -\frac{\omega_\beta}{A}, \tag{G.16}$$

$$\frac{df}{d\tau} = 2A^2 f. \tag{G.17}$$

The amplitude equation integrates to

$$A(\tau) = \frac{A_0}{\sqrt{1 + A_0^2 \tau}}, \tag{G.18}$$

where A_0 is the initial amplitude at $\tau = 0$. Inverting this relation gives

$$A_0 = \frac{A}{\sqrt{1 - A^2\tau}}, \tag{G.19}$$

which defines the domain of validity $\tau < A^{-2}$ for real-valued trajectories.

We next solve for the phase ϕ by integrating the characteristic equation $d\phi/dt = -\omega_\beta/A(t)$ with $A(t) = A_0/\sqrt{1 + A_0^2 t}$. Solving with initial condition $\phi(0) = \phi_0$, and inverting to express ϕ_0 in terms of $\phi(t)$, A, and t, we obtain

$$\phi_0 = \frac{(1 - A^2 t/\lambda)^{3/2}}{3A^3}\left[3A^3\phi - 2\lambda\omega_\beta + 2\lambda\omega_\beta\left(1 + \frac{A^2 t}{\lambda(1 - A^2 t/\lambda)}\right)^{3/2}\right], \tag{G.20}$$

valid within the domain $t < \lambda/A^2$. This expression captures how amplitude-dependent cooling distorts phase evolution.

In the adiabatic limit where $\lambda \gg 1$, corresponding to slow cooling compared to the betatron period, the phase evolution simplifies to

$$\phi(t) \approx \phi_0 + \frac{\omega_\beta t}{A}, \tag{G.21}$$

which highlights that phase advances inversely with amplitude.

We now solve for the distribution function $f(A, \phi, t)$ along characteristics. Using Eq. (G.17) and the solution for $A(\tau)$, we integrate

$$\frac{df}{d\tau} = 2A^2 f, \tag{G.22}$$

which yields

$$f(A, \phi, t) = \frac{f_0(A_0, \phi_0)}{(1 - A^2\tau)^2}, \tag{G.23}$$

where we used $A_0 = A/\sqrt{1 - A^2\tau}$ to express the solution in terms of final amplitude A and time t.

Substituting A_0 and ϕ_0 in terms of A, ϕ, and t, and using the adiabatic expression for ϕ_0, the full solution becomes

$$f(A, \phi, t) = \frac{f_0\left(\frac{A}{\sqrt{1-A^2\tau}}, \phi - \frac{\omega_\beta t}{A}\right)}{(1 - A^2\tau)^2}. \tag{G.24}$$

This expression describes the evolution of the distribution function under amplitude-dependent radiative cooling, including both phase-space compression and phase mixing.

G.3 Coherent conditions for ICL

For the coherent, or near coherent amplification of radiation via FEL or ICL processes, the beam necessitates that the so-called wiggler parameter K has a small and same for energy spread [126]

$$\frac{\Delta\gamma}{\gamma} < \frac{2}{3}\rho \tag{G.25}$$

and

$$\frac{\Delta K}{K} < \frac{2 + K^2}{2K^2}\rho, \tag{G.26}$$

where γ is the Lorentz factor of the electrons, ρ is the so-called pierce parameter [164, 189]

$$\rho = \left[\frac{I}{I_A}\frac{2\left(2 + K^2\right)^2 [\mathrm{JJ}]^2}{\left(4 + K^2\right)^2 \gamma}\right]^{1/3}, \tag{G.27}$$

where I is the beam current, I_A is the Alfvén current, and

$$[\mathrm{JJ}] = J_0\left(\frac{K^2}{4 + 2K^2}\right) - J_1\left(\frac{K^2}{4 + 2K^2}\right), \tag{G.28}$$

where $J_n(x)$ is the nth order Bessel function. It can be shown that $\frac{2(2+K^2)^2[\mathrm{JJ}]^2}{(4+K^2)^2}$ is bounded between $1/2$ and 0.9699393. The most stringent Pierce parameter corresponds to the small K limit, and simplifies to

$$\rho = \left[\frac{1}{2}\frac{I}{I_A}\frac{1}{\gamma}\right]^{1/3}. \tag{G.29}$$

Thus, a sufficient energy spread condition can be expressed as $\Delta\gamma/\gamma < 2\rho/3 = 2\left[I/(2I_A\gamma)\right]^{1/3}/3$.

In a similar manner, $\frac{2+K^2}{2K^2}\left(\frac{2(2+K^2)^2[\mathrm{JJ}]^2}{(4+K^2)^2}\right)^{1/3}$ is bounded between ∞ and $0.494846 \sim 1/2$. Thus, the sufficient condition the wiggler spread parameter must fulfill is

$$\frac{\Delta K}{K} < \frac{1}{2}\left[\frac{I}{I_A}\frac{1}{\gamma}\right]^{1/3} = \rho' = 2^{-2/3}\rho, \tag{G.30}$$

The wiggler parameter corresponds to the radial amplitude in phase-space, what we have described as A. Therefore, Eq. 4.15, can be employed to obtain K average, and ΔK.

$$K = \int_0^\infty A^2 f(A,t)\, 2\pi dA, \tag{G.31}$$

and ΔK defined as the standard deviation

$$\Delta K^2 = \int_0^\infty (A-K)^2 f(A,t)\, 2\pi A\, dA \tag{G.32}$$

For a gaussian beam, that is emittance matched $f_0(A) = e^{-A^2/(2\sigma_\perp^2)}/2\pi\sigma_\perp^2$, where $\sigma_\perp$ is the amplitude of oscillation, and f such that it is symmetric in phase ϕ. We can obtain

$$K = \frac{\sqrt{\pi}}{2\sqrt{\tau}} U\left(\frac{1}{2}, 0, \frac{1}{2\sigma_\perp^2\tau}\right), \tag{G.33}$$

where $U(a,b,c) = \Gamma(a)^{-1}\int_0^\infty \lambda^{a-1}e^{-c\lambda}(1+\lambda)^{b-a-1}d\lambda$ is the confluent hypergeometric function of the second kind, and $\Gamma(x)$ is the complete gamma function [251]. Notably,

$$\lim_{\tau\to\infty} U\left(\frac{1}{2}, 0, \frac{1}{2\sigma_\perp^2\tau}\right) = \frac{2}{\sqrt{\pi}}, \tag{G.34}$$

and therefore, as $t \to \infty$ $K \to \tau^{-1/2}$. This is expected as the distribution as discussed in the main text the whole phase-space volume is constricted into a region.

Then ΔK

$$\Delta K = \sqrt{\frac{1}{\tau} - \frac{\pi}{4\tau}U\left(\frac{1}{2}, 0, \frac{1}{2\sigma_\perp^2\tau}\right)^2 - \frac{e^{-2\sigma_\perp^2\tau}}{2\sigma_\perp^2\tau^2}\Gamma\left(0, \frac{1}{2\sigma_\perp^2\tau}\right)}, \tag{G.35}$$

where $\Gamma(a,b) = \int_b^\infty t^{a-1}e^{-t}dt$ is the incomplete gamma function. It can easily be shown that $\Delta K/K \to 0$ as t increases for any fixed $\sigma_\perp$. Which demonstrates that the wiggler conditions are eventually fulfilled in a finite time, and beams undergoing betatron cooling develop the conditions for coherent amplification of betatron radiation.

The exact form of $\Delta K/K$ is cumbersome to obtain the time at which the wiggler condition is fulfilled. Therefore, we approximate $K = r_r(\tau)$ as the radius in phase-space defined in Eq. (4.16) and $\Delta K = 2(\tau^{-1/2} - r_r(\tau))$, this slightly overestimates $\Delta K/K$. Therefore the critical time for the wiggler condition to be fulfilled is

$$\tau_c > \frac{(2+\rho')^2}{4\rho'(4+\rho')\sigma_\perp^2}. \tag{G.36}$$

Finally, the gain length of the radiation power

$$L_{\mathrm{GP}} = \frac{2\left(2+K^2\right)}{\left(4+K^2\right)\sqrt{3}\rho}\frac{c}{\omega_\beta} \tag{G.37}$$

must be shorter than the skin-depth of the beam k_{pb}^{-1} to avoid damping of the radiation [126, 252]. This yields the following condition

$$L_{\mathrm{GP}}k_{\mathrm{pb}} \simeq \frac{2}{K}\left(\frac{I}{I_A}\frac{1}{\gamma}\right)^{1/6}. \tag{G.38}$$

APPENDIX H

FIREBALL BEAM PROPERTIES

H.1 BEAM MOMENTUM DISTRIBUTIONS

The momentum distributions of the electron-positron beams were obtained from FLUKA simulations of the converter-target generation process. These distributions are modeled as separable in longitudinal and transverse momentum components:

$$f(p_z, p_\perp) = f_\parallel(p_z)\, f_\perp(p_\perp \mid p_z), \tag{H.1}$$

where the longitudinal distribution $f_\parallel(p_z)$ is described by a broken power-law and the transverse distribution $f_\perp(p_\perp \mid p_z)$ is modeled as a Gaussian with a p_z-dependent width.

H.1.1 ELECTRON DISTRIBUTION

The longitudinal momentum distribution of the electrons is fitted by a three-segment power law:

$$f_{\parallel,e}(p_z) = A_{\parallel,e}\, p_z^{k_1} (p_z + p_{1,2})^{k_2-k_1} (p_z + p_{2,3})^{k_3-k_2}, \tag{H.2}$$

with best-fit parameters:

$$k_1 = -1.6, \quad k_2 = 0.8, \quad k_3 = -2.2, \quad p_{1,2} = 0.012\,\mathrm{GeV}/c, \quad p_{2,3} = 0.25\,\mathrm{GeV}/c,$$

and normalization constant $A_{\parallel,e}$ chosen such that $\int f_{\parallel,e}(p_z)\,\mathrm{d}p_z = 1$ over the range $p_z \in [0.01, 10]\,\mathrm{GeV}/c$.

The transverse distribution is modeled as a Gaussian:

$$f_\perp(p_\perp \mid p_z) = A_\perp(p_z)\, \exp\left(-\frac{p_\perp^2}{2\, p_{\mathrm{th}}^2(p_z)}\right), \tag{H.3}$$

with $p_{\mathrm{th}}(p_z) = \Delta\theta\, p_z$ and best-fit angular spread $\Delta\theta = 0.025$. The normalization $A_\perp(p_z) = (2\pi\, p_{\mathrm{th}}^2)^{-1}$ ensures $\int f_\perp(p_\perp \mid p_z)\, 2\pi p_\perp\, \mathrm{d}p_\perp = 1$.

The full electron distribution is thus:

$$f_e(p_z, p_\perp) = f_{\parallel,e}(p_z)\, f_\perp(p_\perp \mid p_z), \tag{H.4}$$

normalized so that $\iint f_e(p_z, p_\perp)\, 2\pi p_\perp\, \mathrm{d}p_\perp\, \mathrm{d}p_z = 1$.

H.1.2 POSITRON DISTRIBUTION

The positron longitudinal distribution is best described by a two-segment power law:

$$f_{\parallel,p}(p_z) = A_{\parallel,p}\, p_z^{k_1} (p_z + p_{1,2})^{k_2 - k_1}, \tag{H.5}$$

with parameters:

$$k_1 = 0.17, \quad k_2 = -2.2, \quad p_{1,2} = 0.17\ \mathrm{GeV}/c,$$

and $A_{\parallel,p}$ chosen so that $\int f_{\parallel,p}(p_z)\, \mathrm{d}p_z = 1$ over the same range.

The transverse distribution is assumed to follow the same Gaussian form as for the electrons:

$$f_\perp(p_\perp \mid p_z) = \frac{1}{2\pi\, p_{\mathrm{th}}^2}\, \exp\left(-\frac{p_\perp^2}{2\, p_{\mathrm{th}}^2}\right), \quad p_{\mathrm{th}}(p_z) = \Delta\theta\, p_z.$$

The full positron distribution is then:

$$f_p(p_z, p_\perp) = f_{\parallel,p}(p_z)\, f_\perp(p_\perp \mid p_z), \tag{H.6}$$

with full normalization as above.

H.2 INITIALIZATION SCHEME

To initialize the beam momentum distribution in the simulation, we adopted an inverse transform sampling approach tailored to the longitudinal momentum distribution $f(p_\parallel)$. First, we obtained an analytical fit to this distribution based on the output of the FLUKA simulations, providing a smooth and tractable representation of $f(p_\parallel)$ suitable for numerical integration.

Before the start of the simulation, we computed the cumulative distribution function (CDF) by numerically integrating $f(p_\parallel)$ over a finely discretized grid using a small step size $dp_\parallel$. We then constructed an inverse mapping from the unit interval $[0, 1]$ to $p_\parallel$ by recording the values of $p_\parallel$ each time the cumulative integral crossed fractional thresholds i/n for $i = 1, 2, ..., n-1$, where n is the number of desired bins. This yielded a monotonic array of CDF values and their corresponding $p_\parallel$ values.

To assign momenta to particles, we drew random numbers $r \in [0, 1]$ and used linear interpolation between neighboring stored values in the CDF to compute the corresponding $p_\parallel$. This allowed us to sample from the continuous distribution with high fidelity, avoiding discretization artifacts and ensuring that the initialized particle ensemble closely follows the target distribution. Then a random angle is sampled to account for the effects of divergence and the full momentum is initialized. The results of this methods are seen in Fig. H.1. Importantly, this sampling method allows to efficiently sample distribution functions with very large value differences, such as in this case power-law distributions, where a sampling-rejection method would necessitate many more samples to initialize such distrbution. This scheme guarantees a single sample per particle to be initialized and still accuretaly describes power-law distirbutions and their region with low probabilities.

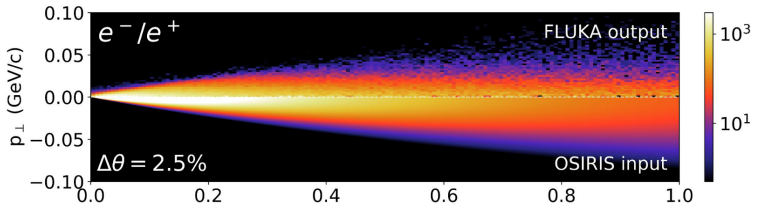

FIGURE H.1: Initial conditions of the electron-positron distribution in the OSIRIS PIC simulations compared against the FLUKA obtained distributions.

Interestingly, we found no significant qualitative difference in 2D3V simulations employing this initialization method vs the use of a Maxwell-Jüttner distribution Lorentz boosted with the correct Lorentz factor such that the beam has the correct perpendicular pressure and the correct emmittance. As the exact finer details of the distribution shape are not that important as long as the key quantities that characterise the beam are equivalent.

H.3 SEED MAGNETIC FIELD DUE TO CHARGE IMBALANCE

We calculate the initial seed field from which the current filamentation instability (CFI) can grow, based on the initial conditions of the proton and electron-positron beams. Since the beam is not fully charge neutral, it provides an initial modulation that can seed the instability.

The current density $J(r)$ is given by the sum of the species profiles:

$$J(r) = c\rho_{p+}(r) + c\rho_{e+}(r) - c\rho_{e-}(r). \tag{H.7}$$

From FLUKA simulations, we know the profiles follow Cauchy distributions. However, for simplicity, we approximate them with Gaussian profiles, which makes the calculation analytically tractable and does not significantly affect the result.

From Ampère's law, the azimuthal magnetic field is

$$B_\phi(r) = \mu_0 c \frac{r_e^2(n_{e-} - n_{e+})\left(e^{-\frac{r^2}{2r_e^2}} - 1\right) + r_p^2 n_p \left(1 - e^{-\frac{r^2}{2r_p^2}}\right)}{\sqrt{2\pi} r}, \tag{H.8}$$

where $r_e = 2.2\,\text{mm}$ and $r_p = 1.0\,\text{mm}$ are the beam widths for the pair and proton beams, respectively. The peak densities are $n_{e-} = 6.04 \times 10^{11}\ \text{cm}^{-3}$, $n_{e+} = 4.71 \times 10^{11}\ \text{cm}^{-3}$, and $n_p \sim 3 \times 10^{11}\ \text{cm}^{-3}$.

To obtain the spectrum of this seed field, we take the Fourier transform of Eq. (H.8):

$$B_k(k) = \frac{\mu_0 c}{2} i \left[r_e^2(n_{e-} - n_{e+}) \left(\text{erf}\left(\frac{r_e k}{\sqrt{2}}\right) - 1 \right) - r_p^2 n_p \left(\text{erf}\left(\frac{r_p k}{\sqrt{2}}\right) + 1 \right) \right], \tag{H.9}$$

where $\text{erf}(x)$ is the error function. The result is purely imaginary since $B_\phi(r)$ is an odd function of r.

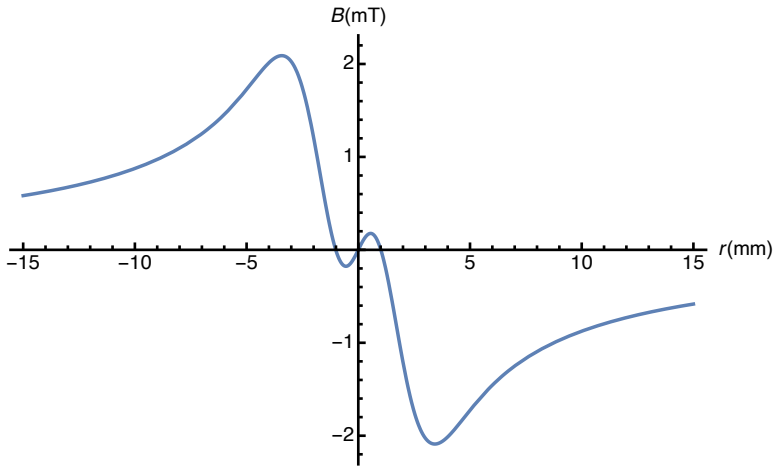

FIGURE H.2: Radial structure of the seed magnetic field calculated using experimental beam parameters.

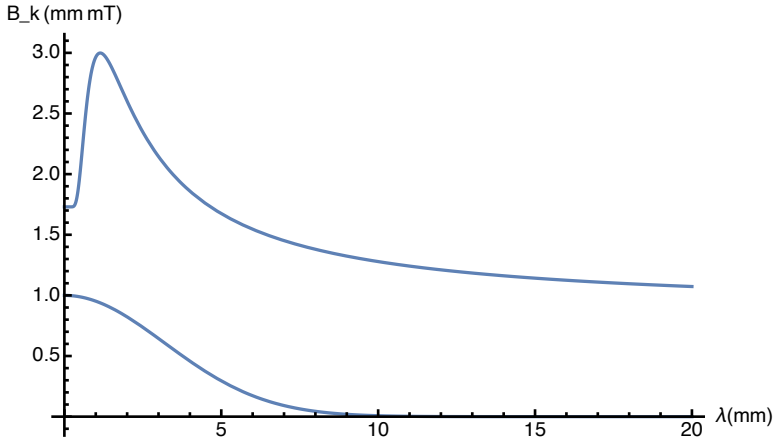

FIGURE H.3: Fourier spectrum of the seed field as a function of wavelength λ. The seed peaks around $\lambda \sim$ 2–3 mm, consistent with the beam size.

In real units, the azimuthal magnetic field becomes:

$$B_\phi(r) = -10.2\,\mathrm{mT}\,\frac{r_e}{r}\left(1 - e^{-\frac{r^2}{2r_e^2}}\right) + 7.22\,\mathrm{mT}\,\frac{r_p}{r}\left(1 - e^{-\frac{r^2}{2r_p^2}}\right). \tag{H.10}$$

In Fourier space, the field amplitude is:

$$B_k(k) = \left[14.53\left(\mathrm{erf}\left(\frac{r_e k}{\sqrt{2}}\right) - 1\right) - 12.8\left(\mathrm{erf}\left(\frac{r_p k}{\sqrt{2}}\right) + 1\right)\right]\mathrm{mm\,mT}. \tag{H.11}$$

The imaginary part, corresponding to the phase, is dropped here as we are only interested in the amplitude spectrum.

The seed field spectrum can be compared to the growth rate of the instability to determine which modes are amplified. As expected, modes with wavelengths longer than the beam

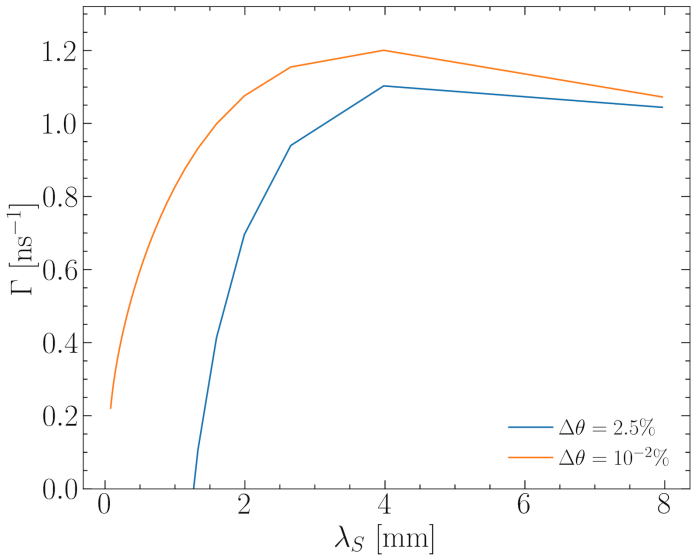

FIGURE H.4: Growth rate of the current filamentation instability for collimated and divergent beams. The collimated case shows a higher growth rate.

width are not supported. The seed peaks near 2–3 mm, within the size of the beam. For the collimated case, filaments are spaced by approximately 4 mm, about twice the magnetic field modulation wavelength, which is consistent.

The growth rate is approximately 1 ns^{-1} for the perfectly collimated case, in good agreement with simulations. For the divergent beam, the growth rate is reduced to about 0.5 ns^{-1}.

To excite modes with longer wavelengths, the beam width must be increased to allow for larger-scale modes, and the proton beam should be broader to imprint seed fields at those scales.

H.4 Pitch-Angle Evolution Equation (Eq. (5.6))

We work in the guiding-center, collisionless limit where the field varies slowly compared to the gyro-motion, so the first adiabatic invariant is conserved. Assuming negligible parallel electric field and radiative losses, the energy is constant, $\dot{\gamma} = 0$, and the first invariant is

$$\mu \equiv \frac{p_\perp^2}{2m\gamma B} = \text{const.} \tag{H.12}$$

Here $p = \gamma m v$ is the relativistic momentum, $B = B(z)$, and $v_\parallel = \frac{c\, p_\parallel}{\gamma m}$.

Differentiate μ along the trajectory:

$$0 = \frac{d}{dt}\left(\frac{p_\perp^2}{2m\gamma B}\right) = \frac{p_\perp}{m\gamma B}\frac{dp_\perp}{dt} - \frac{p_\perp^2}{2m\gamma B^2}\frac{dB}{dt}, \tag{H.13}$$

which gives

$$\frac{1}{p_\perp}\frac{dp_\perp}{dt} = \frac{1}{2B}\frac{dB}{dt}. \tag{H.14}$$

With constant γ the magnitude $p = \sqrt{p_\perp^2 + p_\parallel^2}$ is constant, so write $p_\perp = p\sin\theta$ and $p_\parallel = p\cos\theta$ with $\tan\theta = p_\perp/p_\parallel$. Then

$$\frac{dp_\perp}{dt} = p\cos\theta\,\frac{d\theta}{dt}. \tag{H.15}$$

Insert this into (H.14) and use $dB/dt = v_\parallel\, dB/dz = \frac{c\,p_\parallel}{\gamma m}\frac{dB}{dz}$:

$$p\cos\theta\,\frac{d\theta}{dt} = \frac{p\sin\theta}{2B}\,\frac{c\,p_\parallel}{\gamma m}\,\frac{dB}{dz}. \tag{H.16}$$

Cancel p and use $p_\parallel = p\cos\theta$ to obtain

$$\frac{d\theta}{dt} = \sin\theta\,\frac{c\,p}{2\gamma m}\,\frac{1}{B}\frac{dB}{dz}. \tag{H.17}$$

Finally, with $p/(mc) = \sqrt{\gamma^2-1}/\gamma$,

$$\frac{d\theta}{dt} = \sin\theta\,\frac{\sqrt{\gamma^2-1}}{\gamma}\,\frac{c}{2B(z)}\,\frac{dB(z)}{dz} \tag{H.18}$$

which is Eq. (5.6) with the explicit CGS factor c. This result uses only $\dot\gamma = 0$, $\dot\mu = 0$, and guiding-center motion along z with $v_\parallel = \frac{c\,p_\parallel}{\gamma m}$.

BIBLIOGRAPHY

[1] P. Kropotkin. *The conquest of bread*. Penguin UK, 2015.

[2] L. Wittgenstein. *Philosophical investigations*. John Wiley & Sons, 2009.

[3] Y. L. Klimontovich. "On the method of second quantization in phase space". In: *Sov. Phys. JETP* 6.33 (1958), p. 4.

[4] A. A. Vlasov. "The vibrational properties of an electron gas". In: *Soviet Physics Uspekhi* 10.6 (1968), p. 721.

[5] L. Landau and D. Ter Haar. "61–On the vibrations of the electronic plasma". In: *The Collected Papers of LD Landau* (1965), pp. 445–460.

[6] E. S. Weibel. "Spontaneously growing transverse waves in a plasma due to an anisotropic velocity distribution". In: *Physical Review Letters* 2.3 (1959), p. 83.

[7] A. F. Bott, S. C. Cowley, and A. A. Schekochihin. "Kinetic stability of Chapman–Enskog plasmas". In: *Journal of Plasma Physics* 90.2 (2024), p. 975900207.

[8] A. A. Schekochihin. "MHD turbulence: a biased review". In: *Journal of Plasma Physics* 88.5 (2022), p. 155880501.

[9] S. Lebedev et al. "Laboratory astrophysics and collimated stellar outflows: The production of radiatively cooled hypersonic plasma jets". In: *The Astrophysical Journal* 564.1 (2002), p. 113.

[10] J. Meinecke et al. "Developed turbulence and nonlinear amplification of magnetic fields in laboratory and astrophysical plasmas". In: *Proceedings of the National Academy of Sciences* 112.27 (2015), pp. 8211–8215.

[11] F. Fiuza et al. "Electron acceleration in laboratory-produced turbulent collisionless shocks". In: *Nature physics* 16.9 (2020), pp. 916–920.

[12] C. Chen et al. "Multi-species measurements of the firehose and mirror instability thresholds in the solar wind". In: *The Astrophysical Journal Letters* 825.2 (2016), p. L26.

[13] D. Hatch et al. "Microtearing modes as the source of magnetic fluctuations in the JET pedestal". In: *Nuclear Fusion* 61.3 (2021), p. 036015.

[14] N. R. Council et al. *Frontiers in high energy density physics: the x-games of contemporary science*. National Academies Press, 2003.

[15] D. Uzdensky et al. "Extreme plasma astrophysics". In: *arXiv preprint arXiv:1903.05328* (2019).

[16] J. Schwinger. "On gauge invariance and vacuum polarization". In: *Physical Review* 82.5 (1951), p. 664.

[17] A. Lightman. "Relativistic thermal plasmas-Pair processes and equilibria". In: *The Astrophysical Journal* 253 (1982), pp. 842–858.

[18] V. I. Ritus. "Quantum effects of the interaction of elementary particles with an intense electromagnetic field". In: *J. Sov. Laser Res.; (United States)* 6.5 (Sept. 1985).

[19] A. Di Piazza et al. "Extremely high-intensity laser interactions with fundamental quantum systems". In: *Reviews of Modern Physics* 84.3 (2012), p. 1177.

[20] T. Blackburn. "Radiation reaction in electron–beam interactions with high-intensity lasers". In: *Reviews of Modern Plasma Physics* 4.1 (2020), p. 5.

[21] T. Grismayer et al. "Laser absorption via quantum electrodynamics cascades in counter propagating laser pulses". In: *Physics of Plasmas* 23.5 (2016), p. 056706.

[22] T. Grismayer et al. "Seeded QED cascades in counterpropagating laser pulses". In: *Physical Review E* 95.2 (2017), p. 023210.

[23] P. J. Bilbao and L. O. Silva. "Radiation reaction cooling as a source of anisotropic momentum distributions with inverted populations". In: *Physical Review Letters* 130.16 (2023), p. 165101.

[24] V. Zhdankin, M. W. Kunz, and D. A. Uzdensky. "Synchrotron Firehose Instability". In: *The Astrophysical Journal* 944.1 (2023), p. 24.

[25] A. Griffith, K. Qu, and N. J. Fisch. "Particle deceleration for collective QED signatures". In: *Physics of Plasmas* 29.7 (2022), p. 073104. DOI: 10.1063/5.0095928.

[26] R. C. Duncan and C. Thompson. "Formation of very strongly magnetized neutron stars-Implications for gamma-ray bursts". In: *Astrophysical Journal, Part 2-Letters (ISSN 0004-637X), vol. 392, no. 1, June 10, 1992, p. L9-L13. Research supported by NSERC.* 392 (1992), pp. L9–L13.

[27] V. M. Kaspi and A. M. Beloborodov. "Magnetars". In: *Annual Review of Astronomy and Astrophysics* 55 (2017), pp. 261–301.

[28] M. Vranic et al. "Quantum radiation reaction in head-on laser-electron beam interaction". In: *New Journal of Physics* 18.7 (2016), p. 073035.

[29] A. A. Philippov, A. Spitkovsky, and B. Cerutti. "Ab initio pulsar magnetosphere: three-dimensional particle-in-cell simulations of oblique pulsars". In: *The Astrophysical Journal Letters* 801.1 (2015), p. L19.

[30] F. Cruz et al. "Coherent emission from QED cascades in pulsar polar caps". In: *The Astrophysical Journal Letters* 919.1 (2021), p. L4.

[31] F. Cruz, T. Grismayer, and L. O. Silva. "Kinetic model of large-amplitude oscillations in neutron star pair cascades". In: *The Astrophysical Journal* 908.2 (2021), p. 149.

[32] A. A. Philippov, A. Spitkovsky, and B. Cerutti. "Ab initio pulsar magnetosphere: three-dimensional particle-in-cell simulations of oblique pulsars". In: *The Astrophysical Journal Letters* 801.1 (2015), p. L19.

[33] R. Torres et al. "OSIRIS-GR: General relativistic activation of the polar cap of a compact neutron star". In: *New Astronomy* 112 (2024), p. 102261.

[34] A. Timokhin and A. Harding. "On the polar cap cascade pair multiplicity of young pulsars". In: *The Astrophysical Journal* 810.2 (2015), p. 144.

[35] A. Timokhin and A. Harding. "On the maximum pair multiplicity of pulsar cascades". In: *The Astrophysical Journal* 871.1 (2019), p. 12.

[36] A. Y. Chen and Y. Yuan. "Physics of pair producing gaps in black hole magnetospheres. II. General relativity". In: *The Astrophysical Journal* 895.2 (2020), p. 121.

[37] A. Pe'er and E. Waxman. "Prompt gamma-ray burst spectra: detailed calculations and the effect of pair production". In: *The Astrophysical Journal* 613.1 (2004), p. 448.

[38] A. P. Lightman and A. A. Zdziarski. "Pair production and Compton scattering in compact sources and comparison to observations of active galactic nuclei". In: *Astrophysical Journal, Part 1 (ISSN 0004-637X), vol. 319, Aug. 15, 1987, p. 643-661.* 319 (1987), pp. 643–661.

[39] D. R. Lorimer et al. "A bright millisecond radio burst of extragalactic origin". In: *Science* 318.5851 (2007), pp. 777–780.

[40] E. Petroff, J. Hessels, and D. Lorimer. "Fast radio bursts". In: *The Astronomy and Astrophysics Review* 27 (2019), pp. 1–75.

[41] J. M. Cordes and S. Chatterjee. "Fast radio bursts: an extragalactic enigma". In: *Annual Review of Astronomy and Astrophysics* 57 (2019), pp. 417–465.

[42] B. D. Metzger, B. Margalit, and L. Sironi. "Fast radio bursts as synchrotron maser emission from decelerating relativistic blast waves". In: *Monthly Notices of the Royal Astronomical Society* 485.3 (2019), pp. 4091–4106.

[43] M. Lyutikov. "Brightness temperature constraints on coherent processes in magnetospheres of neutron stars". In: *The Astrophysical Journal Letters* 918.1 (2021), p. L11.

[44] C. D. Bochenek et al. "A fast radio burst associated with a Galactic magnetar". In: *Nature* 587.7832 (2020), pp. 59–62.

[45] C. Collaboration et al. "Sub-second periodicity in a fast radio burst". In: *Nature* 607.7918 (2022), pp. 256–259.

[46] S. Olausen and V. Kaspi. "The McGill magnetar catalog". In: *The Astrophysical Journal Supplement Series* 212.1 (2014), p. 6.

[47] T. Gold. "Rotating neutron stars and the nature of pulsars". In: *Nature* 221.5175 (1969), pp. 25–27.

[48] I. Plotnikov and L. Sironi. "The synchrotron maser emission from relativistic shocks in Fast Radio Bursts: 1D PIC simulations of cold pair plasmas". In: *Monthly Notices of the Royal Astronomical Society* 485.3 (2019), pp. 3816–3833.

[49] M. Lyutikov. "Coherent Emission in Pulsars, Magnetars, and Fast Radio Bursts: Reconnection-driven Free Electron Laser". In: *The Astrophysical Journal* 922.2 (2021), p. 166.

[50] G. D. entürk et al. “Gamma-ray Observational Properties of TeV-detected Blazars”. In: *The Astrophysical Journal* 764.2, 119 (Feb. 2013), p. 119. DOI: 10.1088/0004-637X/764/2/119. arXiv: 1301.3697 [astro-ph.HE].

[51] F. Aharonian et al. “A low level of extragalactic background light as revealed by γ-rays from blazars”. In: *Nature* 440.7087 (2006), pp. 1018–1021.

[52] D. A. Uzdensky. “Relativistic turbulence with strong synchrotron and synchrotron self-Compton cooling”. In: *Monthly Notices of the Royal Astronomical Society* 477.3 (2018), pp. 2849–2857.

[53] V. Zhdankin et al. “Kinetic turbulence in shining pair plasma: intermittent beaming and thermalization by radiative cooling”. In: *Monthly Notices of the Royal Astronomical Society* 493.1 (2020), pp. 603–626.

[54] V. Zhdankin, D. A. Uzdensky, and M. W. Kunz. “Production and persistence of extreme two-temperature plasmas in radiative relativistic turbulence”. In: *The Astrophysical Journal* 908.1 (2021), p. 71.

[55] A. Socrates, S. W. Davis, and O. Blaes. “Turbulent comptonization in black hole accretion disks”. In: *The Astrophysical Journal* 601.1 (2004), p. 405.

[56] D. Groelj et al. “Radiative particle-in-cell simulations of turbulent comptonization in magnetized Black-Hole Coronae”. In: *Physical Review Letters* 132.8 (2024), p. 085202.

[57] J. Mehlhaff, M. Zhou, and V. Zhdankin. “Radiative relativistic turbulence as an in situ pair-plasma source in blazar jets”. In: *arXiv preprint arXiv:2504.01072* (2025).

[58] H.-S. Park et al. “Laboratory astrophysical collisionless shock experiments on Omega and NIF”. In: *Journal of Physics: Conference Series*. Vol. 688. 1. IOP Publishing. 2016, p. 012084.

[59] A. Stockem et al. “Exploring the nature of collisionless shocks under laboratory conditions”. In: *Scientific Reports* 4.1 (2014), p. 3934.

[60] A. F. Bott et al. “Time-resolved turbulent dynamo in a laser plasma”. In: *Proceedings of the National Academy of Sciences* 118.11 (2021), e2015729118.

[61] E. Los et al. “Observation of quantum effects on radiation reaction in strong fields”. In: *arXiv preprint arXiv:2407.12071* (2024).

[62] D. Burke et al. “Positron production in multiphoton light-by-light scattering”. In: *Physical Review Letters* 79.9 (1997), p. 1626.

[63] J. Cole et al. “Experimental evidence of radiation reaction in the collision of a high-intensity laser pulse with a laser-wakefield accelerated electron beam”. In: *Physical Review X* 8.1 (2018), p. 011020.

[64] K. Poder et al. “Experimental signatures of the quantum nature of radiation reaction in the field of an ultraintense laser”. In: *Physical Review X* 8.3 (2018), p. 031004.

[65] V. Yakimenko et al. “FACET-II facility for advanced accelerator experimental tests”. In: *Physical Review Accelerators and Beams* 22.10 (2019), p. 101301.

[66] H. Chen and F. Fiuza. "Perspectives on relativistic electron–positron pair plasma experiments of astrophysical relevance using high-power lasers". In: *Physics of Plasmas* 30.2 (2023).

[67] A. Maksimchuk et al. "Zettawatt-equivalent ultrashort pulse laser system (ZEUS) at the University of Michigan". In: *APS Division of Plasma Physics Meeting Abstracts*. Vol. 2019. 2019, YP10–049.

[68] N. Elkina et al. "QED cascades induced by circularly polarized laser fields". In: *Physical Review Special Topics–Accelerators and Beams* 14.5 (2011), p. 054401.

[69] C. P. Ridgers et al. "Modelling gamma-ray photon emission and pair production in high-intensity laser–matter interactions". In: *Journal of computational physics* 260 (2014), pp. 273–285.

[70] A. Gonoskov et al. "Charged particle motion and radiation in strong electromagnetic fields". In: *arXiv preprint arXiv:2107.02161* 94.4 (2021), p. 045001.

[71] P. Zhang et al. "Relativistic plasma physics in supercritical fields". In: *Physics of Plasmas* 27.5 (2020).

[72] C. Arrowsmith et al. "Laboratory realization of relativistic pair-plasma beams". In: *Nature Communications* 15.1 (2024), p. 5029.

[73] N. Shukla et al. "Conditions for the onset of the current filamentation instability in the laboratory". In: *Journal of Plasma Physics* 84.3 (June 2018). arXiv: 1709.09747 Publisher: Cambridge University Press. ISSN: 14697807. DOI: 10/gdr5xj.

[74] C. D. Arrowsmith et al. "Generating ultradense pair beams using 400 GeV/c protons". In: *Physical Review Research* 3.2 (2021), p. 023103.

[75] C. Arrowsmith. "The stability of electron-positron jets in laboratory plasmas". PhD thesis. University of Oxford, 2024.

[76] M. Simon and W. Axford. "Thermal Instability Resulting from Synchrotron Radiation". In: *Astrophysical Journal, vol. 150, p. 105* 150 (1967), p. 105.

[77] C. D. Arrowsmith et al. *in prep.* 2025.

[78] D. R. Nicholson and D. R. Nicholson. *Introduction to plasma theory*. Vol. 1. Wiley New York, 1983.

[79] A. A. Schekochihin. "Lectures on kinetic theory and magnetohydrodynamics of plasmas". In: *Lecture Notes for the Oxford MMathPhys Programme* (2022).

[80] I. B. Bernstein, J. M. Greene, and M. D. Kruskal. "Exact nonlinear plasma oscillations". In: *Physical Review* 108.3 (1957), p. 546.

[81] R. A. Fonseca et al. "OSIRIS: A three-dimensional, fully relativistic particle in cell code for modeling plasma based accelerators". In: *International Conference on Computational Science*. Springer. 2002, pp. 342–351.

[82] J. Dawson and C. Smith. *Some investigations of plasma instabilities in one-dimensional plasmas*. Tech. rep. Princeton Univ., N.J. Plasma Physics Lab., Nov. 1962. URL: https://www.osti.gov/biblio/4749412.

[83] J. Dawson. "One-dimensional plasma model". In: *The Physics of Fluids* 5.4 (1962), pp. 445–459.

[84] J. M. Dawson. *Electrostatic sheet model for a plasma and its modification to finite-size particles.* Tech. rep. Princeton Univ., NJ, 1970.

[85] J. M. Dawson. "Particle simulation of plasmas". In: *Reviews of modern physics* 55.2 (1983), p. 403.

[86] I. N. Ellis et al. "Studies of particle wake potentials in plasmas". In: *High Energy Density Physics* 7.3 (2011), pp. 191–196.

[87] M. Touati et al. "Kinetic theory of particle-in-cell simulation plasma and the ensemble averaging technique". In: *Plasma Physics and Controlled Fusion* 64.11 (2022), p. 115014.

[88] R. J. Ewart et al. "Collisionless relaxation of a Lynden-Bell plasma". In: *Journal of plasma physics* 88.5 (2022), p. 925880501.

[89] R. J. Ewart. "Universal equilibria, phase-space structure of collisionless plasma systems, and turbulence in non-Maxwellian plasmas". en. PhD thesis. 2024.

[90] M. Vranic et al. "All-optical radiation reaction at 1 0 21 w/cm 2". In: *Physical Review Letters* 113.13 (2014), p. 134801.

[91] M. Vranic et al. "Classical radiation reaction in particle-in-cell simulations". In: *Computer Physics Communications* 204 (2016), pp. 141–151.

[92] M. Vranic et al. "Particle merging algorithm for PIC codes". In: *Computer Physics Communications* 191 (2015), pp. 65–73.

[93] T. Liseykina, S. Popruzhenko, and A. Macchi. "Inverse Faraday effect driven by radiation friction". In: *New Journal of Physics* 18.7 (2016), p. 072001.

[94] Z. Gong et al. "Radiation reaction as an energy enhancement mechanism for laser-irradiated electrons in a strong plasma magnetic field". In: *Scientific reports* 9.1 (2019), pp. 1–11.

[95] K. Qu, S. Meuren, and N. J. Fisch. "Signature of collective plasma effects in beam-driven QED cascades". In: *Physical review letters* 127.9 (2021), p. 095001.

[96] L. Comisso and L. Sironi. "Pitch-angle anisotropy controls particle acceleration and cooling in radiative relativistic plasma turbulence". In: *Physical Review Letters* 127.25 (2021), p. 255102.

[97] A. Griffith, K. Qu, and N. J. Fisch. "Radiation Reaction Kinetics and Collective QED Signatures". In: *arXiv preprint arXiv:2312.04700* (2023).

[98] K. Qu, S. Meuren, and N. J. Fisch. "Creating pair plasmas with observable collective effects". In: *Plasma Physics and Controlled Fusion* 65.3 (2023), p. 034007.

[99] S. Bulanov et al. "On the energy spectrum evolution of electrons undergoing radiation cooling". In: *Fundamental Plasma Physics* (2024), p. 100036.

[100] L. D. Landau and E. M. Lifshitz. *The Classical Theory of Fields*. Vol. 2. Pergamon Press, Oxford, 1975.

[101] B. Cerutti and A. M. Beloborodov. "Electrodynamics of pulsar magnetospheres". In: *Space Science Reviews* 207.1 (2017), pp. 111–136.

[102] Y. Xue et al. "A magnetar-powered X-ray transient as the aftermath of a binary neutron-star merger". In: *Nature* 568.7751 (2019), pp. 198–201.

[103] R. Turolla, S. Zane, and A. Watts. "Magnetars: the physics behind observations. A review". In: *Reports on Progress in Physics* 78.11 (2015), p. 116901.

[104] A. Di Piazza, K. Hatsagortsyan, and C. Keitel. "Strong signatures of radiation reaction below the radiation-dominated regime". In: *Physical Review Letters* 102.25 (2009), p. 254802.

[105] A. Thomas et al. "Strong radiation-damping effects in a gamma-ray source generated by the interaction of a high-intensity laser with a wakefield-accelerated electron beam". In: *Physical Review X* 2.4 (2012), p. 041004.

[106] A. Fedotov et al. "Advances in QED with intense background fields". In: *Physics Reports* 1010 (2023), pp. 1–138.

[107] D. Nakamura et al. "Record indoor magnetic field of 1200 T generated by electromagnetic flux-compression". In: *Review of Scientific Instruments* 89.9 (2018), p. 095106.

[108] M. Murakami et al. "Generation of megatesla magnetic fields by intense-laser-driven microtube implosions". In: *Scientific reports* 10.1 (2020), p. 16653.

[109] K. Jiang, A. Pukhov, and C. Zhou. "Magnetic field amplification to gigagauss scale via hydrodynamic flows and dynamos driven by femtosecond lasers". In: *New Journal of Physics* 23.6 (2021), p. 063054.

[110] E. Hirvijoki et al. "Radiation reaction induced non-monotonic features in runaway electron distributions". In: *Journal of Plasma Physics* 81.5 (2015), p. 475810502. DOI: 10.1017/S0022377815000513.

[111] J. Decker et al. "Numerical characterization of bump formation in the runaway electron tail". In: *Plasma Physics and Controlled Fusion* 58.2 (2016), p. 025016.

[112] Z. Gong et al. "Radiation reaction induced spiral attractors in ultra-intense colliding laser beams". In: *Matter and Radiation at Extremes* 1.6 (2016), pp. 308–315.

[113] P. J. Bilbao et al. "Ring momentum distributions as a general feature of Vlasov dynamics in the synchrotron dominated regime". In: *Physics of Plasmas* 31.5 (2024).

[114] P. J. Bilbao, T. Silva, and L. O. Silva. "Radiative cooling induced coherent maser emission in relativistic plasmas". In: *Science Advances* 11.15 (2025), eadt8912.

[115] G. B. Rybicki and A. P. Lightman. *Radiative processes in astrophysics*. John Wiley & Sons, 1991.

[116] L. Kuz'menkov. "The Bogolyubov hierarchy of equations for relativistic systems. Radiation damping of waves in a plasma". In: 23 (1978), pp. 469–471.

[117] R. Hazeltine and S. Mahajan. "Radiation reaction in fusion plasmas". In: *Physical Review E* 70.4 (2004), p. 046407.

[118] M. Tamburini et al. “Radiation reaction effects on electron nonlinear dynamics and ion acceleration in laser–solid interaction”. In: *Nuclear Instruments and Methods in Physics Research Section A: Accelerators, Spectrometers, Detectors and Associated Equipment* 653.1 (2011), pp. 181–185.

[119] D. Le Quéau, R. Pellat, and A. Roux. “Direct generation of the auroral kilometric radiation by the maser synchrotron instability: Physical mechanism and parametric study”. In: *Journal of Geophysical Research: Space Physics* 89.A5 (1984), pp. 2831–2841.

[120] R. Bingham and R. Cairns. “Generation of auroral kilometric radiation by electron horseshoe distributions”. In: *Physics of Plasmas* 7.7 (2000), pp. 3089–3092.

[121] R. Cairns et al. “A cyclotron maser instability with application to space and laboratory plasmas”. In: *Physica Scripta* 2005.T116 (2005), p. 23.

[122] R. Cairns, I. Vorgul, and R. Bingham. “Cyclotron maser radiation from an inhomogeneous plasma”. In: *Physical Review Letters* 101.21 (2008), p. 215003.

[123] D. Melrose and M. Wheatland. “Is cyclotron maser emission in solar flares driven by a horseshoe distribution?” In: *Solar Physics* 291.12 (2016), pp. 3637–3658.

[124] D. Melrose. “The models for radio emission from pulsars–The outstanding issues”. In: *Journal of Astrophysics and Astronomy* 16.2 (1995), pp. 137–164.

[125] M. Lyutikov, R. D. Blandford, and G. Machabeli. “On the nature of pulsar radio emission”. In: *Monthly Notices of the Royal Astronomical Society* 305.2 (1999), pp. 338–352.

[126] X. Davoine et al. “Ion-channel laser growth rate and beam quality requirements”. In: *Journal of Plasma Physics* 84.3 (2018), p. 905840304.

[127] D. Melrose, M. Rafat, and A. Mastrano. “Pulsar radio emission mechanisms: a critique”. In: *Monthly Notices of the Royal Astronomical Society* 500.4 (2021), pp. 4530–4548.

[128] P. A. M. Dirac. “Classical theory of radiating electrons”. In: *Proceedings of the Royal Society of London. Series A. Mathematical and Physical Sciences* 167.929 (1938), pp. 148–169.

[129] F. Hartemann and N. Luhmann Jr. “Classical electrodynamical derivation of the radiation damping force”. In: *Physical Review Letters* 74.7 (1995), p. 1107.

[130] A. Bell and J. G. Kirk. “Possibility of prolific pair production with high-power lasers”. In: *Physical Review Letters* 101.20 (2008), p. 200403.

[131] M. Tamburini et al. “Radiation reaction effects on radiation pressure acceleration”. In: *New Journal of Physics* 12.12 (2010), p. 123005.

[132] C. Shen and D. White. “Energy straggling and radiation reaction for magnetic bremsstrahlung”. In: *Physical Review Letters* 28.7 (1972), p. 455.

[133] C. Shen. “Magnetic bremsstrahlung in an intense magnetic field”. In: *Physical Review D* 6.10 (1972), p. 2736.

[134] R. Hakim and A. Mangeney. “Relativistic kinetic equations including radiation effects. I. Vlasov approximation”. In: *Journal of Mathematical Physics* 9.1 (1968), pp. 116–130.

[135] R. Hakim and A. Mangeney. “Collective oscillations of a relativistic radiating electron plasma”. In: *The Physics of Fluids* 14.12 (1971), pp. 2751–2761.

[136] A. Stahl et al. "Effective critical electric field for runaway-electron generation". In: *Physical Review Letters* 114.11 (2015), p. 115002.

[137] V. Berezhiani, S. Mahajan, and Z. Yoshida. "Plasma acceleration and cooling by strong laser field due to the action of radiation reaction force". In: *Physical Review E* 78.6 (2008), p. 066403.

[138] R. Hazeltine and S. Mahajan. "Closed fluid description of relativistic, magnetized plasma interacting with radiation field". In: *Physical Review E* 70.3 (2004), p. 036404.

[139] J. Decker et al. "Bump formation in the runaway electron tail". In: *arXiv preprint arXiv:1503.03881* (2015).

[140] T. Silva, P. J. Bilbao, and L. O. Silva. *in prep.* 2025.

[141] M. L. Nastac et al. "Phase-space entropy cascade and irreversibility of stochastic heating in nearly collisionless plasma turbulence". In: *Physical Review E* 109.6 (2024), p. 065210.

[142] F. Assunçao, P. J. Bilbao, and L. O. Silva. *in prep.* 2025.

[143] F. Miniati and A. Elyiv. "Relaxation of blazar-induced pair beams in cosmic voids". In: *The Astrophysical Journal* 770.1 (2013), p. 54.

[144] B. Trubnikov. "Particle interactions in a fully ionized plasma". In: *Rev. Plasma Phys.* 1 (1965).

[145] D. Sivukhin. "Coulomb collisions in a fully ionized plasma". In: *Rev. Plasma Phys.(USSR)(Engl. Transl.)* 4 (1966).

[146] R. Goldston and P. Rutherford. *Introduction to plasma physics*. IOP Publishing, UK, 1995.

[147] J. J. Thomson. *Conduction of electricity through gases*. University press, 1906.

[148] A. H. Compton. "A quantum theory of the scattering of X-rays by light elements". In: *Physical review* 21.5 (1923), p. 483.

[149] O. Klein and Y. Nishina. "Über die Streuung von Strahlung durch freie Elektronen nach der neuen relativistischen Quantendynamik von Dirac". In: *Zeitschrift für Physik* 52.11 (1929), pp. 853–868.

[150] M. Lyutikov, N. Otte, and A. McCann. "The very high energy emission from pulsars: a case for inverse compton scattering". In: *The Astrophysical Journal* 754.1 (2012), p. 33.

[151] S. Wang et al. "X-ray emission from betatron motion in a plasma wiggler". In: *Physical Review Letters* 88.13 (2002), p. 135004.

[152] W. Lu et al. "Generating multi-GeV electron bunches using single stage laser wakefield acceleration in a 3D nonlinear regime". In: *Physical Review Special Topics-Accelerators and Beams* 10.6 (2007), p. 061301.

[153] Y. Glinec et al. "Direct observation of betatron oscillations in a laser-plasma electron accelerator". In: *EPL (Europhysics Letters)* 81.6 (2008), p. 64001.

[154] A. Pukhov, Z.-M. Sheng, and J. Meyer-ter-Vehn. "Particle acceleration in relativistic laser channels". In: *Physics of Plasmas* 6.7 (1999), pp. 2847–2854.

[155] Z. Wadiasingh and A. Timokhin. "Repeating fast radio bursts from magnetars with low magnetospheric twist". In: *The Astrophysical Journal* 879.1 (2019), p. 4.

[156] P. Goldreich and W. H. Julian. "Pulsar electrodynamics". In: *Astrophysical Journal, vol. 157, p. 869* 157 (1969), p. 869.

[157] A. Levinson and B. Cerutti. "Particle-in-cell simulations of pair discharges in a starved magnetosphere of a Kerr black hole". In: *Astronomy & Astrophysics* 616 (2018), A184.

[158] G. Sarri et al. "Generation of neutral and high-density electron–positron pair plasmas in the laboratory". In: *Nature communications* 6.1 (2015), p. 6747.

[159] C. Zhang et al. "Ultrafast optical field–ionized gases-A laboratory platform for studying kinetic plasma instabilities". In: *Science Advances* 5.9 (2019), eaax4545.

[160] K. Qu, A. Griffith, and N. J. Fisch. "Pair filamentation and laser scattering in beam-driven QED cascades". In: *Physical Review E* 109.3 (2024), p. 035208.

[161] M. Zhou et al. "Magnetogenesis in a collisionless plasma: from Weibel instability to turbulent dynamo". In: *The Astrophysical Journal* 960.1 (2023), p. 12.

[162] A. Vanthieghem et al. "The role of plasma instabilities in relativistic radiation-mediated shocks: stability analysis and particle-in-cell simulations". In: *Monthly Notices of the Royal Astronomical Society* 511.2 (2022), pp. 3034–3045.

[163] P. Sprangle and A. Drobot. "The linear and self-consistent nonlinear theory of the electron cyclotron maser instability". In: *IEEE Transactions on Microwave Theory and Techniques* 25.6 (1977), pp. 528–544.

[164] K.-R. Chen et al. "Unified theory and comparative study of cyclotron masers, ion-channel lasers, and free electron lasers". In: *Physics of Fluids B: Plasma Physics* 3.5 (1991), pp. 1270–1278.

[165] D. Melrose. "Coherent emission mechanisms in astrophysical plasmas". In: *Reviews of Modern Plasma Physics* 1.1 (2017), pp. 1–81.

[166] B. Zhang. "The physical mechanisms of fast radio bursts". In: *Nature* 587.7832 (2020), pp. 45–53.

[167] R. A. Treumann. "The electron–cyclotron maser for astrophysical application". In: *The Astronomy and Astrophysics Review* 13.4 (2006), pp. 229–315.

[168] I. E. Ochs. "Synchrotron-driven instabilities in relativistic plasmas of arbitrary opacity". In: *arXiv preprint arXiv:2407.13106* 975.1 (2024), p. 30.

[169] A. F. Alexandrov, L. S. Bogdankevich, A. A. Rukhadze, et al. *Principles of plasma electrodynamics*. Vol. 9. Springer, 1984.

[170] R. Winglee. "Fundamental and harmonic electron cyclotron maser emission". In: *Journal of Geophysical Research: Space Physics* 90.A10 (1985), pp. 9663–9674.

[171] L. Mandel and E. Wolf. "Coherence properties of optical fields". In: *Reviews of modern physics* 37.2 (1965), p. 231.

[172] A. E. Siegman. *Lasers*. University science books, 1986.

[173] W. Lu and P. Kumar. "On the radiation mechanism of repeating fast radio bursts". In: *Monthly Notices of the Royal Astronomical Society* 477.2 (2018), pp. 2470–2493.

[174] J. M. Jauch and F. Rohrlich. *The theory of photons and electrons: the relativistic quantum field theory of charged particles with spin one-half*. Springer Science & Business Media, 2012.

[175] S. Mereghetti et al. "INTEGRAL discovery of a burst with associated radio emission from the magnetar SGR 1935+ 2154". In: *The Astrophysical Journal Letters* 898.2 (2020), p. L29.

[176] T. H. Stix. *Waves in plasmas*. Springer Science & Business Media, 1992.

[177] T. Hankins, G. Jones, and J. Eilek. "The Crab pulsar at centimeter wavelengths. I. Ensemble characteristics". In: *The Astrophysical Journal* 802.2 (2015), p. 130.

[178] K. R. Lind and R. D. Blandford. "Semidynamical models of radio jets-Relativistic beaming and source counts". In: *Astrophysical Journal, Part 1 (ISSN 0004-637X), vol. 295, Aug. 15, 1985, p. 358-367. Research supported by the Alfred P. Sloan Foundation.* 295 (1985), pp. 358–367.

[179] L. W. Casperson. "Threshold characteristics of mirrorless lasers". In: *Journal of Applied Physics* 48.1 (1977), pp. 256–262.

[180] A. Philippov and M. Kramer. "Pulsar magnetospheres and their radiation". In: *Annual Review of Astronomy and Astrophysics* 60 (2022), pp. 495–558.

[181] M. Bailes. "The discovery and scientific potential of fast radio bursts". In: *Science* 378.6620 (2022), eabj3043.

[182] W. Zhu et al. "A radio pulsar phase from SGR J1935+ 2154 provides clues to the magnetar FRB mechanism". In: *Science advances* 9.30 (2023), eadf6198.

[183] S. P. Mangles et al. "Monoenergetic beams of relativistic electrons from intense laser–plasma interactions". In: *Nature* 431.7008 (2004), pp. 535–538.

[184] J. Faure et al. "A laser–plasma accelerator producing monoenergetic electron beams". In: *Nature* 431.7008 (2004), pp. 541–544.

[185] M. J. Hogan et al. "Multi-GeV energy gain in a plasma-wakefield accelerator". In: *Physical review letters* 95.5 (2005), p. 054802.

[186] A. Gonsalves et al. "Petawatt laser guiding and electron beam acceleration to 8 GeV in a laser-heated capillary discharge waveguide". In: *Physical review letters* 122.8 (2019), p. 084801.

[187] C. Joshi et al. "Plasma wakefield acceleration experiments at FACET II". In: *Plasma Physics and Controlled Fusion* 60.3 (2018), p. 034001.

[188] A. Pukhov. "Strong field interaction of laser radiation". In: *Reports on progress in Physics* 66.1 (2002), p. 47.

[189] D. H. Whittum, A. M. Sessler, and J. M. Dawson. "Ion-channel laser". In: *Physical review letters* 64.21 (1990), p. 2511.

[190] D. H. Whittum. "Electromagnetic instability of the ion-focused regime". In: *Physics of Fluids B: Plasma Physics* 4.3 (1992), pp. 730–739.

[191] A. Arefiev et al. "Beyond the ponderomotive limit: Direct laser acceleration of relativistic electrons in sub-critical plasmas". In: *Physics of Plasmas* 23.5 (2016).

[192] M. Vranic, R. A. Fonseca, and L. O. Silva. "Extremely intense laser-based electron acceleration in a plasma channel". In: *Plasma physics and controlled fusion* 60.3 (2018), p. 034002.

[193] R. Babjak et al. "Direct laser acceleration in underdense plasmas with multi-PW lasers: a path to high-charge, GeV-class electron bunches". In: *Physical Review Letters* 132.12 (2024), p. 125001.

[194] R. Babjak and M. Vranic. "Betatron radiation emitted during the direct laser acceleration of electrons in underdense plasmas". In: *arXiv preprint arXiv:2502.06744* (2025).

[195] A. Rousse et al. "Production of a keV X-Ray Beam from Synchrotron Radiation in Relativistic Laser-Plasma Interaction". In: *Physical review letters* 93.13 (2004), p. 135005.

[196] E. P. Lee. *Radiation damping of betatron oscillations*. Tech. rep. Lawrence Livermore National Lab., 1982.

[197] P. Michel et al. "Radiative damping and electron beam dynamics in plasma-based accelerators". In: *Physical Review E-Statistical, Nonlinear, and Soft Matter Physics* 74.2 (2006), p. 026501.

[198] P. J. Bilbao, T. Silva, and L. O. Silva. *Simulation results: Radiative cooling induced coherent maser emission in relativistic plasmas (v1.0)*. 2024. DOI: 10.5281/zenodo.13947842. URL: https://doi.org/10.5281/zenodo.13947842.

[199] J. Vieira and J. Mendonça. "Nonlinear laser driven donut wakefields for positron and electron acceleration". In: *Physical Review Letters* 112.21 (2014), p. 215001.

[200] W. Lu et al. "Nonlinear theory for relativistic plasma wakefields in the blowout regime". In: *Physical review letters* 96.16 (2006), p. 165002.

[201] J. Ng et al. "Observation of plasma focusing of a 28.5 GeV positron beam". In: *Physical review letters* 87.24 (2001), p. 244801.

[202] M. Hogan et al. "Ultrarelativistic-positron-beam transport through meter-scale plasmas". In: *Physical review letters* 90.20 (2003), p. 205002.

[203] E. Esarey, C. B. Schroeder, and W. P. Leemans. "Physics of laser-driven plasma-based electron accelerators". In: *Reviews of modern physics* 81.3 (2009), pp. 1229–1285.

[204] N. M. Krylov and N. N. Bogoliubov. *Introduction to non-linear mechanics*. 11. Princeton university press, 1950.

[205] H. Goldstein, C. Poole, and J. Safko. "Classical Mechanics, 3rd edn. Addision Wesley". In: *Reading, MA* (1990).

[206] A. Popp et al. "All-optical steering of laser-wakefield-accelerated electron beams". In: *Physical review letters* 105.21 (2010), p. 215001.

[207] S. F. Martins et al. "Exploring laser-wakefield-accelerator regimes for near-term lasers using particle-in-cell simulation in Lorentz-boosted frames". In: *Nature Physics* 6.4 (2010), pp. 311–316.

[208] J. W. Yoon et al. "Realization of laser intensity over 10 23 W/cm 2". In: *Optica* 8.5 (2021), pp. 630–635.

[209] M. Cernaianu et al. "Commissioning of the 1 PW experimental area at ELI-NP using a short focal parabolic mirror for proton acceleration". In: *Matter and Radiation at Extremes* 10.2 (2025).

[210] T. Piran. "The physics of gamma-ray bursts". In: *Reviews of modern physics* 76.4 (2004), pp. 1143–1210.

[211] P. Meszaros and M. Rees. "Relativistic fireballs and their impact on external matter-Models for cosmological gamma-ray bursts". In: *Astrophysical Journal, Part 1 (ISSN 0004-637X), vol. 405, no. 1, p. 278-284.* 405 (1993), pp. 278–284.

[212] Y. Kazimura et al. "Generation of a small-scale quasi-static magnetic field and fast particles during the collision of electron-positron plasma clouds". In: *The Astrophysical Journal* 498.2 (1998), p. L183.

[213] M. V. Medvedev, L. O. Silva, and M. Kamionkowski. "Cluster magnetic fields from large-scale structure and galaxy cluster shocks". In: *The Astrophysical Journal* 642.1 (2006), p. L1.

[214] S. Martins et al. "Ion dynamics and acceleration in relativistic shocks". In: *The Astrophysical Journal* 695.2 (2009), p. L189.

[215] N. Shukla et al. "Interaction of ultra relativistic e^-/e^+ fireball beam with plasma". In: *New Journal of Physics* 22.1 (2020), p. 013030.

[216] Z. Gong, K. Z. Hatsagortsyan, and C. H. Keitel. "Electron polarization in ultrarelativistic plasma current filamentation instabilities". In: *Physical Review Letters* 130.1 (2023), p. 015101.

[217] L. O. Silva et al. "On the role of the purely transverse Weibel instability in fast ignitor scenarios". In: *Physics of Plasmas* 9.6 (2002), pp. 2458–2461.

[218] A. Spitkovsky. "Particle acceleration in relativistic collisionless shocks: Fermi process at last?" In: *The Astrophysical Journal* 682.1 (2008), p. L5.

[219] T. Silva, B. Afeyan, and L. O. Silva. "Weibel instability beyond bi-Maxwellian anisotropy". In: *Physical Review E* 104.3 (2021), p. 035201.

[220] B. D. Fried and S. D. Conte. *The plasma dispersion function: the Hilbert transform of the Gaussian*. Academic press, 2015.

[221] C. Ruyer and F. Fiuza. "Disruption of current filaments and isotropization of the magnetic field in counterstreaming plasmas". In: *Physical Review Letters* 120.24 (2018), p. 245002.

[222] M. Tzoufras et al. "Space-charge effects in the current-filamentation or Weibel instability". In: *Physical review letters* 96.10 (2006), p. 105002.

[223] T. Silva and J. Vieira. "Positron acceleration in plasma waves driven by non-neutral fireball beams". In: *Physical Review Accelerators and Beams* 26.9 (2023), p. 091301.

[224] M. Lemoine et al. "Physics of weibel-mediated relativistic collisionless shocks". In: *Physical review letters* 123.3 (2019), p. 035101.

[225] A. W. Chao et al. *Handbook of accelerator physics and engineering*. World scientific, 2023.

[226] E. E. Los et al. *in prep.* 2025.

[227] J. Vieira, W. Mori, and P. Muggli. "Hosing instability suppression in self-modulated plasma wakefields". In: *Physical Review Letters* 112.20 (2014), p. 205001.

[228] J. W. D. Halliday et al. *in prep.* 2025.

[229] D. C. Speirs et al. "Numerical simulation of auroral cyclotron maser processes". In: *Plasma Physics and Controlled Fusion* 50.7 (2008), p. 074011.

[230] D. C. Speirs et al. "Numerical investigation of auroral cyclotron maser processes". In: *Physics of Plasmas* 17.5 (2010), p. 056501.

[231] C. Wu et al. "Saturation and energy-conversion efficiency of auroral kilometric radiation". In: *Astrophysical Journal, Part 1, vol. 248, Aug. 15, 1981, p. 384-391.* 248 (1981), pp. 384–391.

[232] A. Kulikov, S. Ecklund, and E. Reuter. *SLC positron source pulsed flux concentrator*. Tech. rep. Stanford Linear Accelerator Center, Menlo Park, CA (USA), 1991.

[233] E. E. Los et al. *in prep.* 2026.

[234] P. Pritchett. "Electron-cyclotron maser instability in relativistic plasmas". In: *The Physics of fluids* 29.9 (1986), pp. 2919–2930.

[235] D. Speirs et al. "Backward wave cyclotron-maser emission in the auroral magnetosphere". In: *Physical review letters* 113.15 (2014), p. 155002.

[236] K. Chu and J. Hirshfield. "Comparative study of the axial and azimuthal bunching mechanisms in electromagnetic cyclotron instabilities". In: *The Physics of Fluids* 21.3 (1978), pp. 461–466.

[237] A. D. Phelps et al. "Experimental and numerical investigation of auroral cyclotron maser processes". In: *2007 IEEE International Vacuum Electronics Conference*. IEEE. 2007, pp. 1–2.

[238] N. Shukla et al. "Enhancement in the electromagnetic beam-plasma instability due to ion streaming". In: *Journal of Plasma Physics* 78.2 (2012), pp. 181–187.

[239] G. W. F. Hegel. *Elements of the philosophy of right*. Cambridge University Press, 1991.

[240] M. Pouyez et al. "Multiplicity of electron-and photon-seeded electromagnetic showers at multipetawatt laser facilities". In: *Physical Review E* 110.6 (2024), p. 065208.

[241] N. Neitz and A. Di Piazza. "Stochasticity effects in quantum radiation reaction". In: *Physical review letters* 111.5 (2013), p. 054802.

[242] F. Niel et al. "From quantum to classical modeling of radiation reaction: A focus on stochasticity effects". In: *Physical Review E* 97.4 (2018), p. 043209.

[243] J. Schwinger. "On the classical radiation of accelerated electrons". In: *Physical review* 75.12 (1949), p. 1912.

[244] J. Schwinger et al. *Classical electrodynamics*. CRC Press, 2019.

[245] G. Bekefi. *Radiation processes in plasmas*. 1966.

[246] R. Pawula. "Approximation of the linear Boltzmann equation by the Fokker-Planck equation". In: *Physical review* 162.1 (1967), p. 186.

[247] M. Touati et al. "A reduced model for relativistic electron beam transport in solids and dense plasmas". In: *New Journal of Physics* 16.7 (2014), p. 073014.

[248] C. E. Shannon. "A mathematical theory of communication". In: *The Bell system technical journal* 27.3 (1948), pp. 379–423.

[249] V. Zhdankin. "Dimensional measures of generalized entropy". In: *Journal of Physics A: Mathematical and Theoretical* 56.38 (2023), p. 385002.

[250] L. D. Landau and E. Lifshitz. *Physical Kinetics: Volume 10*. Vol. 10. Pergarmon, 2012.

[251] M. Abramowitz and I. A. Stegun. *Handbook of mathematical functions: with formulas, graphs, and mathematical tables*. Vol. 55. Courier Corporation, 1965.

[252] J. Rosenzweig et al. "Space-charge oscillations in a self-modulated electron beam in multi-undulator free-electron lasers". In: *Nuclear Instruments and Methods in Physics Research Section A: Accelerators, Spectrometers, Detectors and Associated Equipment* 393.1-3 (1997), pp. 376–379.